

TROPICAL TROPOSPHERIC OZONE COLUMNS FROM NADIR  
SATELLITE RETRIEVALS USING THE CONVECTIVE  
CLOUDS DIFFERENTIAL (CCD) TECHNIQUE  
ON GOME, SCIAMACHY, AND GOME-2 DATA

M.Sc. Env. Phys.  
Elpida Leventidou



Dissertation zur Erlangung des Grades  
*Doktor der Naturwissenschaften*

 **Universität Bremen**

Institut für Umweltphysik  
Fachbereich 1  
Universität Bremen  
September 2017



# **Tropical tropospheric ozone columns from nadir satellite retrievals using the Convective Cloud Differential technique on GOME, SCIAMACHY and GOME-2 data**

Dissertation zur Erlangung des akademischen Grades des  
Doktor der Naturwissenschaften

(Dr. rer. nat.)

Vorgelegt von **Elpida Leventidou**

1. Gutachter: Prof. Dr. John P. Burrows  
2. Gutachter: Prof. Dr. Mihalis Vrekoussis  
Betreuer: Dr. Mark Weber

Datum des Kolloquiums: 17.11.2017



Universität Bremen  
Institut für Umweltphysik  
Fachbereich Physik and Elektrotechnik (FB1)  
Otto-Hahn-Allee 1, Gebäude NW1  
Postfach 330440, D-28334, Bremen



## Contents

	Page
<b>Abstract</b>	<b>vii</b>
<b>Publications</b>	<b>xi</b>
<b>Acknowledgements</b>	<b>xv</b>
<b>Motivation and Outline</b>	<b>xvii</b>
<b>1 Fundamentals</b>	<b>1</b>
1.1 Ozone in the Earth's atmosphere . . . . .	1
1.1.1 Evolution of the atmosphere . . . . .	1
1.1.2 The present atmosphere . . . . .	2
1.1.3 Discovery and distribution of atmospheric ozone . . . . .	5
1.2 Tropospheric ozone . . . . .	9
1.2.1 Tropospheric ozone chemistry . . . . .	10
1.2.2 Transport and mixing of tropospheric ozone . . . . .	16
1.2.3 Deposition of tropospheric ozone . . . . .	20
1.2.4 Impact of tropospheric ozone on climate and air pollution . . . . .	21
1.2.5 Impact of tropospheric ozone on biosphere . . . . .	23
1.3 Absorption spectroscopy . . . . .	24
1.3.1 Electromagnetic radiation . . . . .	24
1.3.2 Molecular energy states . . . . .	25
1.3.3 Radiation from the sun . . . . .	27
1.3.4 Atmospheric radiative transfer . . . . .	29
1.3.5 Absorption of UV-radiation from the atmosphere . . . . .	31
1.3.6 Spectroscopic parameters of O <sub>3</sub> . . . . .	32
1.4 Measuring total and tropospheric ozone from space . . . . .	35
1.4.1 The standard Differential Optical Absorption Spectroscopy (DOAS) . . . . .	35
1.4.2 The modified WFDOAS method for satellite total ozone retrieval . . . . .	38

---

1.4.3	Satellite-based tropospheric ozone measurement techniques . . . . .	39
1.5	Instruments . . . . .	40
1.5.1	GOME . . . . .	41
1.5.2	SCIAMACHY . . . . .	41
1.5.3	GOME-2 . . . . .	42
1.5.4	TROPOMI . . . . .	42
<b>2</b>	<b>CCD retrieval algorithm</b>	<b>45</b>
2.1	The Convective Cloud Differential (CCD) method . . . . .	45
2.2	Summary and discussion . . . . .	51
<b>3</b>	<b>TTCO retrievals, validation and uncertainty estimation</b>	<b>53</b>
3.1	Tropical tropospheric ozone column (TTCO) results from CCD . . . . .	53
3.2	Uncertainty estimation . . . . .	56
3.3	Validation with ozonesondes . . . . .	61
3.4	Comparison with Limb/Nadir Matching tropospheric ozone columns . . . . .	68
3.5	Summary and discussion . . . . .	71
<b>4</b>	<b>Tropical tropospheric ozone trends</b>	<b>73</b>
4.1	Harmonisation and merging of the multiple instrument TTCO data record . . . . .	73
4.2	Tropical tropospheric ozone trends . . . . .	77
4.2.1	Overview on known contributions to tropospheric ozone changes . . . . .	78
4.2.2	The multi-linear regression trend model . . . . .	81
4.2.3	Sensitivity and uncertainty of the trend . . . . .	85
4.2.4	Tropical tropospheric ozone trend results . . . . .	85
4.2.5	Comparisons of tropospheric ozone trends with ozonesondes . . . . .	93
4.2.6	Tropospheric ozone trends over mega-cities . . . . .	94
4.3	Summary and discussion . . . . .	97
<b>5</b>	<b>Variability of tropical tropospheric ozone</b>	<b>101</b>
5.1	Seasonal and annual variability of tropospheric ozone . . . . .	101
5.2	ENSO, QBO, Solar and seasonal cycle response to tropical tropospheric ozone . . . . .	105
5.3	Summary and discussion . . . . .	107
<b>6</b>	<b>El Niño and tropical tropospheric ozone</b>	<b>109</b>
6.1	El Niño Southern Oscillation (ENSO) and its influence on tropospheric ozone . . . . .	109
6.2	Comparing the influence of El Niño and La Niña events on tropical tropospheric ozone . . . . .	111
6.3	Tropical tropospheric ozone and its precursors during 2015 El Niño . . . . .	117
6.3.1	Tropospheric ozone precursors from satellite data . . . . .	117
6.3.2	Comparison with ECHAM5/MESy Atmospheric Chemistry (EMAC) model simulations . . . . .	123
6.4	Impact of biomass burning and dynamics during 2015 El Niño event . . . . .	132

---

6.5 Summary and discussion . . . . .	134
<b>7 Conclusions and Outlook</b>	<b>137</b>
7.1 Conclusions . . . . .	137
7.2 Outlook . . . . .	141
<b>Bibliography</b>	<b>143</b>
<b>Appendix</b>	<b>173</b>
<b>List of Figures</b>	<b>181</b>
<b>List of Tables</b>	<b>189</b>



## Abstract

While stratospheric ozone ( $O_3$ ) is well known for protecting the surface from harmful ultraviolet solar radiation, tropospheric ozone plays a more complex role in Earth's climate and biosphere being one of the most important atmospheric pollutants close to surface. Remote sensing from satellites can be extremely useful for providing consistent information of tropospheric ozone concentrations over large areas. When looking down from space, in nadir direction the reflected sunlight from the Earth at UV, it is possible to obtain vertically integrated measurements of  $O_3$  (total columns), from the surface to the top of the atmosphere. Since 1995 the Institute of Environmental Physics (IUP) at the University of Bremen provides total ozone data retrieved from nadir radiance spectra of the European satellite instruments: GOME/ERS-2 (1995-2003), SCIAMACHY/Envisat (2002-2012), and GOME-2/MetOpA (2007-today) by using the Weighting Function Differential Optical Absorption Spectroscopy (WFDOAS) method. Removing the stratospheric contributions by assuming that the monthly averaged ozone column amounts measured over Deep Convective Clouds (DCC) are representative for stratospheric ozone columns in the tropics, it is feasible to estimate monthly mean tropospheric ozone columns over the tropics and to study their large scale temporal and spatial behavior. The focus of this thesis is twofold: to retrieve monthly mean tropical tropospheric ozone amounts with the Convective Cloud Differential (CCD) technique from 1996 to 2015 and to study variability and trends using this long-term tropospheric ozone dataset on a regional and tropical scale. Within this framework, a detailed uncertainty analysis of the CCD-IUP algorithm has been performed along with a study upon the trend uncertainties due to the harmonisation. Finally, the influence of ENSO on tropospheric ozone and the origin of its anomalies due to dynamics or emissions has been investigated.

An improved CCD-IUP algorithm was developed and a unique long-term record (1996-2015) of monthly averaged tropical tropospheric ozone columns (TTCO) was created using total ozone columns and cloud parameters from the three European satellite instruments (GOME, SCIAMACHY, and GOME-2). The TTCO dataset was extensively validated by comparisons with SHADOZ ozonesonde data and Limb-Nadir Matching (LNM) tropospheric ozone data. The comparison showed good agreement with respect to range, inter-annual variation, and variance. The mean absolute bias with the ozonesonde measurements is  $\sim 5$  DU, the RMS is between 3.5 and 13 DU, and the mean relative difference is between -8 and 28%. When comparing the retrieved TTCOs with LNM data up to 200 hPa, the mean absolute bias is less than 5 DU and the mean relative difference is about 12%. A detailed uncertainty budget analysis shows that the CCD-IUP algorithm has an average uncertainty of  $\pm 3$  DU (<10%). Each satellite instrument has different spatial and spectral resolution, use different cloud algorithms

and has different local passing time, all of which may introduce biases and drifts between instruments. Therefore, the three datasets were harmonised into one consistent time series by testing six different scenarios.

Various harmonisation scenarios were tested and uncertainties related to the merging approach have been estimated. These were shown to be one of the major source of uncertainty in the long-term trend estimates. The calculated trends from all scenarios, range between  $\pm 4$  DU/decade and the mean difference between them is in the order of 2 DU/decade. The preferred harmonised TCO dataset is afterwards used to assess the trends of tropical tropospheric ozone. The trends range between -3 to 3 DU/decade, with an average value of  $-0.1 \pm 1.23$  ( $2\sigma$ ) DU/decade which is statistically non significant. Regionally, tropospheric  $O_3$  is increasing significantly by 3 DU/decade over south tropical Atlantic Ocean, south Africa, south-east tropical Pacific and central Oceania and by 2 DU/decade over the Caribbean sea and south India, while it is decreasing by -3 DU/decade over central America, parts of the northern tropical Pacific Ocean and by -2 DU/decade over some parts of the southern tropical Pacific Ocean. Comparing the trend results from the current study with the trends calculated from ozonesonde profiles for six ozonesonde stations and with the ones from Ebojie et al. [2016] and Heue et al. [2016] for eight tropical mega-cities, we found that they agree well within the uncertainty of the trends. Studying the seasonal variability of tropical tropospheric ozone, a monthly zonal TCO climatology for the last 20-year was created. Several factors such as, El Niño Southern Oscillation (ENSO), quasi-biennial oscillation (QBO), the solar, and the seasonal cycle have a response to the TCO variability. ENSO contributes by about +7 DU over the western Pacific and Indian ocean and by  $\sim -10$  DU over the eastern Pacific ocean. The solar cycle contributes  $\pm 7$  DU, and QBO contributes in total  $\sim 5$  DU, mainly over the southern latitudes. The seasonal cycle was found to have the strongest influence on tropospheric ozone variability, by more than 15 DU over the northern tropics and the Atlantic ocean, whereas elsewhere its total contribution is less than 7 DU, with weakest contributions noticed over the west Pacific Ocean ( $< 5$  DU). These results, show reasonable agreement compared to other studies.

In a case study, the influence of two major El Niño (1997 and 2015) and La Niña (1999 and 2010) events on TCO was investigated. It was shown that both El Niño events increased tropospheric  $O_3$  over Indonesia by 10–15 DU, and decreased it over the east Pacific ocean by 10–20 DU. La Niña events were found to decrease tropospheric ozone over Indian Ocean and central tropics by 5–10 DU and increase it elsewhere by 6–8 DU. The 2015 El Niño and 2010 El Niña caused larger positive  $O_3$  anomalies whereas 1997 El Niño and 1999 La Niña larger negative  $O_3$  anomalies, revealing that there is strong variability in ozone respond to ENSO events. The tropical tropospheric ozone results for the months September to December 2014 and 2015 were compared with simulated ozone columns from the ECHAM-Messy Atmospheric Chemistry model (EMAC). The EMAC model was found to overestimate tropospheric ozone columns by 10-15 DU, mainly over northern Africa, Indian ocean, and north-east Pacific ocean and to underestimate over the Atlantic, west Pacific ocean, and the central-south Africa by 10-15 DU compared to the CCD results. The comparison of ozone precursors emissions ( $NO_2$  and CO), from the EMAC model with satellite observations (GOME-2 for  $NO_2$  and MOPITT for CO) showed that the EMAC model generally underestimates their abundances, which impacts the modelled tropospheric  $O_3$ . Finally, the contribution of dynamics and biomass burning on troposphere  $O_3$  anomalies during the 2015 El Niño event was studied. Using the EMAC tropospheric  $O_3$  simulations from September to December 2015

(during El Niño), and September to December 2014 (neutral year), in two modes, one with and one without biomass burning emissions, it was concluded that mostly dynamics have modulated tropical tropospheric ozone concentrations during the 2015 El Niño event, with the exception of the Indonesian region where biomass burning emissions resulted in tropospheric ozone increases of about  $\sim 8$  DU. In October 2015, the increase reaches  $+20$  DU over the Indonesian peninsula.



## Publications

Parts of this thesis are based on and/or cited from peer reviewed articles, conference talks, and conference posters, being produced during this thesis. Sections and subsections containing such text, figures, and tables, are indicated by an asterisk and explanatory footnotes throughout this thesis.

### Peer-reviewed publications

**Leventidou, E.**, Eichmann, K.-U., Weber, M., and Burrows, J. P.: Tropical tropospheric ozone columns from nadir retrievals of GOME-1/ERS-2, SCIAMACHY/Envisat, and GOME-2/MetOp-A (1996–2012), *Atmos. Meas. Tech.*, 9, 3407-3427, doi:10.5194/amt-9-3407-2016, 2016.

**Leventidou, E.**, Weber, M., Eichmann, K.-U., and Burrows, J. P.: Harmonisation and trends of 20-years tropical tropospheric ozone data, *Atmos. Chem. Phys. Discuss.*, doi:org/10.5194/acp-2017-815, in review, 2017.

**Leventidou, E.**, Eichmann, K.-U., Weber, M., and Burrows, J. P.: Tropical tropospheric ozone variability and the case of 2015 el Niño event, Manuscript in preparation for publication in *Atmos. Chemistry and Physics Discussions*, 2017.

### Technical Reports

**Leventidou E.**, Weber M.: S5P/TROPOMI Science Verification Report, S5P-IUPL2-ScVR-RR, European Space Agency, Issue 2.1, available at:

[https://earth.esa.int/web/sentinel/user-guides/sentinel-5p-tropomi/document-library/-/asset\\_publisher/w9Mnd6VPjXlc/content/sentinel-5p-tropomi-science-verification-report](https://earth.esa.int/web/sentinel/user-guides/sentinel-5p-tropomi/document-library/-/asset_publisher/w9Mnd6VPjXlc/content/sentinel-5p-tropomi-science-verification-report) (last access: 22 July 2017), 2015.

### Proceedings

**Leventidou E.**, Eichmann K.-U., Burrows J.P., Weber M., Tropical tropospheric ozone columns from nadir retrievals of GOME-1/ERS and SCIAMACHY/Envisat, COMECAP 2014 e-book of proceedings, Vol 2., pp. 131-136. ISBN: 978-960-524-430-9. 12th International Conference on Meteorology, Climatology and Atmospheric Physics, COMECAP, Heraklion, Crete, Greece, 2014.

## Conference contributions

### Posters

**Leventidou E.**, Eichmann, K.-U., Weber, M., and Burrows, J. P: Tropical tropospheric column ozone from GOME-1, SCIAMACHY, and GOME-2 using the Convective Cloud Differential (CCD) method, EGU General Assembly, Vienna, Austria, April 2014

**Leventidou E.**, Eichmann K.-U., Burrows J.P, Weber M.: Tropical tropospheric ozone columns from nadir retrievals of GOME-1/ERS and SCIAMACHY/Envisat, 12th International Conference on Meteorology, Climatology and Atmospheric Physics, COMECAP, Heraklion, Crete, Greece, 2014.

**Leventidou E.**, Eichmann, K.-U., Weber, M., and Burrows, J. P: Tropical tropospheric ozone from satellite observations with the Convective Clouds Differential (CCD) technique, ECC 5th Early Career Scientists Conference for Marine and Climate Research, Bremen, 21 September 2014 - 24 September, 2014.

**Leventidou E.**, Eichmann, K.-U., Weber, M., and Burrows, J. P: Tropical tropospheric ozone from satellite observations with the Convective Clouds Differential technique, DPG, Heidelberg, Germany, March 2015

**Leventidou E.**, Ebojie, F, Eichmann, K.-U., Weber, M., and Burrows, J. P: Long-term tropical tropospheric ozone column retrievals using the Convective Clouds Differential (CCD) technique, EGU General Assembly, Vienna, Austria, April 2015.

**Leventidou E.**, Weber, M., Eichmann, K.-U., Valks, P, Ebojie, F, and Burrows, J. P: Tropical tropospheric ozone columns from nadir retrievals of GOME, SCIAMACHY and GOME-2, ESA. ATMOS 2015, Heraklion, Crete, Greece, 8 -12 June, 2015.

Eichmann, K.-U., Weber, M., **Leventidou E.**, Richter, A., and Burrows, J. P: Tropical Upper Tropospheric Ozone Volume Mixing Ratios Retrieved using the Cloud Slicing Method: SCIATRAN/WFDOAS Sensitivity Studies and Ozone Sonde Comparisons, ESA ATMOS 2015, Heraklion, Crete, Greece, 8 -12 June, 2015.

**Leventidou E.**, Eichmann, K.-U., Weber, M., and Burrows, J. P: Multiannual tropical tropospheric ozone columns and the case of the 2015 el Niño event, EGU General Assembly, Vienna, Austria, April 2016.

Eichmann, K.-U., Weber, M., Heue, K.-P, **Leventidou E.**, Richter, A., and Burrows, J. P: Tropical Upper Tropospheric Ozone Volume Mixing Ratios Retrieved with the Cloud Slicing Method using SCIATRAN/GOME2 data: Methodology, Ozone Sonde Comparisons, and Verification of the new S-5P Operational Processor, Living Planet Symposium 2016, Prague, Czech Republic, 9-13 May, 2016.

**Leventidou E.**, Weber, M., Eichmann, K.-U., and Burrows, J. P: 17 years of Tropical tropospheric ozone columns from nadir retrievals of GOME, SCIAMACHY and GOME-2 and trends, Quadrennial Ozone Symposium 2016, Edinburgh, United Kingdom, 4-9 September, 2016

Eichmann, K.-U., Weber, M., **Leventidou E.**, and Burrows, J. P: Tropical Upper Tropospheric Ozone Volume Mixing Ratios Retrieved with the Cloud Slicing Method using SCIATRAN/GOME2 data: Methodology, Results, and Verification , Quadrennial Ozone Symposium 2016, Edinburgh, United Kingdom, 4-9 September, 2016

**Leventidou E.**, Weber, M., Eichmann, K.-U., Burrows, J. P., and A. Pozzer: 20 years of tropical tropospheric ozone columns from nadir retrievals of GOME, SCIAMACHY and GOME-2 using the Convective Clouds Differential technique, DPG, Bremen, Germany, March 2017.

**Leventidou E.**, Weber, M., Eichmann, K.-U., Burrows, J. P.: 20 years of tropical tropospheric ozone columns and trends from a harmonised dataset using the Convective Clouds Differential (CCD) technique, Joint IAPSO-IAMAS-IAGA Assembly, Cape Town, South Africa, August 2017.

### **Talks**

**Leventidou E.**, Weber, M., Eichmann, K.-U., Burrows, J. P., and A. Pozzer: 17 years of Tropical tropospheric ozone columns from nadir retrievals of GOME, SCIAMACHY and GOME-2 and trend analysis, Living Planet Symposium 2016, Prague, Czech Republic, 9-13 May, 2016



## Acknowledgement

They say, science is the tool to help us understand the world we live in and change it. However, the challenge of how to make this change beneficial to humanity and the Earth's environment was always the motivation throughout my studies in physics. I am very grateful for having the opportunity to work during my PhD studies on a field so close related with human health and the environment, such as tropospheric ozone. For this reason, I would like to express my sincere thanks to Prof. John P. Burrows and Dr. Mark Weber for accepting me as a PhD student at the Institute of Environmental Physics (IUP) in Bremen. Thank you both for your advice, motivation, and support during all these years. Making research in IUP and being part of the atmospheric chemistry teaching team was a great opportunity for me to learn and benefit from the experience that this institute holds.

I am very thankful to Prof. Mihalis Vrekoussis for the inspiring conversations and for accepting to review my PhD thesis as second examiner. I would also like to thank Prof. Dimitris Balis for traveling from Greece for my examination. Many thanks to Dr. Andrea Pozzer and the MPI-Mainz team for providing the EMAC simulations. During the S5P verification project I shared numerous e-mails and discussions with Dr. Pieter Valks and Dr. Klaus-Peter Heue from DLR, to whom I am very thankful for their invaluable help. I owe my gratitude to SHADOZ network directed by Dr. Anne Thompson for performing the valuable ozonsonde profile measurements in various tropical stations.

I am extremely grateful to Hella van Asperen, Conor Murray and Malte Schottmayer for reading parts of my thesis draft and providing me their helpful comments. Many thanks to Petra Horn, Geraldine Schmiechen, Stephanie Drath, Anja Gatzka and the Heikos for their administrative support. Special thanks to Andreas Meier and Lisa Kattner for being the best team-mates while tutoring Atmospheric Chemistry. Many thanks to Luca for being something like an older/wise brother here for me.

I am very lucky because all these years I have been surrounded by wonderful colleagues in IUP. Therefore, I owe special thanks to my officemate Kai-Uwe Eichmann for answering hundreds of questions and sharing vivid conversations and fun in the office. I would also like to thank Alik, Andreas, Fanis, Hella, Georgia, Jia, Julia, Katerina, Leonardo, Luca, Manolis, Markus, Martin, Ola, and Sven for sharing coffee, beer and wine together, along with lots of fun inside and outside of the university. To my old friends back in Greece; Dora, Frideriki, Kosta, Maria, Mimi, and Sisi, I am very happy that you still care about me.

Last but not least, I would like to thank my parents and sister for their love, unconditional support and encouragement to do always my best in life. I love you more than anything! My life here in Bremen would not be the same without my beloved sister and her husband who are always here for me at good

and bad times. Finally, my best thanks to Nicolai for bringing love and harmony in my life, making the time of writing this thesis less stressful.

## Motivation and Outline

Since the industrial revolution (which chronologically begins in 1787, when James Watt designed the first steam engine), humans and their societies have considerably changed the global environment. Mankind activities have become a geological force, and the Earth has passed into the era called the "*Anthropocene*" [Crutzen, 2002]. During these three centuries, the Earth is transformed to a less biologically diverse, less forest covered, much warmer, and probably wetter and stormier planet [Steffen et al., 2007].

Human population has increased dramatically, reaching 7.5 billion today (see Fig. 1). Half of this population resides in urban areas. The wealthy nations (belong to Organisation for Economic Cooperation and Development (OECD), <http://www.oecd.org/>), despite their relative small proportion to the global population (~ 1 billion), still have the largest contribution to the Gross Domestic Product (GDP). Energy use has grown tremendously by a factor of 15 since 1950. Transportation has also increased, with the number of vehicles being six times more than 1960 levels. Today, about 30 % of the total Earth's surface is domesticated by humans. Tropical rain-forest land has decreased by more than 25% the last three centuries. Fossil-fuel combustion, deforestation and agriculture have caused dramatic increases in *greenhouse gas* (GHG) concentrations and *ozone precursor* emissions (volatile organic compounds (VOCs) and nitrogen oxides ( $\text{NO}_x$ )). Carbon dioxide ( $\text{CO}_2$ ) has increased by ~30 %, methane ( $\text{CH}_4$ ) by more than 60%, and nitrous oxides ( $\text{NO}_x$ ) by more than 20 % since the industrial revolution. Meanwhile, the global surface temperature has increased by more than 0.5 °C since the 1950s. Today it is more obvious than ever that socio-economic changes and climate are interactively related.

Tropospheric ozone ( $\text{O}_3$ ) is regarded as one of the most important atmospheric pollutants close to surface having a burden of 337 Tg. It is secondarily produced in the troposphere as a byproduct of the oxidation of volatile organic compounds (VOCs), carbon monoxide (CO) and methane ( $\text{CH}_4$ ) in the presence of nitrogen oxides ( $\text{NO}_x$ ) and sunlight. Only a small amount of ozone (~550 Tg/year) is transported from the stratosphere through the stratosphere to troposphere (STE) exchange. Consequently it is mainly of anthropogenic origin [IPCC, 2013, Jacob, 2000, Seinfeld and Pandis, 2006]. Close to the surface it is the main component of the photochemical smog that covers the atmosphere of mega-cities in developed and developing countries [Jacob, 2000, Wallace and Hobbs, 2006]. Ozone can oxidize biological tissues, and at high amounts, it can cause respiratory problems and even death [WHO, 2006]. In 2012, 16,000 premature deaths across 26 EU countries have been attributed to Ozone pollution [EEA, 2015]. Surface ozone can also cause massive damages to agricultural crops and forest

## Socio-economic trends

## Earth system trends

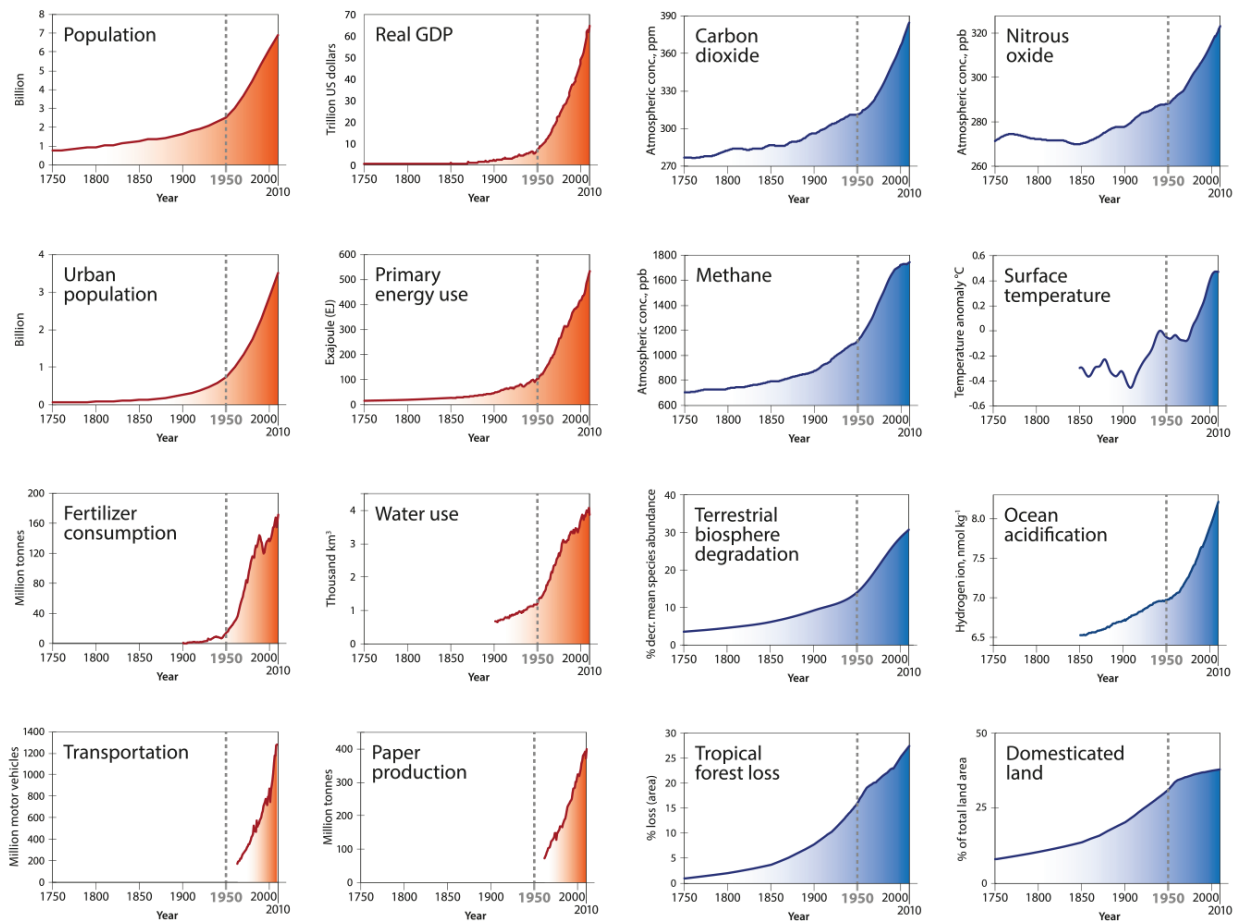


Figure 1: Socio-economic and Earth System trends from 1750 to 2010 [Steffen et al., 2015].

areas [Fowler et al., 2008, Monks et al., 2015]. In the troposphere, ozone is the third most important GHG, contributing  $0.4 \pm 0.2 \text{ W}\cdot\text{m}^{-2}$  in global radiative forcing (RF) [IPCC, 2013]. Since it is the primary tropospheric source of the hydroxyl (OH) radical, it can modulate the lifetime of other GHGs via their oxidation with OH and control the oxidizing capacity of the troposphere [Jacob, 2000]. Having a mean lifetime of  $\sim 23$  days in the troposphere, it can be transported on a global scale, influencing the global climate system [Stevenson et al., 2006, Young et al., 2013].

The present day mean tropospheric ozone burden of  $337 \pm 23 \text{ Tg}$  has increased by  $\sim 30\%$  since preindustrial times [IPCC, 2013, Young et al., 2013]. Tropospheric ozone is expected to increase 7% by 2030 (18% in 2100) under the RCP 8.5 IPCC scenario or decrease by 2% over the same time period (-7% in 2100) according to RCP 2.6 IPCC scenario (see Fig. 2) [IPCC, 2013, Young et al., 2013]. These scenarios represent extreme cases of the Representative Concentration Pathways (RCP) chosen by the Intergovernmental Panel on Climate Change (IPCC). The predicted increase of surface ozone for the next years is mainly located in the tropics and subtropics, and more specifically in Southeast Asia, India and Central America [Grenfell et al., 2003, IPCC, 2013, Wild, 2012]. Therefore, tropical tropospheric

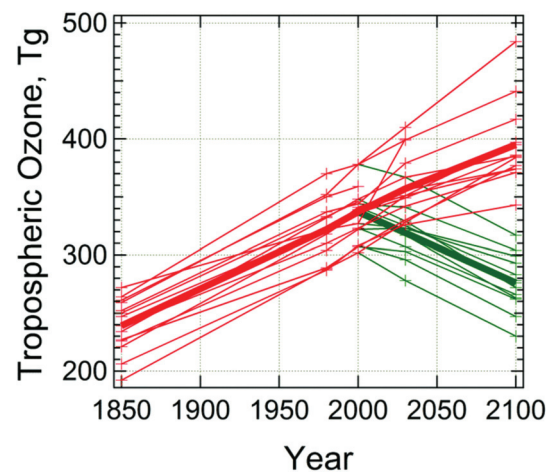


Figure 2: Global tropospheric ozone burden and its changes between 1850 and 2100 simulated by different models. Two scenarios of future emissions have been used as defined by the Intergovernmental Panel on Climate Change, IPCC. RCP 2.6, assumes that ozone precursors peak between 2010-2020 and decline thereafter (green) and RCP 8.5 assumes high precursor emissions (mainly methane) and a strong warming throughout the 21st century (red). Thin lines are for individual model results and thick lines are multi-model averages. (Source: Madronich et al. [2015], figure based on data from Young et al. [2013]).

ozone should receive particular attention. The acquisition of accurate measurements is the precondition to understand the production cycle of tropospheric ozone in order to reduce its abundance.

Remote sensing of the atmosphere with satellite instruments provides global information about the atmospheric trace gas composition over land and ocean for long periods. In order to observe tropospheric ozone from space, the stratospheric contributions must be removed. Tropospheric ozone was retrieved for the first time from space with the tropospheric ozone residual (TOR) method [Fishman et al., 1990] which subtracts the stratospheric ozone retrieved using profile measurements down to the tropopause from limb observations, while using the collocated total ozone columns from nadir measurements to derive tropospheric ozone columns.

Using the location of deep convective clouds (DCCs), and assuming that UV radiation does not penetrate these clouds, stratospheric ozone columns can be retrieved from nadir observations as well. This way the tropospheric column amounts can be retrieved from nadir observations alone by subtracting the ozone columns above very high clouds (usually in the Pacific region) from total ozone columns from cloud-free scenes. This works only if one assumes that stratospheric ozone is invariant which is only approximately true in the tropics [Hudson and Thompson, 1998]. Ziemke et al. [1998] used these two assumptions to develop a statistical method called the *Convective Clouds Differential* (CCD) method using Total Ozone Mapping Spectrometer (TOMS) ozone and reflectivity data. Monthly mean tropical tropospheric columns of ozone (TTCO) were retrieved by averaging total ozone columns above deep convective clouds in a pre-defined grid (latitude bands) from a reference region (over western Pacific ocean) and subtracting them from the monthly averaged total columns from the corresponding cloud free grid box. The advantage of this method is that it is computationally easy compared with the profile retrievals and requires only one satellite instrument, eliminating collocation problems. The same method was further optimised by Valks et al. [2003] who applied it to GOME [Burrows et al.,

1999] and GOME-2 [Callies et al., 2000] data. Heue et al. [2016] extended the Valks et al. [2003] CCD dataset using SCIAMACHY [Burrows et al., 1995] and OMI [Levelt et al., 2006] data by creating a merged time-series.

In this study, an improved CCD retrieval algorithm using total ozone and cloud properties data from three European space-borne instruments, GOME, SCIAMACHY, and GOME-2 has been developed. A detailed uncertainty estimation has been performed taking into account the main contributing factors (total ozone retrieval, cloud top height, cloud fraction uncertainties). 20 years of harmonised and merged tropical tropospheric ozone column data are now available forming the basis for determining long-term trends and to study natural variability of tropical tropospheric ozone.

This thesis is structured as follows:

- In Chapter 1 the fundamental scientific information are given about ozone in the Earth's atmosphere and particularly in the troposphere, along with the principles of absorption spectroscopy and a description of methods and instruments for satellite based ozone retrievals.
- In Chapter 2 the convective clouds differential algorithm, developed for three different instruments (GOME, SCIAMACHY, and GOME-2) is described and the improvements and corrections needed for the retrieval of the above cloud columns of ozone (ACCO) are discussed in detail.
- In Chapter 3 the main results of the advanced CCD retrieval are presented along with the uncertainty budget for each instrument. The validity of the individual datasets is tested using comparisons to vertically integrated in-situ measurements from the Southern Hemisphere Additional OZonesondes (SHADOZ) network [Thompson et al., 2003] and tropospheric ozone columns from Limb/Nadir matching data (for SCIAMACHY data only) [Ebojje et al., 2014].
- In Chapter 4 six different scenarios are tested in order to harmonise and merge the individual TCO datasets. A multi-linear regression model (fitting linear trend, seasonal cycle, ENSO, QBO, and the solar cycle) is applied to all merged datasets in order to investigate the influence of harmonisation on tropical tropospheric ozone trends. The spatial distribution and magnitude of tropospheric ozone trends for one of the harmonised datasets that is considered the optimum dataset is discussed in detail. Regional and mega-cities' trends are presented and compared with results from other studies.
- In Chapter 5 the seasonal behavior and variability of tropical tropospheric ozone are presented. The factors that can influence tropospheric ozone variability are described and their tropical tropospheric ozone response is quantified and discussed.
- In Chapter 6 the influence of ENSO (El Niño Southern Oscillation) on tropical tropospheric ozone abundance is investigated. Comparison between the two major El Niño and El Niña events (1997 and 2015) of the last 20 years is performed. The 2015 El Niño event is studied in more detail looking at inter-annual differences of tropical tropospheric ozone columns and its precursors between satellite data and ECHAM5/Messy Atmospheric Chemistry (EMAC) model simulations. The origin and magnitude of tropospheric ozone enhancements during El Niño are investigated with the EMAC model.

- Finally, in Chapter 7 a summary of the main research and conclusions of this thesis are presented, as well as an outlook for further improvements in the retrievals of TTCO and suggestions for future studies are given.



Tropospheric ozone ( $O_3$ ) is regarded as one of the most important surface pollutants due to the fact that it oxidizes the biological tissues, causes respiratory problems or even death [WHO, 2006], acts as a greenhouse gas [IPCC, 2007], and controls the oxidizing capacity of the troposphere [Jacob, 2000]. Tropospheric ozone presents considerable variability mainly due to its chemical lifetime, which coincides with the timescales of weather systems (1–2 weeks). Remote sensing from satellites is an essential tool for providing consistent information of tropospheric ozone concentrations over large areas. These measurements show large spatial and temporal variability which is controlled by several atmospheric processes. This chapter gives an introduction to the Earth's atmosphere and describes the role that ozone is playing in it, along with a brief history of the study of atmospheric ozone in Section 1.1. The chemical and dynamical processes associated with tropospheric ozone production and destruction, and the impact that ozone has on climate and the biosphere are discussed in Section 1.2. The basic absorption spectroscopy principles are presented in Section 1.3. A brief introduction to several satellite-based techniques for measuring total and tropospheric ozone is given in Section 1.4. Finally, the relevant satellite instruments for measuring tropospheric ozone from the current study are described in a few words in Section 1.5.

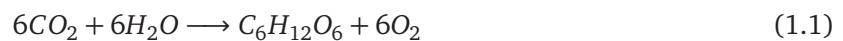
## 1.1 Ozone in the Earth's atmosphere

### 1.1.1 Evolution of the atmosphere

Our solar system is believed to have formed from the gravitational attraction of a cold cloud consisting of interstellar gas and dust, about more than 4.5 billion years ago. As the size of the Earth grew by a cold accretion process, the weight of the outer layers compressed the center, melting the interior core of heavy elements such as iron and nickel [Dickerson, 1971]. The atmosphere (Greek: "ατμος" + "σφαιρα" = "steam" + "sphere") is a relatively thin layer (up to 1000 km) of gases surrounding the Earth's crust. From the absence of noble gases on Earth compared with their high abundance on the Sun and other stars, it is evident that Earth lost its original atmosphere. The first atmosphere was formed from the out-gassing of the Earth's interior by volcanism and consisted of water vapour, ( $H_2O$ ), carbon monoxide, ( $CO$ ), carbon dioxide, ( $CO_2$ ), methane, ( $CH_4$ ), sulfur dioxide, ( $SO_2$ ), hydrogen sulfide ( $H_2S$ ), and

nitrogen (N<sub>2</sub>) [Wallace and Hobbs, 2006]. Water vapor condensed to form seas approximately 4.4 billion years ago [Lunine, 2006]. The out-gassed CO<sub>2</sub> and other gases dissolved in the water, forming sedimentary rocks in the ocean. N<sub>2</sub> is chemically inert, non-condensable, and is non-soluble in water, so most of the out-gassed N<sub>2</sub> accumulated in the atmosphere, thereby becoming the most abundant constituent [Seinfeld and Pandis, 2006].

Until 2–3.8 billion years ago, the terrestrial atmosphere was essentially anoxic (lacked free oxygen or O<sub>2</sub> gas). The milestone in evolution of life on Earth was the increase of oxygen in the atmosphere, 2.1–2.4 billion years ago. Although cyanobacteria were already present in the oceans some billion years earlier and were capable of releasing oxygen, the amount of oxygen released was not much. Only after most minerals were oxidised and hydrogen (H<sub>2</sub>) gradually escaped from the Earth's gravitational force, could the released oxygen from photosynthesis accumulate in the atmosphere.[Wallace and Hobbs, 2006]. This sudden increase is known as the "*Great Oxidation Event*" [Lyons et al., 2014]. The present level of atmospheric O<sub>2</sub> is maintained by the balance between production from photosynthesis (Reaction 1.1) and removal from respiration and decay of organic carbon (Reaction 1.2) [Seinfeld and Pandis, 2006].



Ultraviolet (UV) solar radiation (wavelength range 100-400 nm) is extremely energetic, proportional to its frequency, and therefore extremely harmful to a number of macromolecules (proteins and nucleic acids), particularly DNA which can be damaged at wavelengths <290 nm [Charles et al., 2002, Wayne, 1991]. Oxygen is capable of filtering UV radiation emitted by the Sun up to 230 nm. Only ozone (trioxygen, O<sub>3</sub>) has the ability to absorb at the critical for life wavelengths of 230-290 nm which allowed for the colonization of the land [Charles et al., 2002, Margulis, 1976, Wayne, 1991]. Ozone was formed in the atmosphere by the addition of atomic oxygen (O(<sup>3</sup>P)) to molecular oxygen. The atomic oxygen was formed after the photolysis of molecular oxygen at  $\lambda < 240$  nm. The absolute concentrations and the altitude distribution of ozone is an equilibrium between production and loss [Wayne, 1991]. In the region where ozone concentrations are at its maximum, the absorbed UV radiation is converted into heat which consequently warms the atmosphere, altering the temperature profile and stability of the atmosphere. For all these reasons, ozone is one of the most outstanding constituents of the Earth's atmosphere and played a significant role in the evolution of life.

### 1.1.2 The present atmosphere

The Earth's atmosphere is the main reason for the existence and maintenance of life on Earth. Table 1.1 lists the mixing ratios of the major atmospheric gases. The present Earth atmosphere provides O<sub>2</sub> (21%) for respiration, CO<sub>2</sub> (400 ppm) for photosynthesis, H<sub>2</sub>O (0-5 %) for nourishment, and N<sub>2</sub> (78 %) for fertilization of land. CO<sub>2</sub>, H<sub>2</sub>O, O<sub>3</sub>, CH<sub>4</sub>, and N<sub>2</sub>O, known as "*greenhouse gases*", keep the surface warm enough (the average surface temperature was 12 °C at the end of the 20<sup>th</sup> century [NOAA, 2017]) for living organisms [Wallace and Hobbs, 2006]. These gases have this ability due to their characteristic structure that can absorb and re-emit infrared (IR) radiation at all directions. O<sub>3</sub> also absorbs the harmful ultraviolet (UV) solar radiation (100 nm and 300 nm) that could damage biological tissues

Table 1.1: Mixing ratio of gases in the Earth's atmosphere, with respect to dry air (taken from Jacob [2000], p.4 and [http://library.wmo.int/opac/doc\\_num.php?explnum\\_id=3084](http://library.wmo.int/opac/doc_num.php?explnum_id=3084).  $10^{-6}$  mol/mol = 1 ppmv (parts per million volume) and  $10^{-9}$  mol/mol=1 ppbv (parts per billion volume). Values followed by an asterisc (\*) denote mean values in 2015.

Gas	Mixing ratio (mol/mol)
Nitrogen (N <sub>2</sub> )	0.78
Oxygen (O <sub>2</sub> )	0.21
Argon (Ar)	0.0093
Water vapor (H <sub>2</sub> O)	0-0.05
Carbon dioxide (CO <sub>2</sub> )	$400 \times 10^{-6}$ *
Neon (Ne)	$18 \times 10^{-6}$
Ozone (O <sub>3</sub> )	$0.01-10 \times 10^{-6}$
Helium (He)	$5.2 \times 10^{-6}$ m
Methane (CH <sub>4</sub> )	$18.4 \times 10^{-6}$ *
Krypton (Kr)	$14.1 \times 10^{-6}$ m
Hydrogen (H <sub>2</sub> )	$500 \times 10^{-9}$
Nitrous oxide (N <sub>2</sub> O)	$328 \times 10^{-9}$ *

and vegetation. However, human activities such as fossil fuel combustion and industrialization, release high amounts of atmospheric constituents like greenhouse gases, volatile organic chemicals, particulate matter, nitrogen and halogen compounds, which can harm humans, animals, vegetation, or materials and are categorised as atmospheric pollutants [U.S. Environmental Protection Agency, 2009].

The Earth's atmosphere consists of a series of layers, each with a specific structure and characteristic properties. Moving upwards from the ground, these layers are categorised according to the vertical temperature profile of the atmosphere as shown in Fig. 1.1. Temperature generally decreases with altitude although two temperature inversions can be noticed at  $\sim 10$  and  $\sim 90$  km. The temperature variations shown in Fig. 1.1 are due to solar radiation absorption from atmospheric constituents at these altitudes.

The lowest layer of the atmosphere is called the *troposphere* and is characterised by decreasing temperature with height with an average dry adiabatic lapse rate of  $\sim 9.5^\circ\text{C}/\text{km}$ . The air is considered to be well mixed (turbulent mixing) and has the greatest density compared to other layers, containing about 80% of the total mass of the atmosphere. The troposphere is also the layer where the weather systems develop. The depth of the troposphere varies with season and latitude and ranges between 7 to 15 km, with higher altitudes being located in the tropics [Wallace and Hobbs, 2006]. The inversion level, called the *tropopause*, is defined as the lowest level at which the lapse rate decreases to less than 2 K/km and the lapse rate averaged between this level and any other level within the next 2 km does not exceed 2K/km as defined by the World Meteorological Organization (WMO) [WMO, 1957]. However, several recent studies approach the tropopause as a layer of 50 hPa (1-3 km) thickness, instead of a sharp point in the atmosphere [Fueglistaler et al., 2009, Sherwood and Dessler, 2001].

The layer above the tropopause is called the *stratosphere* and extends up to the stratopause ( $\approx$  45–55 km). Temperature increases with altitude in this (inversion) layer prohibiting vertical mixing and causing atmospheric stability. The stratospheric inversion is caused by absorption of ultraviolet radiation from the Sun by ozone. The production of ozone from atomic and molecular oxygen depends

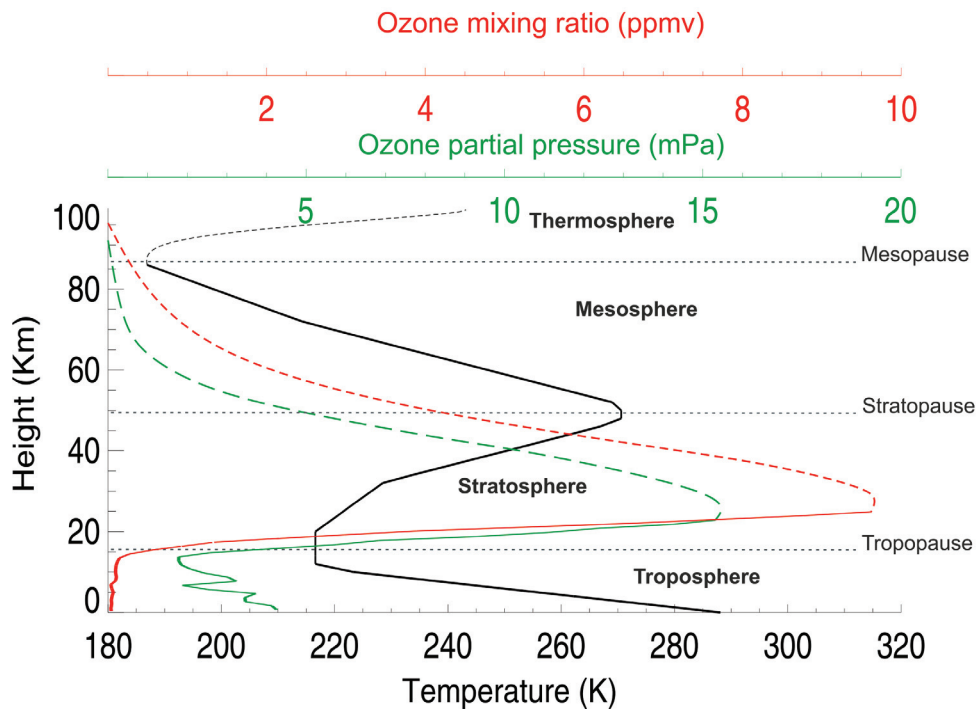


Figure 1.1: Temperature and ozone profile in the atmosphere. Temperature data taken from the U.S. Standard Atmosphere 1976, see U.S. Government Printing Office [1976]. The volume mixing ratio with red solid line and the partial pressure of ozone ( $\text{mixing ratio} \times \text{atmospheric pressure}$ ) with solid green line are taken from SHADOZ ozonesonde network, for October 2008 in Natal [Thompson et al., 2003]. The dashed lines represent the ideal ozone profile after the ozonesonde burst altitude.

on the optical depth and the density of the atmosphere. At high altitudes the solar radiation is more intense but the atmospheric density is not enough to support large rates of atomic oxygen production from  $\text{O}_2$  photolysis. At lower altitudes  $\text{O}_2$  concentrations are more than enough but most of the UV radiation is already absorbed by the atmospheric constituents at higher altitudes. Therefore,  $\text{O}_3$  is mainly concentrated within the stratosphere (between 20 to 30 km, see Fig. 1.1). This layer is called the *ozone layer* or the *ozonosphere* and the shape of it can be approximated by the "Chapman function" [Wayne, 1991].

At the *stratopause* the temperature stops increasing. The overlying layer called the *mesosphere* lacks significant solar radiation absorbers and the temperature continues to decrease gradually again. The top of this layer, called the *mesopause* (80-90 km), is the coldest area of the atmosphere, with temperatures down to  $-80^\circ\text{C}$ . Above the mesopause the temperature begins to increase again as a result of short-wave radiation absorption by  $\text{N}_2$  and  $\text{O}_2$  which are getting excited. This layer is called the *thermosphere* and this is the first layer which is reached and warmed by intense solar radiation. The last atmospheric layer is the *exosphere* extending from altitudes  $> 500$  km where gas molecules have sufficient energy to

escape from the gravitational force of the Earth [Seinfeld and Pandis, 2006].

The atmospheric temperature and pressure at a specific height  $z$ , is described by the exponential function (*hydrostatic equation*):  $p(z) = p(0) \cdot e^{-\frac{z}{H}}$ , where  $H = RT/M_{air}g$  is the *scale height* (the e-folding depth which is the characteristic length scale for pressure decrease with height),  $R$  is the Molar gas constant (8.314 J/mol K),  $T$  is the temperature in Kelvin,  $M_{air}$  is the molecular weight of air (28.97 g/mol),  $g$  is the acceleration due to gravity, and  $p(0)$  is the surface pressure. The SI unit for pressure is Pascal ( $\text{Pa} = \frac{\text{N}}{\text{m}^2}$ ). The relationships between different pressure units are: 1 atm =  $1.01325 \cdot 10^5$  Pa = 1013.25 mbar = 1013.25 hPa. 1 hPa = 100 Pa.

### 1.1.3 Discovery and distribution of atmospheric ozone

Ozone (trioxygen,  $\text{O}_3$ ) is a blueish gas with a strong irritating smell and is produced naturally in trace amounts in the Earth's atmosphere. For industrial purposes ozone is produced for air and water purification or bleaching of textiles [Fahey and Hegglin, 2011]. It has a melting point of  $-193^\circ\text{C}$  and a boiling point of  $-112^\circ\text{C}$ . It is more soluble in inert non-polar solvents but at standard pressure and temperature its solubility is thirteen times the one of oxygen. The central atom is  $sp^2$  hybridised, similar to  $\text{H}_2\text{O}$ , with one lone pair and a  $117^\circ$  angle between the two bonds (theoretically,  $120^\circ$ ), see Fig.1.2. The two bonds are of one and a half order, with lengths of  $1.28 \text{ \AA}$  (0.128 nm). It is a polar molecule with a dipole moment of 0.53 D, which makes it strongly electronegative. It is a very strong oxidising agent (accepts electrons) and an endothermic substance (storing energy) which can violently explode to yield a nascent oxygen (O) and a molecular oxygen ( $\text{O}_2$ ). Ozone strongly absorbs UV-B (280-320 nm) and UV-C ( $< 280\text{nm}$ ) radiation but the absorption decreases at wavelengths higher than 320 nm radiation and Infrared radiation (IR) at around  $9.6 \mu\text{m}$ . Due to its absorption in IR, it can act as a greenhouse gas in the troposphere.

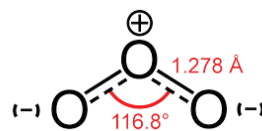


Figure 1.2: Lewis structure of Ozone molecule.

Ozone was discovered by Christian Friedrich Schönbein in 1839. Schönbein suggested the presence of an atmospheric gas having a peculiar odor (the Greek word for "to smell" is  $\sigma\zeta\epsilon\iota\nu$ ) which was produced in the electrolysis of water and the accompanying discharge of frictional electricity in air [Leeds, 1880]. Schönbein was the pioneer of detecting and measuring tropospheric ozone in several European cities using chemical methods [Holloway and Wayne, 2010]. Later, spectroscopic studies in visible and ultraviolet regions by N.W. Hartley showed that ozone strongly absorbs ultraviolet radiation, which later led to the conclusion that ozone is present at a higher mixing ratio in the upper atmospheric layers in comparison to the ground. Quantitative analysis by Fabry and Dobson showed that ozone is mainly concentrated within a layer, located at 15-30 km, the so-called "*ozone layer*" [Holloway and Wayne, 2010].

The vertical and horizontal distribution of ozone in the atmosphere varies with season, latitude and

longitude. The amount of ozone is commonly reported in Dobson Units in honor of Dobson's work on ozone. One *Dobson Unit* (DU) is the number of ozone molecules per square centimeter ( $\text{cm}^2$ ) that can occupy a layer of  $10 \mu\text{m}$  thick at standard temperature and pressure (STP) conditions (temperature of  $273.15 \text{ K}$  ( $0 \text{ }^\circ\text{C}$ ) and pressure of  $10^5 \text{ Pa}$  ( $1 \text{ atm}$ )). The conversion between DU and column density at STP is:  $1 \text{ DU} = 2.69 \times 10^{16} \text{ molecules/cm}^2$  [Holloway and Wayne, 2010]. The amount of total ozone existing in a vertical column of the atmosphere with a base of  $1 \text{ cm}^2$ , compressed to STP conditions occupies a column of approximately  $3 \text{ mm}$  thick, which is equal to  $300 \text{ DU}$ . In Fig. 1.3 the average global distribution of total ozone columns (in DU) at different latitudes and seasons is presented. The maximum ozone concentrations ( $>400 \text{ DU}$ ) are found in the Northern hemisphere ( $>55 \text{ }^\circ\text{N}$ ) during late northern winter and early spring and during summer and autumn at the Southern hemisphere ( $\sim 340 \text{ DU}$ ), close to middle latitudes ( $40\text{--}60 \text{ }^\circ\text{S}$ ), surrounding a "collar" the low ozone values ( $< 200 \text{ DU}$ ) over Antarctica, known as the "Ozone hole". By December, the ozone hole has disappeared, and the values have returned to  $\sim 280 \text{ DU}$ . Low ozone values ( $< 300 \text{ DU}$ ) are also found during the northern autumn in the Arctic. During all seasons, total ozone columns are considerably thinner over the tropics ( $20^\circ\text{S}\text{--}20^\circ\text{N}$ ), with very low variability, ranging between  $260\text{--}280 \text{ DU}$ .

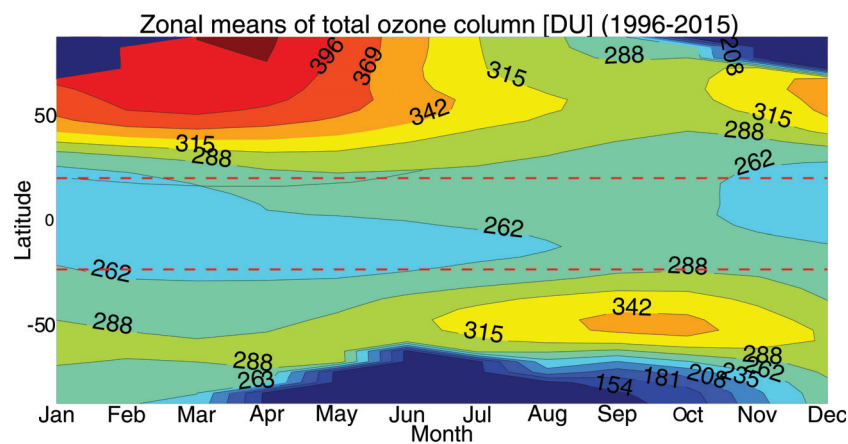
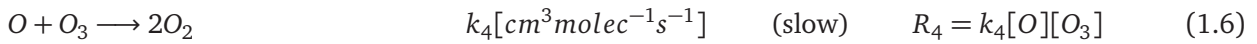
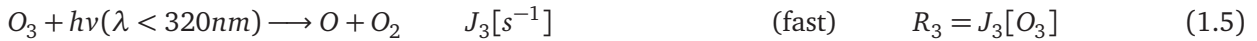
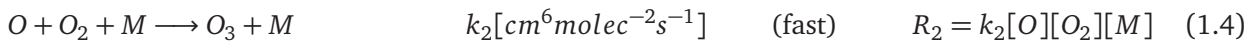


Figure 1.3: Zonal mean climatology (1996-2015) of total ozone columns in DU from GOME/SCIAMACHY/GOME-2 merged WFDOAS total ozone measurements (Global mean  $290 \text{ DU}$ ). Red dashed lines indicate the tropics ( $20 \text{ }^\circ\text{N}\text{--}20 \text{ }^\circ\text{S}$ ). Data found in: [http://www.iup.uni-bremen.de/UVSAT\\_material/data/to3/GSG\\_merged\\_zonalmean.dat](http://www.iup.uni-bremen.de/UVSAT_material/data/to3/GSG_merged_zonalmean.dat) (Courtesy: M. Weber).

In 1920, Dobson built an instrument to monitor the thickness of ozone within an atmospheric column by comparing the intensity of solar radiation that has passed through the atmosphere at two different UV regions, of which one was strongly and one was weakly absorbed by ozone. Using the ratio between these intensities on the ground it is possible to determine the amount of ozone that is present in the atmosphere. This instrument is still the backbone of several instruments used even today at observatories around the world [Farman, 1989, Komhyr and Grass, 1972, 1989]. In 1931, Götz discovered a method to determine the vertical profile of ozone using the reflected, rather than direct, UV intensities. He used the ratio of zenith sky radiances at two wavelengths in the ultraviolet, one were ozone absorbed strongly and one were ozone absorbed weakly, at different solar zenith angles. He noticed that this ratio increases with increasing solar zenith angles to about  $86^\circ$  when suddenly reverses and starts

to decrease. He named this method the *Umkehr effect*, and realised that such measurements contain information about the vertical distribution of ozone [Götz et al., 1934]. Since the late 1950s, filter ozonometers were extensively used at 44 stations in the former Soviet Union [Bojkov et al., 1994]. At the same time, balloon ozonesondes provided ozone profile data from the troposphere and the lower stratosphere, with maximum altitudes (at balloon burst) usually near 30 km [Komhyr, 1964, 1967]. In the last three decades a new instrument, the Brewer ozone spectrophotometer, has been developed. The basic measurement principle is similar to Dobson instrument [Fioletov et al., 2001].

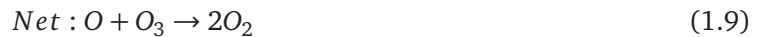
Already in 1930, the photochemical theory of ozone formation was proposed by Chapman, including a static pure-oxygen photochemical steady model which consisted of the following reactions [Chapman, 1930]:



where  $M=N_2, O_2$ .  $M$  (third body) is necessary to remove the excess energy from the intermediate excited product ( $O_3^*$ ) by collision, and to release it back as heat to the environment, in order to yield the final product of the reaction,  $O_3$ . The energy from solar radiation is represented by  $hv$ , which is the product of Planck's constant,  $h$ , and the frequency of the electromagnetic wave of solar radiation,  $\nu$ , corresponds to a specific wavelength band.

Reactions  $R_2$  and  $R_3$  rapidly inter-convert  $O$  and  $O_3$  providing the concept of the "odd oxygen" family ( $O_x=[O]+[O_3]$ ) [Wayne, 1991]. This simplified oxygen model implies the latitudinal variation of solar intensity and zenith angle, the density and the temperature profile of the atmosphere, etc., which makes the production rates of ozone to be dependent on these conditions. However, ozone production by the Chapman mechanism is five times faster than it is being destroyed, resulting in predicted ozone concentrations higher than the observed ones [Baird and Cann, 2005, Wayne, 1991].

In 1950, Bates and Nicolet introduced the idea of catalytic *odd oxygen* loss cycles. The role of a catalyst is to initiate or accelerate chemical reactions without being produced or destroyed by the reactions that it is involved. This leads to the conclusion that *odd oxygen* loss reactions should be cyclic [Holloway and Wayne, 2010]. The loss cycle consists of two steps that can be generalised as:



wherein  $X$  are the catalytic species, of which most important are hydrogen (H), hydroxyl radical (OH), nitrogen (N), nitrogen oxide (NO), and chlorine (Cl).

In 1970s, Paul Crutzen showed that nitrogen oxides ( $NO_x=NO$  and  $NO_2$ ) can catalytically destroy ozone by following the general cycle in reactions (1.7)–(1.9). The nitrogen oxides come from the decay of the chemically stable nitrous oxide ( $N_2O$ ), which originates from microbiological transformations at the ground [Crutzen, 1970]. This was the first indication highlighting the connection between the

thickness of the ozone layer and the biogeochemical cycles. In 1971, Harold Johnston revealed the potential threat for the ozone layer from planned supersonic aircrafts. These aircrafts would be able to fly at altitudes of about 20 km, and thus would be capable of releasing nitrogen oxides right in the middle of the ozone layer [Johnston, 1971]. Crutzen's and Johnston's work gave rise to a very intense debate among researchers as well as among technologists and decision-makers which contributed to the decision to cancel the supersonic planes. In 1974, Mario Molina and Sherwood Rowland pointed out that the chemically inert chlorofluorocarbon (CFC) gases -"freons", which were extensively used in spray bottles or as the cooling mediums in refrigerators, could gradually be transported from the troposphere up to the ozone layer [Molina and Rowland, 1974]. In the ozone layer, the intensive ultraviolet radiation could photolyze these gases into their constituents, resulting in notable chlorine atoms which could destroy ozone.

In 1987, Mario and Luisa Molina proposed that ClO could react with itself to form a dimer, (ClOCl), which in turn could photolyze into Cl atoms, which contribute to ozone destruction [Molina and Molina, 1987].



This cycle of reactions (1.11)-(1.14) was later confirmed by aircraft measurements [Anderson et al., 1989]. After a lot of debates during the late 1970s and early 1980s, Molina's and Rowland's work led to restrictions on CFCs release.

In 1985 Joseph Farman and his colleagues, using a Dobson spectrophotometer, noted a drastic depletion of the ozone layer over the Antarctic station of Halley Bay. This depletion, famously called "the ozone hole", could neither be explained by transport processes nor by gas phase chemical reactions [Farman et al., 1985, WMO, 1985]. Chlorine from the photolysed CFCs may reach the poles through *Brewer-Dobson circulation* (see Sect: 1.2.2). These chlorine atoms react with methane (CH<sub>4</sub>) or NO<sub>2</sub> to form non-reactive hydrogen chloride (HCl) and chlorine nitrate (ClONO<sub>2</sub>). Paul Crutzen and Frank Arnold proposed an alternative mechanism, where reactions on the surface of cloud particles in the stratosphere (polar stratospheric clouds (PSC)) could convert the reservoir species of ClONO<sub>2</sub> and HCl, to a most reactive form, ClO [Crutzen and Arnold, 1986].



The ClO<sub>x</sub> catalytic mechanism (1.11)-(1.14) can be activated with the first sun light, in spring. The ozone depletion is more intense over Antarctica since temperatures during wintertime are low enough (-78°C) to cause condensation of water and nitric acid (HNO<sub>3</sub>) to form persistent PSCs in the lower stratosphere (15–25 km). Additionally, stratospheric aerosols, containing water and sulfuric acid

( $\text{H}_2\text{SO}_4$ ), may also provide the surface for reactions (1.15) and (F14). The polar vortex, also established during winter, inhibits the exchange of Antarctic air with air masses from outside [Jacob, 2000].

For their contribution on stratospheric ozone chemistry, Molina, Rowland, and Crutzen shared the 1995 Nobel Prize in chemistry [Royal Swedish Academy of Sciences, 1995]. It was apparent that anthropogenic emissions could cause significant depletion of the ozone layer in the stratosphere. Ironically, during the same period of the later 1970s, it was realised that anthropogenic emissions could also lead to ozone increases in the troposphere. In this case, the "good" ozone goes "bad", as it will be discussed in the following section.

## 1.2 Tropospheric ozone

In the stratosphere and the upper atmosphere, ozone forms a protecting layer from ultraviolet radiation. Meanwhile in the troposphere, ozone is a hazardous air pollutant, harmful to both human and plant health, is a major component of urban smog, and acts as a greenhouse gas [Fowler et al., 2008, UNEP/WMO, 2011, U.S. National Research Council, 1992, WMO/IGAC, 2012]. Ozone is naturally present in the (unpolluted) troposphere, occupying approximately 10% of the total ozone column density. Downward transport of ozone from the stratosphere (STE exchange) occurs either by stratospheric intrusions at mid-latitudes or by wave breaking in the subtropics (552 Tg/yr [IPCC, 2013]). However, the main source of tropospheric ozone is in-situ photochemical production (5110 Tg/yr [IPCC, 2013]). Photochemical mechanisms being responsible for ozone production were first proposed by Haagen-Smit [1952] and Leighton [1961]. By the beginning of the 1970s it was clear that carbon monoxide ( $\text{CO}$ ) and hydrocarbons, catalysed by hydroxyl radicals ( $\text{HO}_x$ ) and nitrous oxides ( $\text{NO}_x$ ), lead to ozone production in the troposphere [Chameides, 1973, Crutzen, 1974]. It is estimated that approximately 30% of the present day total ozone burden is attributed to human activity [Young et al., 2013]. Tropospheric ozone losses are a result of photochemical processes (4668 Tg/year [IPCC, 2013]) and of deposition and destruction at the earth's surface (1003 Tg/year [IPCC, 2013]) [Crutzen, 1995, Jacob, 2000, Monks et al., 2015, U.S. National Research Council, 1992, Young et al., 2013].

The sources of ozone precursors such as VOCs and  $\text{NO}_x$  can be both anthropogenic and natural. Anthropogenic VOC emissions are caused by combustion processes, energy production, biomass burning, agriculture, solvent use, and chemical manufacturing, whereas the main sources for  $\text{NO}_x$  are fossil fuel combustion, transport, electricity production and industrial processes. The majority of emitted  $\text{NO}_x$  is in the form of  $\text{NO}$  while  $\text{NO}_2$  is mainly produced in situ by the oxidation of  $\text{NO}$ . The dominant natural sources of VOCs are several kinds of terrestrial vegetation, mainly forests and of  $\text{NO}_x$  are lightning, biomass burning, and soil [EEA, 2016, Jacob, 2000, Monks et al., 2015]. According to model studies, the net global chemical tropospheric ozone production from its precursors is about  $450 \pm 300$  ( $1\sigma$ ) Tg/year [Stevenson et al., 2006]. The global mean annual tropospheric ozone burden has been simulated by models and is estimated to be equal to  $337 \pm 23$  ( $1\sigma$ ) Tg [IPCC, 2013]. Tropospheric ozone concentrations have increased by 50–100% (mainly close to the surface) since preindustrial times [Jacob, 2000]. Commonly observed surface ozone abundances range between less than 10 ppb (20 DU) over the tropical Pacific Ocean to more than 100 ppb ( $>50$  DU) over polluted regions [IPCC, 2013, Ziemke et al., 2011]. Ozone concentrations are higher in the northern than in the southern hemisphere,

due to the excess of precursor emissions [Jacob, 2000]. The globally averaged tropospheric ozone lifetime, calculated by two recent studies to be  $22.3 \pm 2$  ( $1\sigma$ ) days [Stevenson et al., 2006] and  $23.4 \pm 2$  ( $1\sigma$ ) days [Young et al., 2013], is comparable to the timescales of weather systems. However, tropospheric ozone's lifetime varies strongly with season, location and altitude. For example, in the boundary layer its lifetime is in the order of a few hours (because it is more likely to be destroyed by surface deposition and chemical reactions), whereas in the middle and upper troposphere its lifetime is in the order of weeks to months [Cooper et al., 2014].

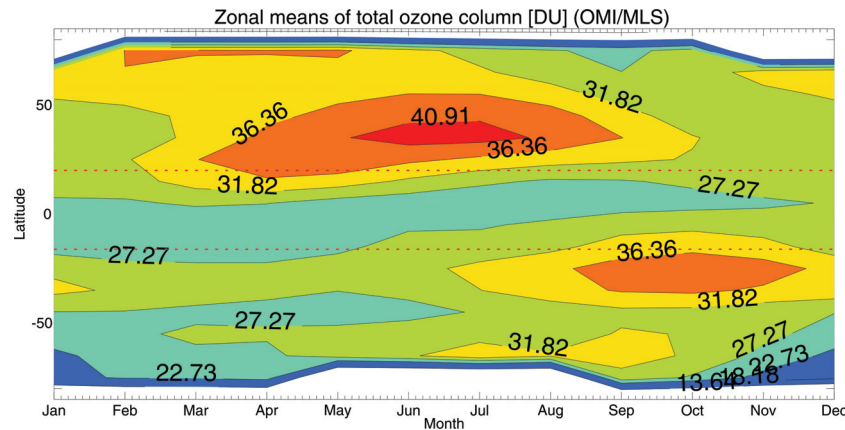


Figure 1.4: Zonal mean tropospheric ozone climatology (in Dobson Units) from OMI/MLS for the period October 2004 until December 2010. Red dashed lines indicate the tropics ( $20^{\circ}\text{N}$ – $20^{\circ}\text{S}$ ). Data found in: [https://acd-ext.gsfc.nasa.gov/Data\\_services/cloud\\_slice/](https://acd-ext.gsfc.nasa.gov/Data_services/cloud_slice/) [Ziemke et al., 2011].

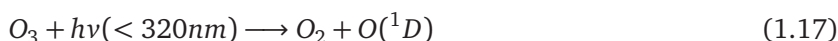
Tropospheric ozone concentrations are characterised by low amounts ( $<24$  DU) in the southern tropics ( $\sim 10^{\circ}\text{S}$ ) in winter to mid–spring and also in the northern and southern mid-latitudes in late autumn to winter–spring ( $<30$  DU). High tropospheric ozone columns ( $>40$  DU) occur in the northern mid-latitudes during summer and in the southern subtropics during autumn. The high tropospheric ozone in the northern subtropics during spring (March–May) are shifted to the summer months (June–July) in the mid-latitudes (see Fig. 1.4). Tropospheric ozone accumulates in the tropical south Atlantic throughout the year and in the Mediterranean/subtropical Asian region in the summer months [Ziemke et al., 2011].

### 1.2.1 Tropospheric ozone chemistry

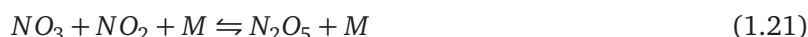
The concentration of ozone in the troposphere is controlled by chemical production and destruction processes, loss at the Earth's surface, transport, and vertical mixing in the atmosphere. Ozone formation and removal is essential for tropospheric chemistry, since it is one of the most abundant oxidants in the atmosphere, contributing greatly to the oxidation efficiency of the atmosphere. Oxidizing agents (compounds that accept electrons) are considered as the cleaning substances of the troposphere which prevent the accumulation of many pollutants. They can be removed from the atmosphere through electron transfer chemical reactions. However, ozone's large bonding energies causes it to be mainly active with radicals (atoms, molecules, or ions with unpaired valence electrons) [Jacob, 2000]. Nevertheless, ozone controls indirectly the oxidation efficiency of the atmosphere, since it is the primary

tropospheric source of hydroxyl radical (OH). OH is a very strong oxidant, reacting rapidly with the most reduced non-radical species, and especially with organic compounds, to produce water (H<sub>2</sub>O) [Ehhalt, 1994, Jacob, 2000]. Therefore, tropospheric ozone indirectly controls the concentration and lifetime of longer-lived greenhouse gases such as CH<sub>4</sub> (lifetime ~10 years), thereby affecting also the carbon cycle [Cooper et al., 2014, Crutzen, 1974, Monks, 2005, Shindell et al., 2009].

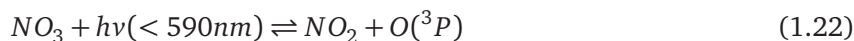
The OH radical production, shown in the following reactions 1.17 – 1.19, depends on tropospheric ozone abundance and on the Sun's radiation (in the troposphere the O(<sup>1</sup>D) is produced in a narrow wavelength band of 290–320 nm).



At night-time, the concentration of OH is almost zero (no photolysis of O<sub>3</sub>). Instead, another oxidant, the nitrate radical (NO<sub>3</sub>), becomes more important. NO<sub>3</sub> is generated at night by the reaction of NO<sub>2</sub> with ozone. NO<sub>3</sub> radicals further react with NO<sub>2</sub> to produce N<sub>2</sub>O<sub>5</sub> which is in equilibrium.

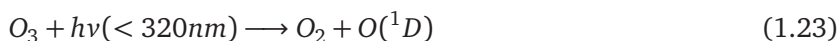


Reaction 1.20 also takes place during the day, however, NO<sub>3</sub> is rapidly photolysed, and therefore the concentrations of NO<sub>3</sub> and N<sub>2</sub>O<sub>5</sub> are both very low during the day-time.



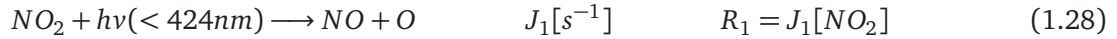
NO<sub>3</sub> and N<sub>2</sub>O<sub>5</sub> can react with water to create nitric acid (HNO<sub>3</sub>), which is later scavenged out from the troposphere by precipitation (acid rain), since it has a high solubility in water [Jacob, 2000].

Ozone chemical loss in the troposphere is mainly driven through photolysis to produce O(<sup>1</sup>D) (Reaction 1.17), which later forms OH via reaction 1.19. An OH<sub>x</sub> catalysed cycle, similar to reactions 1.7 – 1.9, also takes place in a remote (clean) troposphere, as shown in the following reactions 1.23 – 1.27 [Jacob, 2000].



Although OH<sub>x</sub> photochemistry is the main ozone loss cycle in the troposphere (25–100% contribution), halogen (specifically Br, and I) catalysed cycles of organic origin (via reactions 1.7 – 1.9) contribute by 15–30% to ozone loss in the tropical marine troposphere [Fowler et al., 2008, Saiz-Lopez et al., 2012].

The reaction that produces ozone in the atmosphere, as discussed in subsection 1.1.3, is  $O + O_2 + M \longrightarrow O_3 + M$ . The difference between stratospheric and tropospheric ozone formation lays in the source of atomic oxygen (O) (reaction 1.3). Since little radiation with wavelengths less than 290 nm penetrates the troposphere, the source of atomic O in the troposphere comes from the photolysis of  $NO_2$ , which produces O and NO at wavelengths less than 424 nm. However, NO will react with ozone, which leads to a photochemical steady state known as the *Leighton photo-stationary state* [Leighton, 1961]. The cycle is shown in the following reactions 1.28 – 1.30, and has no net effect on ozone.

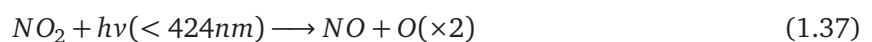


At daytime, the photolysis of  $NO_2$  (Reaction 1.28) balances the NO loss. At night, and when NO concentrations are too high, reaction 1.29 is dominant, resulting in ozone loss ( $NO_x$  titration). At one point,  $NO_2$  is being destroyed and reformed so fast that a steady-state equilibrium between reactions 1.28–1.30 is reached [Seinfeld and Pandis, 2006]. The equilibrium concentration of ozone is then:

$$[O_3]_{PSS} = \frac{J_1[NO_2]}{k_2[NO]}. \quad (1.31)$$

The ratio between NO and  $NO_2$  depends on the local concentration of ozone, the photolysis frequency ( $J_1$ ) of reaction 1.28 and the rate coefficient ( $k_2$ ) in reaction 1.29. If typical concentrations of NO and  $NO_2$ , and typical values for ( $J_1$ ) and  $k_2$  are substituted to equation 1.31, the concentrations of  $O_3$  are much less than the observed ones for the free troposphere [Wallace and Hobbs, 2006].

While the Leighton relationship is important for recycling NO and  $NO_2$ , it can not represent a production mechanism for tropospheric ozone since it does not lead to net ozone production. Hence, another mechanism that includes methane ( $CH_4$ ) was proposed by Chameides [1973] and Crutzen [1974], who suggested that the methane oxidation provides a photochemical source of odd oxygen and consequently of ozone in the troposphere. Today we know that tropospheric ozone is produced as a by-product of volatile organic compounds (VOCs) oxidation (plus carbon monoxide (CO), methane ( $CH_4$ ), and non- $CH_4$  hydrocarbons), which takes place in the presence of nitrogen oxides ( $NO_x$ ) to produce organic oxy and peroxy radicals (RO and  $RO_2$ ). In general, the tropospheric ozone production cycle is summarised in the following reactions 1.32 – 1.39, where R is an organic group, in the simplest form  $CH_3$ , and R' is an organic group having one less carbon atom than R [Jacob, 2000].





In the troposphere, this cycle is also known as the *methane photochemical oxidation cycle*. Another cycle with the oxidation of CO is present in the troposphere, where HO<sub>2</sub> fulfills a similar role with RO<sub>2</sub>. The carbonyl products (e.g. formaldehyde (R'CHO)) can afterwards react with OH or photolyse to generate more HO<sub>x</sub> radicals and finally produce more ozone (branching) or react with OH to continue the propagation of the chain reactions. The chain is terminated by the loss of hydroperoxy (HO<sub>x</sub>) and peroxy (RO<sub>x</sub>) radicals [Holloway and Wayne, 2010, Jacob, 2000, Lightfoot et al., 1992, Wallace and Hobbs, 2006].

There are two main pathways for the HO<sub>x</sub> and RO<sub>x</sub> loss:

- **When NO<sub>x</sub> is too low:**

Hydroperoxy and peroxy radicals react with each-other, instead of with NO, and to produce peroxides according to reactions 1.40 and 1.41,



or with ozone to produce OH (O<sub>3</sub> loss):



H<sub>2</sub>O<sub>2</sub> is removed from the atmosphere by deposition or it can also photolyse or react with OH.



- **When NO<sub>x</sub> is too high:**

The dominant sink for HO<sub>x</sub> is the reaction of OH with NO<sub>2</sub>:



The net tropospheric ozone production depends on the rate of reactions 1.34 and 1.36, that regenerates NO<sub>2</sub>. Each time an RO<sub>2</sub>/HO<sub>2</sub> molecule reacts with NO, an additional "new" O<sub>3</sub> molecule is produced since the resulting NO<sub>2</sub> is formed without any ozone molecule consumption, as shown in reaction 1.29 (the ratio [NO<sub>2</sub>]/[NO] in equation 1.31 increases).

The production of ozone is then given by the following relation:

$$P_{O_3} = k_{34}[RO_2][NO] + k_{36}[HO_2][NO] \approx 2k_{36}[HO_2][NO] \quad (1.46)$$

Assuming an efficient HO<sub>x</sub> recycling (reactions 1.32–1.36), the rate of HO<sub>x</sub> production is balanced by its loss through reactions 1.40 and 1.42:

$$P_{HO_x} = L_{HO_x} = k_{40}[HO_2]^2 + k_{45}[NO_2][OH][M] \quad (1.47)$$

The limited concentrations of VOCs and  $NO_x$  levels have a strong effect on ozone production in the troposphere.

- **$NO_x$  limited regime** (*Low  $NO_x$  concentrations*)

The rate of reaction 1.40 is much greater than the rate of reaction 1.45. This means that the principal sink of  $HO_x$  is reaction 1.40. For this reason, the second right part of equation 1.47 can be neglected. The steady-state concentration of  $HO_2$  under low  $NO_x$  conditions is then:

$$[HO_2] \cong \sqrt{\frac{P_{HO_x}}{k_{40}}} \quad (1.48)$$

Substituting this concentration to equation 1.46 yields:

$$P_{O_3} \cong 2k_{36} \sqrt{\frac{P_{HO_x}}{k_{40}}} \cdot [NO] \quad (1.49)$$

indicating that the rate of ozone formation is linearly related to the concentration of  $NO$ , and independent of VOCs concentration [Jacob, 2000, Seinfeld and Pandis, 2006].

- **VOCs limited regime** (*High  $NO_x$  concentrations*)

The rate of reaction 1.40 is much smaller than the rate of reaction 1.45. This means that the principal sink of  $HO_x$  is reaction 1.45, and that the first term of relation 1.47 can be neglected. From Eq. 1.47:

$$[OH] = \frac{P_{HO_x}}{k_{45}[NO_2][M]} \quad (1.50)$$

But the concentration of  $OH$  is the balance between production from reaction 1.36 and loss from reaction 1.32:

$$[OH] = \frac{k_{36}[HO_2][NO]}{k_{32}[RH]} \quad (1.51)$$

From Eq. 1.50 and 1.51, the steady-state concentration of  $HO_2$  under high  $NO_x$  conditions is then:

$$[HO_2] \cong \frac{P_{HO_x} k_{32}[RH]}{k_{36} k_{45}[NO][NO_2][M]} \quad (1.52)$$

Substituting now this  $[HO_2]$  concentration to equation 1.46 the ozone production is:

$$P_{O_3} \cong 2k_{32} \frac{P_{HO_x}[RH]}{k_{45}[NO_2][M]} \quad (1.53)$$

meaning that ozone production is linearly related to VOCs concentrations and inversely related to  $NO_x$  concentrations (increased  $NO_x$  result in lower  $O_3$  concentrations) [Jacob, 2000, Seinfeld and Pandis, 2006].

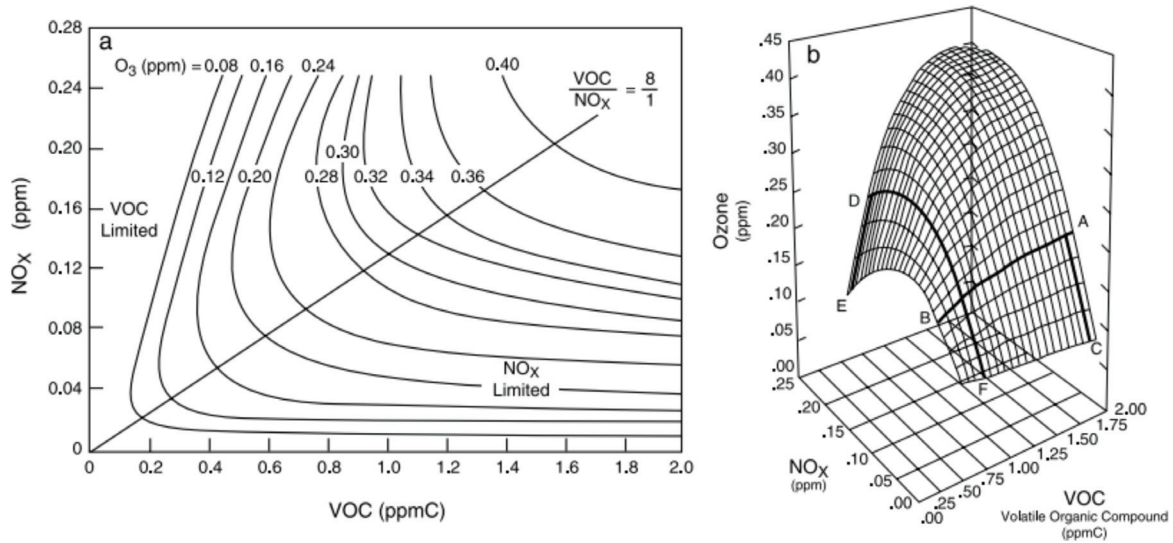


Figure 1.5: a) Two typical dimensional peak ozone isopleths from the EKMA (Empirical Kinetic Modeling Approach) model [Dimitriadis and Dodge, 1983], versus the initial VOCs and  $\text{NO}_x$  mixing ratios. b) Two-dimensional plot of the VOC-  $\text{NO}_x$  limited regions. The VOC-limited region (Point D) is located in a highly polluted urban area while the  $\text{NO}_x$  limited region (point A) is typical for a rural area, downwind of a suburban or urban areas (Figure adapted from: Finlayson-Pitts and Pitts [2000]).

The ratio of VOCs to  $\text{NO}_x$  ambient concentrations (the differentiation between  $\text{NO}_x$  sensitive and VOCs sensitive regime) plays a key role in the rate of ozone production. The EKMA (Empirical Kinetic Modelling Approach) [Dimitriadis and Dodge, 1983], is a simple box model which can be used to estimate the amount of ozone produced from various ambient VOCs and  $\text{NO}_x$  concentrations. The results of the ozone amounts produced by this model have been later tested with environmental chamber data [Finlayson-Pitts and Pitts, 2000]. According to EKMA, which assumes an absence of large transport of ozone into a region, a VOC to  $\text{NO}_x$  ratio of about 8/1 is optimal for ozone production. Figure 1.5.a shows the peak ozone isopleths (in ppm) as a function of VOC (in ppmC) and  $\text{NO}_x$  concentrations (in ppm). The VOC limited regime occurs when VOC/ $\text{NO}_x$  less than 8/1, whereas the  $\text{NO}_x$  limited regime occurs when the VOC/ $\text{NO}_x$  is much more than 8/1 (below the 8/1 line). The same data are plotted in a 3-dimensional contour plot (Figure 1.5.b), where the overall shape of the contours gives useful information about the  $\text{O}_3$  production regime, and consequently of measures to reduce VOCs or  $\text{NO}_x$  emissions, meant to reduce  $\text{O}_3$  abundances [Finlayson-Pitts and Pitts, 2000].

At high VOCs/ $\text{NO}_x$  ratios ( $\text{NO}_x$ -limited regime, point A in Fig. 1.5.b), a decrease in VOCs while keeping  $\text{NO}_x$  emissions constant (moving along the AB line) results in a slight reduction of  $\text{O}_3$ . However, decreasing  $\text{NO}_x$  concentrations while keeping VOCs-levels constant (moving along the AC line), is much more effective in reducing  $\text{O}_3$ . High VOCs/ $\text{NO}_x$  ratios are typical for rural and suburban downwind areas. When VOC/ $\text{NO}_x$  ratios are low (VOCs-limited regime), point D in Fig. 1.5.b, a reduction in VOC while  $\text{NO}_x$  concentrations remain constant (moving along the DE line) results in a reduction in  $\text{O}_3$  concentrations. However, reducing  $\text{NO}_x$  while VOC is constant (moving along the DF line), increases  $\text{O}_3$  until one point. These ratios are typical for polluted urban areas. It is important to note that, while the EKMA model is a very useful simplified approach, which links the precursors concentrations with

instantaneous ozone production, it does not include complex meteorology which could explain the ambient ozone concentrations. Mixing, long-range transport, boundary layer inversions, and deposition can strongly influence the ambient ozone concentrations in the areas with precursor emissions, and in its downwind regions [Finlayson-Pitts and Pitts, 2000, Sillman et al., 1999].

### 1.2.2 Transport and mixing of tropospheric ozone

The differential heating of the Earth by the Sun at various latitudes activates atmospheric motions with air-masses rising up at the Equator, moving polewards within the tropical upper troposphere, and descending due to adiabatic cooling at the subtropics ( $\sim 30^\circ$ ). The dominant transport pathway in the tropics follows the surface *trade winds*, propagating from north (south) east direction towards the Equator. Trade winds consist of the surface manifestation of the overturning circulation, called the *Hadley cell* (see Fig. 1.6). The trade winds meet with the extra-tropical westerly winds (*Ferrel cell*), and a subtropical high-pressure belt appears on the surface [Wallace and Hobbs, 2006]. Right above it, close to the tropopause, the wind stress produces a counterclockwise circulation called the *subtropical jet stream*, with wind speeds reaching 442 km/h [Seinfeld and Pandis, 2006]. However, this idealised tropical circulation pattern does not totally represent the reality. The low pressure belt where the northeast and southeast trade winds come together, called the *Inter Tropical Convergence Zone* (ITCZ), follows the location of the thermal equator. Therefore, the ITCZ position varies with the seasons, moving northwards in summer and southwards in winter [Seinfeld and Pandis, 2006, Wallace and Hobbs, 2006]. The ITCZ location is linked with deep convective clouds occurrences and heavy rainfall. This global circulation pattern contributes to the long-range transport of atmospheric pollutants.

Due to its chemical lifetime ( $\sim 22$  days), which coincides with the timescales of tropical cyclones, frontal zones, and weather systems, tropospheric ozone can be regionally, intercontinentally and hemispherically transported. Several studies have shown that ozone and its precursors are redistributed from their production area or their emission source to remote regions [Diab et al., 2003, Martin et al., 2002, Sauvage et al., 2006]. For example, tropospheric ozone originating from eastern China increases the ozone abundance over Japan and North America's West Coast [Cooper et al., 2010, Oltmans et al., 2013, Parrish et al., 2009, Verstraeten et al., 2016]. Additionally, high tropospheric ozone amounts over the southern Atlantic ocean originate from ozone precursors released from biomass burning in south America and Africa which are transported there through pressure systems, such as cyclones [Diab et al., 2003, Martin et al., 2002]. In smaller scales, convection influences tropospheric ozone and its precursors burden by redistributing them via vertical mixing. Lower tropospheric ozone is lifted up to the upper troposphere (UT) where ozone lifetime is longer, while due to mass balance conservation, this UT air, rich in  $O_3$ , mixes and submerges into regions where ozone lifetime is shorter. As a result, the UT  $O_3$  as well as the overall tropospheric  $O_3$  column decreases [Doherty et al., 2005].

Besides the typical circulation pattern of the atmosphere, there are also seasonal and irregularly periodical circulations that influence tropospheric ozone concentrations in the tropics. The *El Niño Southern Oscillation* (ENSO) is one of the most important ocean-atmosphere interconnections in the tropics. Under regular (neutral) conditions, the sea-level pressure is higher on the East than on the West Pacific ocean. This difference in the sea surface pressure and temperature results in a zonal circulation

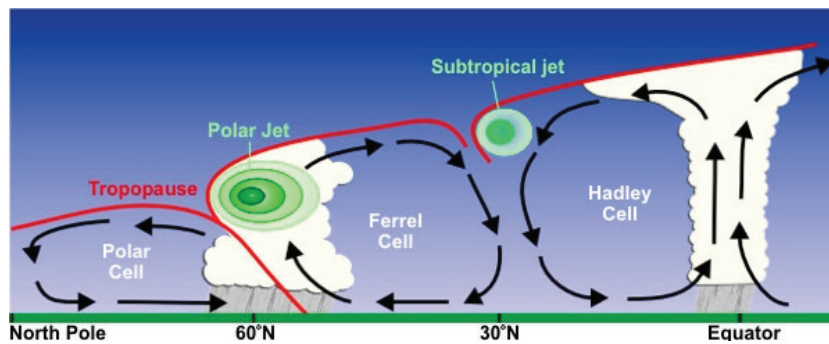


Figure 1.6: North hemisphere longitudinal section showing the Hadley, Ferrel, Polar cells, the sub-tropical and polar jet streams, and the tropopause elevations (Figure taken from NOAA/NWS: <http://www.srh.noaa.gov/jetstream/global/jet.html>).

known as the *Walker circulation* (see Fig. 1.7 top), which consists of rising and sinking cells. Air masses strongly rise over the western Pacific ocean (warm pool), and more weakly over eastern Africa and northern South America. The upwelling branches are related to deep convective clouds and heavy precipitation. The loops are closing with descending branches of dry air over the eastern Pacific Ocean and the Arabian Sea [UNEP, 1986]. During *El Niño* events, the sea-level pressure in the western Pacific exceeds the normal climatological values so that the easterly surface winds are weakened [Wallace and Hobbs, 2006]. Figure 1.7 (middle) shows the modification of the Walker circulation due to the anomalous ocean warming in the central and eastern Pacific (orange) which drives a rising branch of the Walker Circulation over the East Pacific Ocean and eastern Africa, while the descending branches are shifted to the Indonesian/West Pacific Ocean and northern South America. *La Niña* conditions follow the El Niño events (Fig.1.7 bottom), when the sea surface temperature in the western Pacific are even warmer and in the eastern Pacific, even colder than normal, which is similar to an enhanced case of the neutral conditions. The temperature, humidity, biomass burning emissions, and thus trace gases emissions including ozone, are strongly affected by these events which can even last for a whole year. The ENSO effects on tropospheric ozone have been extensively studied and documented by use of ground-based measurements and global chemical transport and general circulation models (e.g [Chandra et al., 2009, Doherty et al., 2006, Murray et al., 2013, Neu et al., 2014, Oman et al., 2011, Randel and Thompson, 2011, Randel et al., 2009, Thompson et al., 2001, Valks et al., 2003, Ziemke et al., 2010]).

The *monsoon circulation* is another cause of surface winds with seasonal variation. During summer, the southeast trade winds from the south hemisphere that cross the equator are refracted eastwards in the Northern Hemisphere due to the Coriolis effect, thereby forming an arc. The opposite circulation takes place in winter [Wallace and Hobbs, 2006]. As a result, clean ozone air reaches the Indian ocean in summer and polluted continental air masses in winter [Loschnigg and Webster, 2000, Yonemura et al., 2002]. The *Madden-Julian Oscillation* (MJO) is an intra-seasonal (30-60 days) eastward propagating disturbance of clouds, rainfall, winds, and pressure in the tropics [Madden and Julian, 1971]. The MJO is divided into two phases producing a dipole. The first one, wherein the rainfall is enhanced, and the second one, wherein the rainfall is suppressed. MJO can affect the occurrence and strength of monsoons and tropical cyclones, modulate the subtropical jet stream, and cause extreme heat events or

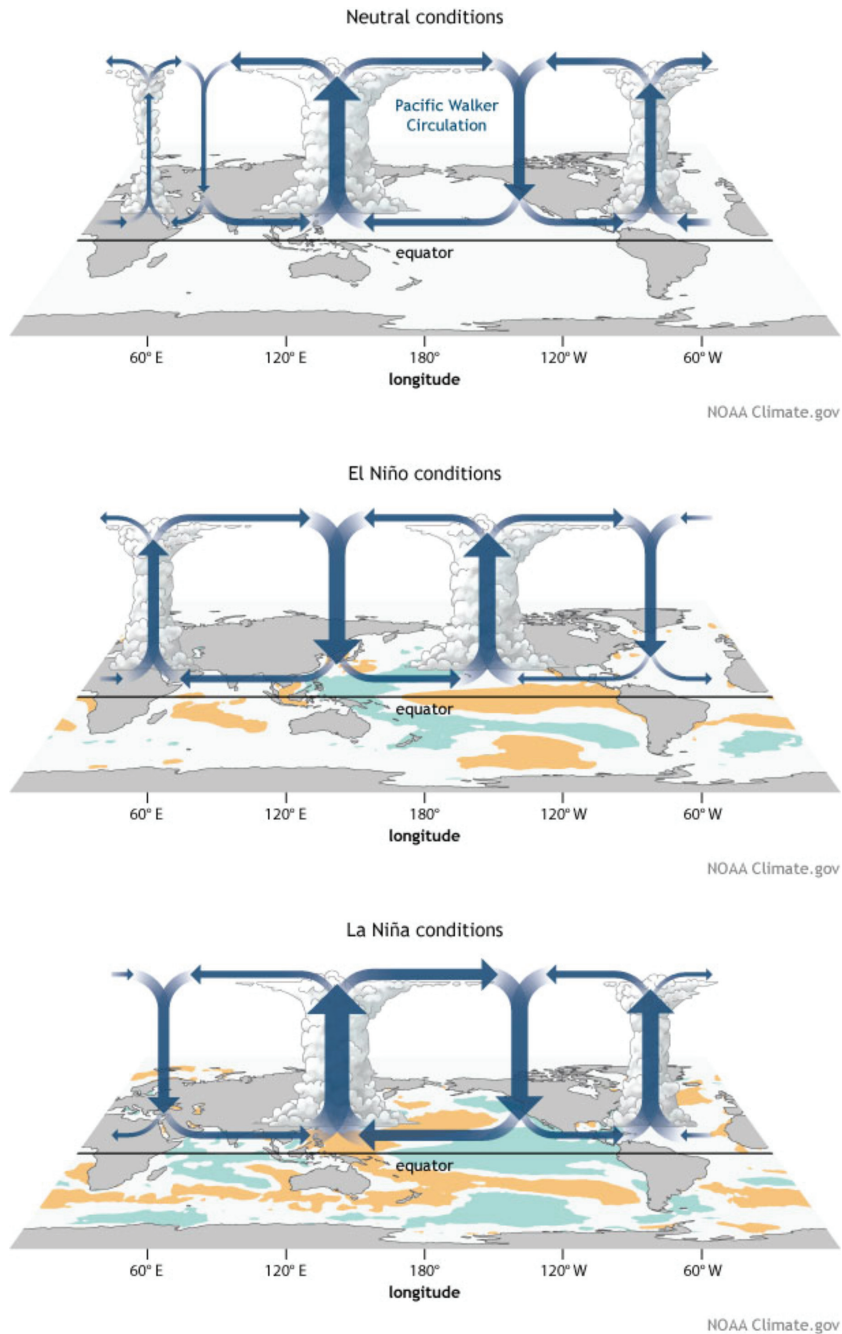


Figure 1.7: Standard Walker Circulation for December-February during neutral (Top), El Niño (middle), and La Niña (bottom) conditions. (Figure taken from NOAA: <https://www.climate.gov/news-features/blogs/enso/walker-circulation-ensos-atmospheric-buddy>, drawing by Fiona Martin.)

floods. The MJO events influence the atmospheric composition, including ozone. Ziemke et al. [2015] showed that the MJO has a bigger impact on tropical tropospheric ozone than ENSO (by a factor of  $\sim 3-10$ ), however they appear only in weekly time scales.

Tropospheric ozone abundance is also influenced by the exchange of air masses from the stratosphere to troposphere (STE) (552 Tg/year [IPCC, 2013]). There are also cases where deep convection penetrating the tropopause, decreases regionally the tropospheric ozone columns [Fueglistaler et al., 2009, Hong et al., 2007]. However, tropopause folds and wave breaking, mainly in the middle latitudes during winter/spring, are significant sources of ozone-rich air to the troposphere [Lamarque et al., 2005, Neu et al., 2014, Terao et al., 2008, Zanis et al., 2003]. This process is balanced with ozone-poor air masses entering the stratosphere, mainly in the tropics via the *Brewer Dobson* (BD) circulation. The Brewer-Dobson circulation consists of the meridional transport of air from the tropics to the poles. The air masses from the ozone production region (mid- to upper stratosphere) descent at the polar (north hemisphere) or extra-tropical (south hemisphere) lower stratosphere, where ozone lifetime is longer, thereby accumulating ozone. During autumn and winter, BD is stronger in the Northern hemisphere than in the south, resulting in higher total ozone values in the Arctic in comparison to the Antarctic [Brewer et al., 1949, Butchart et al., 2014, Castanheira et al., 2012, Dobson, 1956, Holloway and Wayne, 2010, Stevenson et al., 2000]. An increase in the tropical upwelling is expected to reduce both lower stratospheric ozone and the total column ozone in the tropics, increasing the UV-B radiation reaching the troposphere [WMO, 2014]. This could result in an enhance of tropospheric ozone photolysis (photochemical ozone sink). However, the increase of UV-B radiation at the surface would also lead to increased concentrations of OH (hydroxyl radicals) and subsequently increased concentrations of HO<sub>2</sub> and RO<sub>2</sub> radicals, which could enhance the production of ozone if NO<sub>x</sub> are available (e.g. in mega-cities) [UNEP, 1998].

The *quasi-biennial oscillation* (QBO) is the dominant source of inter-annual variability in the tropical stratosphere. QBO is the quasi-periodic oscillation of stratospheric zonal wind above the equator between the easterlies (winds moving toward the east) and the westerlies (winds moving toward the west) with a mean period of  $\sim 26$  months. These wind regimes transport momentum, and propagate downwards with a rate of 1 km per month, until they are degraded at the tropical tropopause [Plumb and McEwan, 1978, Rohli and Vega, 2011]. The east phase QBO winds are approximately two times stronger and last longer than the west phase winds [Baldwin et al., 2001, Rohli and Vega, 2011]. QBO affects the temperature structure and the photochemistry of the stratosphere, along with the Brewer Dobson circulation [Mohankumar, 2008]. Ziemke and Chandra [1999] showed that there is a response of QBO on tropospheric ozone in anti-correlation with the stratospheric ozone with a 3 months delay. The descending QBO westerlies are associated with a downward motion in the tropics and an upward motion in the subtropics. Weakening the normal Brewer Dobson circulation in the tropics, tropospheric ozone is increased in the tropics and decreased in the subtropics. The descending easterly phase of the QBO enhances the Brewer Dobson circulation in the tropics resulting in decreased tropospheric ozone in the tropics and increased tropospheric ozone in the subtropics [Bruhwiler and Hamilton, 1999].

### 1.2.3 Deposition of tropospheric ozone

The rate of tropospheric ozone deposition on land, water and vegetation determines its exposure time in biosphere. Ozone being a reactive gas and potent oxidizing agent, deposits on most surfaces simply by oxidative reactions [Grontoft et al., 2004].

Ozone's dry deposition is being measured using micrometeorological methods. It has been estimated to have a positive flux of 1003 Tg/year [IPCC, 2013]. Most deposition models use resistance analogies

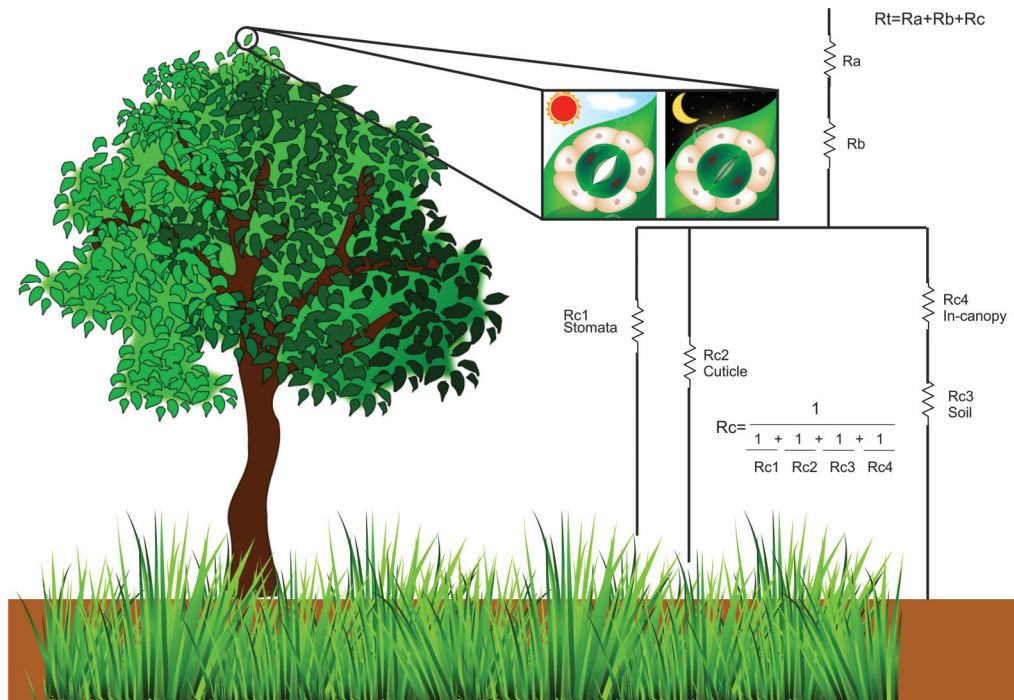


Figure 1.8: Pathway of resistances (R) to dry deposition of ozone.

which simulate the deposition or exchange of ozone between the atmosphere and surface (see Fig. 1.8). These resistances parameterize fundamental physical, chemical and vegetative factors [Wesely and Hicks, 2000]. In Fig. 1.8,  $R_a$  represents the aerodynamic resistance above the surface and depends mainly on the local atmospheric turbulence conditions,  $R_b$  represents the diffusivity of ozone, and  $R_c$  represents the ability of leaf stomata, vegetation cuticle, in-canopy chemistry and soil to act as an ozone sink.

Stomatal openings are used by plants to control their humidity level and to receive  $\text{CO}_2$  for photosynthesis. During this procedure, plants take up ozone as well, which contributes to their oxidation. Stomata are usually open during sunlit hours, although humidity, temperature and aerosols may change this behavior. Although stomatal uptake ( $R_{c1}$ ) is the main factor regulating surface fluxes during day time [Fowler et al., 2009], other processes (non-stomatal uptake) are dominant during night-time. The non-stomatal uptake ( $R_{ns}$ ) comprise the reaction of ozone with the cuticle of the plants ( $R_{c2}$ ), the in-canopy chemistry, and the deposition on soil ( $R_{c3}$ ).  $R_{ns}$  is the sum of  $R_{c2}$ ,  $R_{c3}$  and  $R_{c4}$  and is usually calculated as the residual term from the total deposition flux,  $R_c$  minus the stomatal flux,  $R_{c1}$ , in a

parallel circuit analogy [Monks et al., 2015, Zhang et al., 2003]:

$$R_{ns} = \left( \frac{1}{R_c} - \frac{1}{R_{c1}} \right)^{-1},$$

where:

$$R_c = \left( \frac{1}{R_{c1}} + \frac{1}{R_{c2}} + \frac{1}{R_{c3}} + \frac{1}{R_{c4}} \right)^{-1}$$

While ozone has a low solubility in open water [Battino et al., 1983], its deposition into the ocean comprises almost 40% of the total annual surface dry deposition [Hardacre et al., 2015]. The type of underlying vegetation, the degree of water turbulence and opacity, and the presence of reactive chemical compounds can strongly influence ozone solubility in water [Monks et al., 2015]. Large NO soil emissions and VOCs from vegetation can rapidly destroy or produce ozone over the canopy (in-canopy chemistry) [Coyle et al., 2005, Kurpius and Goldstein, 2003, Neiryneck et al., 2012]. Surface temperature and solar irradiance can also increase ozone deposition by increasing the reaction rates between ozone and hydrocarbons over the canopy [Coyle et al., 2009, Fowler et al., 2009].

### 1.2.4 Impact of tropospheric ozone on climate and air pollution

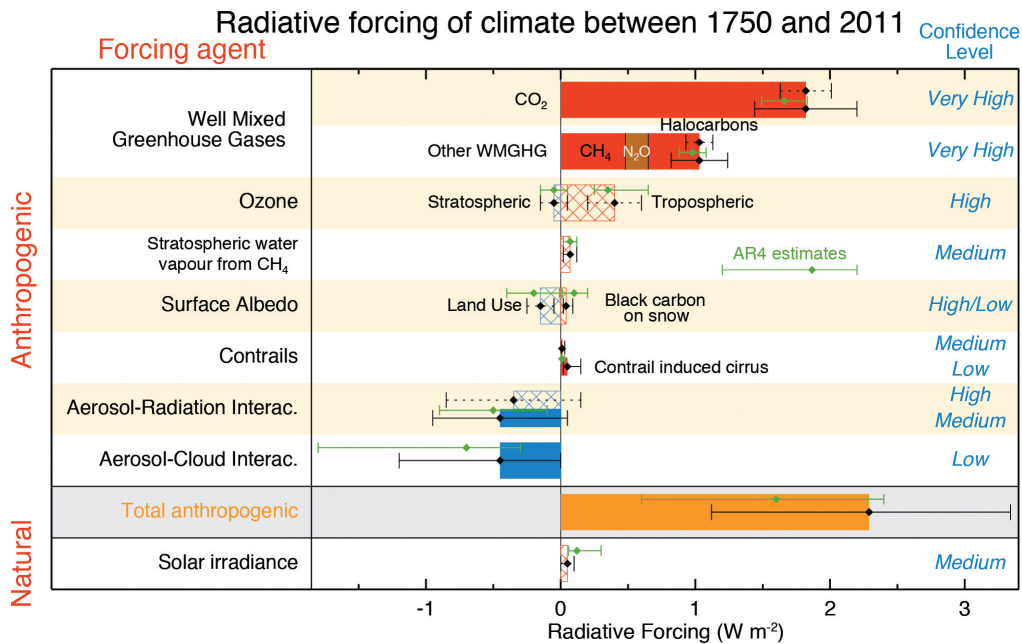


Figure 1.9: Radiative forcing, (RF), (hatched) and effective radiative forcing, (ERF), (solid) of several forcing agents and their confidence level for the period 1750–2011. (Figure taken from: Stocker et al. [2013], as part of the Physical Science Basis, contributing in the Working Group I (WGI) to the Fifth Assessment Report (AR5) of IPCC [2013]).

Tropospheric ozone is considered to be the third most important anthropogenic greenhouse gas, after CO<sub>2</sub> and CH<sub>4</sub> (see Fig. 1.9) [IPCC, 2013]. In the troposphere, ozone can interact both with solar as well as with terrestrial radiation in the infra-red (IR) wavelengths (700 nm–1 mm). Since ozone strongly

absorbs thermal IR (maximum absorption at  $9.6 \mu\text{m}$ ), the molecule heats and vibrates. After absorption, the  $\text{O}_3$  molecule gives up the extra energy by emitting photons in the IR region. By this process,  $\text{O}_3$  traps the outgoing terrestrial IR radiation, and warms the upper troposphere and lower stratosphere. For this reason, a change in ozone distribution causes *radiative forcing* (RF). Radiative forcing is the change in net downward radiative flux at the tropopause, after allowing stratospheric temperatures to reach radiative equilibrium, while holding surface and tropospheric temperatures and state variables constant at the unperturbed values, representing pre-climate change conditions [IPCC, 2007]. Another term which can be used is *effective radiative forcing* (ERF), which is the change in net top of the atmosphere (TOA) downward radiative flux after allowing atmospheric temperatures, water vapour and clouds to reach equilibrium, while surface temperature or a portion of the surface conditions remain unchanged [IPCC, 2007]. The Fifth Assessment Report of the Intergovernmental Panel on Climate Change (IPCC) states that changes in tropospheric ozone between the years 1750 and 2010 have caused a positive RF of about  $0.40 \text{ W}\cdot\text{m}^{-2}$  (90% confidence range:  $0.20$  to  $0.60 \text{ W}\cdot\text{m}^{-2}$ ) [IPCC, 2013, Myhre et al., 2013]. RF from tropospheric ozone is maximum in the tropics ( $+0.6$  to  $1 \text{ W}\cdot\text{m}^{-2}$ ) and is strongly dependent on location and distribution of its precursor emissions ( $\text{NO}_x$ ,  $\text{CO}$ ,  $\text{CH}_4$ , VOCs, and non-methane volatile organic compounds (NMVOCs)) [Myhre et al., 2013].

Ground level ozone is an important atmospheric pollutant. Mainly in large urban areas, where meteorological conditions favor boundary layer inversions, ozone precursors can lead to extremely high ozone concentrations that last for several days. The highest ever recorded hourly average  $\text{O}_3$  mixing ratio was 680 ppb, in Los Angeles in 1955 [Seinfeld and Pandis, 2006]. These high concentrations which mostly occur in summer, are broadly known as *Los-Angeles or photochemical smog episodes* (smog=smoke+fog), and receive significant attention due to their impact on human health and visibility. Air pollution is strongly linked with climate change, affecting the Earth's climate regionally and globally, and, inversely, climate change may impact air pollution events [WMO/IGAC, 2012]. Climate change effects tend to balance some of the tropospheric ozone increase driven by emissions [IPCC, 2013]. For example, the increased sea surface temperatures may result in enhanced water vapor concentrations, which in combination with low overhead (stratospheric) ozone, results in high actinic fluxes of  $\lambda < 340 \text{ nm}$ , which maximizes the efficiency of ozone loss [Rex et al., 2014]. The enhanced water vapour and OH concentrations can also affect the rates of  $\text{CH}_4$  oxidation, further reducing the lifetime of tropospheric  $\text{CH}_4$ . Stevenson et al. [2000] calculated that the lifetime of  $\text{CH}_4$  will decrease by 5–12% between the years 1990 and 2100. Lower  $\text{CH}_4$  concentrations lead to reduced tropospheric ozone. Since the photochemical ozone production depends on  $\text{NO}_x$  concentrations, additional water vapour can cause more  $\text{NO}_x$  to be dissolved in water molecules and to be converted to nitric acid ( $\text{HNO}_3$ ), which later can be removed from the atmosphere through precipitation [Grewe et al., 2001]. On the other hand, controls on anthropogenic emissions of  $\text{CH}_4$  in order to control ozone abundances on the surface, have a positive feedback on climate change since  $\text{CH}_4$  is also a powerful greenhouse gas. However,  $\text{NO}_x$  emissions also control the lifetime of  $\text{CH}_4$ , and is more likely to cause warming, although it might be expected to have a cooling effect as they could reduce tropospheric ozone concentrations [IPCC, 2013].

### 1.2.5 Impact of tropospheric ozone on biosphere

Ozone is a strong oxidant and can cause direct and indirect oxidative damage to biological cells. As an allotrope of oxygen, ozone can displace  $O_2$  in the lungs, causing respiratory problems. The impacts may vary from changes in lung functioning to asthma or premature mortality [Fowler et al., 2008, WHO, 2006]. Enhanced ozone is also linked to chronic obstructive pulmonary disease (COPD) and to lung cancer [Burnett et al., 1997, Lelieveld et al., 2015, Medina-Ramon et al., 2006, Uysal et al., 2003]. Ozone may also affect heart functioning, causing arrhythmia that increases the risk of a stroke [Rich et al., 2006]. It can also irritate the eyes, causing red and itchy eyes. Respiratory problems, caused by exposure to ozone, are responsible for roughly 150,000 deaths per year [Lim et al., 2012]. Increasing tropospheric ozone concentrations, is expected to increase the mortality and hospital admissions. An increase of ozone exposure in the order of  $10 \mu\text{g}/\text{m}^3$  may increase the daily mortality by 0.3%, and the heart diseases by 0.4% [WHO, 2015]. According to the European Union (EU) Air Quality Directive, the maximum daily 8-hour mean exposure limit is  $120 \mu\text{g}/\text{m}^3$ , whereas according to the World Health Organization (WHO) air-quality guidelines (AQGs), it is  $100 \mu\text{g}/\text{m}^3$ . The 1 hour information threshold defined in the EU Ambient Air Quality Directive is  $180 \mu\text{g}/\text{m}^3$  and the alert threshold, is  $240 \mu\text{g}/\text{m}^3$  [EU, 2008, WHO, 2006]. In 2014, 16 out of the 28 EU member states exceeded the surface ozone concentrations limits for the protection of human health set by the EU. It was estimated that in 2014 around 96 % of the EU-28 urban population lives in areas where the ozone levels are higher than the WHO AQG threshold for human health protection [EEA, 2016].

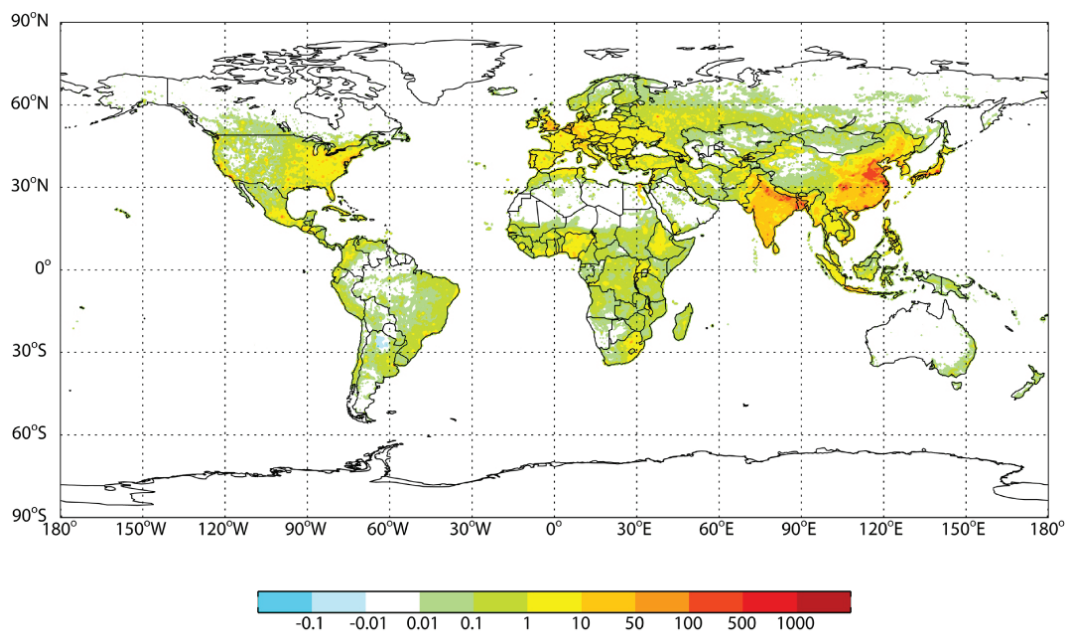


Figure 1.10: Current premature mortality due to ozone pollution (2000–1850). The results from a 14 models are presented in deaths/year per  $1000 \text{ km}^2$  (Figure taken from: Silva et al. [2013].)

Plants are also affected by ozone; during respiration, ozone enters the leaves, causing chlorosis and necrosis, reducing the photosynthetic ability of the plants and the seed production [Monks et al., 2015, U.S. Department of Agriculture, 2012]. The impact is more intense above a threshold of 40 ppb,

although it depends on the species and the environmental conditions [Felzer et al., 2004, WHO, 2015]. A study by Van Dingenen et al. [2009] on four crop types including, wheat, soybeans, rice and maize, estimated that current ozone levels cause yield losses of 3-16%, and is dependent on crop type and modeling assumptions. The same study estimated that for the year 2000, the economic loss was in the range of 14-26 billion dollars. According to model results, China, India, and USA are the most affected countries by crop damage due to ozone [Monks et al., 2015]. In 2013, the EU vegetation protection limit for ozone (40 ppb (AOT40)) was exceeded in about 21% of the EU-28 agricultural land area mainly in southern Mediterranean regions [EEA, 2016].

### 1.3 Absorption spectroscopy\*

#### 1.3.1 Electromagnetic radiation

Electromagnetic radiation is a form of energy, of which oscillating electric and magnetic waves propagate through space with the speed of light ( $c \approx 2.998 \cdot 10^8$  m/s in vacuum), thereby also having a particle-like nature (photons). Electromagnetic radiation has certain characteristics as frequency,  $\nu$  and wavelength  $\lambda$ , related by:

$$c = \nu \times \lambda \quad (1.54)$$

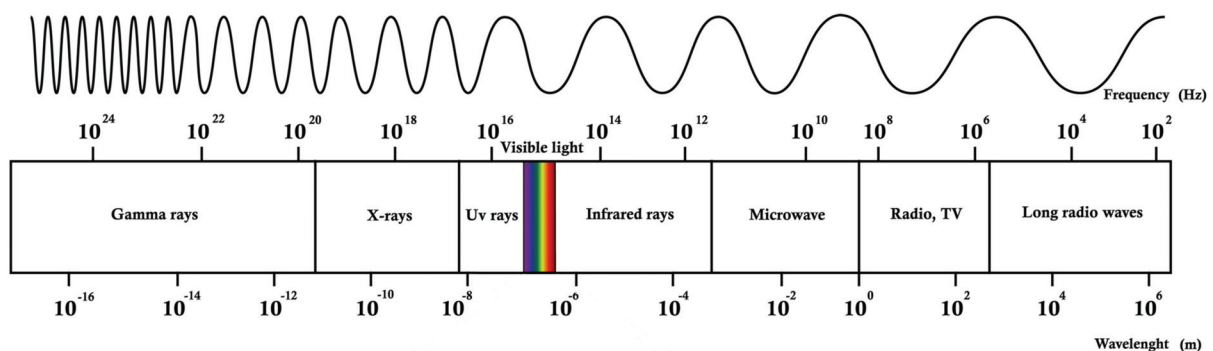


Figure 1.11: Sketch of the electromagnetic spectrum at different wavelength (m) ranges from  $\gamma$ -rays to radio waves. (Figure taken from: <http://www.livescience.com/38169-electromagnetism.html>)

The electromagnetic spectrum is divided into 7 general regions (see Fig 1.11).  $\gamma$  and X rays reach to 30 nm, UV radiation extends at wavelengths between 100 nm and 390 nm, visible radiation ranges between 390 nm to 780 nm, IR from 780 nm to 1 mm, and wavelengths longer than 1 mm are known as microwave and radio-wave radiation. The  $\gamma$  and X-ray region usually characterises radiation by the photon energy (eV), the UV and visible region usually characterises radiation by wavelengths in nm, the IR region characterises radiation by the wavenumber ( $1/\lambda = \nu/c$ ) in  $\text{cm}^{-1}$ , and the radio wave region characterises radiation by the frequency (Hz). The UV-region is subdivided into 4 regions. The short wavelength region (100 - 200 nm) is commonly called vacuum-UV, since it is absorbed very easily and can only be studied in vacuum. The other regions are UVC (200 – 280 nm) which is absorbed at

\*This section has been based on Wallace and Hobbs [2006], Liou [2002], and Burrows et al. [2011]

the upper atmosphere, UVB (280 – 320 nm), and UVA (320 – 400 nm) that are mainly absorbed in the stratosphere, however they can reach the ground. According to *Planck–Einstein relation*, the energy,  $E$ , of a photon is related with the frequency of radiation:

$$E = h\nu = hc/\lambda \quad (1.55)$$

where  $h=6.626\times 10^{-34}$  Js, denotes the Planck's constant.

Except from the wave-like nature, electromagnetic radiation can also be described as a stream of particles. When passing through the atmosphere is either scattered or absorbed. It is possible that a photon collides with a molecule and that the molecule remain unaffected but the photon changes direction. This procedure is called "*Rayleigh scattering*" and depends on the wavelength of the light ( $I \propto \frac{1}{\lambda^4}$ ). Rayleigh scattering is responsible for the colors of the sky, e.g. blue is dominant since the scattering is larger for shorter wavelengths, and the sunsets are red since it is the remaining light after the loss of all blue scattered light, due to longer light path through the atmosphere. Scattering in the atmosphere may also occur from larger constituents such as aerosols, particles or clouds. In this case the dimension of the matter is comparable to the wavelength of the photon and such scattering is called "*Mie scattering*". Mie does not depend so strongly on wavelengths as Rayleigh scattering ( $I \propto \frac{1}{\lambda^\alpha}$ , where  $\alpha$  is the Ångström exponent which is large for small particles and small for larger particles (e.g.  $\approx 1.3$ ), and produces the white color of the clouds and fog. It is also responsible for the white blaze around the sun when sufficient particulate matter is present in the atmosphere. Compared to Rayleigh scattering, Mie has a much stronger distribution of the scattered light on the forward direction. Due to the corresponding matter size, the geometric scattering is not considered in clear-sky conditions. Except from scattering, the photons can be absorbed by molecules which undergo an internal energy change. *Raman scattering* is a weak interaction of radiation with matter that can be described partly as scattering and partly as absorption. It can best be described as the interaction of light with an air molecule that changes its energy state of excitation during the scattering process. The photon transfers part of its energy to the molecule, or loses a part of its energy.

### 1.3.2 Molecular energy states

A molecule is an electrically neutral group of two or more atoms held together by chemical bonds. A molecule may absorb or emit electromagnetic radiation by a transition to a higher or lower energy level. The absorption or emission can occur only in quanta (discrete changes of energy,  $\Delta E$ ), as described in Eq. 1.55. This means that its internal energy is quantised and it has discrete energy states. The molecular energy states consist of: the rotation (angular momentum) of the entire molecule (rotational energy states), the vibration of the atoms that the molecule consists of (vibrational energy states), and the changed configuration of the electrons (electronic energy states).

The rotational energy levels are calculated as:

$$E_j = B \cdot J(J + 1) \quad (1.56)$$

with  $B = \frac{\hbar^2}{2\Theta}$  denoting the rotational constant of the particular molecule and its rotation mode (rotation axis) with moment of inertia  $\Theta$ .  $\hbar$  is equal to the Planck constant divided by  $2\pi$ , and  $J$  is the rotational

quantum number. For a rotational transition, the molecule should have a dipole moment with  $\Delta J = \pm 1$ . The energy difference between two allowed rotational states is:

$$\Delta E_j = E_{j+1} - E_j = 2B(J + 1) \propto J \quad (1.57)$$

Consequently a rotational band consists of a series of equally spaced lines with the difference between them being  $2B$ .  $2B$  ranges between  $10^{-3}$ – $100^{-2}$  eV, meaning that the pure rotational transitions may occur at wavelengths in the sub- to microwave region.

Molecular vibrations can be described by harmonic oscillations with their energy levels given by:

$$\Delta E_\nu = \left(\nu + \frac{1}{2}\right) \cdot \hbar\omega_0 \propto \nu \quad (1.58)$$

where  $\nu$  is the vibrational quantum number (vibration level),  $\omega_0$  is the oscillation frequency, and  $1/2\hbar\omega_0$  is the zero point energy of the molecular oscillator. The energy of each vibrational state is proportional to their vibrational quantum number,  $\nu$ . The oscillation frequency is in the order of 0.1 eV ( $\sim 24,000$  GHz) which corresponds to the infrared wavelength region. Only molecules with an inertia dipole moment (such as greenhouse gases) or dipole moment created by vibration can absorb in the IR. The selection rule for a vibrational transition is  $\Delta \nu = \pm 1$ . Each vibrational state is subdivided into rotational levels. During vibrational excitations at ambient temperatures, the molecules are likely to be also rotationally excited.

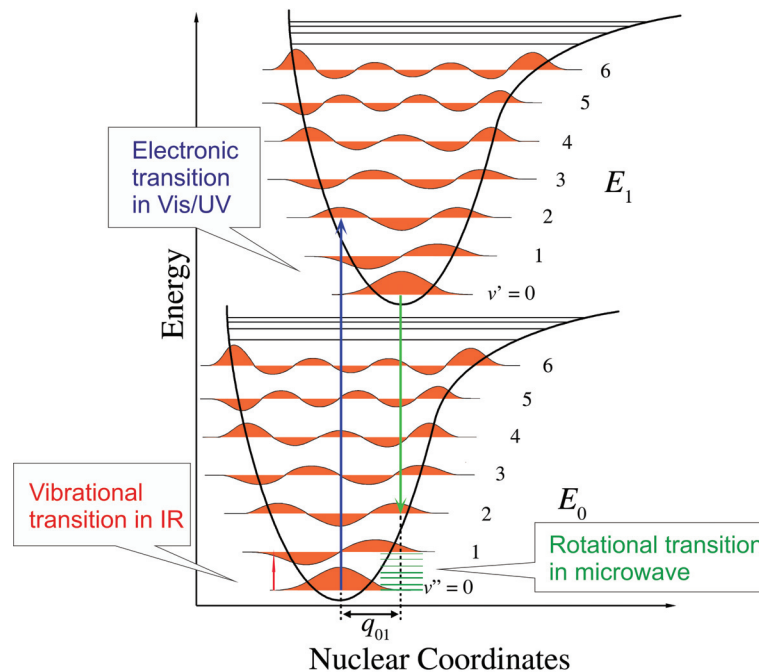


Figure 1.12: Franck-Condon principle diagram for a diatomic molecule. The curves represent the electronic energy levels ( $E_0$  is the ground, and  $E_1$  is the excited electronic state) as function of the distance between the nuclei of the atoms within the molecule. The lines marked with  $\nu$  describe the vibrational states, and the green lines above the  $\nu'' = 0$  vibrational levels represent the rotational states.

The electronic energy states result from changes in the configuration of the electrons in the molecule (orbital change). Each electronic state consists of a set of ro-vibrational states. There are no simple

selection rules for electronic transitions which are determined by the quantum mechanical characteristics of the individual states. Figure 1.12 shows the electronic and ro-vibrational energy levels of two electronic states of a diatomic molecule. Also, over-plotted are the variations of the probability density functions,  $\psi^2$ , with the internuclear distance, where  $\psi$  is the vibrational wave function. Electronic transitions occur vertically as following the *Frank-Condon* principle. In quantum mechanics, the Franck-Condon principle states that the molecule undergoes a transition to an upper vibrational state which most closely resembles the vibrational wave-function of the vibrational ground state of the lower electronic state. The two wave-functions in Fig. 1.12 that have the greatest integral overlap of all the vibrational states are the ones connected with a blue arrow which indicate the most probable electronic transition in an excited state.

A transition between electronic and vibrational states might cause an energy difference between the absorbed and the emitted photon. For example, the molecule may absorb a photon and decay back to the ground state, with the emitted and absorbed photons having the same energy and frequency. This is the case of the Rayleigh scattering. There is also the case where a molecule decays to a higher energy level than it originated from, and the emitted photon has lower energy than the absorbed one. This case is called *Stokes shift*. The opposite case, where the molecule decays to a lower state than the one that it originated from, and the emitted photon has higher energy than the absorbed one, is called *anti-Stokes shift*.

As a first approach, the change in the total energy of a diatomic molecule can be approximated by:  $\Delta E_{total} = \Delta E_{rotation} + \Delta E_{vibration} + \Delta E_{electronic}$ . The orders of magnitude of these respective changes are  $\Delta E_{electronic} \approx \Delta E_{vibration} \times 10^3 \approx \Delta E_{rotation} \times 10^6$ , so that the vibrational transitions may create coarse structure, and the rotational transitions more fine structure in a spectra. Thus, the absorption lines of molecules are not practically lines. They have finite width due to the inherent uncertainty of their quantised energy levels which is referred as "*natural broadening*". The shifting of frequencies, when gas molecules experience incident radiation, due to their random motions (Brownian motion) toward or away from the source of radiation is called "*Doppler broadening*" (Gaussian distribution). The "*pressure or collisional broadening*" is associated with the molecular collisions that reduce the lifetime of the excited state below the one that determines the natural line width (Lorentzian distribution).

### 1.3.3 Radiation from the sun

As discussed in Section 1.1.3, the sun plays an essential role in the formation and destruction of ozone. The majority of electromagnetic radiation that reaches the surface of the earth originates from the nuclear reactions taking place in the sun's interior. The rate at which the solar energy is received on a unit surface at the top of the atmosphere, perpendicular to the sun's rays, is approximately  $1366 \text{ W/m}^2$ . This quantity, although not constant, is broadly known as the "*solar constant*". Approximately 30% of the electromagnetic radiation from the sun is reflected by the Earth's surface and the atmosphere back to space (*planetary albedo*). The Earth facing the Sun can be considered as of a circular disc with area of  $\pi r^2$ , where  $r$  is the Earth's radius. The solar irradiance reaches the spherical surface of the Earth with an area of  $4\pi r^2$ , so that average solar flux at the TOA is the one-quarter of the solar constant, approximately equal to  $342 \text{ W/m}^2$ . One part of this radiation is absorbed by the atmosphere ( $67 \text{ W/m}^2$ )

but the most of it ( $168 \text{ W/m}^2$ ) is absorbed by the Earth's surface (see Fig. 1.13). The Earth's surface returns this heat ( $235 \text{ W/m}^2$ ) back to the atmosphere as sensible heat and infrared radiation [IPCC, 2007].

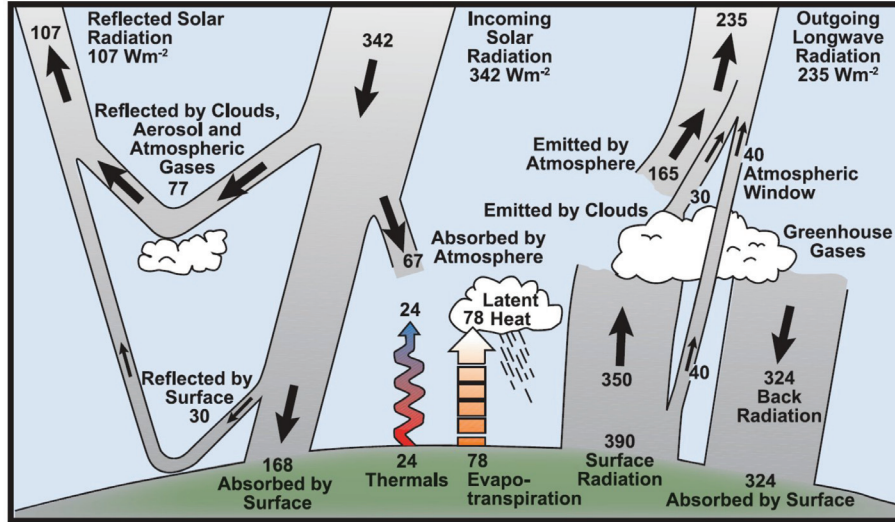


Figure 1.13: The annual global mean energy balance of the Earth. (Figure taken from: IPCC [2007].)

Figure 1.14 illustrates the solar spectrum, where the solar intensity ( $\text{W/m}^2$ ) is given as a function of wavelength (nm) at the outer border of the Earth's atmosphere (*top of the atmosphere* (TOA)) (yellow shaded area), at the Earth's surface (red shaded area), and 10 m below the sea level (blue shaded area). As shown in Figure 1.14, the surface solar radiation at the Earth's surface ranges between  $\sim 290 \text{ nm}$  and  $\sim 2500 \text{ nm}$ . The solar spectrum approximately follows the energy distribution of a *black-body* at temperature  $5800 \text{ K}$ . A black-body is an ideal object that has the ability to absorb all received radiation and emits the maximum radiation possible at its given temperature (brightness temperature). The photon energy of a black-body is described by the *Planck function*:

$$B_{\lambda}(\lambda, T) = \frac{2hc^2}{\lambda^5} \frac{1}{e^{\frac{hc}{\lambda k_B T}} - 1} \quad (1.59)$$

where  $\lambda$  is the wavelength,  $T$  is the temperature,  $c$  is the speed of light,  $h$  is the Planck constant, and  $k_B \approx 1.381 \times 10^{-23} \text{ J/K}$  is the Boltzmann constant.

The Earth can be characterised as a black-body too, with an average temperature of  $15 \text{ }^\circ\text{C}$  ( $255 \text{ K}$ ). The *Stefan-Boltzmann's law* determines the total heat energy radiated from a block body:

$$E = \sigma T^4 \quad (1.60)$$

where  $T$  is the temperature in Kelvin, and  $\sigma = 5.67 \cdot 10^{-8} \text{ W/m}^2 \cdot \text{K}^{-4}$  is the Stefan-Boltzmann constant. Differentiating Eq. 1.59 and setting the derivative equal to zero yields the relationship between the temperature of the black body and the wavelength of maximum intensity:

$$\lambda_{\max} = \frac{2.89 \cdot 10^{-3}}{T} \quad (1.61)$$

This relationship is known as *Wien's displacement law*.

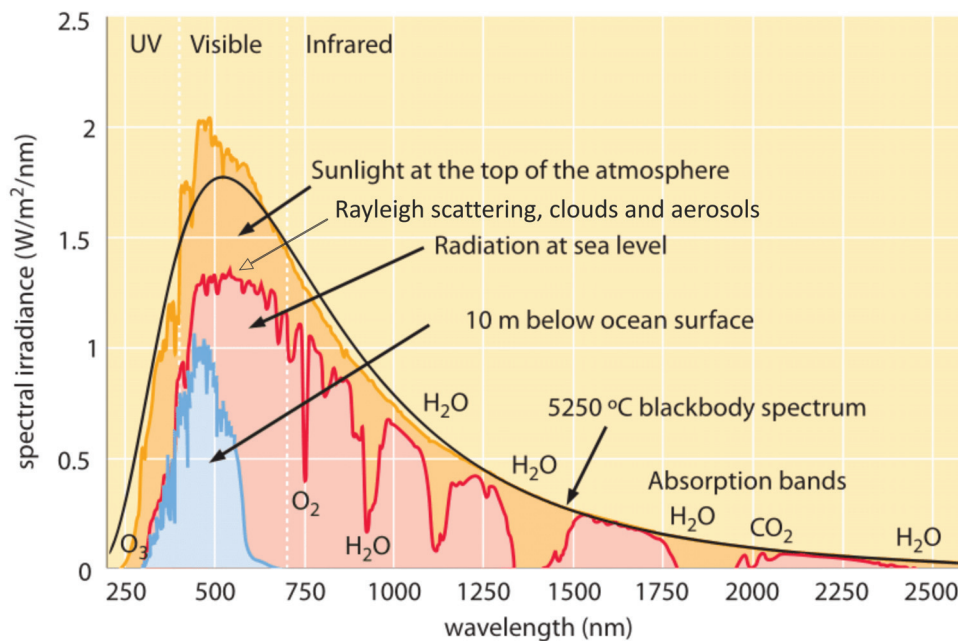


Figure 1.14: Spectral distribution of solar radiation (yellow shaded area) at the top of the atmosphere (TOA), solar irradiance at the surface of the Earth (red shaded area), and solar irradiance at 10 m below the ocean surface (blue shaded area). The black body curve at 5250 °C is plotted with black line. Absorption bands for O<sub>3</sub>, O<sub>2</sub>, H<sub>2</sub>O, and CO<sub>2</sub> are indicated in the plot. (Figure taken from: <http://book.bionumbers.org/how-much-energy-is-carried-by-photons-used-in-photosynthesis/>.)

However, the Sun is not a perfect black-body, emitting and absorbing radiation at characteristic wavelengths. The solar spectrum in Fig. 1.14 consist of continuous emissions with an overlaid line structure. Mainly in the visible and in the infrared spectrum of the photosphere (the lowest layer of the sun's atmosphere) strong absorption lines appear, created by absorption from molecules and ions in the solar atmosphere, also known as *Fraunhofer lines*. The strongest of them are produced by H, Mg, Fe, Ca, and Si, and the slightly ionised Ca and Mg.

As seen in Figure 1.14, the absorption from the atmosphere is much larger in UV-B and UV-C than in UV-A. Most of the solar radiation with wavelengths longer than ~300 nm reaches the Earth's surface.

### 1.3.4 Atmospheric radiative transfer

The absorption of radiation can be described by the *Beer-Lambert's law* (Eq. 1.62). This law states that when a parallel monochromatic beam penetrates a medium (e.g. the atmosphere), the intensity decreases exponentially.

$$I(\lambda) = I_0(\lambda) \cdot \exp[-\sigma(\lambda) \cdot c \cdot L] \quad (1.62)$$

where  $I_0(\lambda)$  is the initial intensity when the radiation hits the absorbing medium,  $I(\lambda)$  the intensity at depth  $L$ ,  $c$  the concentration (number density in  $\text{cm}^{-3}$ ) of the species included in the light-path (in cm), and  $\sigma(\lambda)$  (in  $\text{cm}^2/\text{molecule}$ ) the absorption cross section at wavelength  $\lambda$ , which is the trace gas ability to absorb photons as a function of wavelength. This is a characteristic property of any species.

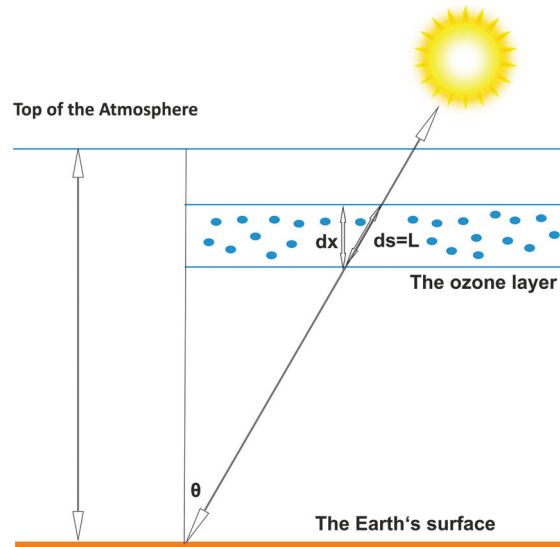


Figure 1.15: The radiative transfer in the atmosphere.

The absorption cross section can be measured in the laboratory and is related to the mass absorption coefficient,  $k$ , by:

$$\sigma(\lambda) = k \cdot 10^4 \cdot \frac{M}{A_v} \quad (1.63)$$

where  $M$  is the molecular weight of the absorber in kg/mole, and  $A_v$  the Avogadro's number =  $6.022 \cdot 10^{23}$  particles/mole.

Integrating Eq.1.62 between two different levels (in a layer), the concentration of a trace gas,  $c$ , can be retrieved by:

$$I(\lambda) = I_0(\lambda) \cdot \exp[-\sigma(\lambda) \cdot \int c(s) \cdot ds] = I_0(\lambda) \cdot \exp[-\sigma(\lambda) \cdot S] \quad (1.64)$$

Knowing the intensities  $I$ ,  $I_0$ , and the cross section  $\sigma$ , the concentration is then:

$$c = \frac{\log(I_0(\lambda)/I(\lambda))}{\sigma(\lambda) \cdot L} = \frac{\tau(\lambda)}{\sigma(\lambda) \cdot L} \quad (1.65)$$

where  $\tau$  is the optical depth or optical density of the layer. If the optical path,  $L$ , is also known, then the column density,  $S$ , can be calculated as:

$$S = \frac{\log(I_0(\lambda)/I(\lambda))}{\sigma(\lambda)} = \frac{\tau(\lambda)}{\sigma(\lambda)} \quad (1.66)$$

In the atmosphere, equation 1.62 should include all the processes including absorption and scattering by all the molecules. Although scattering is not an absorption process, it can be added in the Beer-Lambert law since it also attenuates the radiation passing through the atmospheric layer. Therefore, the relevant *extinction coefficients* for absorption,  $a$ , is  $\epsilon_a = n \cdot \sigma_a(\lambda)$ , and for scattering,  $s$ , is  $\epsilon_s = n \cdot \sigma_s(\lambda)$ .  $n$  is the number of absorbers or scatters per unit volume and  $\sigma_i(\lambda)$  are the absorption and scattering cross sections. Adding the terms for Rayleigh, Mie, and Raman (Ring effect) scatterings, equation 1.62 can be rewritten as:

$$I(\lambda) = I_0(\lambda) \cdot \exp[-(\varepsilon_a(\lambda) + \varepsilon_s(\lambda)) \cdot L] = I_0(\lambda) \cdot \exp[-(\sigma_a(\lambda) + \sigma_s(\lambda)) \cdot n \cdot L] \quad (1.67)$$

Equation 1.67 contains one form of the so-called *radiative transfer equation* (RTE) in the UV range, where the Planck's function is set equal to zero.

### 1.3.5 Absorption of UV-radiation from the atmosphere

Solar radiation is partly absorbed in the Earth's atmosphere (Fig 1.14, red curve). The degree of absorption is analogous to the composition of atoms and molecules in the atmosphere. By analyzing the interactions between matter and electromagnetic radiation, information about the concentration of molecules in the atmosphere may be obtained. This approach is called spectroscopy. The electromagnetic energy required to release electrons and break molecular bonds is very large ( $> 500$  kJ/mol), therefore it takes place in the X-rays–Ultraviolet regions (absorption continua). The photons that have sufficient energy, which exceeds the bonding energy of the particular chemical bond, can cause photo-dissociation or photo-ionisation. The photons are absorbed, and any excess energy is transformed to kinetic energy which increases the temperature of the gas molecule and consequently heats the atmosphere. The rate of photon absorption (*photolysis rate*) of a molecule A is equal to:

$$\frac{d[A]}{dt} = -j \cdot [A]$$

where  $j$  has the units  $s^{-1}$ , and is called the first-order rate coefficient or *photolysis frequency*.  $j$  is the integration of the product of the spectral *actinic flux*, the spectral absorption coefficient or *absorption cross section*,  $\sigma$  (the probability of light absorption), and the *quantum yield*,  $\phi$  (the ratio of the number of molecules that are photolysed to the number of photons that are absorbed). The inverse of  $j$  represents the lifetime of the molecule against photolysis.

The absorption spectrum varies from one compound to another. Figure 1.16 shows the absorption spectrum for several gaseous absorbers. The extreme UV-radiation has sufficient energy to photo-ionize electrons and atoms in the ionosphere and thermosphere above 90 km (*ionization continuum*). UV-radiation with wavelengths  $\lambda < 240$  nm is mainly absorbed by  $O_2$  which photo-dissociates. The *Schumann Runge continuum* (100 – 175 nm) in the thermosphere and the *Schumann Runge bands* (175 – 200 nm) in the mesosphere and upper stratosphere correspond to absorption by  $O_2$ . In the mesosphere the *solar Lyman A line* (121.6 nm) is absorbed by  $O_2$ . From 30 to 60 km, the *Herzberg continuum* (200 – 242 nm) contributes to  $O_2$  photolysis. As explained in Sec. 1.1.3, the oxygen atoms which are released by the break up of  $O_2$  lead to  $O_3$  production. Next, a significant fraction of the UV-radiation in the UVC and UVB range is absorbed by ozone. The absorption of  $O_3$  in these spectral regions is due to electronic transitions. The strongest ozone absorption bands are called the *Hartley bands*, from 242 to 310 nm, and are centered around 255 nm. The absorption of solar flux in these ozone bands takes place primarily in the upper stratosphere and in the mesosphere resulting in the formation of  $O(^1D)$ . The weak bands between 310 and 400 nm have more structure, and are called the *Huggins bands*. There the absorption by  $O_3$  in the stratosphere and troposphere leads to the formation of  $O(^3P)$ . Ozone also shows weak absorption bands in the visible and near-IR regions (440 – 1180 nm), centered at around

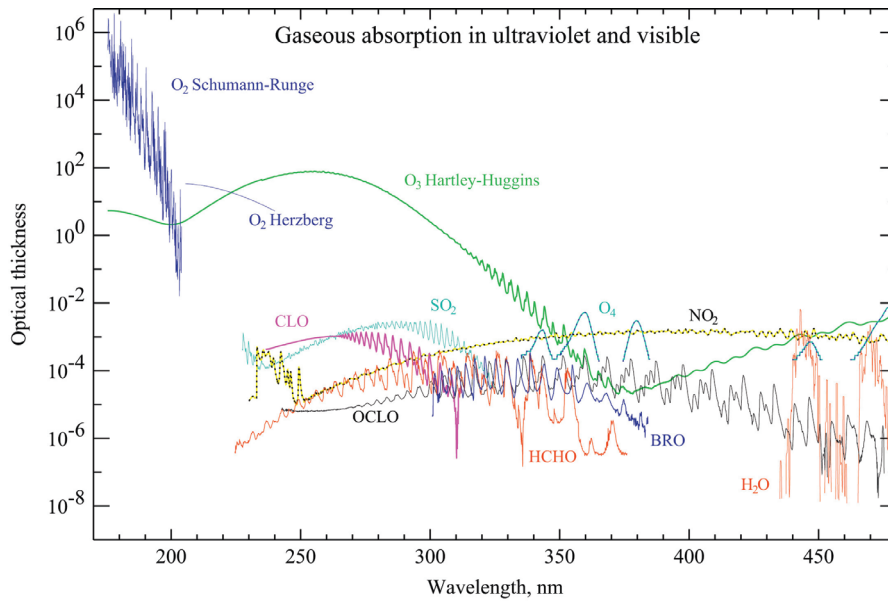
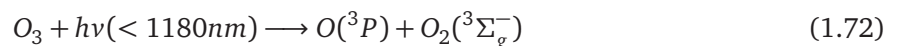
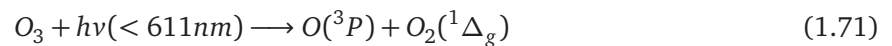
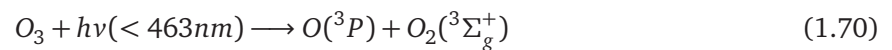
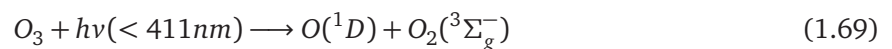
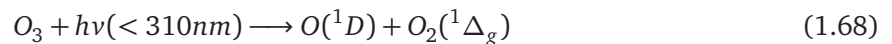


Figure 1.16: Vertical optical thicknesses of  $O_2$ ,  $O_3$ ,  $SO_2$ ,  $NO_2$ ,  $H_2O$ ,  $O_4$ ,  $ClO$ ,  $OCLO$ ,  $HClO$ ,  $BrO$ , and  $HCHO$  in UV–Visible spectral ranges. (Figure taken from: Rozanov et al. [2014])

$9.6 \mu\text{m}$  (not shown in Figure 1.16). These bands are referred to as *Chappuis bands*. The *Wulf band* consists of weak absorptions in the visible and near infrared region (five orders of magnitude lower than the Hartley band) overlapping with the Chappuis band.

### 1.3.6 Spectroscopic parameters of $O_3$

Absorption of radiation by ozone in the atmosphere may lead to a transition from the ground state to higher excited states or depending on the photons wavelength to the dissociation of the molecule producing different excited states of  $O$  and  $O_2$ :



In parentheses are the threshold wavelengths for photolysis. These reactions correspond to transitions in the Hartley, Huggins, Chappuis and Wulf bands. Reactions 1.68 and 1.72 are spin-allowed and have the largest quantum yields in the Hartley band, with the main dissociation channel being the singlet channel (Reaction 1.68) [Schinke and McBane, 2006]. However, also the very weakly populated spin-forbidden channels (Reactions 1.69 to 1.71) have been observed experimentally in the wavelength range corresponding to the Huggins band [Grebenshchikov et al., 2007].

The absorption cross section of ozone in the range from about 1 eV (1240 nm) to 6 eV (206.6 nm) are shown in Fig. 1.17.a. The Wulf, Chappuis, Huggins, and Hartley absorption bands can be identified with different colors (red, green, blue, and black). All four bands exhibit more or less pronounced vibronic structures reflecting different intra-molecular dynamical states. Fig. 1.17.b shows the potential

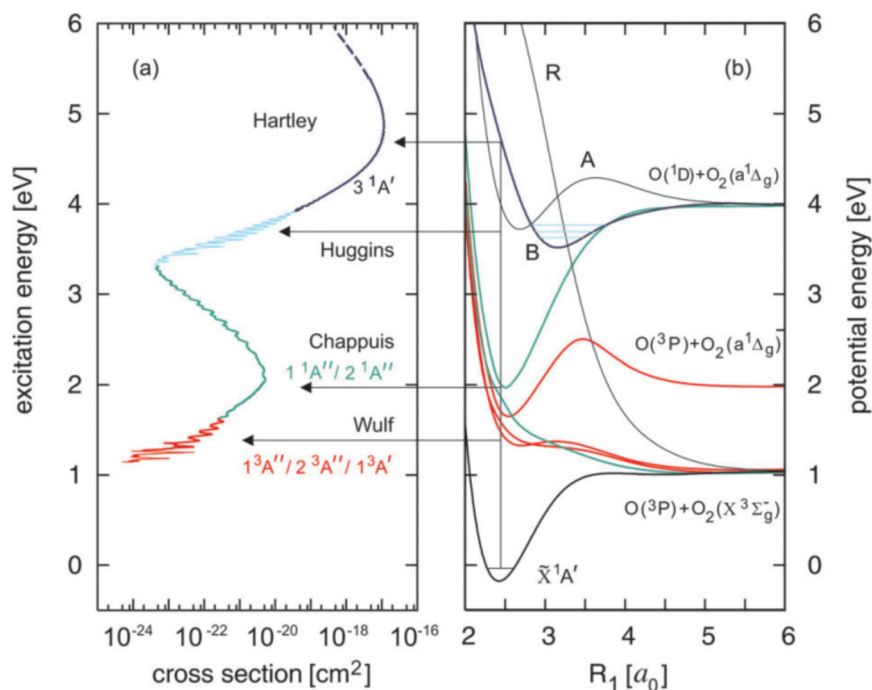


Figure 1.17: (a) Absorption cross section (in cm<sup>2</sup>; logarithmic scale) of ozone as function of the excitation energy. (b) One-dimensional cuts through the potential energy surfaces (PESs) relevant for the photodissociation of ozone.  $R_1$  is one of the O–O bond lengths; the other one is fixed at  $R_2 = 2.43 a_0$  and the bond angle is  $\alpha = 117^\circ$ .  $E = 0$  corresponds to  $O_3(\bar{X})$  in the ground vibrational state (zero point energy). A, B, and R indicate the three states relevant for the Hartley and Huggins bands. The horizontal arrows illustrate the electronic assignments of the absorption bands. Color coding in (a) and (b) stresses the relation between the absorption bands and the underlying electronic states. Figure taken from: Grebenshchikov et al. [2007].

energy surfaces of nine electronic states as a function of the O–O bond length. Different electronic and vibrational states are responsible for the transition to an electronically excited state which corresponds to an absorption band. For example, the Hartley band is due to photo-excitation from the ground state ( $\bar{X}^1A'$ ) to the upper third ( $3^1A'$ ) singlet state with  $^1A'$  symmetry in the  $C_{2v}$  point group (commonly termed as B state) [Qu et al., 2004].

The Hartley band is a strong broad continuum extending from 200 to 310 nm with weak vibrational structures laying on top of the broadband due to the fast dissociation of ozone in the upper electronic band (B state) which lies about 1 eV above the dissociation limit [Gür, 2006]. The absorption cross section maximizes at about 250 to 260 nm, where  $\sigma \approx 10^{-17} \text{cm}^2$ . The largest part of UV absorption by ozone occurs in the Hartley band. The Huggins band (310 to ~370 nm) is characterised by discrete absorption structures originating from the excitation of vibrational states in the shallow potential wells of the diabatic B state [Grebenshchikov et al., 2007]. Meaning that the Huggins and Hartley bands represented different regions of the same transition [Gür, 2006]. The high-energy tail of the Huggins

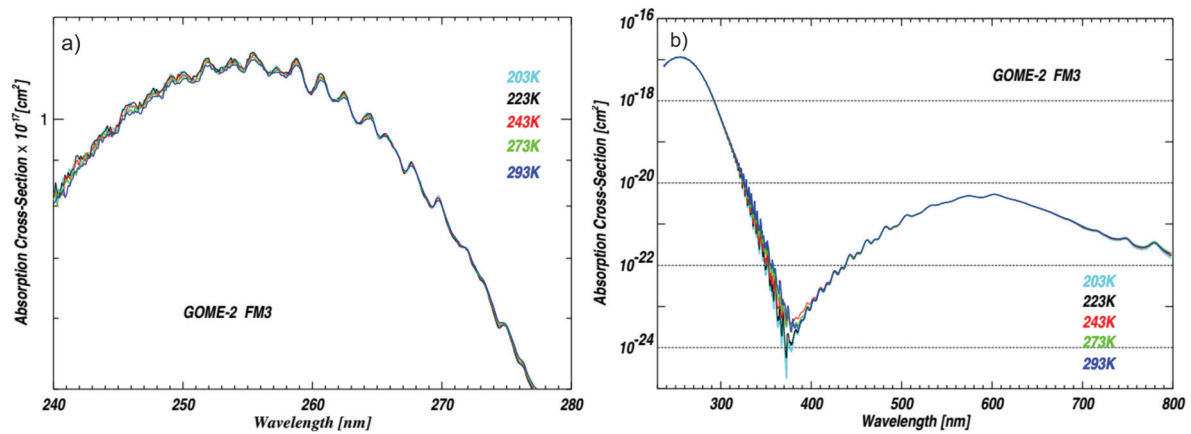


Figure 1.18: a) Absorption cross sections of ozone from 240 to 280 nm measured with the GOME-2 FM3 spectrometer at 5 temperatures ranging between 203 K to 293 K. b) Temperature dependent ozone absorption cross section spectra covering the Hartley, Huggins and the Chappuis bands (230–790 nm). Figures taken from:

band overlaps with the Hartley band. The absorption cross section is about six orders of magnitude smaller than at the maximum of the Hartley band. The Chappuis band is a broad and slightly asymmetric continuum extending from 380 to 800 nm with vibrational structures due to the interactions of two excited electronic states, the  $1^1A''$  and  $2^1A''$  states. The diffusive vibrational structures, overlying at the background, are due to the very short lifetimes in the excited states. The maximum cross section in the Chappuis band is about three orders of magnitude weaker than the Hartley band. The Wulf absorption band in the visible and near IR region ( $\lambda > 700$  nm) is approximately five orders of magnitude weaker than the Hartley band. Its absorption maximum overlaps with the low-energy tail of the much stronger Chappuis band [Grebenshchikov et al., 2007]. The Wulf band originates from excitation of the three low-lying triplet states ( $1^3A''$ ,  $2^3A''$ ,  $1^3A'$ ), just above the photo-dissociation threshold of  $\text{O}_3$  molecules [Grebenshchikov et al., 2007].

Changes in the population distribution in the rotational–vibrational levels of the ground electronic state with temperature may cause discrepancies in the absorption cross-sections. The temperature dependence of the absorption cross-sections becomes significant above 275 nm [Finlayson-Pitts and Pitts, 2000]. Chehade et al. [2013] measured absorption cross section spectra of ozone (shown in Fig 1.18) using the Global Ozone Monitoring Experiment-2 (GOME-2) Flight Model (FM) spectrometer in the laboratory at temperatures between 203 K and 293 K in the wavelength range of 230–790 nm with a medium spectral resolution of 0.24 to 0.54 nm. The cross sections show a weak temperature effect in the Hartley band, decreasing by 1.5 % for a temperature rise from 203 K to 293 K. In the Chappuis band a small increase in the cross sections is noticed with increasing temperature below 565 nm and above 610 nm (inversions points), while between the inversion points the temperature effect is the opposite. Finally, in the Huggins band, which is commonly used for the  $\text{O}_3$  retrieval, the temperature effect is very strong with the cross section increasing with temperature up to 70 %.

The pronounced temperature dependence of the Huggins ozone band can be described by a second-order polynomial, (the *Bass-Paur parameterization*) interpolating between selected temperatures [Serdyuchenko et al., 2014]. The Equation describing the temperature dependence of the cross sections

is:

$$\sigma(\lambda) = 10^{-20} \cdot [C_0(\lambda) + C_1(\lambda)T + C_2(\lambda)T^2] \quad (1.73)$$

The measurement uncertainty of the ozone absorption cross sections in the Huggins band ranges between 1.5 and 2.1% [Weber et al., 2016]. It is obvious that the accuracy of cross sections as well as the correct temperature dependence is of extreme importance for the ozone profiles and columns retrieval from space-board spectrometers [Serdyuchenko et al., 2014].

## 1.4 Measuring total and tropospheric ozone from space

Remote sensing from satellites has been proven to be very useful for measuring ozone concentrations long-term and on global scale. By pointing a satellite instrument in nadir direction, the measured back-scattered UV sunlight from the surface or the constituents of the atmosphere can be detected, providing information on the total column of trace species in the atmosphere. Global map of trace gas concentrations can be created as the instrument orbits around the Earth. The start of such space-born atmospheric observations set off in April 1970 with the launch of the BUV instrument on board of the NASA Nimbus-4 satellite [Heath et al., 1973] and continued with the series of SBUV (Solar Backscatter Ultraviolet) [Bhartia et al., 2013] and TOMS (Total Ozone Mapping Spectrometer) instruments [McPeters et al., 1996].

While the basic absorption spectroscopy principles apply to satellite measurements of scattered sunlight as they would in the laboratory, there are several complications while measuring from space that need to be taken into account. Firstly, the measured backscattered signal of the atmosphere is a result of several trace gases having different concentrations and consequently different contributions to the absorption signal. Secondly, scattering on air molecules, aerosols and clouds as well as absorption on the ground often dominates the extinction of sunlight. As a result, the atmospheric absorption signal is sometimes just a minor part of the signal [Richter A., 2006]. In order to separate these effects, measurements at several different wavelengths are taken simultaneously. The individual absorbers are identified and separated by their characteristic signature at certain wavelengths in the absorption spectrum. In contrast, the attenuation of solar radiation by scattering and absorption on the ground usually varies smoothly with wavelength and can be removed from the signal by applying high pass filters. The retrieval then becomes sensitive only to variations in absorption with wavelength and therefore is called *Differential Optical Absorption Spectroscopy* (DOAS).

### 1.4.1 The standard Differential Optical Absorption Spectroscopy (DOAS)

The Differential Optical Absorption Spectroscopy (DOAS) method [Platt and Perner, 1980] makes use of the structured absorption spectra in the UV-VIS spectral range of atmospheric molecules. DOAS is used to determine the total amount of species in the atmosphere from remote sensing measurements of scattered sunlight. It was originally developed for ground-based measurements using artificial light sources or scattered sunlight [Solomon et al., 1987], but was later successfully adapted to nadir measurements from satellite instruments using the sun as a light source [Burrows et al., 1999].

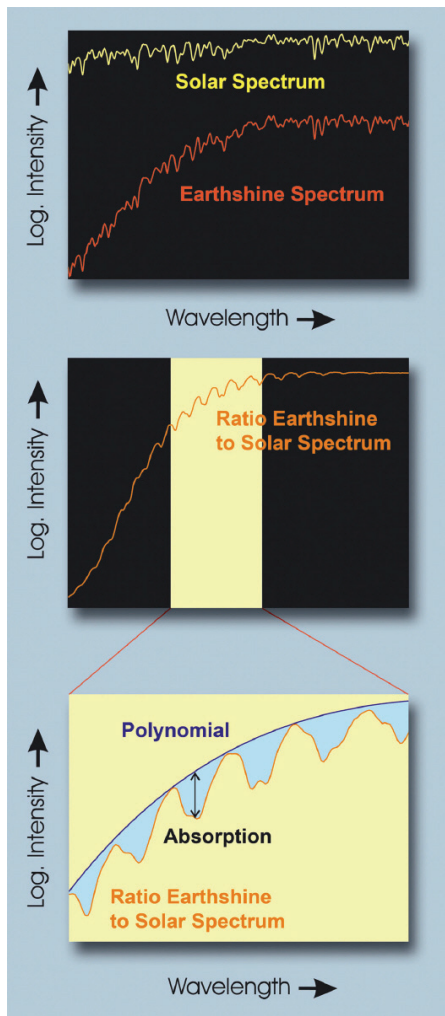


Figure 1.19: The main steps of the DOAS retrieval (Figure taken from: Gottwald et al. [2006]).

The basic idea behind it is to measure several absorbers at many wavelengths simultaneously by separating the absorption signal into two parts. The first part is the high frequency part that provides the atmospheric molecules absorption, and the second is the low frequency part (Rayleigh, Mie scattering), which is treated as a closure term and is approximated by a low order polynomial. Depending on the species of interest, light at different spectral regions is used. First, the integrated amount of the absorbing molecules along the light path (*slant column density*) can be derived by use of the Beer-Lambert's law by dividing the Earthshine radiance,  $I$  (after absorption and scattering), by the direct solar irradiance,  $I_0$  (background free of absorption). The spectral fit of the logarithm of the sun-normalised radiance of the molecular absorption cross section together with the polynomial, yields the trace gas concentration along the light path (*slant column concentration*), see Fig. 1.19. The advantage of the DOAS technique is that multiplicative effects in  $I$  and  $I_0$  will cancel out since they are measured almost at the same time with the same instrument [Burrows et al., 2011, ESA Earthnet Online, 2013].

Analytically, the DOAS slant column equation,  $S$ , as a function of optical depth,  $\tau$ , is

$$\tau(\lambda) = \ln\left[\frac{I_0(\lambda)}{I(\lambda)}\right] \simeq \sum_i^n \sigma_i(\lambda) \cdot S_i + \sum_p \alpha_p \cdot \lambda^p + \alpha_R \cdot R(\lambda) \quad (1.74)$$

Here,  $I(\lambda)$  is the Earthshine spectrum at wavelength  $\lambda$  and  $I_0(\lambda)$  is the solar spectrum; alternatively, spectra from regions where the absorber to be measured shows negligible absorptions.  $S_i$  is the effective slant column density of a gas  $i$  along the light path,  $L=ds$ .  $\sigma_i(\lambda)$  is the absorption cross section of the gas  $i$ . The absorption cross sections are usually highly structured, broadband dependencies appear due to absorption by particles, scattering by molecules and particles, as well as by reflection at the surface [Gottwald et al., 2006]. These broadband modulations are approximated by the second term in Eq. 1.74, which is a common low order (usually of 3, 4 or 5 order) polynomial. The last term on the right hand side of Eq. 1.74 is the additive terms for the Ring reference spectrum  $R(\lambda)$  (to account for inelastic Raman scattering). The Fraunhofer lines (see Sect. 1.3.3) in  $I$  and  $I_0$  are expected to cancel out when their ratio is taken in the DOAS equation. However, their depth is smaller for the Earthshine than the solar spectrum [Grainger and Ring, 1962]. The result is a high structure signal in the sun-normalised ratio. The reason for this effect, which is known as the *Ring effect*, is the inelastic rotational Raman scattering which shifts the intensity of the scattered photons by several nanometers [Joiner and Bhartia, 1995, Kattawar, 1981]. The Fraunhofer lines in the scattered spectrum are filled-in and the amount of

this filling can be calculated with radiative transfer models.

The propagation of radiation in the atmosphere can be simulated by radiative transfer models e.g. SCIATRAN [Rozanov et al., 2014]. The light-path ( $ds=L$ ) depends on the (a priori) vertical trace gas profile, the viewing geometry, the solar zenith angle (SZA), the wavelength, the surface albedo, the altitude, the clouds, and the aerosol load. The light path is often expressed as *airmass factor* (AMF), which is the light path enhancement factor relative to a vertical layering of the atmosphere [Burrows et al., 2011]. Nevertheless, the standard DOAS retrieval works well under the assumption of an optically thin atmosphere, as long as the trace gas absorption is weak and the spectral window is narrow. Under these conditions, the wavelength dependence of the optical thickness, as long as the pressure and temperature dependence of the absorption cross sections can be approximated by the low order polynomial in Eq. 1.74 [Rozanov and Rozanov, 2010].

The resulting slant column density,  $SCD_i$ , is the integration of molecular concentration  $c_i$  along the light path,  $ds$ :

$$SCD_i(\lambda) = \int c_i(s) ds(\lambda) \quad (1.75)$$

With a least squares fit of this linear equation, the best set of slant columns and polynomial coefficients for each wavelength can be calculated by minimising the following quadratic form:

$$\|\tau(\lambda) - \sum_i^n \sigma_i(\lambda) \cdot SCD_i - \sum_p \alpha_p \cdot \lambda^p - \alpha_R \cdot R(\lambda)\|^2 \quad (1.76)$$

The  $SCD_i$  is later converted to vertical column density,  $VCD_i$ :

$$VCD_i = \int_0^{TOA} c(x)_i dx \quad (1.77)$$

by integrating from the ground until the top of the atmosphere and simulating the effective light path,  $dx$ , through the atmosphere by a radiative transfer model. This is done based on AMFs which are obtained by radiative transfer simulations. The vertical column concentration of the absorber can then be calculated by:

$$VCD_i = \frac{SCD_i}{AMF_i} \quad (1.78)$$

Nevertheless, the slant column fitting also depends on the signal-to-noise ratio (SNR) of the measurement, the spectral calibration, the knowledge of the instrument slit function and the separation of interfering spectral structures [Gottwald and Bovensmann, 2011]. Furthermore, the clouds can modify the AMF significantly since they block the light path through the atmosphere (*shielding effect*), and therefore they need to be taken into account in the AMFs calculation. The most important cloud parameter is the *cloud fraction*, which describes the fractional coverage of the Earth's surface by clouds. For stratospheric trace gas retrievals, the AMF strongly increases with SZA since the light-path is increasing. However, for tropospheric trace gases, the AMF are relatively small (small light-path due to scattering in higher layers) and independent on SZA, although at large SZA it rapidly decreases. The dependence on the a-priori trace gas profile, the surface albedo, the clouds and aerosols close to surface is much stronger than for stratospheric trace gases and this introduces an important error source in the vertical column retrieval.

### 1.4.2 The modified WFDOAS method for satellite total ozone retrieval

Using the DOAS algorithm, atmospheric columns of a number of species can be determined, including NO<sub>2</sub>, SO<sub>2</sub>, HCHO, BrO, and OClO [Burrows et al., 2011, ESA Earthnet Online, 2013]. However, limitations of the classical DOAS technique rise from the assumption that the trace gas absorption cross sections are dependent of pressure and temperature (and consequently of altitude) and that the light path is independent of the vertical distribution of the absorber. However, as discussed in Section 1.3.6, for strong-line absorbers such as O<sub>3</sub>, H<sub>2</sub>O, O<sub>2</sub>, CO, CO<sub>2</sub> and CH<sub>4</sub>, this assumption is not yet valid (light path depends on the concentration of the trace gas) and distortion of the absorption structure is observed in the measured optical depth, introducing large errors in the retrieval. The second assumption is that the logarithm of the sun-normalised radiance depends linearly on the vertical column of the retrieved trace gas, as described by the Beer-Lambert law which is only valid for monochromatic radiation. However, the AMFs are wavelength dependent within the spectral intervals defined by the instrument's spectral resolution, and as a result, the slant column is no longer linearly related with the vertical column [Buchwitz et al., 2000, Burrows et al., 2011]. To overcome these drawbacks, a DOAS-type technique using *weighting functions* instead of AMFs was developed to account for such effects and to permit successful retrievals of the trace gas species. This new algorithm is called Weighting Function Differential Optical Absorption spectroscopy (WFDOAS) [Buchwitz et al., 2000, Coldewey-Egbers et al., 2005].

Weighting functions describe the relative radiance change with respect to a parameter's  $d_i$  change (e.g. trace gas concentration or temperature) from its a-priori assumption,  $d_i^0$ :

$$WF_i(\lambda) = \frac{\partial \ln I(\lambda)}{\partial d_i} \Big|_{d_i^0}. \quad (1.79)$$

The measured optical depth (logarithm of the sun-normalised measured intensity,  $\ln I_i^{meas}$ ) at wavelength  $\lambda$  can be approximated by a first-order Taylor expansion of a sun-normalised reference intensity,  $I_i^{mod}$ , calculated from a radiative transfer model (RTM). The RTM calculations require a-priori trace gas profiles as input which are usually taken from climatologies (e.g. for ozone and temperature profiles the Total Ozone Mapping Spectrometer (TOMS) v7 [Wellemeyer et al., 1997]) or chemical transport models. Look-up tables are contracted in order to avoid time-consuming on-line RT simulations [Buchwitz et al., 2000]. Additionally, a low-order polynomial  $P_i$  is added to account for the broadband contributions, such as surface albedo and aerosols, as for the standard DOAS. The optical depth from the WFDOAS equation is calculated as follows:

$$\begin{aligned} \tau(\lambda) = \ln \left[ \frac{I_0(\lambda)}{I(\lambda)} \right] &= \ln I_i^{meas}(\lambda) \simeq \ln I_i^{mod}(\lambda) + WF_V(\lambda)(V - V^0) + WF_T(\lambda)(T - T^0) \\ &+ SCD_{NO_2} \sigma_{NO_2} + SCD_{BrO} \sigma_{BrO} + \sum_P \alpha_p \cdot \lambda^p + \alpha_R \cdot R(\lambda) \end{aligned} \quad (1.80)$$

Here,  $V$  is the vertical column of the absorber to be retrieved (e.g. ozone) and  $V^0$  is the a-priori profile of the absorber.  $T$  is the surface temperature and  $T^0$  is the a-priori surface temperature. The  $\Delta T = T - T^0$  temperature fit represents the dependence of the observed ozone absorption on stratospheric temperatures, since the ozone and temperature weighting functions correlate. The whole right part of Eq.

1.80, except from the reference intensity, has to be adjusted to the measured sun-normalised intensity, for all absorbers,  $i$ , at the same time. The slant column fitting is also applied to the minor absorbers  $\text{NO}_2$  and  $\text{BrO}$ . The ring effect is included, as in the standard DOAS. The unknown fit parameters are derived from a linear least-squares minimisation [Coldewey-Egbers et al., 2005].

The main difficulty with the WFDOAS retrieval is choosing the proper a-priori assumptions (e.g. ozone and temperature climatologies) since the accuracy of the retrieval increases as the retrieved column correction,  $\Delta V = V - V^0$ , is getting small [Burrows et al., 2011]. The fit for ozone in the WFDOAS is done in a wide fitting window (8.2 nm) between 326.8–335 nm, so that the correlation between the temperature and ozone weighting functions is minimised. The precision of WFDOAS total ozone retrieval was found to be better than 3% for SZA lower than  $80^\circ$ , and reaches 1% in the tropics [Coldewey-Egbers et al., 2005].

In the case of cloud covered scenes, the satellite retrievals of total ozone should include the *ghost vertical columns* (GVC) which are the shielded part of the atmosphere. GVC are determined by vertically integrated climatological ozone profiles from the surface until the cloud top height (CTH). For partially cloud covered pixels, the integrated ozone columns are multiplied by the cloud fraction, CF, given by a cloud retrieval algorithm (e.g. the Fast Retrieval Scheme for Clouds from the Oxygen-A Band (FRESCO) [Koelemeijer et al., 2001]). The ghost column is then:

$$GVC = CF \cdot \int_0^{CTH} [O_3(h)] \cdot dh \quad (1.81)$$

The resulting error from the GVC estimation in the retrieval is of the order of 0.2% [Coldewey-Egbers et al., 2005].

### 1.4.3 Satellite-based tropospheric ozone measurement techniques \*

Remote sensing from satellites is a substantial component in order to monitor tropospheric ozone concentrations and study their long term evolution over large areas. Tropospheric ozone was first retrieved from space with the so-called *residual method*. The stratospheric ozone column above 100 mbar retrieved from the Stratospheric Aerosol and Gas Experiment II (SAGE II), was subtracted from the total ozone column, retrieved from the Total Ozone Mapping Spectrometer (TOMS) aboard the Nimbus 7 satellite [Fishman et al., 1990]. The following years, several other methods have been developed, such as the *cloud slicing* (CS) technique [Ziemke et al., 2001]. The later technique was first applied using above cloud column ozone measurements from the Nimbus7 Total Ozone Mapping Spectrometer (TOMS) instrument in combination with Nimbus-7 temperature-humidity and infrared radiometer (HIRS) cloud-top pressure data on TOMS. The CS takes advantage of the almost opaque property of water vapour clouds to ultraviolet wavelength radiation, in order to derive ozone column amounts in the upper troposphere. Later, the CS method was applied to ozone and cloud data from the Ozone Monitoring Instrument (OMI) [Ziemke et al., 2008] and from the Global Ozone Monitoring Experiment-2 (GOME-2) [Valks et al., 2014] to derive ozone mixing ratios inside Deep Convective Clouds (DCC), and was proven that very low ozone amounts exist inside these clouds over the Indian

\*This subsection has been partially published by Leventidou et al. [2016]

Ocean and the western Pacific Ocean. Kim et al. [2001] developed the *Scan Angle Method* (SAM) using TOMS data. The method was based on the use of physical differences in ozone column detection as a function of its scan-angle geometry. The difference in TOMS retrieval information between nadir and high viewing angles maximizes in the troposphere, with a peak near an altitude of 5 km. This analysis suggests that the total ozone difference between two viewing angles contains information about tropospheric ozone. Another residual approach to retrieve tropospheric ozone has been applied to OMI total column ozone measurements in combination with Aura Microwave Limb Sounder (MLS) stratospheric column ozone measurements, producing global maps of OMI/MLS tropospheric ozone [Ziemke et al., 2006]. Tropospheric ozone data have also been produced by the *Limb-Nadir-Matching* (LNM) technique [Ebojie et al., 2014, Sierk et al., 2006] which benefits from the most important feature of SCIAMACHY; the possibility to observe the same atmospheric volume first in limb and then (after about 7 minutes) in nadir geometry. With the knowledge of the tropopause height, the tropospheric  $O_3$  can be retrieved by subtracting the stratospheric (limb) from the total (nadir)  $O_3$  columns. Tropospheric ozone profiles have also been produced from UV spectra of GOME [Munro et al., 1998] and GOME-2 [Miles et al., 2015] taking into account the UV radiometric degradation in the Hartley and in the Huggins bands. Equally important attempts to retrieve tropospheric ozone have been made by using thermal infrared (TIR) emission instruments, such as the Infrared Atmospheric Sounding Interferometer (IASI) on MetOp-A [Boynard et al., 2009, Keim et al., 2009] or by a combination of IR with ultraviolet (UV) measurements [Burrows et al., 2004, Cuesta et al., 2013].

The present thesis focuses on the *Convective Cloud Differential* (CCD) method, which was first developed by Ziemke et al. [1998], and was applied to TOMS (1979–2005) and OMI ozone data (since 2004) [Ziemke and Chandra, 2012]. The original technique used above-cloud (reflectivity  $> 0.9$ ) and clear-sky (reflectivity  $< 0.2$ ) ozone column measurements to derive monthly mean tropical tropospheric ozone columns. The cloudy measurements above the Western Pacific and the Indian Ocean represent stratospheric ozone, which is assumed to be independent of longitude in the tropics. In a subsequent step, the monthly mean Above Cloud Ozone Columns (ACCO) are subtracted from the cloud-free Total Ozone Columns (TOC) assuming a zonally invariant stratospheric column, resulting in monthly averaged Tropical Tropospheric Columns of Ozone (TTCO). The same method was improved and applied to GOME [Valks et al., 2003] and GOME-2 data by Valks et al. [2014]. In contrast to TOMS, GOME was able to determine cloud fractions, cloud albedos, and cloud top pressures by using spectral measurements in the near-infrared wavelength (oxygen A-band) region combined with broadband spectral data from Polarization Measurement Devices (PMDs), which have better spatial resolution than the spectra used in trace gas retrievals. By combining the cloud information with ozone column measurements, monthly-mean values of the tropical tropospheric ozone columns have been determined.

## 1.5 Instruments

In this thesis, a CCD algorithm (CCD\_IUP) has been developed using total ozone column data retrieved with the WFDOAS (Weighting Function DOAS) [Coldewey-Egbers et al., 2005] algorithm applied on spectra from the series of European satellite instruments GOME, SCIAMACHY, and GOME-2/MetopA, spanning a time period of 20 years (1996-2015). In this section, a brief description of the instruments

used in order to obtain the tropical tropospheric ozone columns retrieval from satellite data is given.

### 1.5.1 GOME

The Global Ozone Monitoring Experiment (GOME) was a passive remote sensing instrument on board the European Space Agency's (ESA) Second European Remote Sensing Satellite (ERS-2), which was launched on the 21<sup>st</sup> of April, 1995. GOME was a nadir viewing instrument, consisting of 4 spectrometers, performing hyper-spectral measurements of the backscattered, reflected, transmitted, and/or emitted radiation from the atmosphere and Earth's surface at UV/Vis wavelengths (240–790 nm) with a resolution of about 0.2 and 0.4 nm. The instrument is scanning the Earth moving the scan mirror by  $\pm 31^\circ$ . During each scan, three ground pixels were created from east to west direction, followed by one back-scan pixel. The maximum across-track swath width of GOME was 960-km resulting in a ground pixel spatial resolution of  $40 \times 320 \text{ km}^2$  for the majority of the orbit. Global coverage could be achieved within 3 days after 43 orbits. ERS-2 had a near-polar sun-synchronous orbit crossing the equator in descending-node at 10:30 local time [Burrows et al., 1999]. After June 1997, GOME instrument had the possibility to function in a narrow swath mode (NSM) by reducing the scan mirror angle to  $\pm 8.7^\circ$ , leading to an increased spatial resolution of  $40 \times 80 \text{ km}^2$ , applied three days per month (the 4th/5th, the 14th/15th and the 24th/25th of every month between the sun calibrations of those days). Despite the fact that the NSM improved the spatial resolution, it reduced the global coverage time from 3 days to 120 days, since now 12 measurement days were required, thus the NSM is only applied every 10 days [Beirle et al., 2004a]. On the 22<sup>nd</sup> of June 2003, GOME global coverage was lost due to the ERS-2 tape recorder failure. Initially, the measurement data transmission continued using the ESA ground stations, limiting the coverage to Europe, North Atlantic, the Arctic, Antarctica and western North America. Afterwards, new ground stations were included increasing the coverage and allowing the continuation of the atmospheric monitoring. Unfortunately, data gaps appeared in a large extent, especially over the Pacific Ocean, restraining the studies at the tropical belt. The ERS-2 satellite was finally de-orbited on the 5<sup>th</sup> of September 2011 [ESA Earthnet Online, 2011].

### 1.5.2 SCIAMACHY

The SCanning Imaging Absorption spectroMeter for Atmospheric CartograpHY (SCIAMACHY) was an imaging spectrometer lying on board of the ESA ENVISAT satellite; launched on 28<sup>th</sup> February, 2002. Its name comes from the Greek word "*σκιμαχ $\eta$* " meaning *fighting shadows* [Burrows et al., 1995]. This spectrometer had a relatively high resolution of about 0.2 nm to 1.5 nm at the range of 214 nm to 2386 nm in 8 science channels. The spectral resolution of channel 2, which was used in total ozone retrievals, is 0.26 nm (Huggins bands; 326.6–334.5 nm). SCIAMACHY functioned in three different viewing geometries: nadir, limb, and sun/moon occultations. One of its main objectives was to measure the same atmospheric volume both in nadir and limb (limb/nadir matching) within one orbit ( $\Delta t = 430 \text{ s}$ ) [Gottwald and Bovensmann, 2011]. A typical orbit started with a limb measurement of the twilight atmosphere, followed by the solar occultation measurement during sunrise at high northern latitudes and an optimised limb-nadir sequence. When the moon was visible, lunar occultation measurements were performed in every second orbit [Bovensmann et al., 1999]. ENVISAT circled the Earth in a

near-polar sun-synchronous orbit at 799.8 km, with an equator crossing at 10:00 local time at the descending node, with a repeat cycle of 35 days (501 orbits per cycle). In late October 2010, the orbit was lifted by 17.4 km, leading to a repeat cycle of 30 days (431 orbits per cycle) completing about 14.3 orbits per day [ESA Earthnet Online, 2013]. The swath width of  $\pm 480$  km relative to ground track in nadir and limb scans allowed for global coverage within 6 days. In nadir mode, the forward scan (left to right) was performed in 4 s and the backward scan in 1 s. The instrument's integration time was 0.25 s. The size of the individual ground pixels was dependent on the selected integration time. The typical spatial resolution was approximately  $240 \times 30$  km<sup>2</sup> (across track times along track) with the footprint of a single observation being typically  $30 \times 60$  km<sup>2</sup> [Gottwald and Bovensmann, 2011]. In limb geometry, the instrument observed the scattered light from Earth's atmosphere with scanning horizontally and vertically the atmosphere with elevation steps of approximately 3.3 km at the tangent point. With discrete steps from the surface up to about 100 km, the tangent height was raised in order to scan the atmosphere vertically. For every limb state, a horizontal scan with a cross track coverage of 960 km, and typically four readouts in the visible part of the spectrum, were performed. This resulted in a typical horizontal resolution of 240 km [Gottwald and Bovensmann, 2011]. In occultation mode, SCIAMACHY measured the radiation of the rising sun and moon directly, and its attenuation due to the Earth's atmosphere at the line-of-sight tangent point [Gottwald and Bovensmann, 2011]. The communication with the satellite was lost on 8<sup>th</sup> of April 2012, without any successful recontact by ESA.

### 1.5.3 GOME-2

The Global Ozone Monitoring Experiment-2 (GOME-2) is one of the European instruments on board of the MetOp satellite series, continuing the long-term monitoring of atmospheric trace gases started by GOME on ERS-2, and SCIAMACHY on Envisat. The GOME-2 nadir viewing UV/Vis scanning spectrometer (240–790 nm wavelength region in four different channels; bands 1 (240–315 nm) and 2 (310–403 nm) are used for total ozone retrieval) is designed almost as a carbon copy of the GOME-1 concept, besides small adoptions and minor improvements to the design [Callies et al., 2000]. The footprint of the instrument is  $40 \times 80$  km<sup>2</sup> for main channel data. The instrument is scanning the Earth forward moving from East to West in 12 subsets (4.5 s) and backwards in 4 subsets (1.5 s) of 375 ms each. The default swath width of each scan is 1920 km, which leads to nearly global coverage of the Earth's surface within one day [ESA, 2006]. Metop-A (launched on 19 October 2006) and Metop-B (launched on 17 September 2012) satellites have a sun-synchronous orbit crossing the equator in descending-node at 09:30 local time. They are in a low polar orbit, at an altitude of 817 kilometres [ESA, 2012]. From 15<sup>th</sup> of July 2013, the Metop-A operates with a reduced swath of 960 km and spatial resolution of approximately  $40 \times 40$  km<sup>2</sup> [O3M SAF - EUMETSAT, 2017]. Metop-C is planned to be launched in 2018 [EUMETSAT, 2017].

### 1.5.4 TROPOMI

The TROPOspheric Monitoring Instrument (TROPOMI) is a spaceborne nadir viewing spectrometer jointly developed by ESA and the Kingdom of the Netherlands, coming to continue the heritage of

the European satellite instruments (GOME/SCIAMACHY/GOME2) and Ozone Monitoring Instrument (OMI) aboard the NASA's Earth Observing System's (EOS) AURA satellite. It was launched on board the Sentinel-5P on 13<sup>th</sup> of October, 2017. With no other missions capable to obtain the data acquired by SCIAMACHY and OMI, Sentinel-5P will fill the five-year gap until the launch of Sentinel-5 TROPOMI is a UV-VIS-NIR-SWIR (270- 320 nm, 310-495 nm, 675-775 nm and 2305-2385 nm) instrument with a spectral resolution of 0.25-0.55 nm. The instrument makes use of 4 two-dimensional detectors, allowing it to operate in a push-broom configuration. TROPOMI will scan the Earth for 1 s while the instrument will move approximately 7 km. The swath (scanned strip) will be approximately 2600 km long across track, and 7 km along track. After the 1 s measurement a new measurement will start, so the instrument will scan the Earth's atmosphere as the satellite moves. TROPOMI will provide daily global coverage with a high spatial resolution of  $7 \times 7 \text{ km}^2$ , with a special focus on the troposphere. This high temporal and spectral resolution is expected to increase the cloud-free observations. Sentinel-5 Precursor is expected to fly in loose formation with the NASA/NOAA Suomi-NPP satellite at 824 km orbital height. It's orbit will be near-polar sun synchronous with crossing Equator time at 13:30 local time (early afternoon orbit) with a repeat cycle of 17 days. The foreseen in-orbit lifetime of Sentinel-5 P is 7 years [SP-1332: Sentinel-5 Precursor, 2016].

Table 1.2: Characteristics of satellite instruments.

Instrument	GOME/ERS-2	SCIAMACHY/Envisat	GOME-2/ Metop-A	TROPOMI/ S5-p
Period of operation	06/1995–07/2011	08/2002–04/2012	01/2007–present	10/2017– -
Spectral Coverage	240 - 790 nm	240 - 2380 nm	240 - 790 nm	270 - 2385 nm
Ground pixel size	320 x 40 km <sup>2</sup>	60 x 30 km <sup>2</sup>	40 x 80 km <sup>2</sup>	7 x 7 km <sup>2</sup>
0° cross-ing time	10:30 a.m.	10:00 a.m.	9:30 a.m.	13:30 p.m.
Global coverage	3 days	6 days	almost daily	daily



## CCD retrieval algorithm

Tropical Tropospheric Columns of Ozone (TTCO) can be retrieved from satellite data using the total column of ozone and cloud information from only one satellite instrument. The Convective Clouds Differential (CCD) technique, originally developed by Ziemke et al. [1998], is a statistical method that makes use of known statistical properties of the atmosphere (e.g. location of deep convective clouds, latitudinally invariant stratospheric ozone in the tropics) without using a radiative transfer equation in the retrieval algorithm. This makes CCD computationally easy and appropriate for operational satellite retrievals. This Chapter describes the improved convective clouds differential algorithm, developed for three different instruments (GOME, SCIAMACHY, and GOME-2), and discusses the corrections needed for the retrieval of the above cloud columns of ozone (ACCO).

### 2.1 The Convective Cloud Differential (CCD) method <sup>1</sup>

Figure 2.1, illustrates the method and the considerations concerning the method that will be discussed in this section. The original technique, as applied to TOMS data, assumes that the ozone column above deep convective clouds (ACCO) simulates the stratospheric ozone in the same latitude band and that this amount is invariant with longitude; which is approximately true in the tropics [Ziemke et al., 1998]. However, a zonal variability of less than  $\sim 6$  DU (see Fig. 2.2) exists on monthly time scales in the tropical region. The ACCO retrieval is limited to the western Pacific and Indian ocean ( $70^{\circ}\text{E}$ - $170^{\circ}\text{W}$ ) as it is the area where the most deep convective clouds are found (see Fig. 2.3) and the tropospheric ozone column background is the lowest. The ACCO values elsewhere are overestimated and do not represent the stratospheric columns due to the existence of less high clouds and more polluted background from biomass burning that is up-lifted to the UTLS (upper troposphere and lower stratosphere) region [Avery et al., 2010, Sauvage et al., 2006].

The stratospheric ozone column amount may be influenced by episodic tropical waves (Kelvin waves, mixed Rossby-gravity waves, and equatorial Rossby waves) in the stratosphere [Ziemke and Stanford, 1994]. The assumption made in the original CCD method from Ziemke et al. [1998] that the stratospheric ozone column is independent of longitude in the tropics has been extensively investigated by Valks et

---

<sup>1</sup>This section has been previously published as part of Leventidou et al. [2016]

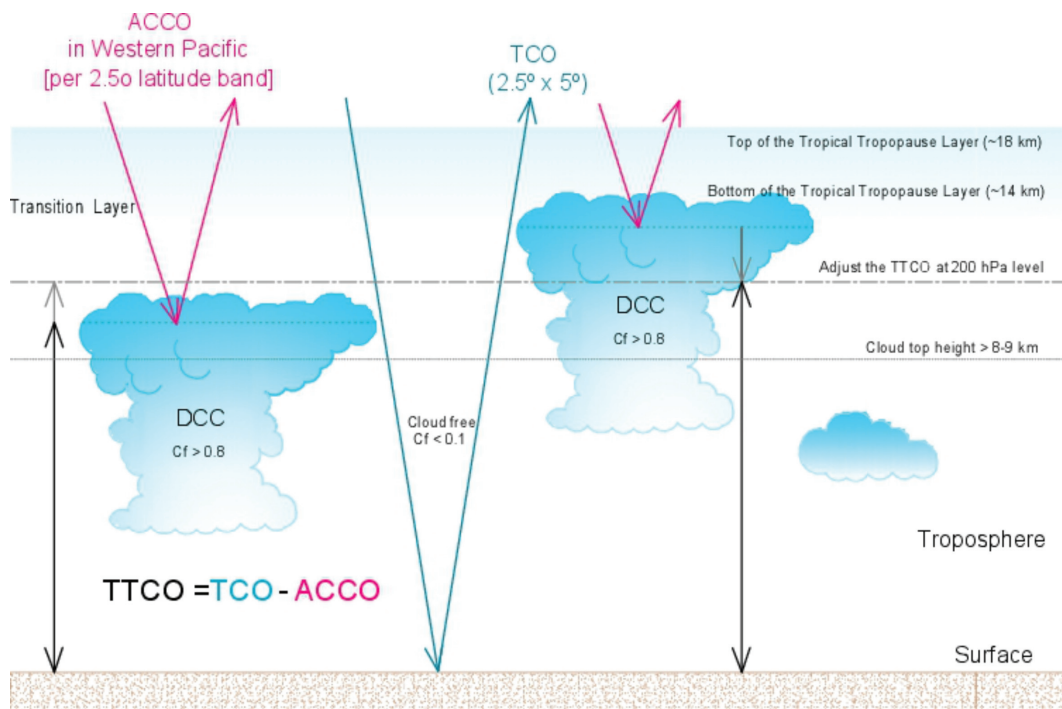


Figure 2.1: The convective cloud differential method.

al. [2003], where they conclude that it is valid above 200 hPa in the tropics. According to Fig. 2.2 the zonal variability in August 2008 for the latitude bands  $5^{\circ}$ - $7.5^{\circ}$  and  $-15^{\circ}$ - $-12.5^{\circ}$  is less than 6 DU ( $1\sigma$  standard deviation of the mean). Another important factor causing the monthly variability of the ACCO is the natural variability of the deep convective clouds (DCC) top height.

The second basic assumption of the CCD method refers to the fact that the tropopause ( $\sim 18$  km or  $\sim 100$  hPa) lies close to the top of the DCC. These clouds are high, thick and bright with greatest occurrence rates over the Inter-Tropical Convergence Zone (ITCZ), the western Pacific, and the Indian Ocean [Hong et al., 2007, Sassen et al., 2009]. Due to the immigration of the ITCZ, these clouds are located south, over the western and central Pacific Ocean, northern South America and equatorial Africa in boreal winter and spring, whereas in boreal summer, the highest DCC occurrences are located over the Indonesian region and the Bay of Bengal [Sassen et al., 2009]. Figure 2.3a shows the distribution of the DCCs in January and August 2008 for SCIAMACHY [ $cf > 0.8$  and  $cth > 9$  km, SACURA] and GOME-2 [ $cf > 0.8$  and  $cth > 7$  km, FRESCO] indicating the ITCZ. Both instruments and cloud algorithms agree in the location of the DCCs but not on the number of the DCCs per grid box, mainly due to differences in the cloud algorithms used and the spatial resolution of the instruments. For example, several cloud algorithms like FRESCO [Koelemeijer et al., 2001] assume that clouds behave as opaque Lambertian surfaces, resulting usually in retrieving the effective (optical centroid) cloud top height (see Fig. 2.1) which lies below the physical cloud top height [Ziemke et al., 2008]. SACURA cloud top height retrieval algorithm [Kokhanovsky et al., 2005] on the other hand, takes into account radiative transfer inside, above and below the clouds [Lelli et al., 2014]. Therefore, it provides more realistic cloud top heights.

In order to define the DCCs measurements with cloud fractions ( $cf$ ) greater than 0.8 and cloud top heights ( $cth$ ) greater than 9 km for SCIAMACHY and 7 km for GOME and GOME-2 were used.

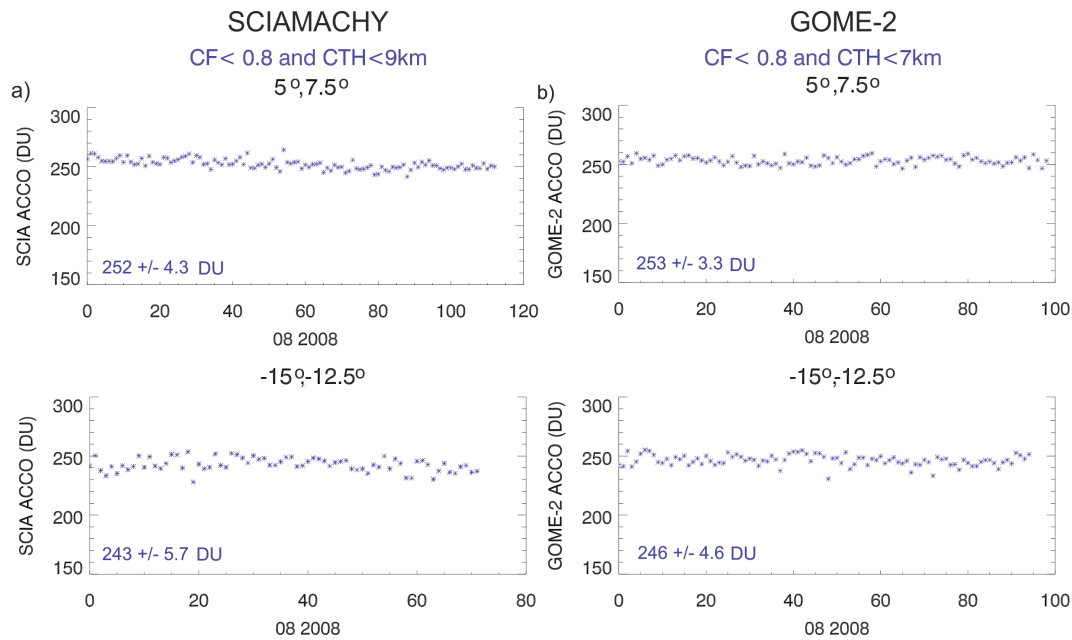


Figure 2.2: a) Above-cloud column ozone (ACCO for the latitude bands  $5^{\circ}\text{N} - 7.5^{\circ}\text{N}$  and  $15^{\circ}\text{S} - 12.5^{\circ}\text{S}$  ( $cf > 0.8$  and  $cth > 9$  km) from SCIAMACHY (using OCRA/SACURA for cloud detection). b) Above-cloud column ozone (ACCO for the latitude bands  $5^{\circ}\text{N} - 7.5^{\circ}\text{N}$  and  $15^{\circ}\text{S} - 12.5^{\circ}\text{S}$  ( $cf > 0.8$  and  $cth > 9$  km) from GOME-2 (using FRESCO for cloud detection) in August 2008. The  $1\sigma$  standard deviation is less than 5 DU.

Even with a higher  $cth$  threshold for SCIAMACHY, SCIAMACHY has the highest frequency of "cloudy" measurements among the three satellites. Fig. 2.3b shows that roughly  $\sim 25\%$  of cloud top heights in the western Pacific are higher than 9 km for SACURA (SCIAMACHY), whereas for FRESCO (GOME-2), the same frequency is met for clouds only above 7 km. Since the cloud algorithms differ between instruments and in order to have sufficient "cloudy" ozone measurements in more than 1% of all the measurements per latitude band, the lower cloud top height limit classifying the DCCs is different for each satellite instrument. It is obvious that the different cloud algorithms calculate different cloud fractions and top heights and as a result, yield different ACCO values (see Fig. 2.4a). However, it was concluded that the ACCO does not change significantly when the  $cf$  is greater than 0.8 and  $cth$  greater than 7 km. The differences in ACCO between the different critical values tested, are within the  $1\sigma$  of the monthly ACCO variability ( $< 10$  DU). The differences are even smaller for SCIAMACHY, since SACURA retrieves more high clouds than FRESCO, making the sampling more uniform between 9 and 12 km (see Fig. 2.3b).

For the calculation of the ACCO, all "cloudy" measurements, (defined separately for each instrument in order to have enough data) are selected and monthly averaged in latitude bands of  $2.5^{\circ}$  width between  $20^{\circ}\text{S}$  and  $20^{\circ}\text{N}$  in the western Pacific and Indian Ocean ( $70^{\circ}\text{E}-170^{\circ}\text{W}$ ). Furthermore, it is known that most DCC tops only reach the bottom of the tropical tropopause layer or "tropical transition layer" (TTL) [Fueglistaler et al., 2009, Gettelman and Forester, 2002, Sherwood and Dessler, 2001], which is well below the thermal (cold point) tropopause ( $\sim 150$  hPa). Only on rare occasions do the DCCs overshoot the top of the TTL [Fueglistaler et al., 2009, Hong et al., 2007]. Therefore, due to the natural variability of clouds, a climatological correction term is applied to each individual measurement of ACCO in order

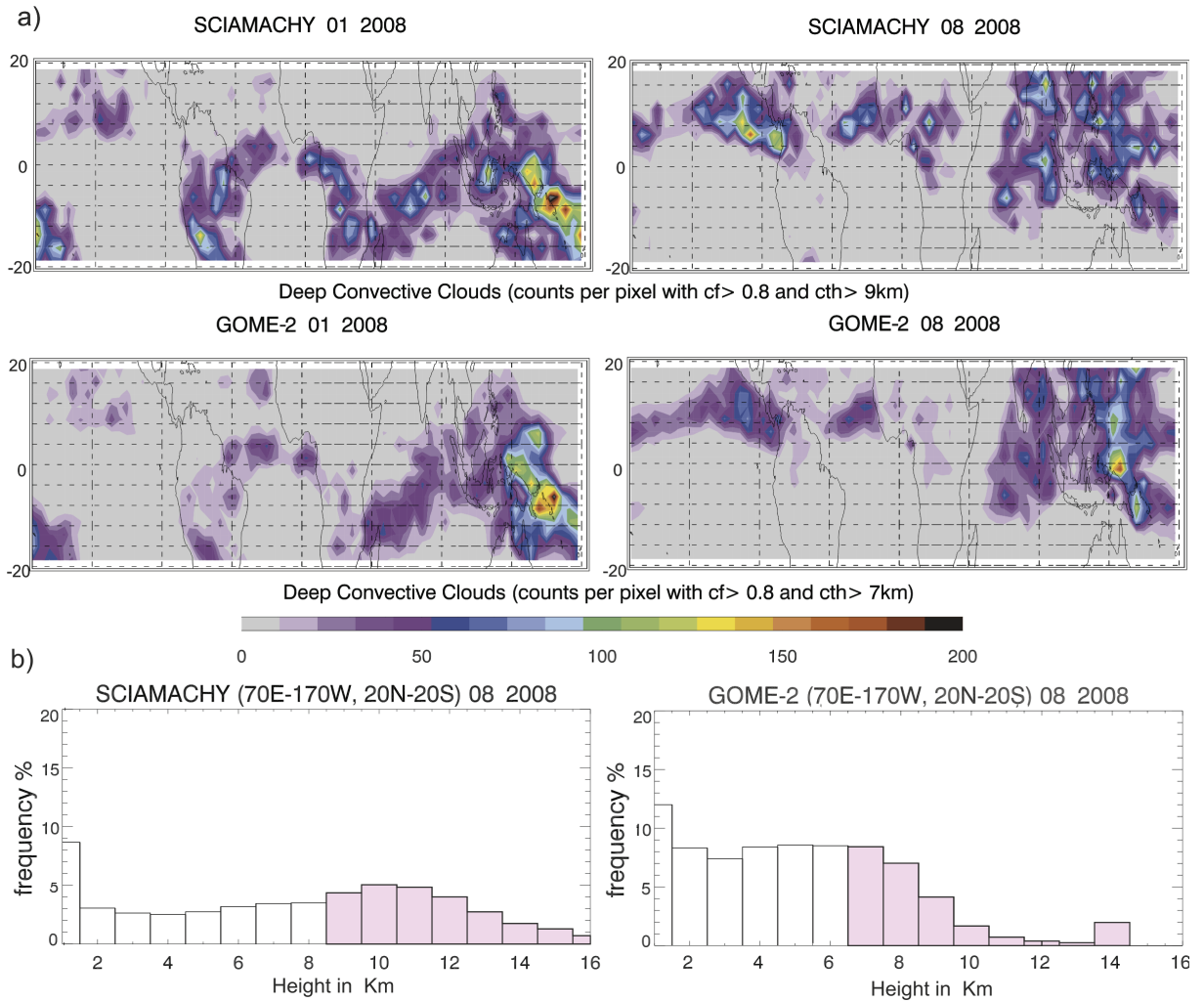


Figure 2.3: a) The number of counts per gridbox with  $cf$  greater than 0.8 and  $cth$  greater than 9 km (SCIAMACHY) and  $cth$  greater than 7 km (GOME-2) for January and August 2008. b) Frequency of cloud top heights ( $cth$ ) for August 2008 from SCIAMACHY (SACURA) and GOME-2 (FRESCO) in the Western Pacific area ( $20^{\circ}\text{S}$ – $20^{\circ}\text{N}$ ,  $70^{\circ}\text{E}$ – $170^{\circ}\text{W}$ ). Pink shaded data are used for the ACCO calculation

to correct for different cloud top heights and adjust the ACCO to a fixed level of 200 hPa ( $\sim 12$  km).

For the calculation of the column amount ( $Cor_{ACCO}$ ), which adjusts the ACCO values to the 200 hPa level, climatological ozone values from Fortuin and Kelder [1998] climatology were used. The Fortuin and Kelder [1998] climatology is reported in volume mixing ratios (vmr) for specific pressure levels. In order to convert the volume mixing ratios (ppm) at the  $i$ -th level to Dobson units (DU), the following formula was used, taking into account the ideal gas law and the horizontal surface density [Ziemke et al., 2001]:

$$Cor_{ACCO}(i) = c \cdot 0.5 \cdot [vmr(i) + vmr(i+1)] \cdot [p(i) - p(i+1)] \quad (2.1)$$

where, vmr is the volume mixing ratio (ppmv),  $p$ , the pressure (Pa), and

$$c = \frac{k_B \cdot T_s \cdot N_A}{\mu \cdot p_s \cdot g} = 0.7889 \quad (2.2)$$

$T_s$  is the standard temperature (273.16 K),  $p_s$ , the standard pressure (101325 Pa),  $k_B$ , Boltzmann's

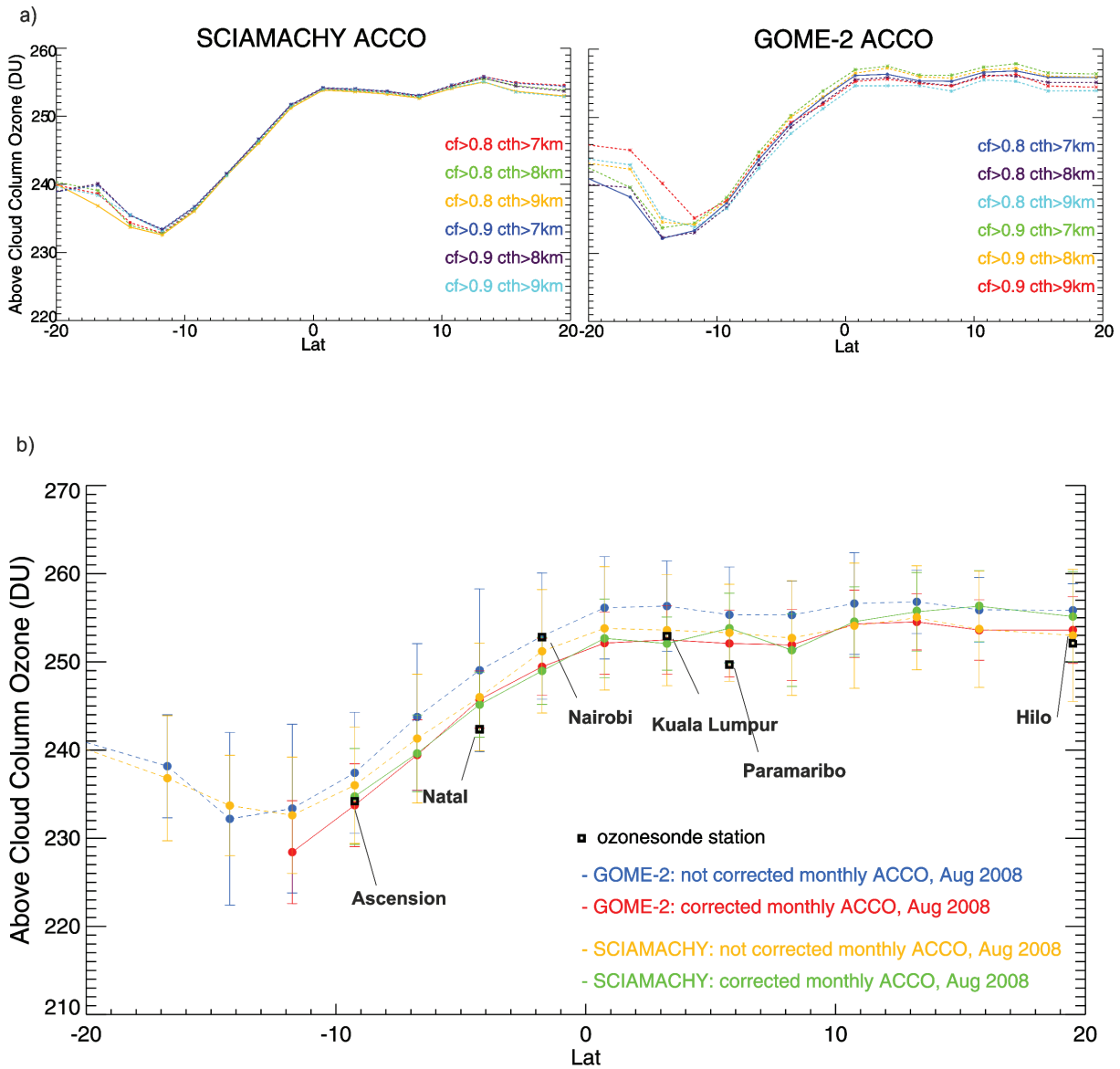


Figure 2.4: a) SCIAMACHY (left) and GOME-2 (right) ACCO per 2.5° latitude bands in the Indian and western Pacific Ocean (70°E–170°W) for different cloud fractions (0.8, 0.9) and cloud top heights (7–9 km) in August 2008. b) Above cloud column of ozone (ACCO) for 2.5° latitude bands in the Indian and western Pacific Ocean from GOME-2 (cf<0.8 and cth<7km) and SCIAMACHY (cf<0.8 and cth<9km) in August 2008. Blue and yellow dashed lines are the zonal ACCO values before applying any corrections for GOME-2 and SCIAMACHY, respectively. Red and green lines are the zonal ACCO values after corrections applied for adjusting to the 200 hPa level and screening out outlier data. Error bars denote 1σ standard deviation. Black boxes show the stratospheric ozone columns from ozonesondes, of the stations Ascension, Natal, Nairobi, Kuala Lumpur, Paramaribo, and Hilo.

constant ( $1.3806 \times 10^{23} \text{ J} \cdot \text{K}^{-1}$ ),  $N_A$ , Avagadro's number ( $6.022 \times 10^{26} \text{ molecules} \cdot \text{kmol}^{-1}$ ),  $\mu$ , the mean molecular weight of the atmosphere (approximately 29), and  $g$ , the mean acceleration of gravity ( $9.81 \text{ m} \cdot \text{s}^{-2}$ ).

Finally, the vertical ozone column of the nearest pressure level as given in the ozone climatology to the retrieved cloud top height (pressure) measurement was used for the adjustment of the ACCO.

- If  $ctp < 200 \text{ hPa}$  then  $ACCO' = ACCO + Cor_{ACCO}$
- If  $ctp > 200 \text{ hPa}$  then  $ACCO' = ACCO - Cor_{ACCO}$

The original CCD method developed by Ziemke et al. [1998] assumed that UV nadir satellite measuring instruments measure ozone above the top of the DCCs, something that is not completely true since UV radiation penetrates inside the cloud, resulting in an additional ozone absorption [Ziemke et al., 2008]. The ozone concentrations inside the high reflective clouds at the regions of the tropical eastern Indian Ocean and western Pacific are about 4–7 ppbv (corresponding to an ozone column of  $\sim 1 \text{ DU}$  between the mean cloud top and the 200 hPa level). This is due to vertical convection of ozone poor oceanic air from the marine boundary layer into the upper troposphere so that the error from ozone below the thermal tropopause is minimal if the retrieved ACCOs are taken from that region [Ziemke et al., 2008]. For this reason, for the cases where  $ctp > 200 \text{ hPa}$  (for the reason discussed above, that FRESCO does not take into account the UV penetration inside the clouds), the value of 1 DU was subtracted from the climatological correction term in the case of GOME and GOME-2 ACCO. As the geometrical top of the cloud is hundreds of meters higher than the one retrieved by FRESCO, the vertical ozone column correction between the cloud top height given from these algorithms and the 200 hPa is higher than it should.

In order to restrict the variability and homogenize the ACCO in a latitude band, all ACCO measurements which result in negative TTCOs or have a daily averaged standard deviation in a  $2.5^\circ \text{ lat}$  by  $5^\circ \text{ lon}$  bin of more than 10 DU or differ more than 5 DU with the neighbouring daily binned measurements are screened out. Figure 2.4b shows the difference between the ACCO values before (blue for GOME-2 and yellow for SCIAMACHY) and after screening out the outliers and adjusting to the 200 hPa level (red for GOME-2 and green for SCIAMACHY). The differences are generally less than 5 DU and can reach 10 DU for latitudes where less cloudy ozone measurements appear (in this case at southern tropics, since the ITCZ moves to northern latitudes on summer, see Fig. 2.3a on the right, were practically where there are no DCCs below  $15^\circ \text{ S}$ ). These cases are excluded from the  $<1\%$  DCCs per latitude band criterion. Another approach for the difference between the cloud pressure level and the 200 hPa level was used by Valks et al. [2014] assuming a constant ozone volume mixing ratio of 5 ppbv between the effective cloud top and the 200 hPa level. They concluded that the correction term is small (less than 2 DU) and therefore the difference with the climatology considered negligible.

After the corrections have been applied in GOME-2 and SCIAMACHY ACCO, the agreement between them improves. The comparison of the ozone column above 200 hPa with six ozonesonde stations from the SHADOZ network (Ascension, Natal, Nairobi, Kulala Lumpur, Paramaribo, and Hilo) is also presented in Fig. 2.4b. The number of ozonesonde data for this month varies between 1 and 4 ozonesonde launches per station. The ozonesonde burst altitude resides within the stratosphere ( $\sim 30 \text{ km}$ ), therefore the above 200 hPa ozone column from the ozonesondes had to be indirectly calculated for these stations. The ozonesonde measurements from the surface up to 200 hPa were integrated, monthly averaged and

then they were subtracted from the GOME-2 monthly averaged total ozone measurements, deriving the ozone column above 200 hPa as done by Valks et al. [2003]. The difference between the ozonesonde's ACCO and the corrected CCD ACCO is less than 3 DU for these six stations.

Finally, the monthly averaged ACCO per 2.5° latitude bands from the western Pacific region (70°E–170°W) was subtracted from the monthly averaged total ozone column (2.5° by 5° bins) of nearly cloud free areas ( $cf < 0.1$ ), yielding the monthly tropical tropospheric column of ozone (TTCO). The developed algorithm has been applied to GOME (1996-2003), SCIAMACHY (2003-2012), and GOME-2 (2007-2015) ozone and cloud data. As discussed in Section 1.5, these instruments have nearly identical spectral channels in the UV so that the same retrieval algorithm for total ozone and the derived tropospheric column ozone can be adopted without significant changes.

## 2.2 Summary and discussion

An improved CCD retrieval algorithm for tropical tropospheric ozone columns (TTCO) has been developed for three different satellite instruments (GOME/ERS-2, SCIAMACHY/ENVISAT and GOME-2/MetopA), covering the period between 1996 and 2015. A climatological correction has been used to adjust the above cloud column of ozone (ACCO) to 200 hPa, the outliers have been screened out to homogenise the ACCOs for each latitude band and 1 DU has been removed from the ACCO of GOME and GOME-2 to take into account the penetration of UV radiation within the clouds. Tests made here indicate that the retrieved ACCO provides a reasonable approximation of the stratospheric ozone columns, although there are still limitations due to cases of limited cloudy data in some latitude bands as a result of the ITCZ seasonal migration. Further optimization of the WFDOAS data using the same algorithm for cloud properties (e.g. SACURA) for all satellite datasets would improve the accuracy of ACCO and TTCO retrieval. Using SACURA, the cloud optical thickness (cot) could be added in the WFDOAS dataset for all instruments. This will provide an additional selection criterion for locations of deep convective clouds (DCC). A sensitivity study for the ACCO retrieval above DCCs with various cloud parameters ( $cf$ ,  $cth$ ,  $cot$ ) could improve further the CCD retrieval and the estimation of its uncertainty. The uncertainty of WFDOAS ozone retrieval above different cloudy scenes could be quantified in a future study by testing the deviation of synthetic data from a radiative transfer model (e.g. SCIATRAN) from a reference ozone profile.



## TTCO retrievals, validation and uncertainty estimation

Tropical tropospheric ozone is a secondary pollutant, following the variation of its precursor emissions ( $\text{NO}_x$ , VOCs, CO,  $\text{CO}_2$ ,  $\text{CH}_4$  etc.) as well as the spatiotemporal changes in atmospheric transport and meteorology. Ozone is removed from the troposphere by several chemical reactions or is dry deposited at the surface [IPCC, 2007]. Its concentration is the net result of these two processes. Remote sensing from satellites has been proven to be very useful in providing consistent information of tropospheric ozone concentrations over large areas. The present study focuses on the convective cloud differential (CCD) method. The CCD technique and the modifications made to the method applied in the past by Ziemke et al. [1998] and Valks et al. [2003, 2014] have been described in Chapter 2. Here, are presented the main results of the advanced CCD retrieval. Additionally, the uncertainty budget of CCD is estimated for the first time here. The validity of CCD results from the individual instruments is tested using comparisons to vertically integrated in-situ measurements from the Southern Hemisphere Additional OZonesondes (SHADOZ) network [Thompson et al., 2003] and tropospheric ozone columns from Limb/Nadir matching data (for SCIAMACHY data only) [Ebojie et al., 2014].

### 3.1 Tropical tropospheric ozone column (TTCO) results from CCD \*

Undoubtedly, the need to control the tropospheric  $\text{O}_3$  increase is crucial [WHO, 2006]. Every potential monitor and study of long-term tropospheric  $\text{O}_3$  changes as well as the quantification of associated radiative forcing using chemical transport or climate models have to rely on the availability of reliable tropospheric ozone data. Using the Convective Cloud Differential (CCD) method, monthly mean tropical tropospheric ozone columns have been derived on a  $2.5^\circ \times 5^\circ$  grid for the years 1996-2015. As shown in Figures 3.1, 3.2, and 3.3, tropical tropospheric  $\text{O}_3$  column exhibits a profound wave-one pattern, with high values over the South Atlantic ( $\sim 30\text{--}40$  DU) and low values over the Indian and Pacific Oceans ( $\sim 10\text{--}20$  DU). This feature is persistent with a maximum in autumn (austral spring). This maximum is a combined result of biomass burning and long-range transport [Chandra et al., 2002, Jonquieres et al., 1998, Thompson et al., 2001, Ziemke et al., 2009b].  $\text{O}_3$  precursors from biomass burning from the African and South American continents are dynamically transported to the mid-Atlantic. The main

---

\*This section has been previously published as part of Leventidou et al. [2016]

dynamical features in the central Atlantic is the African Easterly Jet (AEJ) and the St-Helene high which leads to a redistribution of  $O_3$  from north Africa to the area around Namibia [Diab et al., 2003]. Whereas both the South westerly Harmattan flow and the AEJ bring high  $O_3$  from the ground up to 600 hPa over the African continent, only the AEJ advection exports high  $O_3$  over the north Atlantic [Sauvage et al., 2006]. Lightning produces substantial amounts of nitrogen oxides which are increasing the ozone-forming potential in the outflow of convected air masses [Apel et al., 2012, Pickering et al., 1990]. Winterrath [1999] found that the slant columns of  $O_3$  and  $NO_2$  may increase up to 62% and 320% respectively inside a thunderstorm cloud, however most of the  $O_3$  enhancement is possibly induced by stratospheric air intrusions or prior to lightning in an electrically active cloud (dissociation of  $O_2$ ) by coronal, or silent discharge. The upper tropospheric  $O_3$  produced from thunderstorm clouds (including  $O_3$  from lightning) sediments stronger over the southern tropical Atlantic as part of the Walker circulation and weaker over up-welling regions such as the tropical Pacific [Martin et al., 2002]. Tropospheric  $O_3$  over the tropical Pacific presents a persistent minimum due to ozone loss reactions

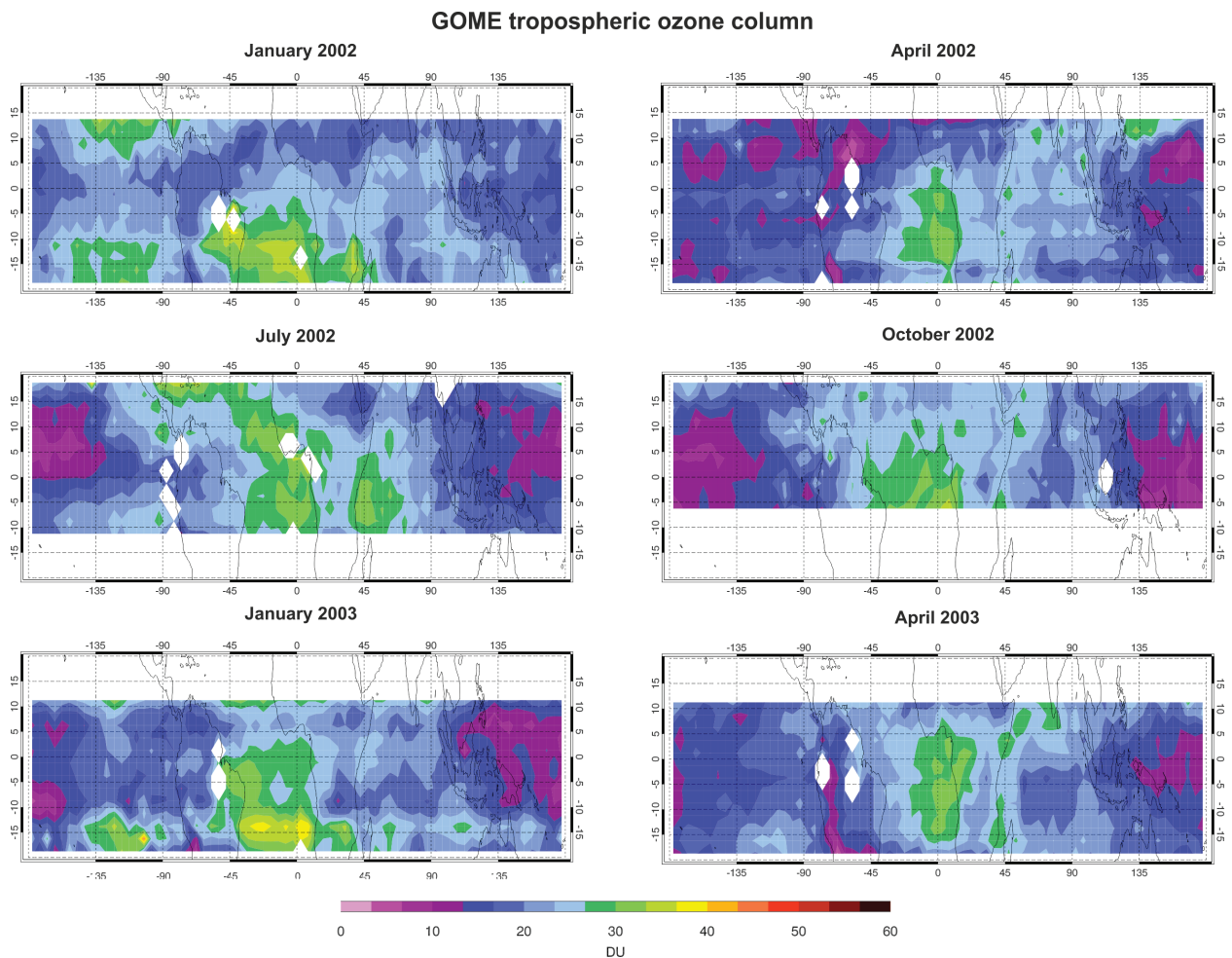


Figure 3.1: Tropical tropospheric ozone column (TTCO) derived with the convective cloud differential (CCD) technique for January, April, July, and October 2002 and January and April 2003 using GOME data.

that are favoured by the specific conditions dominating there, such as the high marine boundary layer air temperature and the low overhead ozone. These conditions favour the strong advection from East

to West by the Walker circulation. For this reason the tropospheric air masses have been in a clean, warm and humid environment for a long time and loss of odd oxygen and ozone from OH and ozone precursors like  $NO_x$  ( $= NO + NO_2$ ) proceeded longer than elsewhere in the tropics [Rex et al., 2014].

In order to compare the CCD results between the different satellite instruments, two overlapping years were selected. 2002 and 2003, for GOME/SCIAMACHY comparison and 2008, for SCIAMACHY/GOME-2 comparison. Figure 3.1, shows the tropical tropospheric ozone columns for January, April, July, and October 2002 derived from GOME data. The wave-one pattern is well represented, as the higher tropospheric  $O_3$  columns appear over the central Atlantic Ocean in October [Martin et al., 2002, Sauvage et al., 2006]. Contrasting the tropospheric  $O_3$  columns retrieved with CCD-IUP using GOME data with

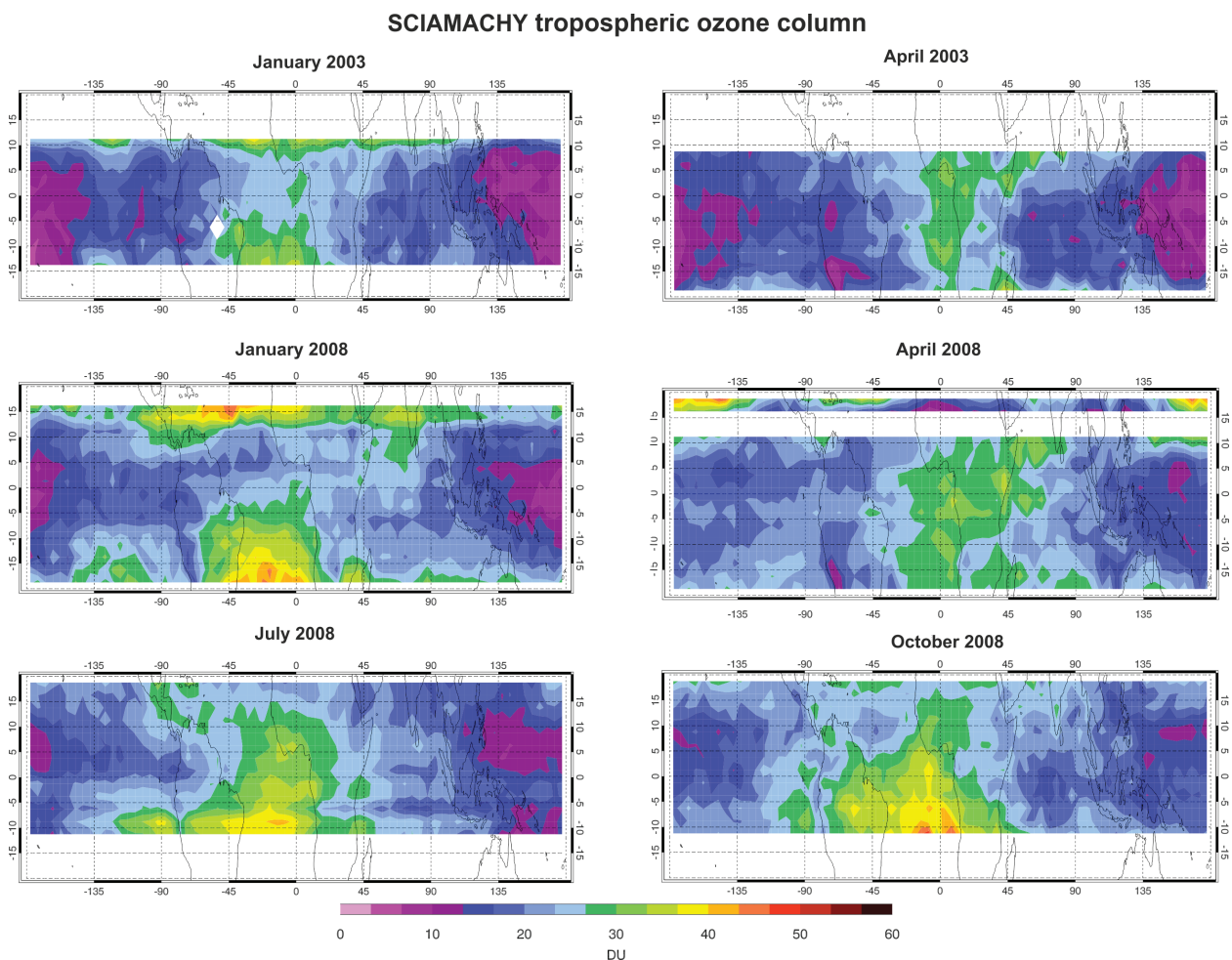


Figure 3.2: Tropical tropospheric ozone column (TTCO) derived with the convective cloud differential (CCD) technique for January and April 2003 and January, April, July, and October 2008 using SCIAMACHY data.

the ones retrieved using SCIAMACHY data for the same months, January and April 2003 (see Fig. 3.2 bottom and Fig. 3.3 top), we conclude that the results are similar. The same pattern on tropospheric ozone for January and April 2002 can be also seen for January and April 2003. In January, the maximum  $O_3$  columns are located for both years at the South Atlantic and South-West Pacific Ocean and the minimum tropospheric  $O_3$  columns at the central-West Pacific. In April 2002 and 2003, tropospheric  $O_3$  is similar with higher values at the West coast of Africa. The comparison between SCIAMACHY and

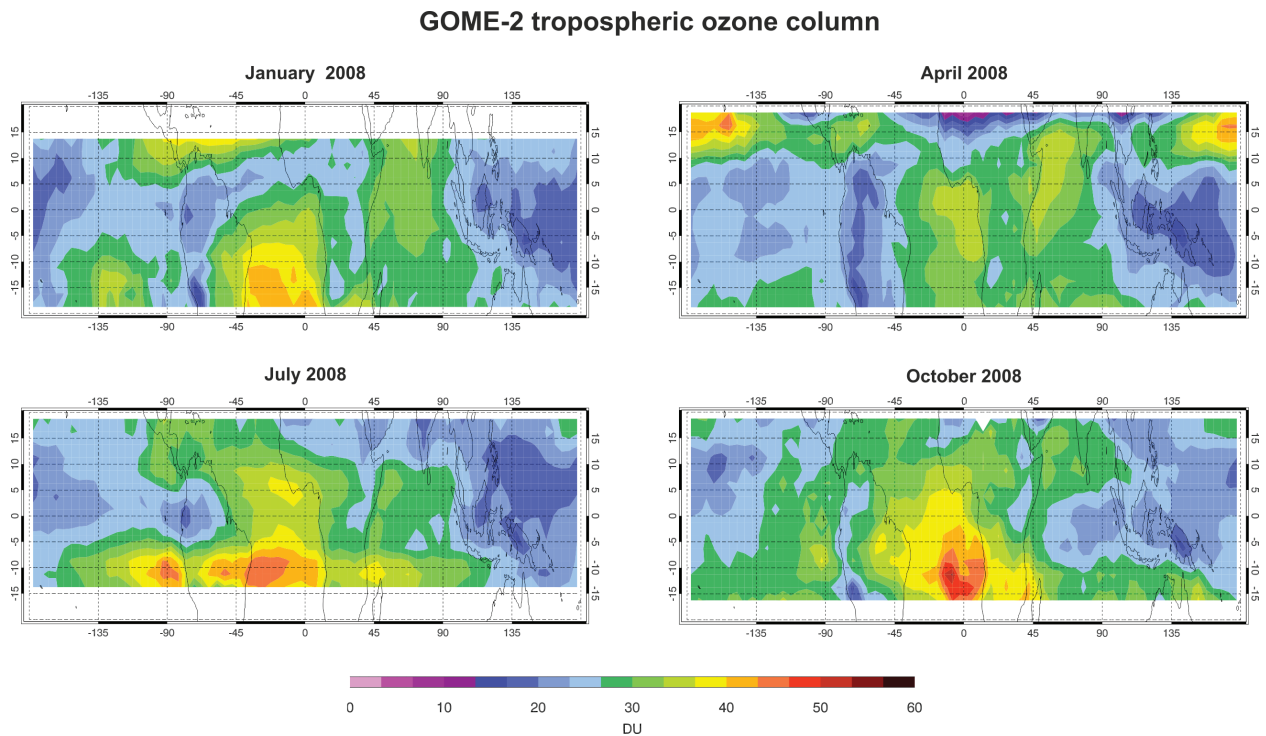


Figure 3.3: Tropical tropospheric ozone column (TTCO) derived with the convective cloud differential (CCD) technique for January, April, July, and October 2008 using GOME-2 data.

GOME-2 TTCOs for January, April, July and October 2008 is presented in Figures 3.2 and 3.3. The tropospheric  $O_3$  burden has the expected pattern for all months and it is similar for both instruments. However, tropospheric  $O_3$  columns retrieved using GOME-2 data are apparently higher than the ones retrieved using SCIAMACHY for all months presented here. These results indicate that a harmonisation between the instruments is necessary in order to create a consistent, merged TTCO dataset.

### 3.2 Uncertainty estimation \*

This section summarizes and gives a rough estimate of the main sources of uncertainty that contribute to the overall uncertainty in the retrieved tropical tropospheric ozone columns (TTCO). The years presented here are 2002, for GOME, and 2008, for SCIAMACHY and GOME-2 ozone and cloud data. The square root of the sum of all individual quadratic uncertainties that contribute in the total column (TCO) and the above cloud column of ozone (ACCO) results in the uncertainty of the mean TTCO. The uncertainty in the TCO and the uncertainty in the ACCO are supposed to follow a Gaussian distribution. This assumption is based to the Central Limit Theorem which states that the convolved distribution ( $Y=c_1X_1 + c_2X_2 + \dots + c_nX_n$ ) of the input quantities ( $X_i$ ) converges towards the normal distribution as the number of input quantities contributing to the convolved distribution variance ( $\sigma^2(Y) = \sum_{i=1}^N c_i^2 \sigma^2(X_i)$ ) increases, regardless of the original probability distributions of the input quantities [JCGM 100, 2008].

Ozone time-series present a statistical dependence on its own past or future values, meaning that

\*This section has been partly published as part of Leventidou et al. [2016]

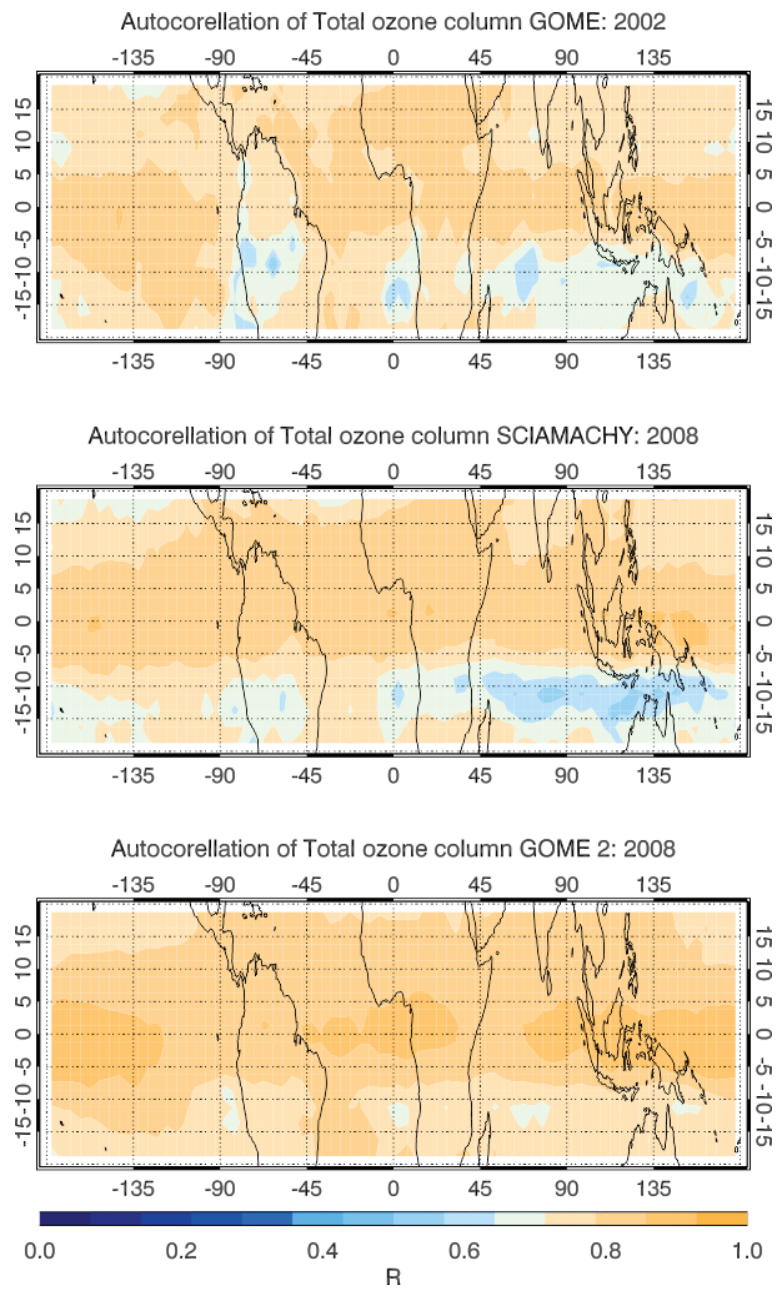


Figure 3.4: First-order (lag-1) autocorrelation of cloud-free ( $cf < 0.1$ ) monthly mean total ozone data for a) GOME (2002), b) SCIAMACHY (2008) and c) GOME-2 (2008) WFDOAS data.

it has the tendency for a month to be similar to the previous and the next month. In atmospheric sciences, this dependence is referred as persistence. Persistence is typically characterised in terms of serial correlation, or temporal autocorrelation ( $\phi$ ). Such correlations are sometimes referred to as lagged correlations. Autocorrelations are computed by substituting the lagged data pairs into the formula for the Pearson correlation (Eq. 3.1). For the lag-1 autocorrelation there are  $n-1$  such pairs. The first-order autocorrelation is the most commonly computed measure of persistence [Wilks, 2011].

$$\phi_{TTCO} = \frac{\sum_{i=1}^{N-1} [(TTCO_i - \overline{TTCO_-})(TTCO_{i+1} - \overline{TTCO_+})]}{[\sum_{i=1}^{N-1} (TTCO_i - \overline{TTCO_-})^2 \sum_{i=2}^N (TTCO_i - \overline{TTCO_+})^2]^{1/2}} \quad (3.1)$$

where  $N$ , is the number of observations,  $+$  indicates the following and  $-$  the previous month. The same equation also applies for the case of the ACCO.

Figure 3.4, shows the first-order (lag-1) autocorrelation of the cloud-free ( $cf < 0.1$ ) monthly mean total ozone columns for GOME (2002), SCIAMACHY and GOME-2 (2008). The autocorrelation may reach 0.9 with lower autocorrelations noticed over south-west Pacific and south Africa and America for the time-series of GOME and SCIAMACHY ( $\sim 0.4 - 0.6$ ). In this case, the autocorrelation indicates that the uncertainty in total, above cloud and tropospheric ozone at one month is linearly related to the uncertainty at the previous month.

An uncritical application of classical methods assuming independence of data within a sample will often give misleading results when applied to strongly persistent series [Wilks, 2011]. For example, the underestimation of the variance of the sample mean may strongly influence the standard  $t$ -statistic  $\left( \frac{\bar{x} - \mu_0}{[Var(x)]^{1/2}} \right)$ , leading to irrational rejections of the null hypothesis [Wilks, 1997]. A wide used method to estimate the variance of the sampling distribution of the mean even when the data are persistent, is to include a "variance inflation factor" equal to:

$$V = 1 + 2 \sum_{k=1}^{N-1} \left(1 - \frac{k}{n}\right) \phi_k \quad (3.2)$$

where  $k$  is the lag of autocorrelation ( $\phi_k$ ) and  $N$  is the sample size. This "variance inflation factor" is also called the time between effectively independent samples,  $T_0$  [Leith, 1973]. For independent data, where  $\phi_k = 0$  and  $k \neq 0$ ,  $V = 1$  and the classical  $t$ -test could be carried through as before. Estimation of the effective sample size is most easily approached if it can be assumed that the underlying data follow a first-order autoregressive process. For lag-1 ( $k=1$ ) autocorrelated data ( $\phi_1$ ), the "variance inflation factor" is equal to  $V = \frac{1+\phi_1}{1-\phi_1}$ , adjusting the variance of the time averaged sampling distribution to reflect the influence of the serial correlation [Wilks, 1997]. The autocorrelated time-series tend to have nearby values more alike than in the independent series, meaning that these averages will be less consistent from batch to batch, resulting in having a higher variance than the independent data [Wilks, 2011].

Estimation of the "effective sample size" or "equivalent number of independent samples" is usually approached by the assumption that the data follow a first-order autoregressive process (when a more complicated time-series model is necessary to describe the persistence, appropriate but more complicated expressions for the effective sample size can be derived [Katz, 1982]). Using the "inflation factor", the effective sample size can be estimated by the following approximation [Leith, 1973, Wilks, 2011]:

$$N' \cong \frac{N}{V} = N \left( \frac{1 - \phi_1}{1 + \phi_1} \right) \quad (3.3)$$

When there is no time correlation,  $\phi_1 = 0$  then  $N' = N$ . As  $\phi_1$  increases the effective sample size becomes progressively smaller. Using Equation 3.3, the variance of the mean TCO becomes:

$$\text{Var}[\overline{TCO}] \cong \frac{s_{TCO}^2}{N'} = \frac{s_{TCO}^2}{N} \left( \frac{1 + \phi_{TCO}}{1 - \phi_{TCO}} \right) \quad (3.4)$$

where  $s_{TCO}$ , is the TCO standard deviation and  $\phi_{TCO}$  is the first-order autocorrelation of TCO time-series [Wilks, 2011]. The positive square root of the TCO variance is called (Type-A) standard uncertainty of the total ozone column,  $u_{TCO}$ . The same equations as Eq. 3.1, 3.2, 3.3 and 3.4 can also apply to the ACCO uncertainties.

The largest contribution in the WFDOAS total ozone column retrieval uncertainty originates from the a-priori errors associated with the use of the ozone climatology and simplifying assumptions made in the derivation of effective parameters (e.g. look up tables for albedo, altitude, and solar zenith angle, other errors like the absorbing aerosol load, the ghost vertical column and the Ring ozone filling) [Coldewey-Egbers et al., 2005]. The individually retrieved total ozone column with WFDOAS has an uncertainty of 3% [Coldewey-Egbers et al., 2005]. The comparison with ground data show an RMS difference of about 1.5% in the tropics [Weber et al., 2005]. Assuming that the precision of satellite and ground data equally contribute to the RMS difference, it results in a precision of WFDOAS total ozone of about 1% ( $u_{TCO_{retrieval}} \simeq 3\text{DU}$  is the estimated average uncertainty for the individual WFDOAS TCO and  $u_{ACCO_{retrieval}} \simeq 2.5\text{DU}$  for the WFDOAS ACCO retrieval). The total uncertainty of the grid-box averaged total column ozone is therefore given by

$$u_{TCO} = \sqrt{\frac{\sum_{i=1}^N u_{TCO(i)_{retrieval}}^2}{N_{TCO}}} \sqrt{\frac{1 + \phi_{TCO}}{1 - \phi_{TCO}}} \simeq \frac{u_{TCO_{retrieval}}}{\sqrt{N_{TCO}}} \sqrt{\frac{1 + \phi_{TCO}}{1 - \phi_{TCO}}}, \quad (3.5)$$

where  $N_{TCO}$  is the number of cloud-free total ozone measurements per grid-box.  $u_{TCO}$  is found to be generally less than 2 DU for SCIAMACHY and GOME-2 whereas it may exceed 6 DU in a few grid boxes in case of GOME (Fig. 3.5a).

However, a notable uncertainty contribution in the tropospheric ozone column arises from the above cloud column calculation. For the CCD method, the above cloud ozone column refers to pixels with cloud fractions greater than 0.8 and cloud top heights greater than 7 km for GOME and GOME-2 and 9 km for SCIAMACHY. The averaged uncertainty in the individual above cloud ozone retrieval from WFDOAS algorithm,  $u_{ACCO(i)_{retrieval}}$  is 1% ( $\sim 2.5\text{DU}$ ). Similar to eq. 3.5 for the total ozone column, the standard uncertainty of the monthly mean ACCO per latitude band in the reference region of the western Pacific (70°E-170°W) is calculated by

$$u_{ACCO_{averaging}} = \frac{u_{ACCO_{retrieval}}}{\sqrt{N_{ACCO}}} \sqrt{\frac{1 + \phi_{ACCO}}{1 - \phi_{ACCO}}} \quad (3.6)$$

where  $N_{ACCO}$  is the number of above cloud column ozone measurements per latitude band and  $\phi_{ACCO}$  is the autocorrelation of the ACCO  $\simeq 0.9$ . The uncertainty of monthly averaged ACCO is found to be less than 2 DU for all instruments (see Fig. 3.5b).

The cloud parameter introduces an additional uncertainty contribution to ACCO. In order to calculate the possible impact of cloud fraction and cloud top height on the monthly mean zonal ACCO, the ACCO

values have been calculated using the marginal values of the known uncertainties in cloud fraction and cloud top height. The half of the deviation between them is then considered to be the parameter uncertainty for a given parameter change [Rahpoe et al., 2013].

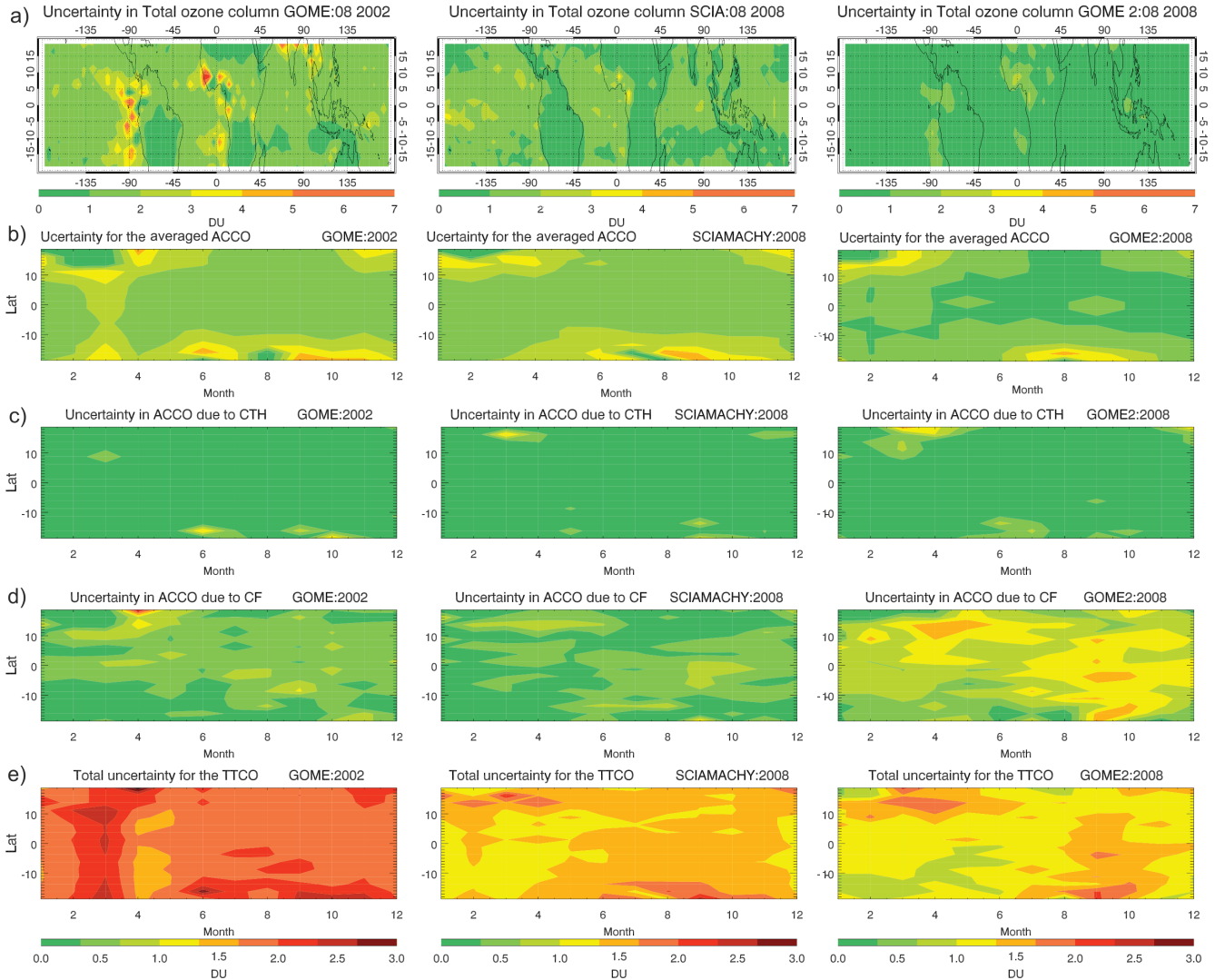


Figure 3.5: a) The uncertainty in the WFDOS TCO retrieval in August 2002 using GOME, and in August 2008 using SCIAMACHY and GOME-2 data b) the uncertainty of monthly averaged zonal ACCO for 2002 using GOME data and 2008 using SCIAMACHY and GOME-2 c) the uncertainty in the monthly averaged zonal ACCO due to CF for the same years as before d) the uncertainty in the monthly averaged zonal ACCO due to CTH for the same years as before e) the total uncertainty in the TTCO using the CCD method on GOME WFDOS total ozone data in 2002 and SCIAMACHY and GOME-2 WFDOS total ozone data in 2008.

The uncertainty in the cloud top height,  $u_{CTH}$  is about  $\pm 500$  m [Lelli, 2013]. Monthly ACCO values for cloud top heights greater than  $CTH - 0.5$  km and  $CTH + 0.5$  km were calculated for each instrument. Eq. 3.7 gives the mathematical formula for the uncertainty in ACCO for  $\pm 500$  m cloud top height change:

$$u_{ACCO_{CTH}} = \frac{|ACCO_{CTH+0.5} - ACCO_{CTH-0.5}|}{2} \quad (3.7)$$

Fig. 3.5c shows the ACCO uncertainty for a cloud top height perturbation of  $\pm 500$  m. This uncertainty is generally less than 0.5 DU for all instruments.

The uncertainty in cloud fraction, is  $u_{CF} \pm 0.1$  [Valks et al., 2011]. Monthly ACCO values for cloud fractions greater than 0.7 and greater than 0.9 were calculated and uncertainty in the ACCO due to cloud fraction is then:

$$u_{ACCO_{CF}} = \frac{|ACCO_{CF>0.7} - ACCO_{CF>0.9}|}{2} \quad (3.8)$$

As seen in Figure 3.5d, the uncertainty in ACCO as a function of latitude and month, for a cloud fraction perturbation of 0.1 is less than 1 DU for GOME and SCIAMACHY and less than 1.5 DU for GOME-2. This factor contributes the most to the total TCO uncertainty. The ACCO uncertainty due to cloud fraction ( $u_{ACCO_{CF}}$ ), cloud top height ( $u_{ACCO_{CTH}}$ ), is combined with the uncertainty from averaging in a grid box to yield the total ACCO uncertainty as follows.

$$u_{ACCO} = \sqrt{\frac{u_{ACCO_{retrieval}}^2}{N_{ACCO}} \left( \frac{1 + \phi_{ACCO}}{1 - \phi_{ACCO}} \right) + u_{ACCO_{CF}}^2 + u_{ACCO_{CTH}}^2} \quad (3.9)$$

Consequently, the total ACCO uncertainty is roughly 2 DU.

Finally, the combined standard uncertainty of the mean tropospheric ozone column ( $u_{TTCO}$ ) is then

$$u_{TTCO} = \sqrt{\frac{u_{TTCO_{retrieval}}^2}{N_{TTCO}} \left( \frac{1 + \phi_{TTCO}}{1 - \phi_{TTCO}} \right) + \frac{u_{ACCO_{retrieval}}^2}{N_{ACCO}} \left( \frac{1 + \phi_{ACCO}}{1 - \phi_{ACCO}} \right) + u_{ACCO_{CF}}^2 + u_{ACCO_{CTH}}^2} \quad (3.10)$$

The total uncertainty of TCO is found to be less than 3 DU (<10%) with GOME showing the greatest values. As shown in Figure 3.5e), for all instruments, larger uncertainties are found in spring and autumn for both years (2002 and 2008) presented.

An additional source of uncertainty in the ACCO retrieval could be the cloud optical thickness (COT) which can either increase or decrease the overlying ozone amount [Jana, 2012]. Unfortunately, WFDOAS dataset does not provide the COT information (values and uncertainties), since it could only be available for the case of SCIAMACHY using SACURA cloud algorithm. Sensitivity tests on synthetic data using a radiative transfer model could be performed instead in the future in order to quantify the effect of different COT in the ACCO retrieval.

### 3.3 Validation with ozonesondes \*

The accuracy of the CCD-IUP algorithm was investigated by comparisons with collocated ozonesonde measurements of tropospheric ozone columns. The ozonesonde data were taken from the Southern Hemisphere ADDitional OZonesondes (SHADOZ) network (Thompson et al., 2003). The closest gridbox that the ozonesonde station belongs was selected for the comparison. Using a fixed gridbox around the sonde station where we could apply the CCD method was also investigated but it was concluded that the statistics do not change significantly. The ozonesonde sites shown here (Fig. 3.6- 3.8), starting from North to South, are: (a) Hilo (19.4°N, 155.4°W), (b) Paramaribo (5.8°N, 55.2°W), (c) Kuala Lumpur

\*This section has been previously published as part of Leventidou et al. [2016]

(2.7°S, 101.7°E), (d) Nairobi (1.4°S, 36.8°E), (e) Natal (5.4°S, 35.4°W), (f) Java (7.6°S, 111°E), (g) Ascension (8°S, 14.4°W), (h) Samoa (14.4°S, 170.6°W), and (i) Fiji (18.1°S, 178.4°E). The time-periods of 1996-2002 for GOME, 2003-2007 for SCIAMACHY and 2008-2012 for GOME-2 were selected for validation. For most stations, the ozonesonde measurements start in 1998 and the launches vary from one to several per month (< 5). The ozone profiles were integrated until 200 hpa and the monthly mean and  $1\sigma$  standard deviation was calculated. No error bars are shown for stations with only one launch per month. Ozonesondes provide measurements along the track of the sonde, whereas tropospheric ozone from CCD covers a larger area (grid box of 2.5° by 5°). Tropospheric ozone can change from 30 to 70 ppbv within a convective cell system [Avery et al., 2010]. Considering these points and the fact that ozonesonde measurements are rather sparse in time, the comparison of monthly averaged tropospheric ozone from CCD with monthly averaged tropospheric ozone from ozonesondes has some limitations.

Table 3.1 lists the mean GOME (1996-2003), SCIAMACHY (2003-2012), and GOME-2 (2007-2015) TTCOs as well as tropospheric ozone columns from ozonesondes at the stations mentioned above. Also presented here are the relative differences between CCD and ozonesonde, the mean bias (the difference between CCD and ozonesondes), the Root Mean Square (RMS) deviation (the standard deviation of the differences between CCD and ozonesondes), and the correlation coefficient (R) between the CCD and ozonesonde time-series. The comparison for all these ozonesonde stations shows that the bias is less than 6.4 DU, the mean relative differences range between -8 and 28 %, the RMS is between 3.5 and 13 DU, and the correlation coefficient R ranges between 0.2 and 0.8. Comparing the CCD results for each instrument with ozonesondes, SCIAMACHY TTCO were found to have the smallest relative differences (0–9%) and RMS (3.5–7.9 (Hilo) DU) with the ozonesondes. The correlation is strong ( $R > 0.6$ ) at four over nine stations used for the comparison. GOME CCD results on the other hand, have generally small biases with the ozonesondes (< 3 DU) with the exception of Hilo, where the bias is 5.4 DU. The RMS differences are less than 7.2 DU (with the exception of Hilo, where the RMS is up to 11.1 DU) and the correlation is strong only at two over nine stations used for the comparison with ozonesondes. GOME-2 CCD results compared with the nine ozonesonde stations show a persistent positive bias (2.5–6.4 DU) with relative differences between 10 and 28%. The RMS differences are greater (5.8–13 (Hilo) DU) among the three instruments, and the correlation is strong at four stations.

Figures 3.6- 3.8 present the tropospheric ozone timeseries from the CCD method (1996-2003 for GOME, 2003-2012 for SCIAMACHY and 2007-2015 for GOME-2) plotted with collocated ozonesondes measurements (until 200 hPa) for the aforementioned stations. In more detail, Fig. 3.8a shows the comparison of tropospheric ozone column with ozonesondes in Ascension island which is located in the South Atlantic. The mean tropospheric ozone columns are the highest among all the stations (~32 DU). The seasonal cycle is strong, with maximum in autumn (biomass burning season) and minimum in late spring, when the ITCZ passes over the island and the wet season begins. Similar seasonal patterns with slightly smaller mean values (~30 DU) can be seen in Natal (Fig. 3.7b), which is located 3400 km Northwest of Ascension. The same seasonal pattern is noticed in Paramaribo (Fig. 3.6b), showing a distinct seasonal cycle (minimum at spring- maximum at autumn) but with even smaller mean tropospheric ozone values (~ 24 DU). The correlation with ozonesondes in these three stations is highest ( $R= 0.4-0.8$ ), mainly due to the fact that they have a distinct seasonal cycle. On the other hand,

Table 3.1: Statistical comparison between GOME, SCIAMACHY, and GOME-2 TTCOs with ozonesondes for nine SHADOZ sites. Information presented here are the ozonesonde site, the mean TTCO for GOME/SCIAMACHY and for ozonesondes, the relative difference, the bias and the RMS difference between CCD-IUP TTCO and sondes and finally the correlation coefficient.

Site (1996-2003)	GOME TTCO (DU)	SONDES TTCO (DU)	Relative difference	BIAS (DU)	RMS (DU)	R
Hilo (19.4N,155.4W)	31.2	25.8	19%	5.4	11.1	0.5
Paramaribo (5.8N,55.2W)	23.2	23.5	-1%	-0.2	5.8	0.2
Kuala Lumpur (2.7N,101.7E)	19.3	19.5	-1%	-0.2	4.1	0.3
Nairobi (1.3S,36.8E)	24.4	22.3	9%	2.1	4.1	0.6
Natal (5.4S,35.4W)	29.7	26.7	11%	3.0	5.6	0.7
Java (7.6S,111E)	21.0	19.2	9%	1.9	4.7	0.3
Ascension (8S,14.4W)	31.3	31.3	0%	-0.0	6.3	0.4
Samoa (14.4S,170.6W)	17.5	16.0	9%	1.5	5.8	0.2
Fiji (18.1S,178.4E)	20.2	18.3	10%	1.9	7.2	0.3
Site (2003-2012)	SCIAMACHY TTCO (DU)	SONDES TTCO (DU)	Relative difference	BIAS (DU)	RMS (DU)	R
Hilo (19.4N,155.4W)	27.0	26.9	0%	0.1	7.9	0.6
Paramaribo (5.8N,55.2W)	19.3	21.0	-8%	-1.6	4.0	0.3
Kuala Lumpur (2.7N,101.7E)	19.4	21.0	8 %	-1.6	3.8	0.3
Nairobi (1.3S,36.8E)	24.4	22.3	9%	2.1	3.5	0.6
Natal (5.4S,35.4W)	27.7	27.5	1%	0.2	4.5	0.8
Java (7.6S,111E)	19.6	20.6	-5%	-1.0	4.1	0.5
Ascension (8S,14.4W)	30.8	31.2	-2%	-0.5	4.5	0.7
Samoa (14.4S,170.6W)	15.2	16.5	-8%	-1.3	4.9	0.5
Fiji (18.1S,178.4E)	18.5	17.5	5%	0.9	5.2	0.4
Site (2007-2015)	GOME-2 TTCO (DU)	SONDES TTCO (DU)	Relative difference	BIAS (DU)	RMS (DU)	R
Hilo (19.4N,155.4W)	33.9	28.2	18%	5.7	13.0	0.6
Paramaribo (5.8N,55.2W)	25.6	23.1	10%	2.5	6.2	0.5
Kuala Lumpur (2.7N,101.7E)	24.8	21.9	12%	2.9	5.8	0.3
Nairobi (1.3S,36.8E)	28.9	22.5	25%	6.4	6.9	0.6
Natal (5.4S,35.4W)	34.4	28.4	19%	6.0	7.2	0.8
Java (7.6S,111E)	25.5	21.0	19%	4.5	5.9	0.5
Ascension (8S,14.4W)	36.4	31.4	15%	5.0	6.2	0.7
Samoa (14.4S,170.6W)	23.7	17.9	28%	5.8	6.8	0.5
Fiji (18.1S,178.4E)	25.3	19.9	24%	5.4	8.4	0.4

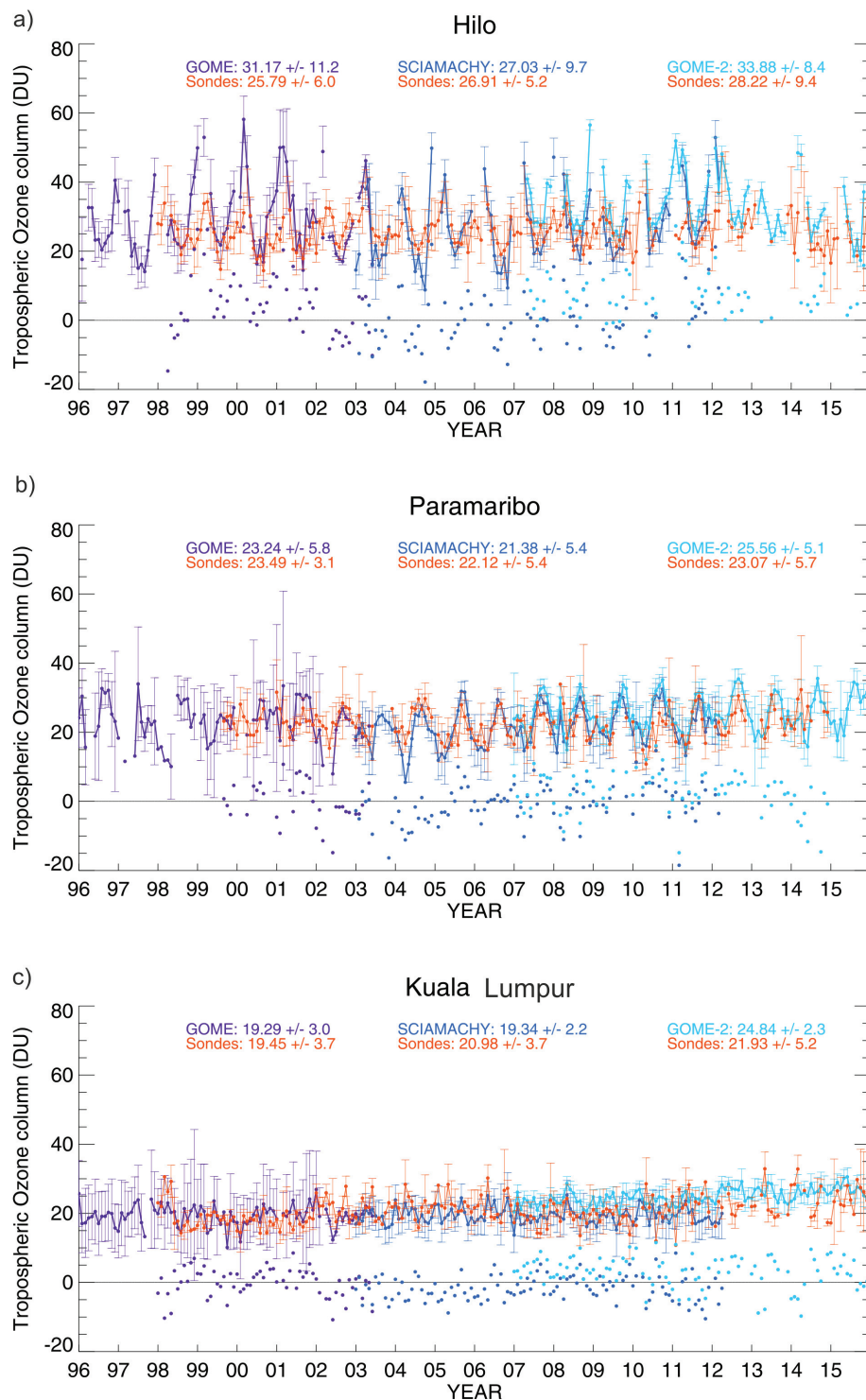


Figure 3.6: Time series of monthly mean CCD tropospheric ozone columns and collocated monthly mean SHADOZ ozonesonde TTCO in Hilo, Paramaribo, and Kuala Lumpur (from top to bottom). The red lines give the integrated ozone column from sonde ozone up to the fixed level of 200 hPa (roughly 12 km). The blue tinted lines are: (a) GOME-1 CCD ozone columns (1996-2003), (b) SCIAMACHY CCD ozone columns (2003-2012), and (c) GOME-2 CCD ozone columns (2007-2015). Error bars indicate the  $1\sigma$  uncertainty of the monthly mean. No error bars are shown for months with only one ozonesonde launch available. The average TTCO for each instrument and sondes with the standard deviation of the mean is shown on top of each plot. The difference between CCD and ozonesondes is plotted in the bottom.

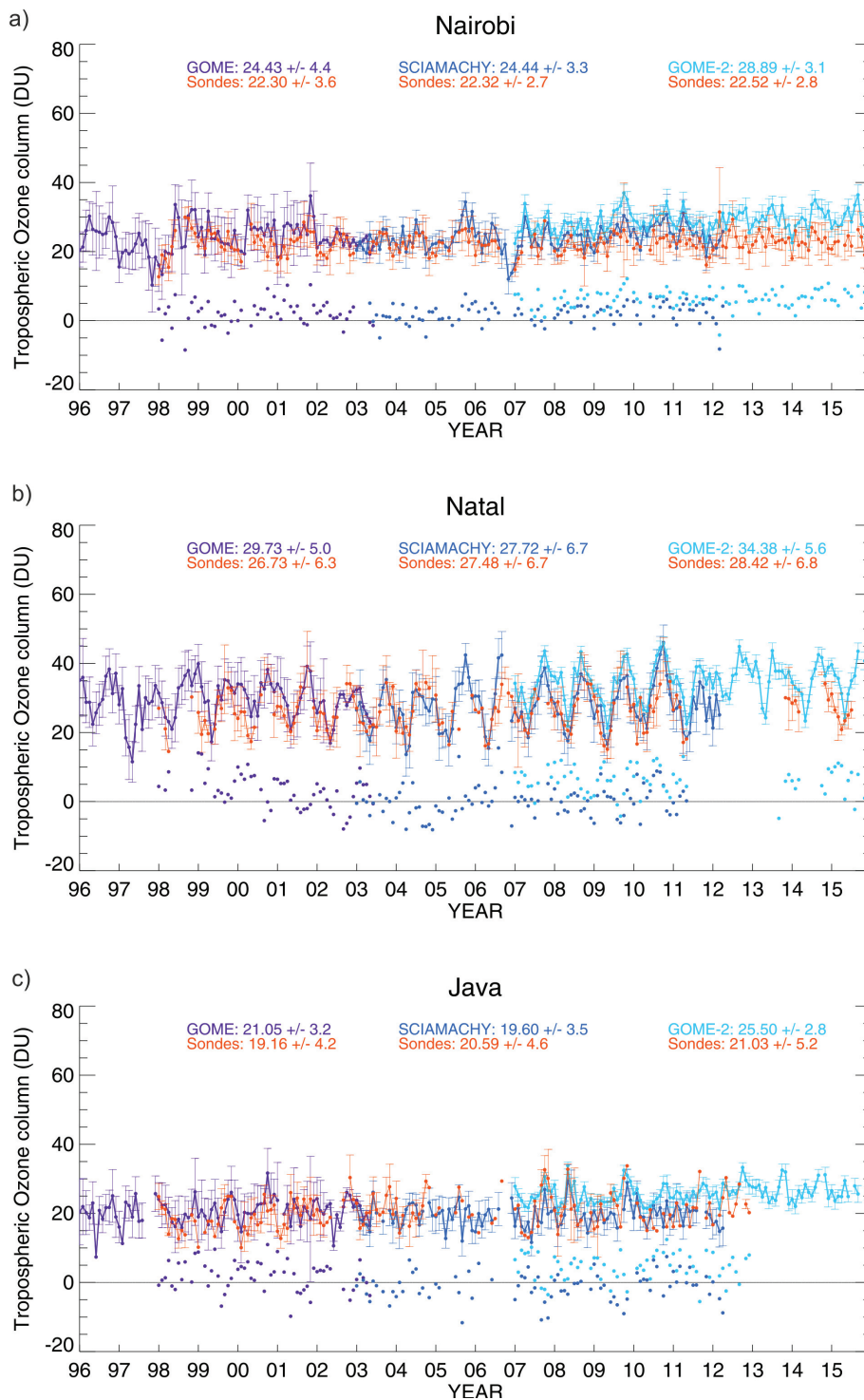


Figure 3.7: Time series of monthly mean CCD tropospheric ozone columns and collocated monthly mean SHADOZ ozonesonde TTCO in Nairobi, Natal, and Java (from top to bottom). The red lines give the integrated ozone column from sonde ozone up to the fixed level of 200 hPa (roughly 12 km). The blue tinted lines are: (a) GOME-1 CCD ozone columns (1996-2003), (b) SCIAMACHY CCD ozone columns (2003-2012), and (c) GOME-2 CCD ozone columns (2007-2015). Error bars indicate the  $1\sigma$  uncertainty of the monthly mean. No error bars are shown for months with only one ozonesonde launch available. The average TTCO for each instrument and sonde with the standard deviation of the mean is shown on top of each plot. The difference between CCD and ozonesondes is plotted in the bottom.

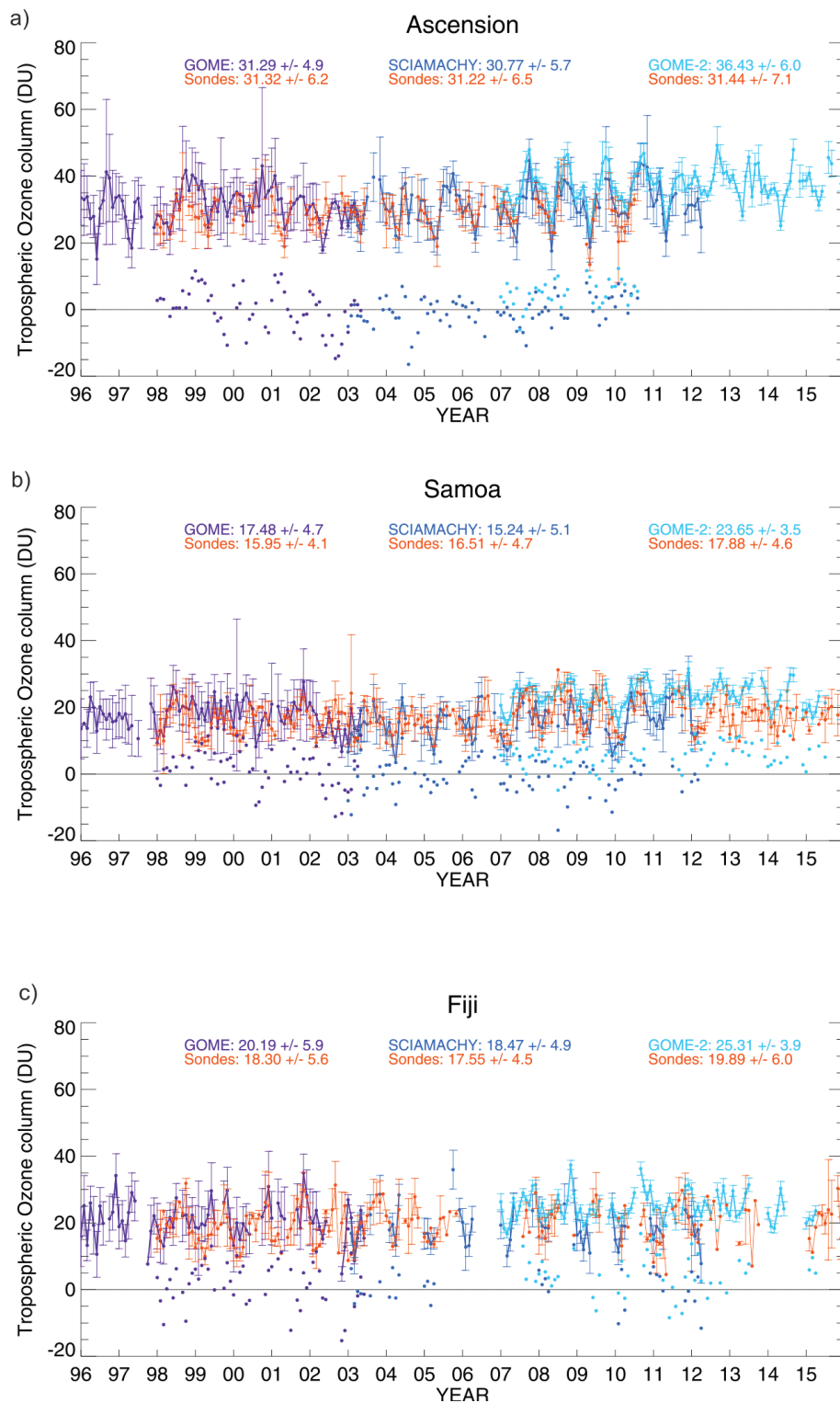


Figure 3.8: Time series of monthly mean CCD tropospheric ozone columns and collocated monthly mean SHADOZ ozonesonde TTCO in Ascension, Samoa, and Fiji (from top to bottom). The red lines give the integrated ozone column from sonde ozone up to the fixed level of 200 hPa (roughly 12 km). The blue tinted lines are: (a) GOME-1 CCD ozone columns (1996-2003), (b) SCIAMACHY CCD ozone columns (2003-2012), and (c) GOME-2 CCD ozone columns (2007-2015). Error bars indicate the  $1\sigma$  uncertainty of the monthly mean. No error bars are shown for months with only one ozonesonde launch available. The average TTCO for each instrument and sondes with the standard deviation of the mean is shown on top of each plot. The difference between CCD and ozonesondes is plotted in the bottom.

Nairobi station (Fig. 3.7a), (central east Africa) shows even lower mean tropospheric ozone abundance ( $\sim 25$  DU) and very small seasonal variations. The reduced seasonal cycle can be explained by the location of Nairobi

The CCD timeseries for the Indian Ocean stations such as Kuala Lumpur and Java (Fig. 3.6c and 3.7c), show very low mean tropospheric ozone values ( $\sim 20$  DU). In the western Pacific, the sea surface temperature is highest favouring strong convective activity which can lead to ozone loss from convective outflow and photochemical reactions [Morris et al., 2010]. Additionally, the  $\text{HO}_x$  are minimum (below  $10^8$  molecules $\cdot\text{cm}^{-3}$ ) due to denoxification (conversion of  $\text{NO}_x$  into  $\text{HNO}_3$  inside the clouds observed in the Pacific region). These ozone precursor levels are too low to effectively produce ozone [Rex et al., 2014]. The ozone abundance gets even lower ( $< 10$  DU) during summer (particularly in the case of SCIAMACHY and GOME retrievals) when the monsoon season is active and the ITCZ moves northwards. The South East Trade winds of the Southern Hemisphere crossing the equator are deflected eastwards in the Northern Hemisphere due to the Coriolis effect, yielding into the C-shape monsoon winds blowing from the South-West direction in the lower troposphere [Loschnigg and Webster, 2000, Yonemura et al., 2002]. As a result, clean ozone air reaches the Indonesian-Malaysian Peninsula. The opposite circulation takes place in winter, where the gradient is turning from South to North bringing polluted continental air to both sites. Additionally, ozone peaks can be seen at Java station (Waturkosek) during the pre-midwinter months of 1997, 2002, 2004, 2006 and 2009 (October-January) due to El Niño conditions [Ziemke et al., 2010]. El Niño is linked to changes in the convection pattern (less clouds over Indonesian region) and increase of biomass burning [Valks et al., 2014]. Generally, the correlation with the Indian ocean stations is weak ( $0.3 < R < 0.5$ ) since tropospheric ozone is low, the seasonal cycle is weak or even non existent while the bias ( $< 4.5$  DU) and the RMS are small ( $< 5.9$  DU) indicating that the CCD TCO can be considered as having acceptable agreement with the ozonesondes.

At the Pacific Ocean site of Hilo (Fig. 3.6a) tropospheric ozone is among the highest ( $\sim 29$  DU). Hilo is located in the northern tropics, at a location where the jet stream passes during winter months. Consequently, Hilo is influenced by stratospheric intrusions via tropopause foldings. Additionally, a large anticyclone located over the Pacific sends air from Asia towards North America during winter and spring [Oltmans et al., 2004]. However, the movement of the ITCZ at southern latitudes in boreal winter months causes less clouds over that region and as a result not sufficient data to retrieve ACCO and consequently TCOs. The opposite picture can be noticed in Fiji (Fig. 3.8c) where higher ozone columns appear during boreal summer months. Both stations are located near the southern and northern boundary of the tropical region. As a result, the ACCO measurements are considered to be statistically doubtful and no TCO is retrieved in these cases. Finally, Fig. 3.8b presents the tropospheric ozone at Samoa island which ranges around 21 DU with slightly higher values in autumn. The comparison of CCD results and ozonesondes at Samoa shows that CCD strongly overestimates the retrieved tropospheric ozone for GOME-2 (relative difference=28%).

### 3.4 Comparison with Limb/Nadir Matching tropospheric ozone columns\*

Tropospheric ozone columns from Limb/Nadir Matching (LNM) observations of SCIAMACHY are available [Ebojie et al., 2014]. The monthly mean tropospheric ozone columns retrieved with the LNM technique have in general errors of less than 6 DU, and the comparison with collocated and integrated ozonesonde profiles up to the tropopause shows agreement within 2–5 DU and mean relative differences of 6–25% in the tropics. [Ebojie et al., 2014]. The comparison with other satellite instruments such as TES and OMI/MLS generally shows similar features, nevertheless, there are obvious differences in regional patterns mainly due to instrumental differences, differences in the vertical resolutions, and overpass times. In order to make the comparison between the tropospheric ozone columns from CCD-IUP and LNM more realistic, the CCD data have been gridded with the same  $2.5^{\circ} \times 5^{\circ}$  grid and the ozone amount between the tropopause and 200 hPa has been subtracted from the LNM ozone columns using the Fortuin and Kelder [1998] climatology.

Figure 3.9 shows the TTCOs from CCD (top) and LNM (middle) from SCIAMACHY in August 2008. Higher ozone columns are located over the central Atlantic Ocean while the lowest is over the Pacific Ocean. However, LNM tropospheric ozone data are sparse between  $70^{\circ}\text{E}$ - $160^{\circ}\text{E}$  and over southern central America. It is also apparent that the LNM tropospheric ozone columns appear somewhat noisier with elevated ozone columns (40 DU) appearing e.g. over the Pacific Ocean where the neighbouring grid-boxes are around 15 DU.

Figure 3.10 presents the comparison between CCD-IUP and LNM tropical tropospheric ozone columns for the years 2003-2011. Fig. 3.10a shows the mean tropospheric ozone column bias (CCD minus LNM TTCO) ranging between  $\pm 5$  DU with the exception of South-east America and central Africa where it reaches 10 DU. The bias is mainly positive over land and negative at the borders of the tropical belt, the central Pacific and Atlantic Ocean. The RMS (Fig. 3.10b) is generally less than 10 DU which is within the range of the comparison of CCD-IUP with the ozonesondes. The mean absolute bias is less than 3 DU and the mean absolute relative difference is  $\sim 12\%$ . Finally, the correlation (Fig. 3.10c) is moderate to low with exception of the areas that present high ozone columns. There are also some anti-correlated grid-boxes which are located in areas where LNM data are usually sparse (e.g. western Pacific ocean). The bias between LNM and CCD-IUP tropospheric ozone could be partly explained by the overestimation of limb V2.9 ozone profiles used for LNM. Comparison with ozonesondes in the tropics show a positive bias of 5 to 10 DU [Jia et al., 2015]. The position of positive and negative biases seem to agree well with the ones for the limb profiles. For the newest limb version 3.0, the seasonal variations in the time series are in better agreement with those from sonde data at most tropical stations [Jia et al., 2015]. Limb V3.0 is planned to be used in the newest LNM tropospheric ozone dataset and an improvement in the agreement between the two methods is expected. However, due to the different sampling of both methods for the total and the stratospheric  $\text{O}_3$  column, there will still be expected differences, despite the fact that the same instrument (SCIAMACHY) is used.

---

\*This section has been previously published as part of Leventidou et al. [2016]

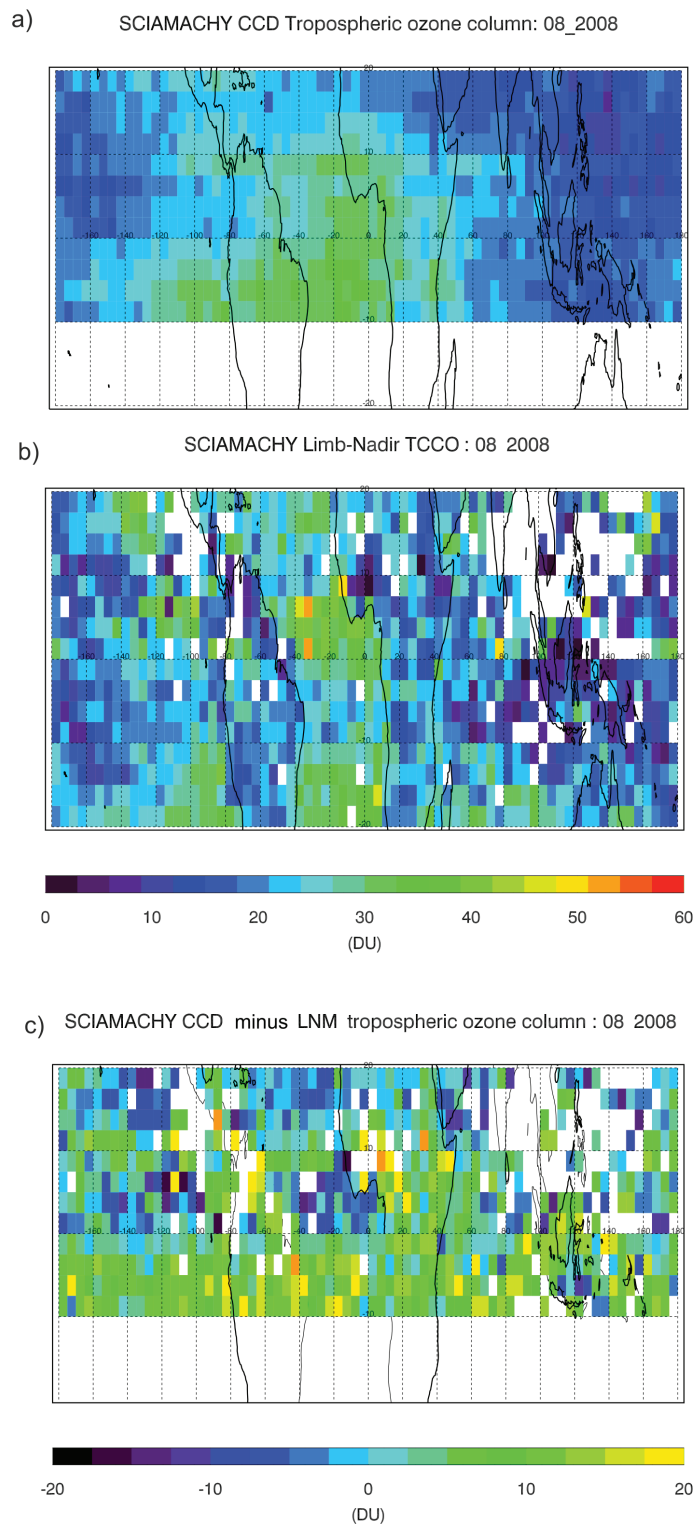


Figure 3.9: a) Tropical tropospheric ozone column from CCD-IUP SCIAMACHY for August 2008. b) SCIAMACHY tropical tropospheric ozone column from Limb/Nadir matching technique up to 200 hPa for August 2008. c) Difference between CCD-IUP and LNM SCIAMACHY data in August 2008.

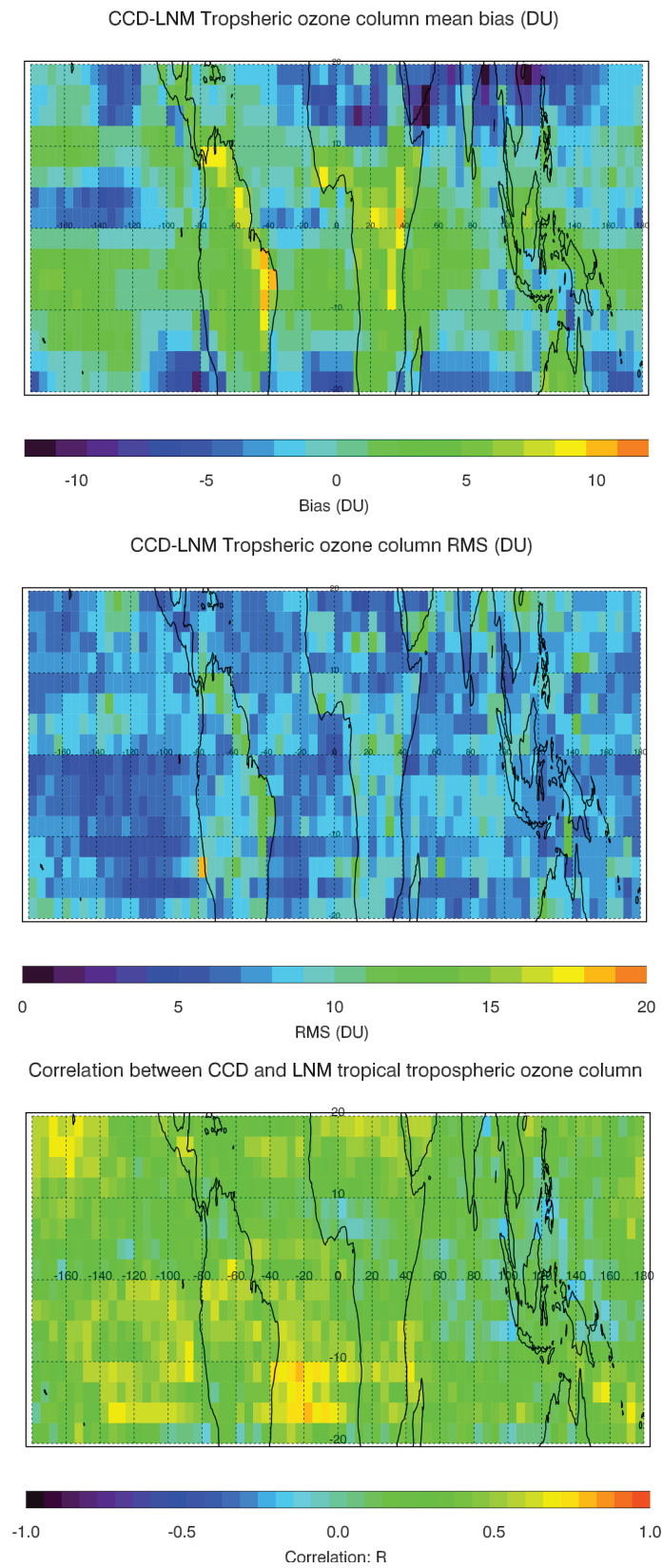


Figure 3.10: a) Mean bias between CCD and LNM for the years 2003 until 2011. b) Correlation (R) between CCD and LNM SCIAMACHY tropospheric ozone for the years 2003 until 2011.

### 3.5 Summary and discussion

Monthly averaged tropospheric ozone columns have been calculated on a  $2.5^\circ$  latitude by  $5^\circ$  longitude grid between  $20^\circ\text{S}$  and  $20^\circ\text{N}$  by applying the CCD method to GOME/ERS-2, SCIAMACHY/ENVISAT and GOME-2/MetopA data covering the period 1996 to 2015. The uncertainty budget of the retrieved tropical tropospheric ozone columns has been estimated here for the first time. The total uncertainty of retrieved TCO is found to be in the order of 3 DU ( $<10\%$ ), with GOME TCO showing the greatest uncertainties. The comparison with nine SHADOZ ozonesonde sites shows average biases less than 6.4 DU, mean relative differences between -8 and 28%, and RMS between 3.5 and 13 DU. Only for the case of GOME-2 TCO the biases are greater than the retrieval uncertainty. The comparison with limb-nadir-matching observations from SCIAMACHY show good agreement (mean absolute bias  $< 5$  DU and the mean absolute relative difference  $\sim 12\%$ ). Further optimization of the WFOAS data (use of the same algorithm for cloud properties for all satellite data) and extension of the CCD algorithm to GOME-2/MetopB and TROPOMI/S5p data is necessary in order to improve the consistency between satellite datasets for long-term trend and variability studies. The TCO time-series with the CCD method can be further continued with the future Sentinel-5 mission (launch 2020) and Sentinel-4 (launch 2025) [Veihelmann et al., 2015]. Sentinel-4 will be able to provide hourly data of ozone from a geostationary orbit, which will allow a modified CCD method to be applied in mid-latitudes and in a daily basis assuming then that stratospheric ozone column remains invariant during a day. The individual tropospheric ozone time series can be harmonised and merged into one consistent long-term dataset in order to be used in climatological and tropospheric ozone trend studies (see: Section 4.1). This unique 20 year tropical tropospheric ozone dataset provides valuable information about the tropospheric ozone distribution and variability as discussed in Chapter 5.



## Tropical tropospheric ozone trends

In this chapter the multi-instrument (GOME, SCIAMACHY, and GOME-2) CCD tropical tropospheric ozone column datasets are harmonised into one merged time-series which is then used to derive long-term trends from. The datasets need to be harmonised in order to remove the biases between the instruments and therefore correction offsets are calculated using SCIAMACHY TTCOs as reference. Six different scenarios are tested in order to find the most appropriate approach to harmonise and merge the individual TTCO datasets. The various possible harmonisation scenarios may have strong impact on the derived tropospheric ozone trends and add to the uncertainties in the retrieved trends beyond the statistics of a multiple linear regression (MLR). Long term TTCO trends are calculated by fitting all natural processes (seasonal cycle, ENSO, QBO, and the solar cycle) that contribute to its variability in a multi-linear regression model. The trend results for the preferred harmonised dataset are discussed in detail and compared with trends from ozonesonde profiles. Regional trends and trends over ten tropical mega cities are presented and compared with results from other studies.

### 4.1 Harmonisation and merging of the multiple instrument TTCO data record

As described in Chapter 3, the tropical tropospheric O<sub>3</sub> data have been retrieved with the CCD method using total ozone and cloud data from three different satellite sensors, GOME, SCIAMACHY and GOME-2 from 1996 to 2015. These instruments have different properties such as spatial resolution, cloud algorithms, overpass time, etc. The individual TTCO datasets have been created taking into account these specific characteristics and have been separately validated with integrated (until 200 hPa) tropospheric ozone columns by ozonesondes from the SHADOZ network [Thompson et al., 2003] (see Section 3.3). The biases between them have been found to be within -1.6 – 6.4 DU and the root mean square (RMS) deviation less than 13 DU for all the instruments. The uncertainty of the tropospheric ozone column retrieval with the CCD method is on the order of 3 DU (~ 10%). For most of the stations, the bias of with the ozonesondes is within the retrieval uncertainty, with the exception of GOME-2 TTCO which is on the order of 5 DU. Finally, the CCD TTCO from SCIAMACHY data have been compared with the Limb-Nadir-Matching (LNM) tropospheric O<sub>3</sub> columns up to 200 hPa altitude from the same

satellite instrument, showing that the bias and the RMS values are within the ones calculated for the comparison with ozonesondes.

In order to remove the biases between the instruments and create one consistent tropical tropospheric columns dataset from the CCD method for the whole timespan of the European satellites operation (1996–2015), correction offsets have been calculated. SCIAMACHY TCO were used as reference for the correction offset calculation, since it is the only instrument that overlaps (2002–2012) both with GOME and GOME-2 and has the smallest bias with respect to the ozonesondes ( $< 2$  DU). The average difference (bias) for each grid-box during the common years of the instruments operation (2002 and the first half of 2003 for SCIAMACHY–GOME and 2007–2012 for SCIAMACHY–GOME-2) was computed and was applied (added) to GOME and GOME-2 TCO data. The mean biases, shown in Fig. 4.1, range between  $-6$  and  $6$  DU for GOME, with positive differences ( $3$ – $6$  DU) located mainly over land. There are also two stripes with positive biases appearing north of  $7.5^\circ\text{N}$  until  $20^\circ\text{N}$ , and between  $-5$  and  $-7.5^\circ\text{S}$ . For GOME-2, the bias ranges between  $-8$  and  $0$  DU, with differences getting smaller over land, especially over south America and north/central Africa. Possible reasons for the biases are the different cloud algorithms used for each instrument (SACURA for SCIAMACHY and FRESCO for GOME and GOME-2) and the small biases noticed in the total ozone columns (e.g.  $\sim -2.5$  DU between SCIAMACHY and GOME-2). In addition to correction offsets, correction factors have been calculated using the mean ratio of SCIAMACHY to GOME and SCIAMACHY to GOME-2 TCO (see Fig. A1). The correction factors have similar pattern as the offsets. Since correction offsets are most commonly used in literature, they have been preferred in order to homogenise the data record.

The latitudinal dependence of the mean bias is shown at the bottom of Fig. 4.1. The average differences between GOME and GOME-2 with SCIAMACHY are generally negative (less than  $5$  DU) in all latitude bands with the exception of the northern tropical latitudes where GOME mean biases are positive ( $0$ – $2$  DU). GOME mean biases have stronger latitudinal variability than the GOME-2 mean biases. This behaviour may be explained by the short time of common operation (Jan. 2002–Jun 2003) between GOME and SCIAMACHY instruments. The  $1\sigma$  standard deviation (uncertainty bars) of the mean bias per latitude band is comparable to the magnitude of the biases, ranging from less than  $5$  DU close to the equator to  $7$  DU for latitude bands close to the tropical borders. For the case of GOME, the mean correction offset is  $-1.2$  DU, whereas for GOME-2 it is  $-5.7$  DU. The mean offset of GOME-2 is almost double as the CCD retrieval uncertainty ( $\sim 3$  DU). For this reason and because of the large biases with the ozonesonde data, it seems reasonable to apply a correction for the GOME-2 TCO dataset.

The drift on the average differences,  $\beta$ , has been estimated using a simple linear regression model such as:  $Y = \alpha + \beta \cdot X_t$ , where  $Y$  is the time-series of the biases,  $X_t$  is the time variable in months, and  $\alpha$  is the offset. The drift between SCIAMACHY and GOME-2 (there are not enough overlapping years to calculate a trend in the GOME-SCIAMACHY difference time-series) is shown in Fig. 4.2. The drift is generally less than  $\sim 0.4$  DU per year and is statistically not significant ( $\beta/\sigma_\beta < 2$ , see Section 4.2.2, Eq. 4.12) for nearly all grid boxes, with the exception of the  $17.5$ – $20^\circ\text{N}$  latitude band, where it is statistically significant and exceeds  $1$  DU/year. During local winter months at the tropical borders, there are often missing TCO data owing to the movement of the ITCZ and the inability to retrieve a reliable stratospheric  $\text{O}_3$  column (the number of data is shown in Fig. A2). For this reason, calculated drifts for these latitudes are not reliable despite the fact that they might appear to be statistically significant.

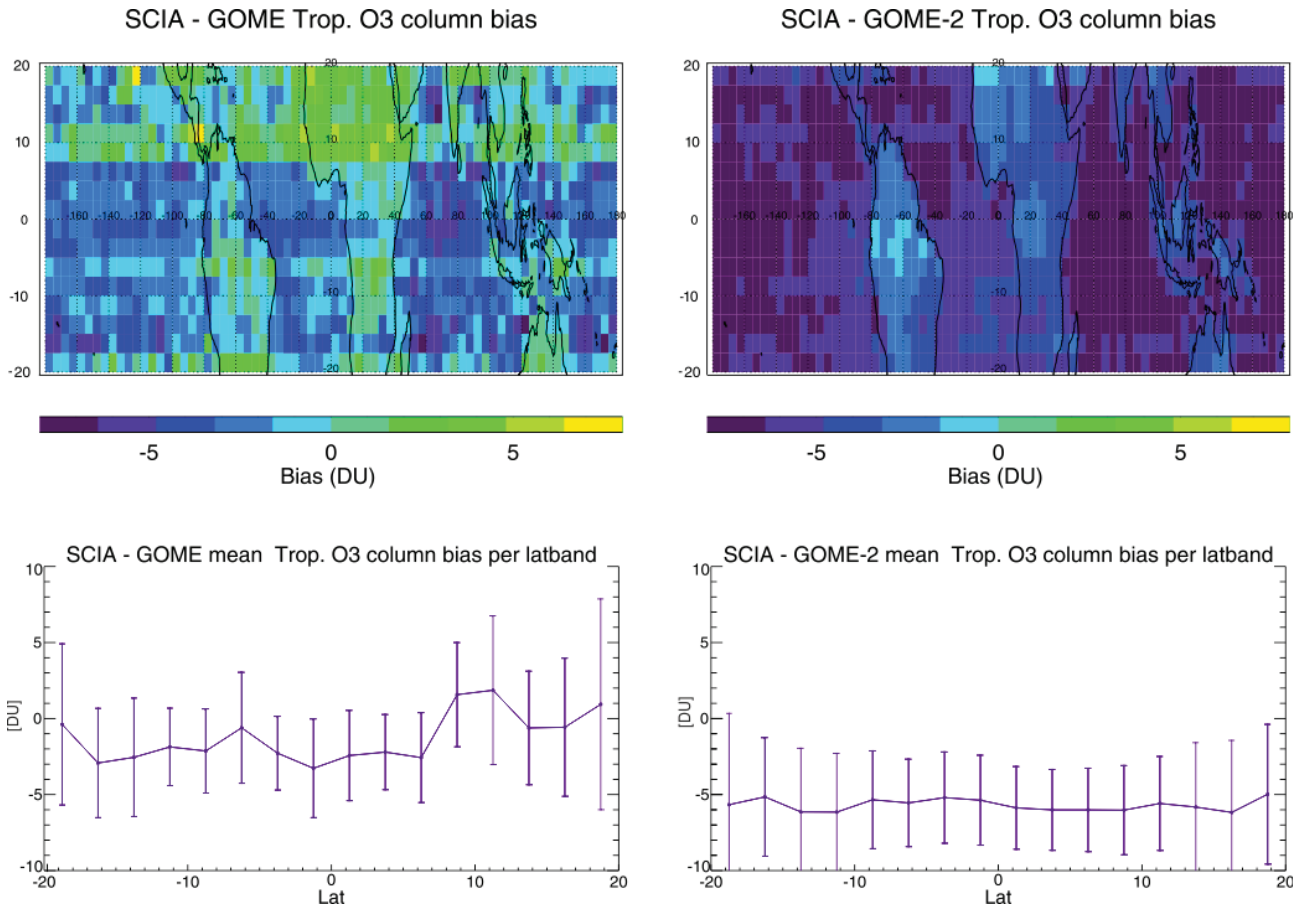


Figure 4.1: Correction offsets using SCIAMACHY TCO as reference. (left) Correction offset for GOME: average difference of GOME from SCIAMACHY TCO for the years 2002-2003. (right). Correction offset for GOME-2: average difference of GOME-2 from SCIAMACHY TCO (in DU) for the years 2007-2012. The error bars denote the  $1\sigma$  standard deviations of the latitudinally averaged biases.

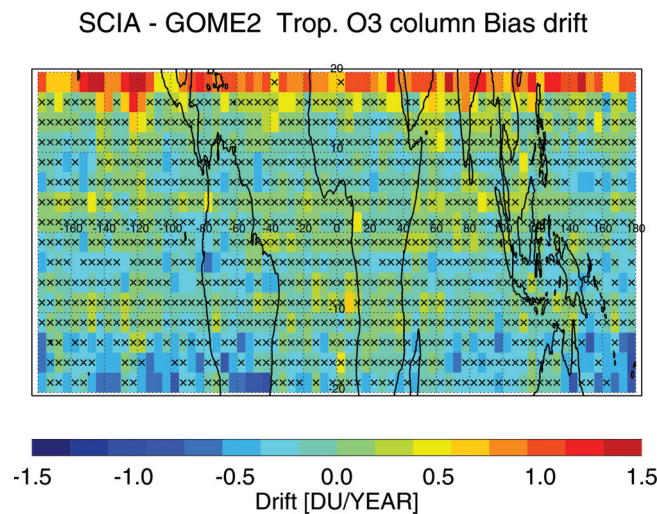


Figure 4.2: Trend in the correction offset for GOME-2. Black "x" denotes statistically non significant trend.

They do not cover the entire studied period (2007–2012) but only a subset of them.

The creation of a consistent tropical tropospheric ozone column dataset from multiple satellite instruments demands a careful selection of the appropriate harmonisation approach, since it introduces additional uncertainty in the merged dataset. For this purpose, six harmonisation scenarios have been tested all of them using the SCIAMACHY TCO dataset as a reference, which is in the middle of the time period, as follows:

- **Scenario 1:** No correction applied to GOME data (which could be justified by the very short overlap period), while GOME-2 is corrected using for each grid-box the mean bias with respect SCIAMACHY for the common years of operation (2007–2012 for GOME-2).
- **Scenario 2:** No correction applied to GOME data and the average bias (-5.7 DU) with respect SCIAMACHY is added to all GOME-2 TCO data.
- **Scenario 3:** GOME and GOME-2 have been corrected using for each grid-box the mean bias with respect to SCIAMACHY for the common years of operation.
- **Scenario 4:** The average bias with respect to SCIAMACHY (-1.2 DU) is added to all GOME TCO data, whereas GOME-2 TCO has been corrected using for each grid-box the mean bias with respect to SCIAMACHY for the common years of operation (2002 for GOME and 2007-2012 for GOME-2).
- **Scenario 5:** The average bias with respect to SCIAMACHY (-1.2 DU) for GOME and for GOME-2 (-5.7 DU) is added to all GOME and GOME-2 TCO data respectively.
- **Scenario 6:** No correction applied to GOME, whereas for GOME-2 both the bias and the drift is included in the correction of GOME-2 TCO in each grid-box.

After the correction terms for all scenarios have been applied to the original data, the "corrected" GOME (1996-2002) and GOME-2 (2007-2015) TCO were averaged with the ones from SCIAMACHY (2003-2012) for the overlapping months (Jan. 2002–Jun. 2003 and Jan. 2007–Dec. 2012, respectively).

In order to conclude which is the most suitable harmonisation scenario, the various merged datasets were compared with integrated ozone columns up to 200 hPa altitude from nine ozonesonde stations: (a) Ascension (8°S, 14.4°W), b) Paramaribo (5.8°N, 55.2°W), c) Java (7.6°S, 111°E), d) Natal (5.4°S, 35.4°W), e) Samoa (14.4°S, 170.6°W), f) Nairobi (1.4°S, 36.8°E), g) Kuala Lumpur (2.7°S, 101.7°E), h) Hilo (19.4°N, 155.4°W), and (i) Fiji (18.1°S, 178.4°E)). As seen in Table 4.1, the mean bias between the six harmonised TCO datasets and the ozonesondes range between -2.5 and 1.8 DU which is well within the retrieval uncertainty. However, the biases of each scenario with ozonesondes are very close to each other in every station. The same, occurs for the correlation between the harmonised TCO datasets and the ozonesondes (see: Fig. A3 and A4). Although the comparison between the TCO from the individual harmonised scenarios and the ozonesonde data does not clearly favor any harmonisation scenario, the scenarios that can be confidently rejected according to this comparison are scenarios 3, 4 and 5, which have the biggest bias with the ozonesondes. Scenario 6, presents smaller bias at four out

Table 4.1: Mean differences (in DU) between the harmonised TCO datasets using six different harmonisation scenarios with integrated ozone columns until 200 hPa from nine ozonesonde stations. Bold are marked the harmonisation scenarios that have the smallest biases with ozonesondes for a given station.

CCD – Sondes TCO [DU] /Site	scenario 1	scenario 2	scenario 3	scenario 4	scenario 5	scenario 6
Ascension (8S,14.4W)	<b>0.03</b>	-0.14	-0.77	-0.42	-0.60	<b>0.03</b>
Paramaribo (5.8N,55.2W)	<b>-1.21</b>	-2.28	-1.28	-1.44	-2.52	<b>-1.21</b>
Java (7.6S,111E)	<b>-0.11</b>	-0.12	-1.12	-0.54	-0.55	<b>-0.11</b>
Natal (5.4S,35.4W)	0.56	0.63	<b>-0.21</b>	0.22	0.28	0.57
Samoa (14.4S,170.6W)	-0.25	<b>0.09</b>	-1.35	-0.61	-0.23	-0.28
Nairobi (1.3S,36.8E)	1.81	1.10	1.80	1.48	<b>0.74</b>	1.84
Kuala Lumpur (2.7N,101.7E)	-1.81	-2.12	-2.12	-2.14	-2.48	<b>-1.78</b>
Hilo (19.4N,155.4W)	0.67	0.65	<b>0.17</b>	0.19	0.23	0.88
Fiji (18.1S,178.4E)	0.19	<b>-0.09</b>	-0.58	-0.21	-0.45	-0.55

of nine ozonesonde stations, whereas scenario 1, at three out of nine ozonesonde stations. Nevertheless, scenario 6, has larger biases with respect to ozonesondes compared to scenario 1 (with the exception of one station). As shown earlier, the drift in the GOME-2 data (scenario 6) is statistically insignificant at most of the grid-boxes and as will be shown later introduces artifacts in tropospheric trends. For these reasons, scenario 1 has been selected to be the preferred harmonisation scenario for merging the TCO datasets. All further results (without explicit indication of the harmonisation scenario used) presented here are based on harmonisation scenario 1.

## 4.2 Tropical tropospheric ozone trends

Long-term evolution of tropospheric ozone is complex and depends upon the evolution of precursor emissions and climate change. Quantifying tropospheric ozone trends is crucial for testing our understanding about the processes that can affect tropospheric ozone in the troposphere and attributing these ozone changes to changes in precursor emissions, removal processes and meteorology [Monks et al., 2015]. Various studies have been performed in urban and rural sites using in situ data in order to estimate tropospheric ozone trends in the tropics. Lelieveld et al. [2004] noticed an increase in surface ozone on the order of 0.4 ppb/year over the northeastern tropical Atlantic, and over the southeastern tropical Atlantic, with a smaller trend of 0.1 ppb/decade over the southwestern tropical Atlantic Ocean, based on ship-borne measurements (1977–2002). Oltmans et al. [2013] using surface and ozonesonde observations noticed a significant increase of 3.8 %/decade (0.16 ppb/year) in surface ozone in Mauna Loa, Hawaii (19.5°N) in 1974 and a smaller insignificant trend on the order of 0.7 %/decade (0.01 ppb/year) in American Samoa (14.5°S) after 1976. Lin et al. [2014] suggest that the increase of ozone in Mauna Loa is even bigger during autumn, in the order of 0.35 ppbv/year, due to the increase of air masses transport from east Asia. Cooper et al. [2014] found a significant increase of 0.19 ppb/year in the subtropical site of Cape Point in South Africa from 1983 to 2011. Additionally, Thompson et al. [2014], using ozonesonde data from the SHADOZ stations in Irene and Réunion noticed statistically

significant trends in the middle and upper troposphere of  $\sim 25$  %/decade (1 ppbv/year) and  $\sim 35 - 45$  %/decade (2 ppbv/year), respectively during winter months (June-August). Smaller positive trends appear in summer, close to the tropopause.

Satellite remote sensing is a very useful tool to perform trend analysis on a regional and global scale. Ziemke et al. [2005], using the Convective Cloud Differential (CCD) method on Total Ozone Mapping Spectrometer (TOMS) version 8 data from 1979 to 2003, found a statistically significant positive linear trend in the mid-latitudes but not in the tropics, where they report an insignificant decline. Beig and Singh [2007] using tropospheric ozone data retrieved with CCD from the Total Ozone Mapping Spectrometer (TOMS) between 1979 and 2005, found an increasing trend of 7 – 9 %/decade over some parts of south Asia, 4 – 6 %/decade over the Bay of Bengal, and 2 – 3 %/decade over the central Atlantic Ocean and central Africa. Kulkarni et al. [2010] using Tropospheric Ozone Residual (TOR) data from TOMS, SAGE and SBUV instruments, calculated statistically significant trends over three Indian mega-cities during 1979–2005. They showed that ozone increased by 3.4 %/decade in Delhi during the monsoon period, while it increased by 3.4 – 4.7 %/decade in Hyderabad and 5 – 7.8%/decade in Bangalore during the pre-monsoon and post-monsoon period, respectively. Ebojie et al. [2016] using the full record of SCIAMACHY limb-nadir matching data (2002–2011) retrieved regional and global tropospheric ozone trends. An insignificant positive trend in the order of 0.5 DU/decade was noticed for the northern tropics (0–20°N) and an even smaller trend of 0.3 DU/decade in the southern tropics (0–20°S). Regionally, they noticed statistically significant trends of -1.6 %/year over Northern South America (10 – 0°S, 75–45°W), 1.6 %/year in Southern Africa (15–5°S, 25–35°E), 1.9 %/year in Southeast Asia (15 – 35°N, 80 – 115°E), and a trend of 1.2 %/year over Northern Oceania (20 – 10°S, 100 – 130°E). Most recently, Heue et al. [2016] published a study about tropical tropospheric ozone trends using the CCD method on a harmonised dataset consisting of data retrieved from GOME, SCIAMACHY, GOME-2 and OMI satellite instruments from July 1995–December 2015. The mean tropical tropospheric ozone trend that they found is 0.7 DU/decade and regionally the trend reaches 1.8 DU/decade on the African Atlantic coast, and -0.8 DU/decade in the western Pacific.

The various study results for tropospheric ozone trends diverse significantly with each other, even while using the same dataset (e.g. the trends retrieved from Ziemke et al. [2005] and Beig and Singh [2007]). In this section, a statistical analysis of the long-term CCD tropical tropospheric ozone trends is performed along with a sensitivity study of how different harmonisation approaches may affect these trend results. Finally, regional trends and trends over mega-cities using one harmonisation approach are calculated and compared with previous studies.

#### 4.2.1 Overview on known contributions to tropospheric ozone changes

Changes in ozone precursor emissions due to urbanization and land use, along with changes in the atmospheric oscillations which affect processes that modulate the tropical upwelling or the horizontal ozone transport may cause long-term changes in the tropospheric ozone burden and influence the photochemical ozone production and loss in the troposphere Chandra et al. [2009], Monks et al. [2015], Neu et al. [2014], Solomon et al. [2007], Voulgarakis et al. [2010], WMO [2011], Ziemke and Chandra [2003]. Some of these factors can be represented by periodic seasonal proxies, such as the El Niño

Southern Oscillation (ENSO), the quasi-biennial oscillation (QBO) and the solar cycle (SC). These indexes are embodied in the trend model described in Section 4.2.2.

### El Niño Southern Oscillation (ENSO)

The El Niño Southern Oscillation (ENSO) is the characteristic signature of the atmosphere-Ocean coupling in the tropical Pacific region, dominating the inter-annual tropical climate variability [Chandra et al., 2009, Doherty et al., 2005, 2006, Randel et al., 2009, Vecchi et al., 2010]. Switching between warm (El Niño) and cold (La Niña) phase, ENSO causes significant disturbances to the Oceanic and atmospheric circulations, and the tropospheric temperature and moisture patterns. Under regular conditions, the atmospheric pressure at the western Pacific Ocean is lower than the eastern Pacific, since the Sea Surface Temperature (SST) in this region (Indonesian warm pool) is higher than in the eastern Pacific. The abnormal warm phase of ENSO (El Niño) is associated with enhanced sea surface temperatures and latent heat release to the atmosphere in the equatorial central and east Pacific. As a result, more cloudy conditions appear over the eastern Pacific Ocean leading to reduced tropospheric ozone burden over that region, whereas the increased dryness over the Indonesian region, enhancing the tropospheric ozone production [Chandra et al., 2009, Doherty et al., 2006, Oman et al., 2011, Ziemke and Chandra, 1999, 2003]. Due to the El Niño large scale circulation, the sub-tropical jet streams and the up-welling branch of the Brewer-Dobson (BD) circulation are strengthening, resulting in more ozone-poor air being transported from the troposphere to stratosphere. The stratospheric meridional transport of ozone is getting stronger in the middle latitudes and the polar vortex is getting weaker [Calvo et al., 2010, Garcia-Herrera et al., 2006, Preethi et al., 2015, Simpson et al., 2011]. Xie et al. [2014] suggested that due to the decrease in stratospheric column ozone during a certain kind of El Niño events, known as Modoki events, more UV radiation reaches the tropical troposphere, leading to significant increases in tropospheric ozone columns. Voulgarakis et al. [2010] showed that the global tropospheric ozone budget can increase due to enhanced stratosphere to troposphere exchange (STE) during El Niño events. Neu et al. [2014], showed that inter-annual variations in the STE ozone flux by 40% can cause changes of the order of 2% in tropospheric ozone in the northern mid-latitudes, which corresponds to around half of its inter-annual variability.

Several ENSO proxies are in use for climate studies, like the Southern Oscillation Index (SOI) [Wolter and Timlin, 1998], the Niño 3.4 SST Index [Gergis and Fowler, 2005] and the Ozone ENSO Index (OEI) [Ziemke et al., 2010] based on measurements of various quantities. In the present study, the Multivariate ENSO Index (MEI) is used, based on six main observed variables over the tropical Pacific such as, sea-level pressure, zonal and meridional components of the surface wind, sea surface temperature, surface air temperature, and cloud fraction of the sky [Wolter and Timlin, 1998]. The ENSO MEI Index integrates more information than other indices and represents better the coupling between Ocean and atmosphere [Wolter and Timlin, 2011]. The ENSO MEI Index data have been downloaded from the NOAA Earth System Research Laboratory (ESRL) web site (<http://www.esrl.noaa.gov/psd/enso/mei/>). The data are reported on a bimonthly basis with negative values representing the cold ENSO phase, (La Niña), while positive values the warm ENSO phase (El Niño).

### Quasi-biennial oscillation (QBO)

The equatorial stratosphere (16 – 50 km) exhibits periodic or quasi-biennial oscillating (QBO) cycles which are characterized by the alternation of nearly symmetric zonal layers of east and west winds with an average period of approximately 28 months [Baldwin et al., 2001]. They result from the vertical transport of momentum by certain types of equatorial and gravity waves [Plumb and McEwan, 1978]. Kelvin waves provide the necessary momentum for the westerly phase and Rossby-gravity waves provide the momentum for the easterly phase of QBO oscillation. Nevertheless, the east phase of QBO is stronger and lasts longer than the west phase [Baldwin et al., 2001]. The maximum amplitudes of both east and west phases are typically near 20 hPa without any seasonal dependence [Naujokat B., 1986].

Although the zonal wind and temperature anomalies of the QBO do not penetrate significantly below the tropopause [Baldwin et al., 2001], several studies have shown that QBO can also affect the tropical tropospheric circulation. The descending QBO westerlies are associated with downward motion in the tropics and upward motion in the subtropics, weakening the normal Brewer-Dobson circulation in the tropics and resulting in a positive ozone anomaly in the tropics and a negative anomaly in the subtropics. The descending easterly phase of the QBO, enhances the Brewer-Dobson circulation in the tropics resulting in a negative ozone anomaly in the tropics and a positive ozone anomaly in the subtropics [Bruhwiler and Hamilton, 1999]. According to Neu et al. [2014], although ENSO and QBO indices are not always in phase, they are found to be highly correlated with each other from the time period between 2005 and 2010 ( $R=0.67$ ). El Niño and easterly QBO phase have been found to enhance meridional overturning in the stratosphere by increasing the poleward and downward transport from the ozone maximum regions and as a result they increase the stratospheric ozone transported to the troposphere in the subtropics. La Niña and westerly QBO shear have been found to decelerate the stratospheric ozone transport, reducing tropospheric ozone originating from the stratosphere.

In order to study the coupling between QBO and tropospheric ozone, the equatorial Singapore (1°N, 104°E) winds at 30 and 50 hPa pressure levels from FU Berlin (<http://www.geo.fu-berlin.de/en/met/ag/strat/produkte/qbo/>) were used as explanatory QBO variables in the multivariate linear regression analysis. The combination of QBO indexes at 30 and 50 hPa, that are phase shifted by about  $\pi/2$  will account also for potential lags in the ozone response to QBO [Randel and Wu, 2007] and prevents the need to find the optimal time lag as described in Bojkov et al. [1990].

### Solar cycle

The sun presents a nearly periodic 11-year change in its activity (changes in solar radiation and coronal mass ejections) and appearance (changes in the number of sunspots, etc). The total solar irradiance (TSI) within an 11 year solar cycle varies (peak to peak) by about 0.1 %. For time-scales shorter than a few days, the changes in TSI may be 2-3 times larger. Solar spectral irradiance (SSI) variations differ from those observed in the TSI. In visible and near-infrared (NIR) wavelengths, the SSI is usually less than 0.5 % whereas at shorter wavelengths, such as UV, where stratospheric ozone strongly absorbs, the SSI variability may reach 10% [Ermolli et al., 2013].

This solar cycle (SC), induces changes in the upper atmospheric chemistry, the temperature and

pressure gradient and as a result in the atmospheric circulation. The direct effects of solar variability may be more dominant in the stratosphere, however, changes occurring in the upper stratosphere are propagating to the troposphere due to the coupling of these two layers. For example, solar energetic protons may lead to nitrogen oxides ( $\text{NO}_x$ ) production in the upper stratosphere [Jackman, et al.] which afterwards could destroy ozone. As a result, more UV radiation may reach the lower atmosphere and tropospheric ozone production could be enhanced. According to WMO [2007], the global total ozone budget vary from 2 to 3% in phase with the 11-year solar cycle.

The solar activity is represented by various proxies such as the solar flux at 10.7 cm, the Mg II index, the Lyman alpha composite data set and the UV 205-nm flux [Fioletov et al., 2009]. In this thesis, the 10.7cm Solar Flux, obtained from Natural Resources Canada web site (<http://www.spaceweather.ca/solarflux/sx-en.php>) is used in the regression analysis. The 10.7cm Solar Flux is a measure of the strength of total solar emission at 10.7cm radio wavelength from all sources present on the solar disc (chromosphere, corona and sunspots) [Tapping, 2013]. The 10.7cm solar flux is directly proportional to the magnetic flux and may vary in intensity ranging from fractions of a second to years [Tapping, 2013].

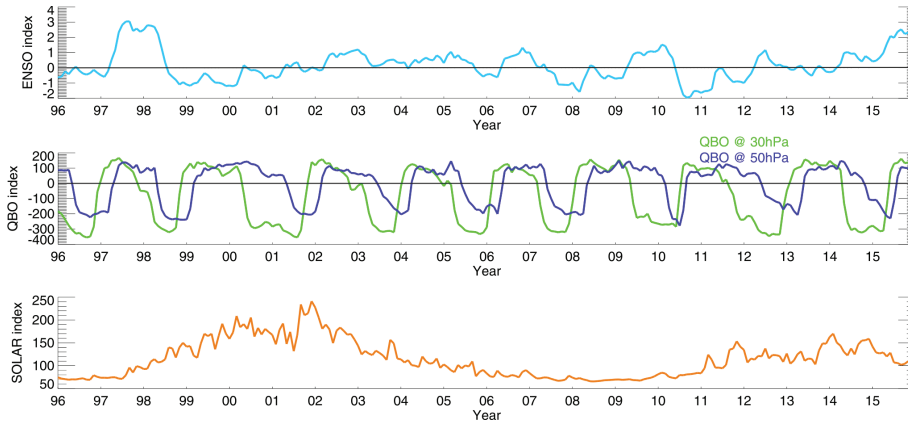


Figure 4.3: Time-series of the explanatory variables used in the regression (Up) ENSO-MEI indexes, (middle) QBO at 30 and 50 hPa from FU-Berlin and (bottom) Solar Cycle (10.7 cm) index from Natural Resources Canada.

#### 4.2.2 The multi-linear regression trend model

The time series of the monthly mean tropical tropospheric ozone columns  $Y_t$  at a specific latitude and longitude  $(i, j)$  (running every  $2.5^\circ$  and  $5^\circ$  respectively) can be generally described by the following trend model:

$$Y_t(i, j) = \alpha(i, j) + \beta(i, j) \cdot X_t + R_t(i, j) + S_t(i, j) + N_t(i, j) \quad (4.1)$$

where  $a$ , is the TCO offset for the first month  $t=1$ ,  $\beta$ , the linear trend in DU/month,  $X$  the time variable (months running from zero to 239) covering the years 1996-2015, and  $R_t$  are the time dependent regression coefficients for the ENSO, QBO, and solar cycle proxies (Fig. 4.3) which can be expressed as:

$$R_t = \delta \cdot ENSO_t + \varepsilon \cdot QBO_{30t} + \zeta \cdot QBO_{50t} + \eta \cdot SC_t. \quad (4.2)$$

$S_t$  is the seasonal variation which is included in the model using harmonic functions that represent the annual, semi-annual and quarterly harmonic oscillations. Analytically the seasonal cycle is modeled

by a Fourier series, with  $\gamma_{11}, \gamma_{21}, \gamma_{12}, \gamma_{22}, \gamma_{13}, \gamma_{23}$  being the regression coefficients for 12-, 6- and 4-month periodicities, with sine and cosine term for each periodicity, for  $n=1,2,3$  respectively.

$$S_t(i, j) = \sum_{n=1}^3 (\gamma_{1n} \cdot \sin(\frac{2 \cdot \pi \cdot n \cdot t}{12}) + \gamma_{2n} \cdot \cos(\frac{2 \cdot \pi \cdot n \cdot t}{12})) \quad (4.3)$$

Finally,  $N_t$ , is the noise of the time series, representing the unexplained portion of the variability in the fit.

Equation 4.1 can be written in vector form as follows:

$$Y = X \cdot b + N \quad (4.4)$$

With  $Y$ , being an  $n \times 1$  vector representing the TCO time-series for each  $(lat, lon)$ ,  $X$  is an  $n \times m$  matrix containing the explanatory variables,  $b$  is an  $m \times 1$  vector consisting of the regression coefficients and  $N$  is an  $n \times 1$  vector consisting of the noise term.

The residual noise is then calculated from the time-series minus the fit:

$$N = Y - X \cdot b \quad (4.5)$$

Since the tropospheric ozone lifetime approaches a month, the pattern of tropospheric ozone for a month has the tendency to recur on the next month. Even after removing to the largest extent the seasonal and other effects in the time series shown in Eq. 2.1, there is still a month-to-month correlation ( $\phi$ ) in residuals. This phenomena is called persistence [Wilks, 2011] and is quantified by the degree of autocorrelation of a parameter, shifted by  $p$  time steps (lag  $p$ ).

Atmospheric variables are continuous and their correlation is well represented by the so-called Box-Jenkins model [Box et al., 1994]. The most simple form of a Box-Jenkins model is the first order or AR(1) model. In this model, the noise is assumed to be autoregressive on the order of 1 (AR(1)). In the same sense, the noise is assumed to be stationary which means that the mean, variance and autocorrelation ( $-1 \leq \phi \leq 1$ ) do not change with time [Weatherhead et al., 1998]. Then the white noise is given by the following equation:

$$\epsilon_t = N_t - \phi N_{t-1} \quad (4.6)$$

where  $\epsilon_t$  is the independent random variable with mean zero and  $\phi = Corr(N_t, N_{t-1})$  is the first order autocorrelation of the noise [Weatherhead et al., 1998]. The variance of the noise is related to the variance of the white noise,  $\epsilon$  by  $\sigma_\epsilon^2 = \sigma_N^2(1 - \phi^2)$ . Fig. 4.4a shows the autocorrelation of the noise for 4 month lag. Although, the mean autocorrelation for lag 1 (AR[1]) is small ( $\phi \simeq 0.1$ ), there are areas that reaches 0.3.

The reason for calculating the autocorrelation of the noise is to include it in the fitting procedure (without using weights in the fit e.g. uncertainty). The autocorrelation is employed in the regression using a linear matrix transformation [Mieruch et al., 2008, Weatherhead et al., 1998, Wilks, 2011]. This transformation does not change the fitting coefficients significantly, however, it reproduces higher uncertainties of the fitting parameters, since the degree of freedom is getting smaller. The degree of freedom,  $\nu$ , is the minimum number of independent variables defined in general as the number of terms

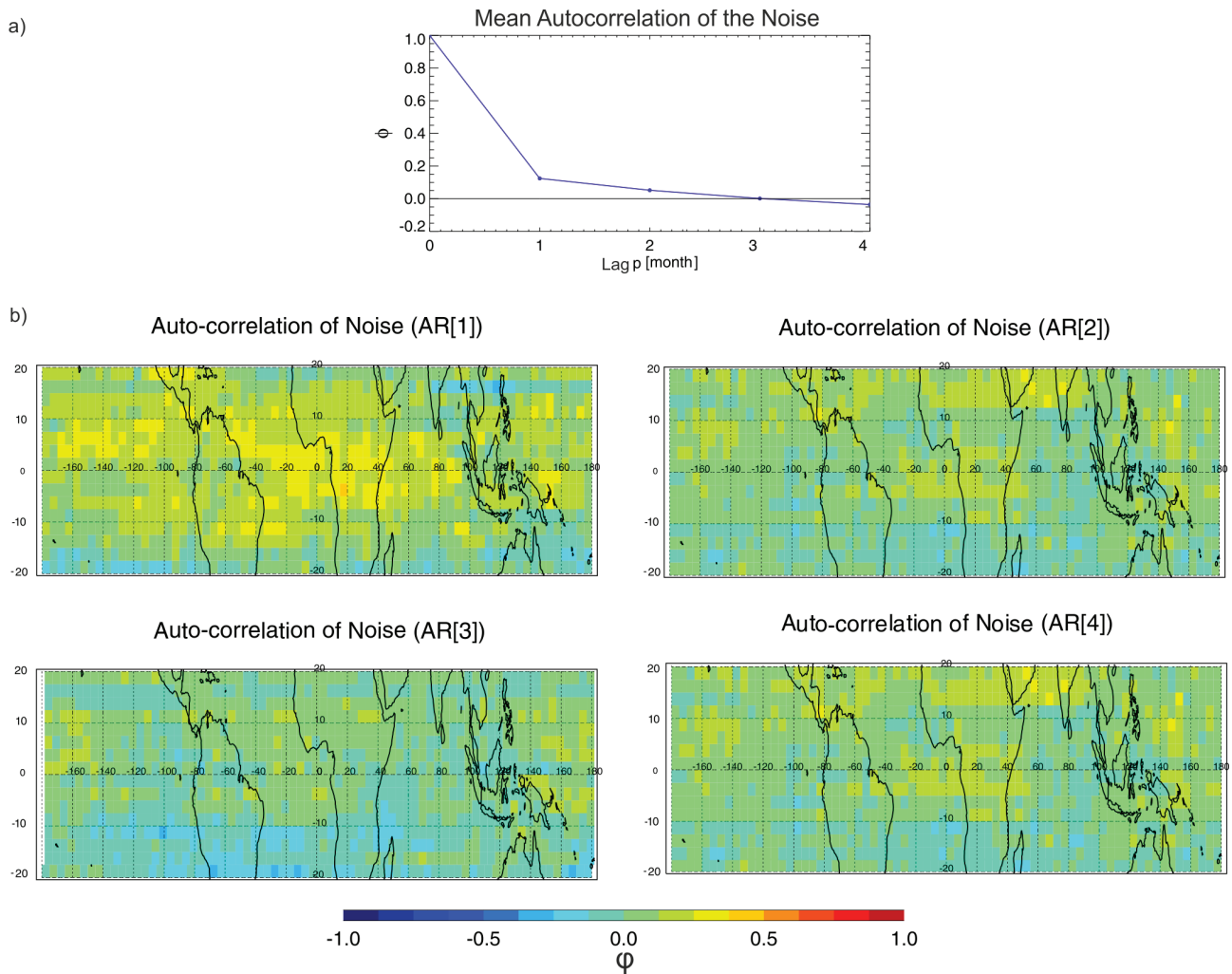


Figure 4.4: a) Example of noise autocorrelation,  $\phi$ , for lags of zero to 4 months. The autocorrelation is equal to 1 for unlagged data ( $p=0$ ) and decays gradually with number of lagged months ( $p=1-4$ ) b) Maps of noise autocorrelation for 1 to 4-month lag.

in a sum minus the number of constrains on the terms of the sum [JCGM 100, 2008]. Now, the noise vector could be written as:  $N = P'^{-1} \cdot \epsilon$ , in a matrix form, where  $P'$ , is a  $t \times t$  matrix equal to:

$$\begin{bmatrix} \sqrt{1-\phi^2} & 0 & \dots & 0 & 0 \\ -\phi & 1 & \dots & 0 & 0 \\ \dots & \dots & \dots & \dots & \dots \\ 0 & 0 & \dots & -\phi & 1 \end{bmatrix}$$

The model in Eq.4.4 becomes:

$$Y = X \cdot b + P'^{-1} \cdot \epsilon \quad (4.7)$$

Using the properties of linear algebra, Eq.4.7 can be transformed as:

$$Y^* = X^* \cdot b + \epsilon \quad (4.8)$$

where,  $Y^* = P'Y$  and  $X^* = P'X$  are the transformed dependent and independent variables, respectively. The regression coefficients are calculated now by:

$$b = (X^{*'} X^*)^{-1} X^{*'} Y^* \quad (4.9)$$

The variance of the regression coefficients vector is:

$$\text{Var}(b) = \sigma_\epsilon^2 (X^{*'} X^*)^{-1} \quad (4.10)$$

where  $\sigma_\epsilon^2$ , is the variance of the white noise. Subsequently, the variance of the trend,  $\beta$  is then:

$$\text{Var}(\beta) = \sigma_\epsilon^2 (X_{(2,t)}^{*'} X_{(2,t)}^*)^{-1} \quad (4.11)$$

Whether the trend is statistically significant or not is tested using standard Gaussian probabilities. Making use of the null hypothesis, that the observed trend is equal to zero,  $H_0 : \beta = 0$ , then a non-zero  $H_1 : \beta = \beta_0$  may be used. The t-test for significance at the 95% confidence level is met, if the probability measuring a trend greater than two times its standard deviation is equal to a critical value, 0.05 in this case ( $P_{H_0} \{|\beta| > 2\sigma_\beta\} = 0.05$ ) [Mieruch et al., 2008, Weatherhead et al., 1998, Wilks, 2011]. This means that the trend is considered statistically significant at the 95% significance level if :

$$\frac{|\beta|}{\sigma_\beta} > 2 \quad (4.12)$$

For the AR(1) autoregressive model, the trend results are more probable to be rejected from the null hypothesis since the standard deviation of the trend,  $\sigma_\beta$ , increases as  $\phi$  increases.

$$\sigma_\beta = \frac{\sigma_\epsilon}{(1-\phi)n^{3/2}} = \frac{\sigma_N}{n^{3/2}} \sqrt{\frac{1+\phi}{1-\phi}} \quad (4.13)$$

where n is the number of months in the regression [Weatherhead et al., 1998].

### 4.2.3 Sensitivity and uncertainty of the trend

The multivariate linear regression model (Eq. 4.1) and correction for AR(1) have been applied to six individual harmonised CCD tropical tropospheric ozone columns datasets (see: Section 4.1) from 1996 to 2015. Figure 4.5 shows the trend map and its statistical significance for the six scenarios. The tropospheric O<sub>3</sub> trends from all scenarios range between  $\sim -4$  and 4 DU/decade, with mean values between 0 and 0.8 DU/decade without any of them being statistically significant. The maximum trend difference among all six harmonisation scenarios is on average 2 DU/decade exceeding the  $2\sigma_\beta$  uncertainty of the trends which is  $\sim 1.2$  DU/decade (see: Fig. A5 and A6). These differences on the trends among the differently harmonised datasets reveal the additional uncertainty which is inherited to the trend from the harmonisation procedure of multiple TCO datasets. The maximum absolute differences ( $>3-6$  DU/decade), are noticed mainly over land and more specifically over south America, and northern Africa, while the minimum absolute differences are over the Oceans with the exception of the Indian and the southern Pacific oceans. Nevertheless, all scenarios shown in Fig.4.5 agree that there is a positive trend of tropospheric ozone over the south tropical Atlantic Ocean, and some parts of central Africa and India, while a negative trend appears over the Caribbean sea and the north and south Pacific Ocean.

Scenarios 1, 4, and 6 have a similar pattern with each other which is caused by the absence of correction of the GOME TCO dataset. Nevertheless, the range of the trends is different, with scenario 4 showing higher positive trends ( $\sim 2 - 4$  DU/decade), mainly over Africa, south America and the southern tropical borders. Scenarios 2 and 5 have also similar pattern with each other, driven by the average offset applied to GOME-2 data. The pattern of these scenarios consist of a characteristic decrease in tropospheric ozone ( $\sim -2$  DU/decade) over central-south America and over the Indonesian peninsula. The tropospheric O<sub>3</sub> trends calculated with scenario 3 repeat the meridional pattern of GOME correction offsets (see: Fig. 4.1), which appears as an artifact in the trend results.

### 4.2.4 Tropical tropospheric ozone trend results

From now on, the discussion about tropical tropospheric ozone trend refers to the preferred harmonisation scenario (scenario 1). As shown in Fig. 4.6.a, the TCO trend varies between  $-3.2$  and  $3.7$  DU/decade, and the average trend for the period 1996–2015 is statistically non-significant and is equal to  $-0.08 \pm 1.23$  DU/decade ( $2\sigma$ ) (see: Fig.4.6a). The noise is random (white noise) following very well a Gaussian distribution (see Fig.4.6b).

The multivariate regression model (Eq. 4.1) has been applied to the global tropical mean time-series ( $20^\circ\text{S}-20^\circ\text{N}$ ). The fit results are shown in Fig. 4.7. The global tropical equals  $0.0 \pm 0.6$  DU/decade. This means that there is no significant trend for tropospheric ozone in the tropics. This result is in agreement with Ziemke et al. [2005] and Ebojie et al. [2016] who found no significant global tropospheric ozone trends in the tropics. The tropical mean tropospheric ozone time-series (black stars) shows a seasonal cycle with higher values in late summer-autumn months. The time-series are well followed by the regressed tropospheric ozone (red line) and the residual (orange line in upper panel) is smaller than 3 DU. The seasonal cycle contributes the most to the TCO variability in the tropics by about  $\pm 3$  DU. Tropical tropospheric ozone reduces up to  $-3$  DU during El Niño years (1997-98, 2006-07, 2009-10,

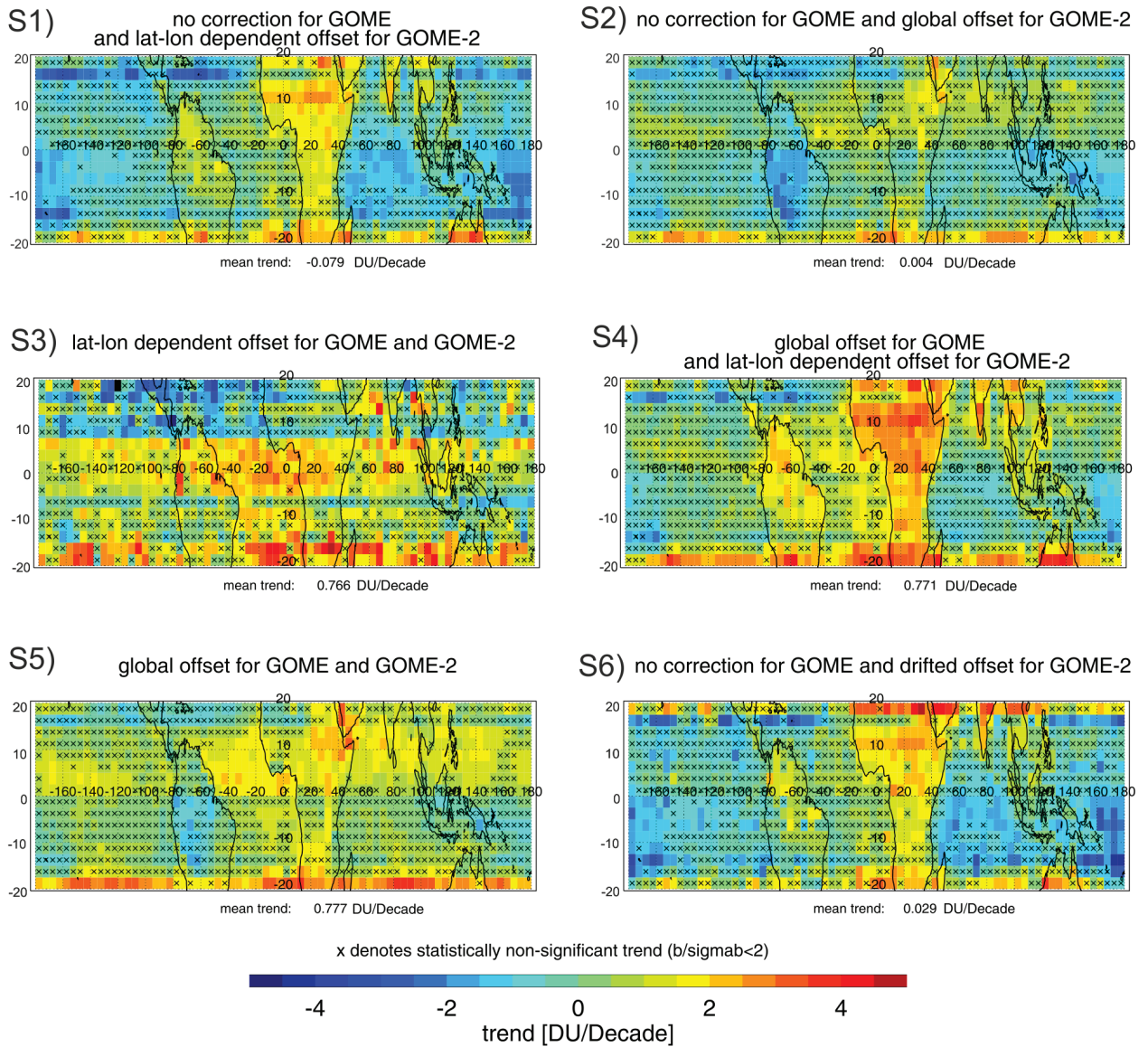


Figure 4.5: Tropical tropospheric ozone trends using a linear multivariate first order auto-regression model for 6 harmonisation scenarios, see Sec. 4.1. The trends are given in DU per decade. Grid-boxes marked with "x" are statistically non-significant at the 95% confidence level.

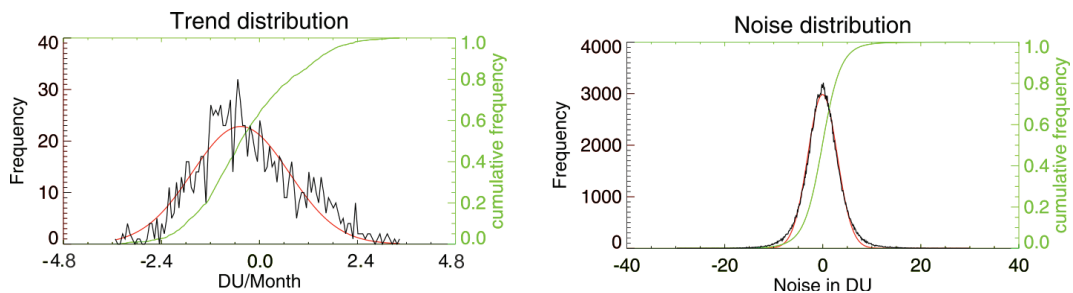


Figure 4.6: Probability density function (PDF) (black) and cumulative density function (CDF) (green) of a) the trend (the frequency equals the number of grid-boxes) and b) the noise (shows the distribution of the noise time-series in all grid boxes for all months). Red lines show the Gaussian distribution calculated using the standard deviation from the distributions.

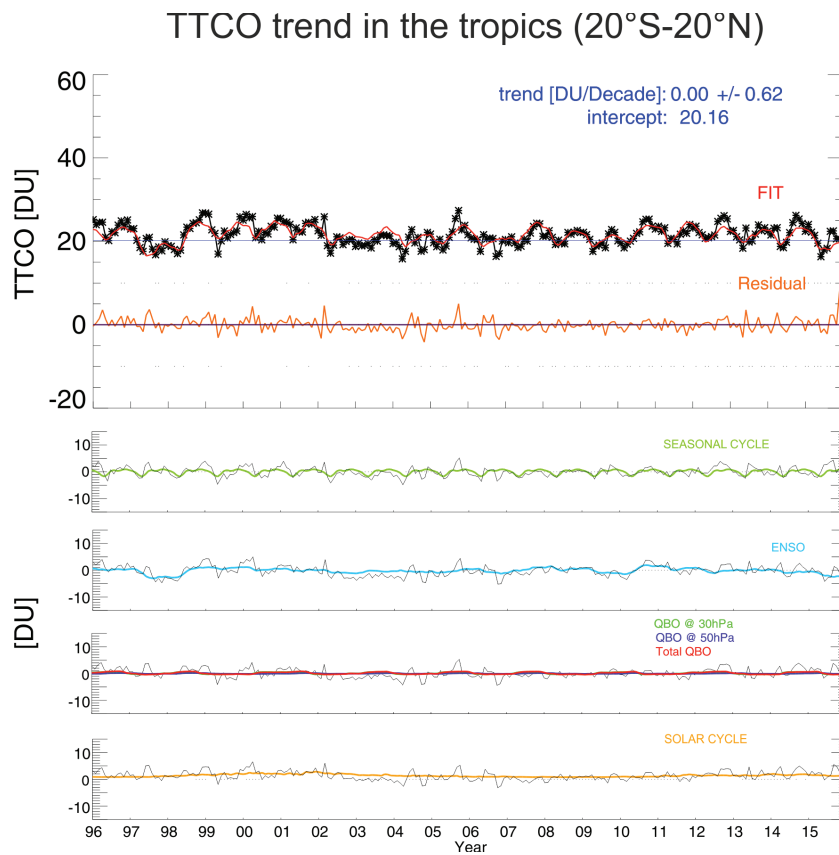


Figure 4.7: Tropospheric ozone trends for the global tropical tropospheric ozone between the years 1996 to 2015. Top: The multivariate linear trend (black), the fit (red) and the residual (orange) are over-plotted. The  $2\sigma$  uncertainty of the trend is reported. The next panels show the harmonic functions (green), ENSO (light blue), QBO (red), solar (orange). Overlaid in black for all proxies are the time series with all fit terms removed except the particular fit parameter.

2015) and slightly increases by 1 – 2 DU during strong La Niña years (1999-00, 2007-08, 2010-11). QBO and the solar cycle, practically do not contribute to the inter-annual mean tropical tropospheric ozone variability. Overlaid in black for all proxies are the time series with all fit terms removed except the particular fit parameter. This allows us to relate the magnitude of changes due to a certain process to the observed residuals (or unexplained variations).

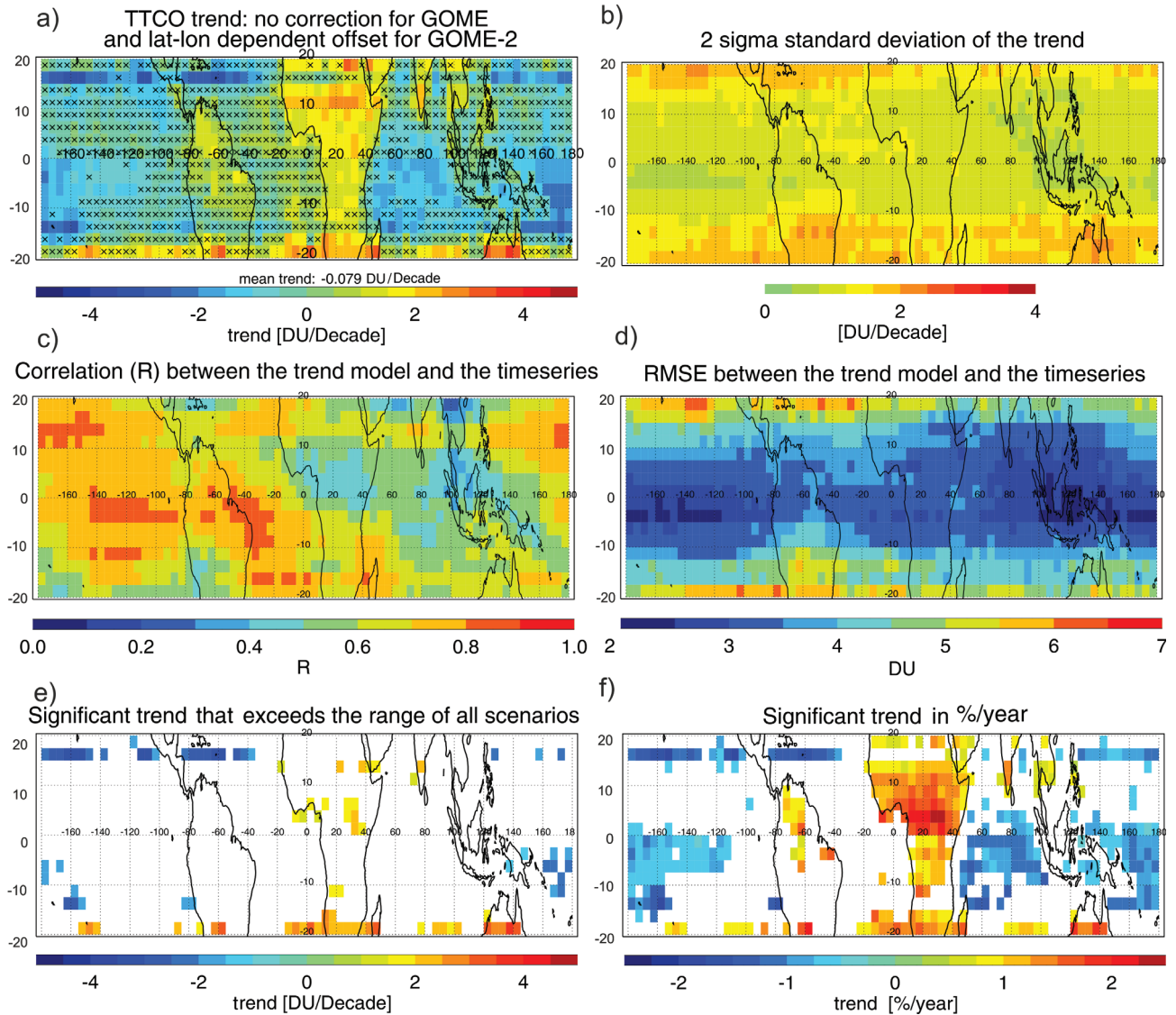


Figure 4.8: (a) Tropical tropospheric ozone trends using a linear multivariate first order auto-regression model for the selected harmonised scenario 1 in DU/decade. Grid-boxes marked with "x" are statistically non-significant at the 95% confidence level ( $b > 2\sigma_b$ ) b)  $2\sigma$  standard deviation of the trend c) The correlation coefficient, R, between the multi-linear trend model fit and the original time-series. d) The RMS error between the trend model and the time-series e) The statistically significant trend that exceeds the maximum absolute difference of the trends calculated for all six scenarios. f) The significant tropical tropospheric ozone trend in %/year.

Figure 4.8 summaries the tropical tropospheric ozone trends calculated in a  $2.5^\circ \times 5^\circ$  grid as derived from the merged CCD TCO dataset between 1996 and 2015. Fig. 4.8b shows the  $2\sigma$  of the trend, which is on the order of  $\sim 0-4$  DU/decade (mean: 1.2 DU/decade), with greater values at the tropical

borders and values close to zero along the equator. Fig. 4.8c shows the correlation between the model and the time-series. The correlation coefficient reaches 1 over the north and central-east Pacific and the southern Atlantic Ocean. The regions of smaller correlations are mostly over the west Pacific, the Caribbean sea, the south-eastern Asia, and over the central African continent. The main reason for the low correlation is the very weak seasonal cycle observed in these regions. Fig. 4.8d shows the RMS between the time-series and the model fit. The RMS is less than 3 DU close to equator and reaches 7 DU at the tropical borders. Fig. 4.8e presents only those grid boxes where the trend is statistically significant and exceeds the maximum difference of the trends calculated from all six scenarios, shown in Fig. A5. This additional criterion (to exceed the differences between harmonisation scenario) allows us to identify grid boxes that have significant trends with higher confidence. Following this stronger criterion, tropospheric ozone increases over some parts of central Africa ( $\sim 2$  DU/decade), southern Africa and the Atlantic Ocean ( $\sim 2 - 3$  DU/decade), India ( $\sim 2$  DU/decade) and Oceania ( $\sim 3 - 4$  DU/decade) and decreases over the Caribbean sea and parts of North Pacific Ocean ( $\sim -2 - -3$  DU/decade), as well as over some regions of the southern Pacific Ocean ( $\sim -2$  DU/decade) seem to be relevant, however, for all other grid boxes trends are highly uncertain and mainly dependent on the choice of the harmonisation scenario. However the negative trends appearing as a stripe at northern latitudes (Caribbean sea and northern Pacific) may still be an artifact of the data-set (low sampling of data). Finally, Fig. 4.8f shows the tropical tropospheric ozone trends in per cent per year (%/year) that are statistically significant for the TCO data harmonised according to scenario 1 (S1). Here the maximum increase is noticed over central Africa,  $\sim 3\%$ /year, over southern Africa, south tropical Atlantic and Oceania  $\sim 1.5\%$ /year, and finally over India and south-eastern Asia  $\sim 1\%$ /year. The maximum tropospheric ozone decrease is noticed over the Caribbean sea and the north-east tropical Pacific, about  $\sim -2\%$ /year, followed by the central-south Pacific and Indian Ocean,  $\sim -1\%$ /year.

### Regional trends

It is also possible to study regional trends focusing on the regions where the trends are statistically significant. The TCO have been regionally averaged for eight regions and the regression analysis applied to them. The regions are: A: Caribbean Sea ( $15^\circ - 17.5^\circ, -85^\circ - -45^\circ$ ), B: India ( $10^\circ - 20^\circ, 70^\circ - 85^\circ$ ), C: north-south America ( $0^\circ - 10^\circ, -75^\circ - -60^\circ$ ), D: North Africa ( $5^\circ - 15^\circ, -17.5^\circ - 50^\circ$ ), E: eastern Pacific Ocean ( $0^\circ - 7.5^\circ, -180^\circ - -110^\circ$ ), F: Indian Ocean ( $0^\circ - 7.5^\circ, 50^\circ - 100^\circ$ ), G: west Pacific Ocean ( $0^\circ - 7.5^\circ, 160^\circ - 180^\circ$ ), and H: southern Africa ( $-20^\circ - -12.5^\circ, 10^\circ - 50^\circ$ ).

As shown in Figure 4.9 and Table 4.2, regions B, C, D and H show significant increase on the order of 1–1.5 DU/decade and regions A, E, F, and G a significant ozone decrease on the order of -1.2–1.9 DU/decade.

The observed significant positive changes in tropospheric  $O_3$  over north Africa and parts of the Arabian sea (D), south Africa and the southern African outflow (H), parts of India (B), and north south America (C) agree well with results of Lelieveld et al. [2004], Beig and Singh [2007], Kulkarni et al. [2010], Ebojie et al. [2016] and Heue et al. [2016] who also noticed an increasing ozone trend over these regions. They can be attributed to changes in anthropogenic  $NO_x$  and other tropospheric  $O_3$  precursors, due to population and energy consumption increases, which are transported to these areas [Cooper et

## Trop. O3 column trend

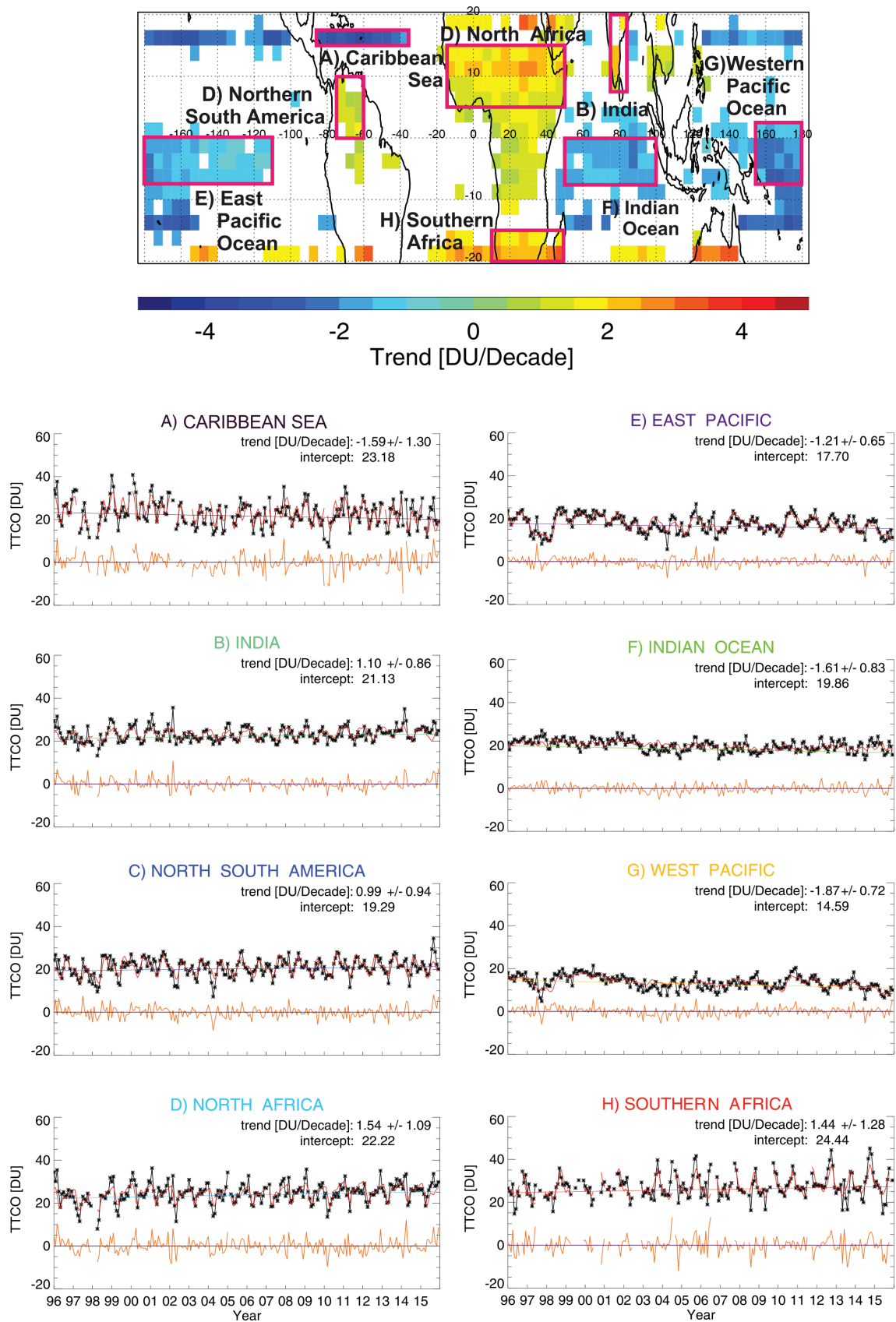


Figure 4.9: Tropical tropospheric ozone trend in A) central America, B) India, C) east Pacific Ocean, D) South America, E) central Atlantic Ocean, F) Indian Ocean, G) south Atlantic Ocean, and H) southern Africa. With orange color is plotted the residual noise.

Table 4.2: Regional tropospheric ozone trends in 8 tropical regions. Bold are the regions where the trend is greater than three times the standard deviation of the trend ( $3\sigma$ ).

Area	Tropospheric O <sub>3</sub> trend $\pm 2\sigma$ in DU/decade
A) Caribbean sea	-1.59 $\pm$ 1.30
B) India	1.10 $\pm$ 0.86
C) North South America	0.99 $\pm$ 0.94
D) North Africa	1.54 $\pm$ 1.09
<b>E) East Pacific Ocean</b>	<b>-1.21 <math>\pm</math> 0.65</b>
<b>F) Indian Ocean</b>	<b>-1.61 <math>\pm</math> 0.83</b>
<b>G) West Pacific Ocean</b>	<b>-1.87 <math>\pm</math> 0.72</b>
H) South Africa	1.44 $\pm$ 1.28

al., 2014, Dahlmann et al., 2011, Duncan et al., 2016, Hilboll et al., 2013b, 2017, Kulkarni et al., 2010, Schneider et al., 2015]. Biomass burning may also have an impact on tropospheric ozone changes. For example, the burned area in southern tropical Africa increased by 1.8 %/yr during the period 2000 to 2011 [Giglio et al., 2013]. Ziemke et al. [2009b] and Wai et al. [2014] estimated that biomass burning can contribute to an increase in tropospheric ozone column by  $\sim 20\%$ . Additionally, changes in meteorology, convection, and dynamical oscillations, such as the MJO, stratospheric intrusions (STE) and shorter timescale atmospheric dynamics or cyclones may have influence the transport of pollutants and contribute locally to observed tropospheric ozone changes [Beig and Singh, 2007, Chandra et al., 2004, Ebojie et al., 2016, Oltmans et al., 2004, Parrish et al., 2009, Sauvage et al., 2007, Ziemke et al., 2009b]. Another factor that could influence tropospheric ozone are the changes in stratospheric ozone column. For example, an increase in the tropical upwelling caused by a stronger Brewer-Dobson circulation is expected to reduce both lower stratospheric and the total column ozone in the tropics, increasing the UV-B radiation reaching the troposphere [WMO, 2014]. This could result in an enhance of tropospheric ozone photolysis (photochemical ozone sink). However, the increase of UV-B radiation at the surface would also lead to increased concentrations of OH (hydroxyl radicals) and subsequently increased concentrations of HO<sub>2</sub> and RO<sub>2</sub> radicals, which could enhance the production of ozone if NO<sub>x</sub> are available (e.g. in mega-cities) [UNEP, 1998]. Consequently, there are multiple feedbacks from these changes that could either increase or decrease ozone in the troposphere.

The negative changes in TTCO over the Caribbean sea (A) are in agreement with the results of Ebojie et al. [2016]. Although they might be influenced by the decrease in NO<sub>x</sub> emissions over the north American continent [Duncan et al., 2016, Hilboll et al., 2013b] or by changes in stratospheric intrusions via the tropopause foldings [Hwang, et al., Ojha et al., 2017], the observed trends over the northern and southern tropical latitudes ( $>18^\circ\text{N}$  and S) should be generally interpreted with caution since they are influenced by low sampling of data. Despite the fact that might appear to be statistically significant, they should be interpreted with caution since they are influenced by gaps in the TTCO time series due

to the movement of the ITCZ, which reduces the cloudy data during local winters and makes the above cloud ozone column (ACCO) retrieval difficult, violating in some cases the invariance of the ACCO per latitude band.

The decreasing trend over the Pacific (E and G) and Indian (F) Oceans agrees well with Heue et al. [2016]. It might be associated with changes in the burden of organic and inorganic halogens on these areas as well as changes in dissolved organic matter (DOM) photochemistry in surface waters could be an additional source of volatile organic compounds that can contribute to ozone destruction [Dickerson et al., 1999, Ebojie et al., 2016]. Additionally it may be attributed to changes in the humidity burden of the troposphere. For example, Fontaine et al. [2011] indicated that the Outgoing Long-wave Radiation (OLR), which allows to differentiate between clear-sky (high OLR) and deep convective regions (low OLR) has been decreasing over these regions, which can indicate deeper convective clouds appearing over the Caribbean, the west-central Africa in summer and the Indian Ocean in autumn. The increased deep convection is associated with ozone loss due to convective outflow and increased cloudiness and humidity which contribute to photochemical O<sub>3</sub> loss (see reactions 1.23 – 1.27 in Chapter 1) [Morris et al., 2010, Wai et al., 2014]. Fontaine et al. [2011] showed that the location of OLR minima has been shifted northwards which can be associated with a shift on the ITCZ by 0.5 – 0.8 ° northwards. These changes are subsequently associated with changes in the location of tropical jets, with changes in rainfall amounts and weather systems. All these changes could be responsible in some degree for the statistically significant tropospheric ozone trends observed close to the location and the branches of the ITCZ (e.g in the Indian and Pacific Oceans), but their contribution remains vague.

### Seasonal tropospheric O<sub>3</sub> trends

Seasonal tropospheric O<sub>3</sub> trends can be very useful for understanding the connection between the factors (e.g. meteorology or emissions) that contribute to tropospheric ozone changes and its distribution. For this reason, the multi-linear regression model has been applied to Dec.–Feb., Mar.–May, Jun.–Aug., and Sep.–Nov. TTCO time-series and proxies (ENSO, QBO, solar cycle) in order to calculate TTCO trends for winter, spring, summer and autumn respectively, with the only difference that the sine and cosine terms that reflect the seasonal cycle are neglected in the regression. According to Fig. 4.10, the maximum decreasing trends appear during winter over the northern tropical Atlantic and Pacific Oceans (~-4 DU/decade). These air masses are more affected by changes occurring in the mid-latitudes due to the southward movement of the ITCZ in winter and the strong westerly air flow over the tropical borders in winter [Ebojie et al., 2016]. Therefore, it is assumed that changes in ozone precursors, such as NO<sub>2</sub>, over North America and Europe may have affected the O<sub>3</sub> trends over these tropical latitudes [Hilboll et al., 2013b, Logan et al., 2012]. The winter decrease might also be associated with the limited number of TTCO measurements on the northern tropical borders, thus it demands a more careful investigation. The trends are mostly insignificant during spring, with the exception of Africa where they are ~ 1 DU/decade and some parts over South America where ozone is decreasing by less than 1 DU/decade. During summer, ozone shows a slight statistically significant decrease over the Pacific and Indian Oceans (1-2 DU/decade). Possible reasons for tropospheric ozone decrease over the oceans may be related to changes in sea surface temperatures (SSTs) which are closely tied to the tropospheric humidity [IPCC, 2007,

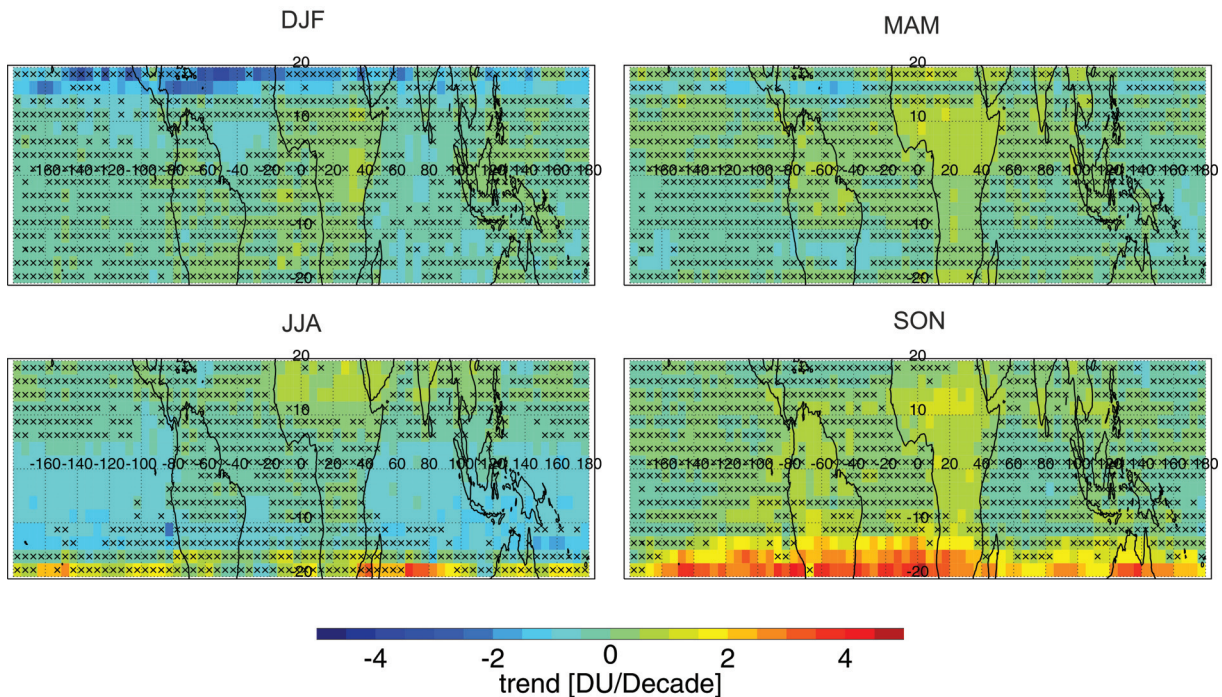


Figure 4.10: Tropical tropospheric ozone trends for winter (DJF), spring (MAM), summer (JJA), and autumn (SON) for the years 1996 to 2015.

Trenberth, 2011]. As discussed earlier (see Chapter 1, Eq. 1.23–1.27) water vapor in the troposphere consists of one of the most important sinks of tropospheric ozone [Jacob, 2000]. An increase in vertical convective patterns over the tropical oceans may result in lower ozone mixing ratios in the upper troposphere where the WFOAS retrieval is more sensitive [Coldewey-Egbers et al., 2005, Fontaine et al., 2011, Morris et al., 2010, Wai et al., 2014, Ziemke et al., 2008]. Several studies have shown that the total column of water vapour (TCWV) has increased over the tropics. Mieruch et al. [2014] and Trenberth et al. [2005] found that the TCWV has increased by  $\sim 1\text{--}2.0\%$ /decade over the oceans. Chen and Liu [2016] found that also the precipitable water vapor (PWV) increased by  $1\text{--}2\%$  in the tropics between 1992–2014. The precipitation increase is about 4% over the ocean, while a decrease of 2% is found over land in the latitude range  $25^\circ\text{S}$  to  $25^\circ\text{N}$ , between 1979 and 2001 [Adler et al., 2003]. The significant increasing trend of ozone at the southern tropical Atlantic, southern Africa, South America, and Oceania maximise during autumn ( $\sim 4$  DU/decade). According to MODIS/TERRA Fire Radiative Power ( $\text{mW}/\text{m}^2$ ) data (<https://disc.gsfc.nasa.gov/neespi/data-holdings/mod14cm1.shtml>) autumn is the season with the most intense fires over southern Africa and South America. Hence, it is very likely that biomass burning could be the origin of the observed ozone increase.

#### 4.2.5 Comparisons of tropospheric ozone trends with ozonesondes

Tropospheric ozone trends retrieved by integrated ozonesonde measurements until 200 hPa have been calculated using the regression model described in Section 4.2.2, in order to validate the trends from the current study. Figure 4.11 and Table 4.3 show the trend results for Ascension, Java, Kuala Lumpur, Nairobi, Natal, and Paramaribo. The calculated trends from ozonesondes show an increase in ozone

at all stations, and especially in Java and Natal this increase is statistically significant (2.83 and 2.25 DU/decade respectively). The CCD trend results show insignificant increasing trend between 0.46 and 0.69 DU/decade, with the exception of Java (-1 DU/decade) and Natal (-0.79 DU/decade), exactly where the ozonesondes show strong significant positive trends. Nevertheless, the CCD trends are within the uncertainty of the calculated trends by ozonesondes. As mentioned in Section 3.3, the comparisons with ozonesonde measurements has specific limitations, since the integrated ozone measurements by ozonesondes represent the tropospheric ozone columns along the track of the sonde for a few days of each month, whereas tropospheric ozone from CCD represents monthly averaged tropospheric ozone columns over a much larger area (a grid box of  $2.5^\circ$  by  $5^\circ$ ). Additionally, the time period available from ozonesonde data is different (usually smaller) than the one from the CCD dataset.

Table 4.3: Tropospheric ozone trends in 6 sites, calculated from the CCD TCO dataset and ozonesonde profiles. With bold are marked the trends if they are greater than two times the standard deviation of the trend ( $2\sigma$ ).

Area	Tropospheric O3 trend from CCD $\pm 2\sigma$	in DU/decade
		Tropospheric O3 trend from ozonesondes $\pm 2\sigma$ in DU/decade
A) Ascension	0.45 $\pm$ 1.10	1.21 $\pm$ 2.96
B) Java	-1.00 $\pm$ 1.22	<b>2.83 <math>\pm</math> 2.25</b>
C) Kuala Lumpur	0.54 $\pm$ 0.75	0.84 $\pm$ 1.55
D) Nairobi	0.69 $\pm$ 1.06	0.70 $\pm$ 0.90
E) Natal	-0.79 $\pm$ 1.32	<b>2.25 <math>\pm</math> 1.23</b>
F) Paramaribo	0.46 $\pm$ 1.24	1.77 $\pm$ 2.05

#### 4.2.6 Tropospheric ozone trends over mega-cities

On local scales, the impact of anthropogenic emissions at mega-cities are of great interest since they affect human health of millions of people. Tropospheric ozone trend at grid-boxes ( $2.5^\circ \times 5^\circ$ ) surrounding 10 tropical mega-cities have been selected in order to perform a quantitative comparison with other studies. The selected mega-cities in descending order of population are: Jakarta ( $-6^\circ$  S,  $106.7^\circ$  E, 26 million people), Mexico ( $19.4^\circ$  N,  $99.1^\circ$  W, 24 million people), Manila ( $14^\circ$  N,  $120^\circ$  E, 22 million people), Mumbai ( $19^\circ$  N,  $72^\circ$  E, 21 million people), Bangkok ( $13.7^\circ$  N,  $100.5^\circ$  E, 14 million people), Lagos ( $6^\circ$  N,  $3^\circ$  E, 13 million people), Kinshasa ( $-4.4^\circ$  S,  $15.3^\circ$  E, 10 million people), Bangalore ( $13^\circ$  N,  $77.6^\circ$  E, 10 million people), Lima ( $-12.1^\circ$  S,  $77^\circ$  W, 10 million people) and Nairobi ( $-1.3^\circ$  S,  $36.8^\circ$  E, 5 million people).

The trend results are presented in Table 4.4 and Fig. A8. The tropospheric ozone trends have been calculated with the regression model described in Section 4.2.2, using tropospheric O<sub>3</sub> data from the current study (first two columns in Table 4.4) and tropospheric ozone data created by Heue et al. [2016] (third column) using the CCD method as well on GOME, SCIAMACHY, GOME-2 and OMI satellite measurements from July 1995–December 2015 (data taken from: <http://www>.

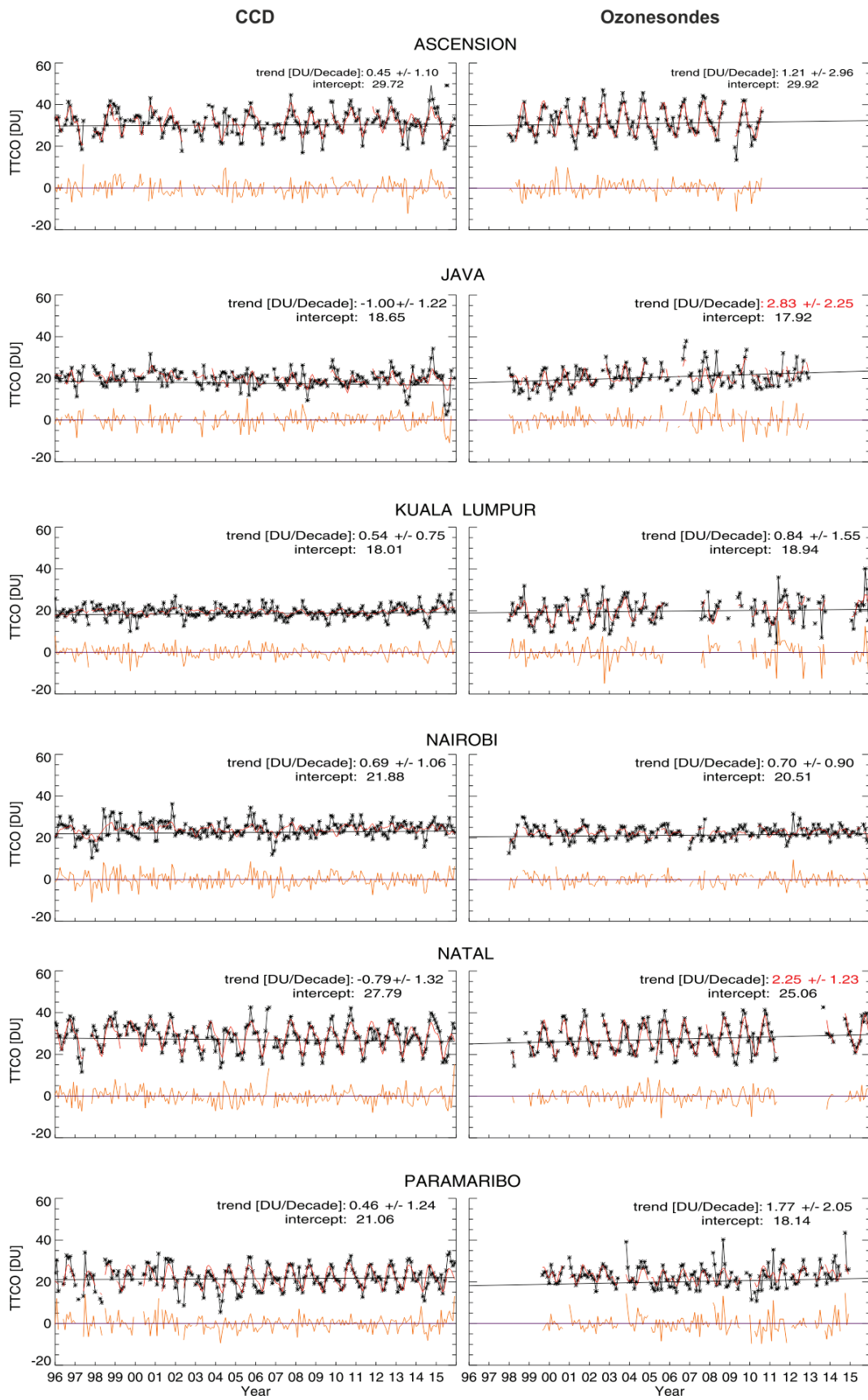


Figure 4.11: Tropospheric ozone trend in A) Ascension, B) Java, C) Kuala Lumpur, D) Nairobi, E) Natal, and F) Paramaribo, calculated using the CCD TTCO dataset and integrated ozone measurements from the SHADOZ network.

esa-ozone-cci.org/?q=node/160). The fourth column in the table shows the trends calculated by Ebojie et al. [2016] (in %/year) using the Limb/Nadir Matching technique on SCIAMACHY ozone data from 2002 to 2011, along with tropospheric NO<sub>2</sub> trends from Schneider et al. [2015] (fifth column) using SCIAMACHY (0.25°×0.25° degrees) NO<sub>2</sub> data, and Hilboll et al. [2013b] (sixth column) using multi-instrument (GOME, SCIAMACHY, GOME-2 and OMI gridded at 1°×0.5° degrees) NO<sub>2</sub> data (in molecules·cm<sup>-2</sup>/decade).

Table 4.4: Tropospheric ozone trends in 10 tropical Mega-cities using CCD<sub>IUP</sub>, (in DU/decade and %/year), CCD<sub>DLR</sub>, and LNM (in %/year) data and tropospheric NO<sub>2</sub> trends with their 2σ uncertainties. With bold are shown the statistically significant trends at the 95% confidence (p < 0.05) level.

Site	Trop. O <sub>3</sub> trend CCD	Trop. O <sub>3</sub> trend CCD	Trop. O <sub>3</sub> trend CCD	Trop. O <sub>3</sub> trend LNM	Trop. NO <sub>2</sub> trend ×10 <sup>15</sup>	Trop. NO <sub>2</sub> trend ×10 <sup>15</sup>
	DU/dec. Current	%/year study	DU/dec. Heue et al., 2016	%/year Ebojie et al., 2016	molec.·cm <sup>-2</sup> /dec. Schneider et al., 2015	molec.·cm <sup>-2</sup> /dec. Hilboll et al., 2013
Jakarta	-0.2 ± 0.9	-0.1 ± 0.5	0.2 ± 0.8	-0.2 ± 1.6	-2.4 ± 1.5	<b>-11.9 ± 4.1</b>
Mexico	-0.3 ± 1.9	-0.1 ± 0.8	-1.2 ± 1.2	<b>-2.0 ± 0.9</b>	-3.5 ± 2.8	5.1 ± 8.2
Manila	<b>1.1 ± 0.7</b>	<b>0.6 ± 0.4</b>	<b>0.9 ± 0.8</b>	<b>1.8 ± 1.3</b>	<b>-3.6 ± 0.7</b>	<b>-10.3 ± 2.0</b>
Mumbai	0.3 ± 1.6	0.2 ± 0.8	<b>1.6 ± 0.9</b>	-0.4 ± 0.9	0.4 ± 0.8	<b>7.0 ± 2.1</b>
Bangkok	<b>1.4 ± 0.9</b>	<b>0.7 ± 0.5</b>	0.5 ± 1.0	–	2.0 ± 1.6	–
Lagos	1.1 ± 1.2	0.4 ± 0.5	0.6 ± 0.9	<b>-1.5 ± 1.0</b>	<b>2.6 ± 0.5</b>	<b>3.3 ± 1.2</b>
Kinshasa	<b>1.3 ± 0.9</b>	<b>0.5 ± 0.4</b>	<b>1.5 ± 0.8</b>	–	0.4 ± 0.3	–
Bangalore	0.8 ± 0.9	0.4 ± 0.4	0.3 ± 0.8	<b>2.3 ± 1.0</b>	<b>1.9 ± 0.6</b>	–
Lima	-0.5 ± 1.5	-0.2 ± 0.7	0.0 ± 1.1	–	<b>3.6 ± 1.1</b>	<b>10.6 ± 3.6</b>
Nairobi	0.7 ± 1.0	0.3 ± 0.5	0.7 ± 0.8	–	<b>1.7 ± 0.4</b>	–

Using our CCD data, statistically significant trends at the 95% confidence level ( $|\beta| > 2 \cdot \sigma_\beta$ ) are found in Manila (1.1 ± 0.7 DU/decade), Bangkok (1.4 ± 0.9 DU/decade), and Kinshasa (1.3 ± 0.9 DU/decade). Elsewhere, the trend is less than 1 DU/decade (< 0.5%/year), while negative but insignificant trends of less than 0.5 DU/decade is noticed in Jakarta (-0.2 ± 0.9 DU/decade), Mexico (-0.3 ± 0.9), and Lima (-0.5 ± 1.5 DU/decade). Using the Heue et al. [2016] dataset, statistically significant positive trends, in the same order of 1–1.5 DU/decade, are retrieved in Mumbai (1.6 ± 0.9 DU/decade), Manila (0.9 ± 0.8 DU/decade), and Kinshasa (1.5 ± 0.8 DU/decade). In other mega-cities, the increase is smaller and insignificant, with the exception of Mexico, where a negative insignificant trend (-1.2 ± 1.2 DU/decade) is found. Ebojie et al. [2016] retrieved a stronger statistically significant ozone increase, of around 2 %/year in Bangalore (2.3 ± 1%/year) and Manila (1.8 ± 1.3%/year), while the trends from the current study do not exceed 0.7 %/year (in Bangkok). Additionally, they found a stronger significant decrease in Mexico (-2.0 ± 0.9 %/year instead of -0.1 ± 0.5 %/year). For the remaining mega-cities, the trends are negative, ranging between -0.2 and -1.5%/year. Nevertheless, although the trends from the three independent studies do not perfectly agree with each other, they are of the same range (± 2 DU/decade) and within the calculated uncertainties.

The derived tropospheric ozone trends clearly show that the tropospheric ozone increase is not proportional to the population and level of industrialisation of the mega-cities. Schneider et al. [2015]

and Hilboll et al. [2013b] studied the  $\text{NO}_2$  trends over some of the selected mega-cities shown in Table 4.4.  $\text{NO}_2$  has been found to decrease strongly over the largest mega-cities (Jakarta, Mexico, and Manila), revealing that possibly  $\text{NO}_2$  emissions legislation polices [Vance, 2012] or/and the economic crisis [Vrekoussis et al., 2013] have affected tropospheric ozone concentration. However, there is no direct correlation between tropospheric ozone and  $\text{NO}_2$  changes shown in Table 4.4. As discussed in Chapter 1, emissions of  $\text{NO}_x$  and VOCs result in ground-level ozone formation. The degree of tropospheric ozone changes strongly depends on the  $\text{NO}_2$  amount and may decrease (moderate  $\text{NO}_2$ ) or enhance ozone (high  $\text{NO}_2$ ). Tropospheric ozone changes are also determined by the regional geography and meteorology (meso-scale circulation) that can transport or trap emissions.

### 4.3 Summary and discussion

Creating a harmonised data-set of tropical tropospheric ozone columns for the last 20 years makes it possible to calculate and study long-term tropospheric  $\text{O}_3$  trends. For this reason, correction offsets have been calculated for GOME and GOME-2 TCO using SCIAMACHY as reference (in the middle of the time-series) in order to reduce the instrumental effects in the long-term time series. Nevertheless, the short overlap period between GOME and SCIAMACHY raised limitations in the harmonisation of GOME TCO dataset. The correction offsets for GOME presented artificial features which have been repeated afterwards in the trend. In order to identify the best way to merge the CCD data and also to investigate how the harmonisation approach may affect the observed trends, six different harmonisation scenarios have been tested. The scenario, using no correction for GOME data and the mean bias of GOME-2 with SCIAMACHY as correction offset has been found to show slightly smaller differences comparing to ozonesondes, and, therefore, it is considered to be the preferred scenario. After the harmonisation, the data obtained from the different instruments agree better with each other and with the ozonesondes.

However, harmonisation is one of the largest sources of uncertainty in the merged dataset. Most of the trend studies that use ozone columns from multiple satellite data (e.g. Xu et al. [2011], Loyola et al. [2009], and Heue et al. [2016]) underestimate the uncertainty that harmonisation might introduce, and they calculate their results using only one harmonisation approach. In order to quantify the uncertainty due to harmonisation, multi-linear tropospheric ozone trends using all six harmonised datasets have been derived and the maximum deviation between them has been calculated. The trends range between  $\sim -4$  and  $4$  DU/decade and the difference between the trends from the six scenarios has been found to be between  $0$  and  $7$  DU, exceeding locally the  $2\sigma$  of the individual trends ( $0$  to  $4$  DU/decade). With this study we conclude that the statistical regression analysis using the  $\beta > 2\sigma_\beta$  as criterion to report significant trends in the 95% confidence level is not adequate in order to conclude whether the trends are significant with confidence since the trends uncertainties may be larger than the statistical ones. This could be a possible reason why the tropical tropospheric ozone trend results from various studies vary significantly [Beig and Singh, 2007, Cooper et al., 2014, Ebojie et al., 2016, Heue et al., 2016, Kulkarni et al., 2010, Lelieveld et al., 2004, Lin et al., 2014, Monks et al., 2015, Oltmans et al., 2013, Ziemke et al., 2005].

Using the preferred merged dataset, the global tropospheric ozone trend during the period 1996–2015 is found to be almost equal to zero ( $0.002$  %/year) and is statistically non significant. This

is in agreement with studies of Ziemke et al. [2005] (nearly zero trend) and Ebojie et al. [2016] ( $\sim 0.55$  DU/decade or  $0.2 \pm 0.5$  %/year ( $2\sigma$ )) however, it is in contrast with the results of Heue et al. [2016] who found a mean increase of  $0.70 \pm 0.12$  DU/decade. Despite the fact that all the trend results from this study are small ( $< \pm 4$  DU/decade or 3 %/ year) and mostly uncertain (66 % are statistically insignificant), there are regions such as over southern Africa, the southern tropical Atlantic, south-east tropical Pacific Ocean, and central Oceania where tropospheric  $O_3$  increased significantly by  $\sim 3$  DU/decade. Additionally, over central Africa and southern India, tropospheric ozone increased by  $\sim 2$  DU/decade. Regional positive tropospheric ozone trends of similar magnitude were also observed in other studies (e.g. [Beig and Singh, 2007, Ebojie et al., 2016, Heue et al., 2016, Kulkarni et al., 2010, Lelieveld et al., 2004]). They could be linked to anthropogenic activities such as emissions in mega cities or biomass burning in combination with changes in meteorology or/and long range transport of precursor emissions [Cooper et al., 2014, Duncan et al., 2016, Giglio et al., 2013, Hilboll et al., 2013b, 2017, Schneider et al., 2015, Wai et al., 2014]. On the other hand, tropospheric  $O_3$  decreases by  $\sim 3$  DU/decade over the Caribbean sea and parts of North Pacific Ocean, as well as by less than 2 DU/decade over some regions of the southern Pacific Ocean. Possible reasons for this decrease could be changes in dynamical processes, such as changes in STE, convection, humidity or precipitation [Adler et al., 2003, Chen and Liu, 2016, Ebojie et al., 2016, Fontaine et al., 2011, IPCC, 2007, Mieruch et al., 2014, Morris et al., 2010, Trenberth et al., 2005, Wai et al., 2014]. The biggest limitation interpreting the observed trends over the northern and southern tropical latitudes ( $> 18^\circ N$  and S) is the low data sampling at these latitudes. Due to the ITCZ movement, cloudy data during local winters are reduced, making the above cloud ozone column (ACCO) retrieval difficult or violating the invariance of the ACCO per latitude band. Therefore, even though they might appear to be statistically significant, they should be referred to with caution.

The comparison of tropospheric ozone trends from the current study with trends using ozonesonde data from six SHADOZ stations showed that our results are within the  $2\sigma$  uncertainty of the ozonesonde trends. Focusing on trends in ten selected mega-cities, a slight tropospheric ozone decrease is observed at the largest cities, such as Jakarta and Mexico ( $\sim -0.3$  DU/decade), whereas statistically significant increases ( $\sim 1$  DU/decade) are noticed over Manila, Bangkok, and Kinshasa. It has been shown that tropospheric ozone increase is not linearly related with the size and the industrialisation of the selected mega-cities. This is not surprising since tropospheric ozone production from its precursors,  $NO_x$  and VOCs, is not linear. For example, very large increase of  $NO_x$  or VOCs may result in strong destruction of ozone (see Chapter 1, subsection 1.2.1). It is also broadly recognised that the mechanisms that modulate tropospheric ozone variability are not straightforward according to precursor emission, in addition meteorological conditions and atmospheric oscillations may play also an important role [Chandra et al., 2009, Monks et al., 2015, Neu et al., 2014, Solomon et al., 2007, Voulgarakis et al., 2010, WMO, 2011, Ziemke and Chandra, 2003]. Comparing the trend results in these ten mega-cities from the current study with Heue et al. [2016] and Ebojie et al. [2016], we found that they agree slightly better (within the combined uncertainties) with the ones from Heue et al. [2016]. The most possible reasons for the mismatch with Ebojie et al. [2016] is the fact that their retrieval reaches up to the tropopause including more upper-tropospheric ozone information and additionally the fact that they investigated a shorter time period between 2003 and 2012.

In summary it can be stated that this chapter provides a unique sensitivity analysis of trend uncertainties based on different TCO harmonisation approaches. Additionally, detailed tropical tropospheric O<sub>3</sub> changes are presented here on global and regional scale. The attribution of observed trends in specific regions to the various processes is not possible based on the current analysis and is out the scope of this chapter. Such a study would require additional multi-annual chemical transport model (CTM) simulations in order to differentiate between contributing processes (chemistry and meteorology).

The launch of Sentinel 5 precursor (S5p) satellite on the 13<sup>th</sup> of October 2017, will extend the TCO record at least for 7 more years (expected lifetime). It is also expected that the extension of the time-series will result in more reliable trend results. The grid box size used in this study was relatively coarse (2.5°×5° degrees), due to the instruments spatial resolution (GOME pixel ≈320 km), and in order to remove the residual noise. The high spatial resolution (7×7 km) of the TROPOMI instrument aboard S5p will also improve the tropospheric ozone trend estimates over mega-cities.



## Variability of tropical tropospheric ozone

The analysis of tropical tropospheric ozone global distribution is a precondition for understanding changes in its natural variability. Therefore, this chapter focuses on presenting the mean seasonal zonal concentrations of tropospheric O<sub>3</sub> along with its longitudinal monthly concentration and anomalies throughout the period 1996 up to 2015. Finally, the 20 year CCD climatology is compared with other studies. The second part of this chapter focuses on quantifying the contribution of oscillating factors such as ENSO, QBO, solar, and seasonal cycles to tropospheric ozone variability, without aiming at quantifying and separating between chemical and dynamical contributors.

### 5.1 Seasonal and annual variability of tropospheric ozone

The global and seasonal distribution of tropospheric ozone is a balance between production and loss processes, along with transport in the atmosphere. Using 20 years of harmonised TCO data, a tropical tropospheric ozone mean state sorted by seasons can be established. This climatology can be useful as background information to understand the chemical cycles of reactive trace gases in the atmosphere and for validating model simulations.

The seasonally averaged TCO in winter (DJF), spring (MAM), summer (JJA), and autumn (SON), are shown in Fig. 5.1. The characteristic wave-one pattern is persistent for all seasons, with higher tropospheric ozone columns over the South Atlantic (~ 40 DU) and lower values over the Pacific Ocean (~ 15 DU). Enhanced ozone columns (~ 35 DU) appear over the northern Atlantic and the northern tropical Pacific Ocean in winter and spring. The maximum over the north Atlantic can be explained by the northern tropical biomass burning season in December–February, ozone production from lightning, and large-scale transport [Martin et al., 2002, Sauvage et al., 2006, Thompson et al., 2003]. The maximum over the north Pacific ocean coincides with the location of the subtropical jet stream and as a result it is influenced by stratosphere-troposphere exchange (STE). The stratospheric winter circulation transports more ozone to middle and high latitudes. The Rossby waves break at the location of the subtropical jet stream (30°-40°) and transport stratospheric air into the tropical upper and middle troposphere [Neu et al., 2014]. One other factor contributing to this maximum, is the persistent anticyclone located over the Pacific which transports air from Asia towards North America

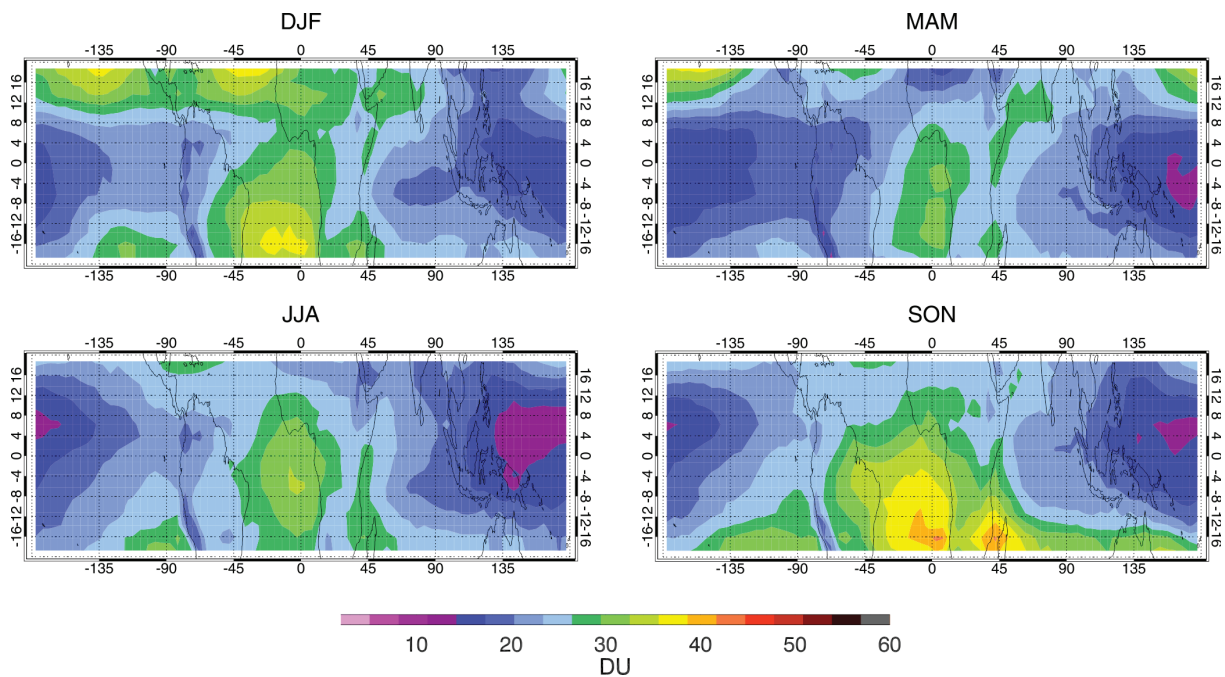


Figure 5.1: Seasonally averaged harmonised tropical tropospheric ozone columns (TTCO) derived from the CCD technique between 1996 and 2015.

during winter and spring [Oltmans et al., 2004].

Tropospheric ozone increases further during austral spring/summer over the South Atlantic and South-West Indian Ocean. Especially during autumn/winter, tropospheric ozone over the South Atlantic Ocean exceeds 40 DU. Although this area is affected by enhanced upper tropospheric  $\text{NO}_x$  concentrations from lightning, meteorology may play the major role in tropospheric ozone burden over the oceans [Edwards et al., 2003, Murray et al., 2013]. Fishman et al. [1996] during TRACE A campaign showed that throughout the biomass burning seasons, June-July and October-November, tropospheric ozone precursor spread both from South America and southern Africa over the South Atlantic Ocean. These precursors are transported by southeast or northeast trade winds and are accumulating at the equatorial region between the near-surface monsoon flow and the easterly flow above 4 km, so that ozone can be in-situ photochemically produced in large quantities [Thompson et al., 2014, WMO, 1996]. Sauvage et al. [2007], using MOZAIC airborne measurements confirmed that the African Easterly Jet (AEJ), centered at 650 hPa, allows transport of ozone and precursors westward to Nigeria during the North hemisphere winter (DJF) dry season. Fishman et al. [1996] during SAFARI-92 campaign showed that smoke and haze observed over South Africa during austral spring (wet season) originate from northern countries (central Africa) exiting off the east coast towards the Indian Ocean. This outflow was also confirmed in the SAFARI-2000 campaign [Swap et al., 2003] and was denoted as the "river of smoke". In this way, air masses from the burning regions in northern Africa can enter a meteorological system which allows them to be transported out over the Atlantic where they can produce tropospheric ozone thousands of kilometers away from the precursor sources [Jonquieres et al., 1998].

In contrast to seasonal variations around the Atlantic Ocean that may exceed 10 DU, the seasonality is weak in the Pacific Ocean region, with variations of  $\sim 5$  DU or less between the seasons. Minimum

tropospheric ozone values are noticed in this area during winter-spring months. The Pacific Ocean is considered to be an ozone clean area as a result of the strong convective uplift (warm pool) which works as a photochemical sink for ozone in all seasons [Newton et al., 2016, O'Connor et al., 2004, Rex et al., 2014]. Ozone loss in the remote troposphere is controlled by its photolysis to atomic oxygen (O(1D)), followed by the reaction of O(1D) with water (H<sub>2</sub>O) to produce two hydroxyl radicals (2OH) as shown in reactions 1.23 to 1.27. The increased sea surface temperatures result in enhanced water vapor concentration and in combination with low overhead (stratospheric) ozone that results in high actinic fluxes of  $\lambda < 340$  nm, maximise the efficiency of ozone loss over the west Pacific Ocean [Rex et al., 2014].

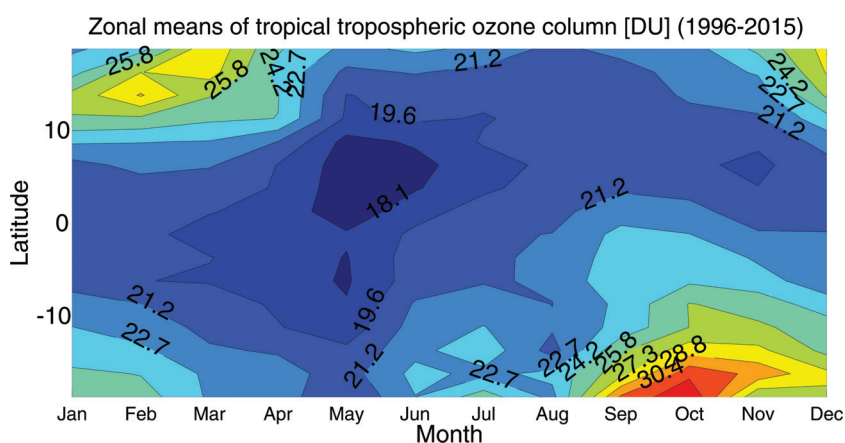


Figure 5.2: Zonal mean climatology (1996-2015) of tropical tropospheric ozone columns in DU using the harmonised CCD dataset. Latitude intervals are 2.5°. Values in DU.

Figure 5.2 and Table 5.1 present the twenty-year zonal mean climatology of tropical tropospheric ozone. The lowest ( $\sim 17$  DU) TTCO occur towards the Equator, especially during boreal spring. TTCO has two distinctive maxima, one during winter-early spring over the northern tropics ( $\sim 26$  DU), and the other during autumn-early winter over the southern tropics ( $\sim 30$  DU). The pattern of the CCD TTCO climatology agrees well with the OMI/MLS climatology by Ziemke et al. [2011] and with EMAC simulations by Righi et al. [2015]. However, in the case of EMAC, the magnitude of the maxima is higher ( $\sim 45$ -50 DU). The fact that the EMAC tropospheric columns go up to tropopause while CCD ozone columns are limited to an altitude of  $\sim 200$  hPa may explain in parts the differences noted here.

Fig. 5.3 shows Hovmöller diagrams of monthly means and anomalies of tropical tropospheric ozone from 1996 to 2015 averaged between 10°S and 10°N. Hovmöller diagrams are very helpful for displaying variability on long-term time scales as a function of longitude. Fig. 5.3 (left) depicts the monthly mean tropospheric ozone columns in absolute units. The inter-annual tropospheric ozone variability is well-pronounced, comprising a wave-one pattern, with maximum values over the Atlantic ( $\sim 35$  DU) and minimum values ( $\sim 5$ -10 DU) over the Pacific for all years. The influence of the El Niño Southern Oscillation (ENSO) is also notable on the ozone anomalies, appearing as an east-west "dipole" feature [Ziemke et al., 2010]. During El Niño events (1997-98, 2002-03, 2004, 2006-07, 2010-09 and 2015), TTCO decreases by 10-15 DU over the east Pacific Ocean (110°W-180°W) and during la Niña conditions (1996, 1999-2000, 2006, 2008-09, 2011-12) TTCO may increase by the same amount in the

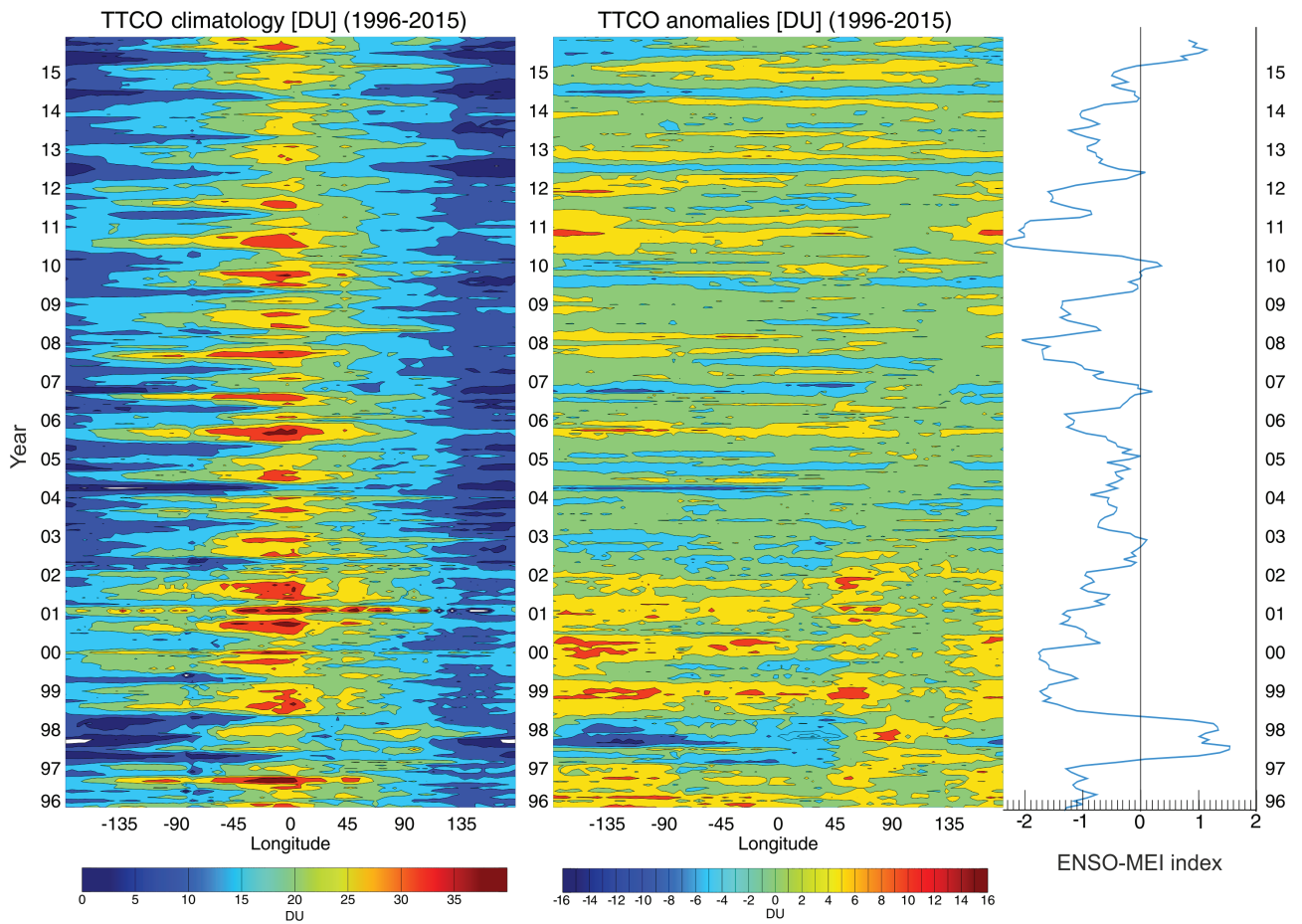


Figure 5.3: Time versus longitude plot of CCD tropical tropospheric ozone; Left: absolute value. Middle: anomalies from January 1996 to December 2015. Right: the ENSO-MEI index [Wolter and Timlin, 1993, 1998].

Table 5.1: Zonal climatology of tropical tropospheric ozone column.

Latitude	Jan	Feb	Mar	Apr	May	Jun	Jul	Aug	Sep	Oct	Nov	Dec
-20° – -17.5°	25	25	22	22	20	23	24	22	31	33	26	27
-17.5° – -15°	25	24	22	22	21	23	22	23	27	31	30	28
-15° – -12.5°	23	23	21	21	20	22	24	21	26	28	28	25
-12.5° – -10°	23	22	21	20	19	22	23	21	23	26	26	25
-10° – -7.5°	22	21	20	19	18	21	22	21	23	26	25	23
-7.5° – -5°	20	20	20	19	18	20	21	21	24	24	23	22
-5° – -2.5°	20	20	20	19	18	20	21	21	23	24	22	21
-2.5° – 0°	20	20	19	19	18	20	21	21	23	23	21	21
0° – 2.5°	20	20	20	19	17	19	20	21	22	22	20	21
2.5° – 5°	20	20	20	20	17	18	19	20	21	21	20	21
5° – 7.5°	21	22	21	20	17	18	19	20	20	20	19	21
7.5° – 10°	23	23	23	21	18	18	20	20	21	21	20	22
10° – 12.5°	26	25	24	24	19	20	20	20	21	21	21	24
12.5° – 15°	26	29	26	24	20	20	20	20	20	21	22	26
15° – 17.5°	24	27	28	24	21	21	21	20	20	22	23	27
17.5° – 20°	22	24	29	24	22	23	22	21	22	22	25	28

same region. Over the west Pacific Ocean (70°E–140 °E) tropospheric ozone increase may reach up to 15 DU during El Niño . These findings are in agreement with studies from Doherty et al. [2006], Ziemke et al. [2010], Oman et al. [2011], and Murray et al. [2013]. The effect of ENSO on tropical tropospheric ozone will be further discussed in Chapter 6 where the observations are compared with model results from a chemistry climate model (CCM).

## 5.2 ENSO, QBO, Solar and seasonal cycle response to tropical tropospheric ozone

As discussed in Section 4.2 there are several factors that can modulate tropospheric ozone variability. The multi-linear regression model (described in Section 4.2) have been used to investigate the oscillating factors that can contribute to tropospheric ozone change. The minimum response of ENSO, solar activity and the two QBO indices to the tropical tropospheric ozone fitted time-series for each grid box has been subtracted from the maximum response ( $FitCoef \cdot (max(index) - min(index))$ ). The QBO contribution on tropospheric ozone changes for the combined QBO indices and the seasonal cycle have been calculated as:  $max(\sum(FitCoef)_i \cdot (index)_i) - min(\sum(FitCoef)_i \cdot (index)_i)$ , where  $i$  is the the  $i_{th}$  QBO proxy or  $i_{th}$  seasonal term used in the regression (2 terms for QBO, 6 for seasons). Regions marked with (x) show statistically non-significant contributions from the processes considered. Figure 5.4 a), shows that ENSO contribution is positive ( $\sim 7$  DU) over the west Pacific Ocean (70°E–140 °E) and

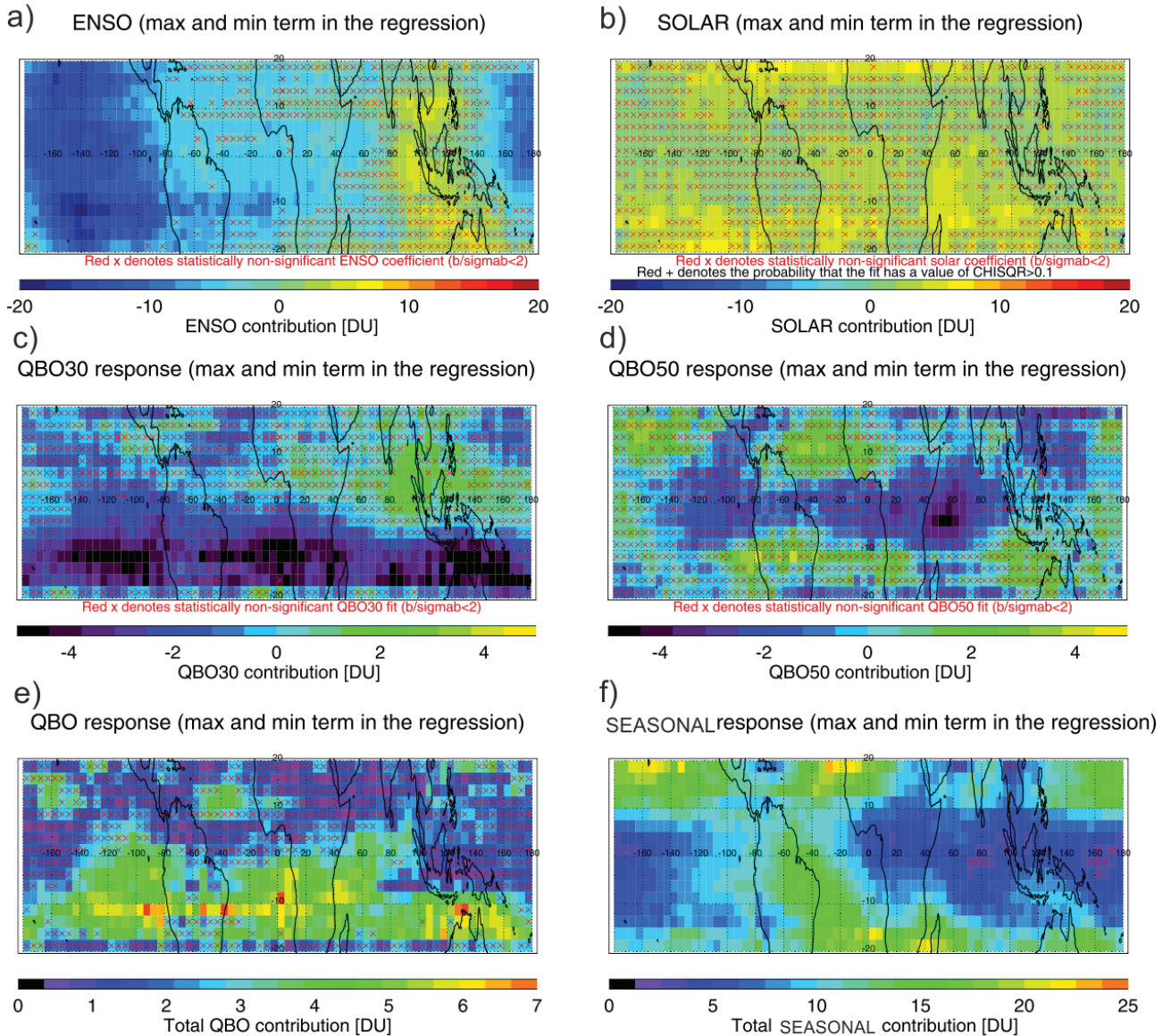


Figure 5.4: Contribution of various factors responsible for tropospheric ozone variability. Their response is derived by subtracting the minimum from the maximum proxy response in the time-series for each grid box. For a)-d) the contribution of each parameter is calculated as:  $\text{FitCoef} \cdot (\max(\text{index}) - \min(\text{index}))$ . For e) and f) the total contribution is calculated as:  $\max(\sum(\text{FitCoef})_i \cdot (\text{index})_i) - \min(\sum(\text{FitCoef})_i \cdot (\text{index})_i)$ , where  $i$  is  $i_{th}$  QBO proxy or  $i_{th}$  seasonal term used in the regression. Grid-boxes marked with "x" are statistically non-significant at the 95% confidence level. For e) and f) red "x" is marked only when all the parameters are statistically non-significant.

negative ( $<10$  DU) over the east Pacific Ocean ( $110^{\circ}\text{W}$ – $180^{\circ}\text{W}$ ). This behavior is consistent with studies from Doherty et al. [2006] and Oman et al. [2011]. Using HadCM3 and GEOS-CHEM model simulations, respectively, they showed that the maximum positive ENSO response is located around  $60^{\circ}$ – $100^{\circ}\text{E}$  in the upper troposphere for altitudes greater than 10 km and the maximum negative response is located at  $120^{\circ}$ – $140^{\circ}\text{W}$ , above 5 km height. Ziemke et al. [2010] used this dipole tropospheric ozone response to develop the so-called "Ozone ENSO Index" (OEI) by subtracting mean eastern Pacific total column ( $15^{\circ}\text{S}$ – $15^{\circ}\text{N}$ ,  $110^{\circ}\text{W}$ – $180^{\circ}\text{W}$ ) from the mean western Pacific ( $15^{\circ}\text{S}$ – $15^{\circ}\text{N}$ ,  $7^{\circ}\text{E}$ – $140^{\circ}\text{E}$ ) total column. Although ENSO contributes to inter-annual tropospheric ozone variability, Ziemke et al. [2015] showed that its influence in the tropics is small compared with the combined intra-seasonal/Madden-Julian Oscillation (MJO) [Madden and Julian, 1971] acting on short (weekly) time scales.

QBO has a strong impact on stratospheric circulation which consequently affects the tropical tropospheric circulation via STE. As a result it may increase or decrease tropical tropospheric ozone. According to Figures 5.4.c, d and e, the QBO signal on tropospheric ozone is rather weak ranging from -4 to 4 DU for the QBO index at 30 hPa (Fig. 5.4.c) and 50 hPa (Fig. 5.4.d) level. Both coefficients are mostly statistically non-significant in the regression, with negative contribution (-4 – -2 DU) over the southern tropics and positive (3 DU) around Indonesia for the QBO<sub>30</sub> index. For the QBO<sub>50</sub> index, the contribution is mainly negative (-4 – -2 DU) along the equator and positive ( $\sim 3$  DU) over the northern tropical Atlantic Ocean. The total QBO signal (Fig. 5.4.e) has a larger contribution over the southern tropics reaching 5–6 DU. These maximum QBO response is in agreement with Ebojie et al. [2016] results, both in range and pattern. Neu et al. [2014] suggested that changes in the Brewer-Dobson circulation and tropospheric ozone are both correlated with QBO and ENSO. Although ENSO and QBO are not always in phase they are correlated ( $R=0.67$ ) from 2005 to 2010 [Neu et al., 2014]. According to Fig. 5.4a, 5.4c, 5.4d, and 5.4e the contributions of ENSO and QBO index at 30 hPa to tropospheric ozone seem to be correlated over the south-eastern Pacific Ocean and over Indonesia.

The 11 year solar cycle affects the chemistry and thermal structure of the atmosphere and as a result alters tropospheric ozone [Chandra et al., 1999]. The solar cycle contribution is mostly statistically significant and positive and varies by up to 5 to 7 DU (see: Fig. 5.4b). The seasonal tropospheric ozone variability is largest over the northern tropics and south Atlantic by about 15 DU (Fig. 5.4f). Elsewhere, the seasonal variations of tropospheric ozone are on the order of 5–10 DU.

### 5.3 Summary and discussion

The tropical tropospheric columns of ozone from 20 years (1996–2015) of harmonised CCD measurements present the distinctive wave-one pattern for all seasons, maximizing ( $\sim 40$  DU) over the south Atlantic Ocean in autumn while having low values ( $<15$  DU) over the Pacific Ocean. The zonal mean TCO climatology agrees well in pattern and magnitude with Ziemke et al. [2011] TCO climatology using OMI/MLS data from October 2004 through December 2010. An agreement in pattern is also noticed with Righi et al. [2015] climatology using EMAC simulations of tropospheric ozone. Nevertheless the amplitude of EMAC TCO is larger since the simulations reach up to the tropopause.

Longitudinal tropical ( $10^{\circ}\text{S}$ – $10^{\circ}\text{N}$ ) tropospheric ozone anomalies show an ENSO response, with decreasing ozone (10–15 DU) over the eastern Pacific Ocean ( $110^{\circ}\text{W}$ – $180^{\circ}\text{W}$ ) during El Niño events

and increasing ozone (10–15 DU) over the western Pacific (70°E–140 °E) during La niña events. The response of tropospheric ozone proxies such as, ENSO, QBO, the solar, and the seasonal cycle have been quantified by applying the multi-linear regression model as discussed in chapter 4.2. ENSO is found to contribute by up to +7 DU over the Indian and western Pacific Oceans and by -10 DU over the eastern Pacific Ocean during 1996 to 2015. The location and magnitude of ENSO contribution to tropical tropospheric ozone variability agrees well with results from Doherty et al. [2006], Oman et al. [2011] and Ziemke et al. [2010]. Tropospheric ozone increases by  $\sim 7$  DU due to solar cycle over parts of the northern and southern tropics. QBO contributes in total  $\sim 5$  DU to the tropical tropospheric ozone variability, mainly over the southern tropics. The seasonal cycle has a stronger contribution in tropospheric ozone over the northern tropics and the Atlantic Ocean on the order of  $\sim 15$  DU and elsewhere its total contribution is less than 10 DU. The seasonal cycle of tropospheric ozone is the weakest over the west Pacific ( $< 5$  DU).

In conclusion the seasonal, latitudinal and longitudinal tropical tropospheric ozone variability has been studied and the contribution of various climatological factors such as ENSO, QBO, the solar, and the seasonal cycle on its variability throughout the last 20 years has been quantified in this chapter. As discussed in section 4.3, the attribution of TTCO variability to the various chemical processes that modulate ozone is a task that requires particular chemical transport model CTM simulations. In Chapter 6 a chemistry-climate model (CCM) is used in order to interpret the influence of El Niño events on tropical tropospheric ozone as a special case. However, background ozone is large enough to be able to identify pure transport events of ozone. Monthly tagged CTM runs could give an insight into tropospheric ozone sources for specific locations (e.g. Coates et al. [2015]). With this method, the fate of emitted species is followed, and a track of their chemical reaction pathways is made. Using labeled CTM mechanisms for  $\text{NO}_x$  and VOCs emissions, and their degradation products, the ozone burden can be attributed to the relevant emission source [Coates et al., 2015, Grewe et al., 2012].

## El Niño and tropical tropospheric ozone

This chapter's focus is on studying the influence of ENSO on tropospheric ozone and its precursors. The pattern and magnitude of tropospheric ozone anomalies during two El Niño and two La Niña events are presented and compared between them and with other studies. The influence of 2015 El Niño event on tropospheric ozone is investigated in more detail. For this study, tropospheric NO<sub>2</sub> columns, total CO columns, fire counts and chemistry-climate model (CCM) simulations of tropospheric ozone along with its precursors are used in order to compare them with the observed CCD TCO anomalies. In addition, tropospheric ozone simulations between September to December 2015 when El Niño was active are used to quantify the influence of biomass burning and dynamics in tropospheric ozone changes.

### 6.1 El Niño Southern Oscillation (ENSO) and its influence on tropospheric ozone

The influence of El Niño Southern Oscillation (ENSO) on tropospheric ozone has been extensively studied in the past using in-situ and satellite measurements in combination with global chemical transport models [Chandra et al., 2009, Doherty et al., 2006, Logan et al., 2008, Murray et al., 2013, Neu et al., 2014, Oman et al., 2011, Randel and Thompson, 2011, Randel et al., 2009, Thompson et al., 2001, Valks et al., 2003, Xie et al., 2014, Ziemke et al., 2010, 2015]. ENSO causes periodical changes in the sea surface temperature distribution in the Pacific Ocean. The sea temperature changes impact the troposphere, by modulating the Walker circulation [Bjerknes, 1966] which modifies the temperature and moisture fields across the tropical Pacific. During neutral ENSO conditions the Pacific warm pool is located over Indonesia creating a strong up-welling stream. These rising air masses are cooled near the Tropopause and continue moving along the equator in two adverse directions until they descend over the Indian and east Pacific Ocean, creating two reverse loops, the so-called Walker circulation. During the warm phase of ENSO (El Niño conditions), the warm pool (> 30°C) is displaced towards the east Pacific coast, near Ecuador and Peru, forming a low pressure system there and a high pressure system over Indonesia. During El Niño, three circulation loops are created. Up-welling air masses are located over Tahiti, Peru and Ecuador while down-welling air masses are located over north Australia/Indonesia and over the east Pacific Ocean [McPhaden et al., 2006]. This modification of the

Walker circulation, causes more dryness combined with more forest fires over Indonesia where humans use fires as a deforestation and fertilization tool [Chandra et al., 2009, Page et al., 2002]. After the end of the warm ENSO phase, the normal sea and atmospheric circulation are re-established. Nevertheless, for some months, the sea temperature near the coast of Peru drops significantly ( $\sim 20^\circ\text{C}$ ). This situation, known as La Niña can be considered as the opposite, cold phase of ENSO. Although the anomalies are of the opposite sign, the spatial patterns are different compared to El Niño [Larkinal et al., 2002].

Tropospheric ozone is very sensitive to these dynamical changes and is expected to respond accordingly. The dislocation of the up-welling centers is expected to alter the ozone losses and production areas. Lelli et al. [2014] showed that low clouds are lifted higher up in the eastern Pacific Ocean during El Niño. Convection induces more ozone being transported to the upper troposphere as well as more clouds and water vapor being released. Clouds, water vapor and rainfall contribute sequentially to photochemical loss of ozone (see Section 5.1). Reduced rainfall and suppressed convection reduces ozone loss leading to higher ozone amounts. Although dynamical changes are fundamental, there is evidence that additional atmospheric chemistry is occurring due to anthropogenic influences [Chandra et al., 2002, 2009, Doherty et al., 2006, Logan et al., 2008, Ziemke et al., 2009b, 2015]. ENSO-driven droughts over Indonesia may result in more forest fires and consequently in tropospheric ozone precursor emissions from biomass burning. Several studies have been made in the past to investigate the influence of convection, meteorology, and biomass burning on tropospheric ozone during El Niño. For example, Chandra et al. [2002] showed that the tropical tropospheric ozone integrated over the tropical region between  $15^\circ\text{N}$  and  $15^\circ\text{S}$  increased by 6-8 Tg above the climatological mean of 77 Tg. Using the GEOS-CHEM model, they suggested that biomass burning and dynamical conditions contribute almost equally ( $\sim 10\text{-}12$  DU) to the tropospheric ozone increase over the Indonesian region. Ziemke et al. [2009b] using the Global Modelling Initiative (GMI) chemical transport model showed a 4-5% increase in global tropospheric ozone due to biomass burning with most contributions coming from the tropics during 2006 El Niño year. Almost half of these increases originated from El Niño related fires in Indonesia. They conclude that biomass burning does not produce large amounts of ozone, however increases vigorously its precursors by 7-9% in  $\text{NO}_x$  and 30-40% in CO during the months of greatest burning. Nevertheless, these increases in ozone precursors are more important in regional scales. In longer timescales, convection and advection have a more dominant role in the tropical Pacific region [Ziemke et al., 2015]. For the same El Niño of 2006, Chandra et al. [2009] calculated the biomass burning influence in tropospheric ozone using OMI/MLS tropospheric ozone retrievals equals to 4–6 DU over Indonesia, where the forest fires are maximum. The dynamical component was about 4–8 DU, covering a much broader area in the Indian Ocean. After December, when the biomass burning is ending, the main drivers on tropospheric ozone increases are atmospheric dynamics [Chandra et al., 2009]. The carbon emissions from the 2015 fires have been the second largest in the maritime south-east Asia after the 1997 El Niño [Huijnen et al., 2016]. The total carbon released from biomass burning during the period of September–October 2015 was  $227 \pm 67$  Tg C. During September–October 1997, the total carbon release from fires was 866 Tg C, four times more than in 2015 [Randerson et al., 2015].

Evidently ENSO events have different strengths and subsequently different effects on tropospheric ozone. Several indexes have been developed for identifying El Niño and La Niña events. In the following

Section 6.2 we attempt to study the influence of different ENSO events on tropospheric ozone by using the Multivariate ENSO Index (MEI) [Wolter and Timlin, 1993, 1998, 2011]. The main focus of this study is to compare the geographical extend, the magnitude, and the amplitude of tropospheric ozone anomalies between two El Niño and two La Niña events and to investigate whether a relationship between the strength of ENSO and the observed tropospheric ozone anomalies exists. The drivers of TTCO anomalies are further studied in Section 6.3 for the case of 2015 El Niño.

## 6.2 Comparing the influence of El Niño and La Niña events on tropical tropospheric ozone

Two regions have been selected to study the regional effects of ENSO on tropospheric ozone. The first region is in Brasilia (7.5 °S–0 °, 45 °W–60 °W) and the second, Indonesia–Sumatra (7.5 °S–0 °, 95 °E–110 °E). The Brazilian region is expected to be affected by increased rainfall and humidity during El Niño events and by drought during La Niña which means that tropospheric ozone is expected to increase during La Niña and to decrease during El Niño Chandra et al. [2002, 2009], Doherty et al. [2006], Logan et al. [2008], Ziemke et al. [2015]. The opposite behaviour is supposedly the case in Sumatra.

Figure 6.1 shows the time-series of tropospheric ozone anomalies in the Brazilian region and Sumatra, along with the Niño MEI index, and the Fire Radiative Power (FRP) for both tropical regions between 1996 and 2015. Positive values of the ENSO MEI index indicate El Niño months and negative values La Niña. In Brasilia, tropospheric ozone is decreasing by ~6–8 DU during El Niño (1997 and 2015) whereas it increases by ~10 DU during La Niña years. The opposite behaviour can be noticed in Indonesia where ozone increased by ~6–8 DU during El Niño events. The biomass burning in South America maximises during autumn and it is even more intense during La Niña years ( $> 25 \text{ mW/m}^2$ ), supplying additional ozone precursors in South America. The strongest TTCO increase is noticed during the winter of 1999 and the summer of 2010 (one of the strongest La Niña years). During El Niño months of May–June 2004, October 2005 and August–September 2006 extreme fires are present in this region, while the ozone anomalies are less than -5 DU. Ozone is either destroyed by the excess of VOCs or  $\text{NO}_x$  released from these fires or the precursors are transported by atmospheric dynamics away from the source resulting in ozone production away from the region of study. The maximum ozone increase in Indonesia is observed during the strong 1997 and 2015 El Niño events. Biomass burning in Indonesia also maximises during autumn ( $22\text{--}25 \text{ mW/m}^2$ ) although it is less than in Brasilia ( $25\text{--}30 \text{ mW/m}^2$ ). During El Niño years, the FRP exceeds  $20 \text{ mW/m}^2$ , increasing tropospheric ozone precursors emissions in the Indonesian region. However, the intense fires in 2004 and 2005 seem to have no effect on tropospheric ozone. It is difficult to attribute the  $\text{O}_3$  decrease during summers of 2003, 2014 and 2015 (El Niño) to precursor emissions or dynamics.

For global influence of ENSO on tropical tropospheric ozone, two major El Niño and La Niña events from the last 20 years have been selected. The two most intense El Niño events occurred during May 1997 to April 1998 and January 2015 until May 2016. The strongest effects on tropospheric ozone are usually observed during boreal autumn. The maximum sea surface temperature anomalies appear

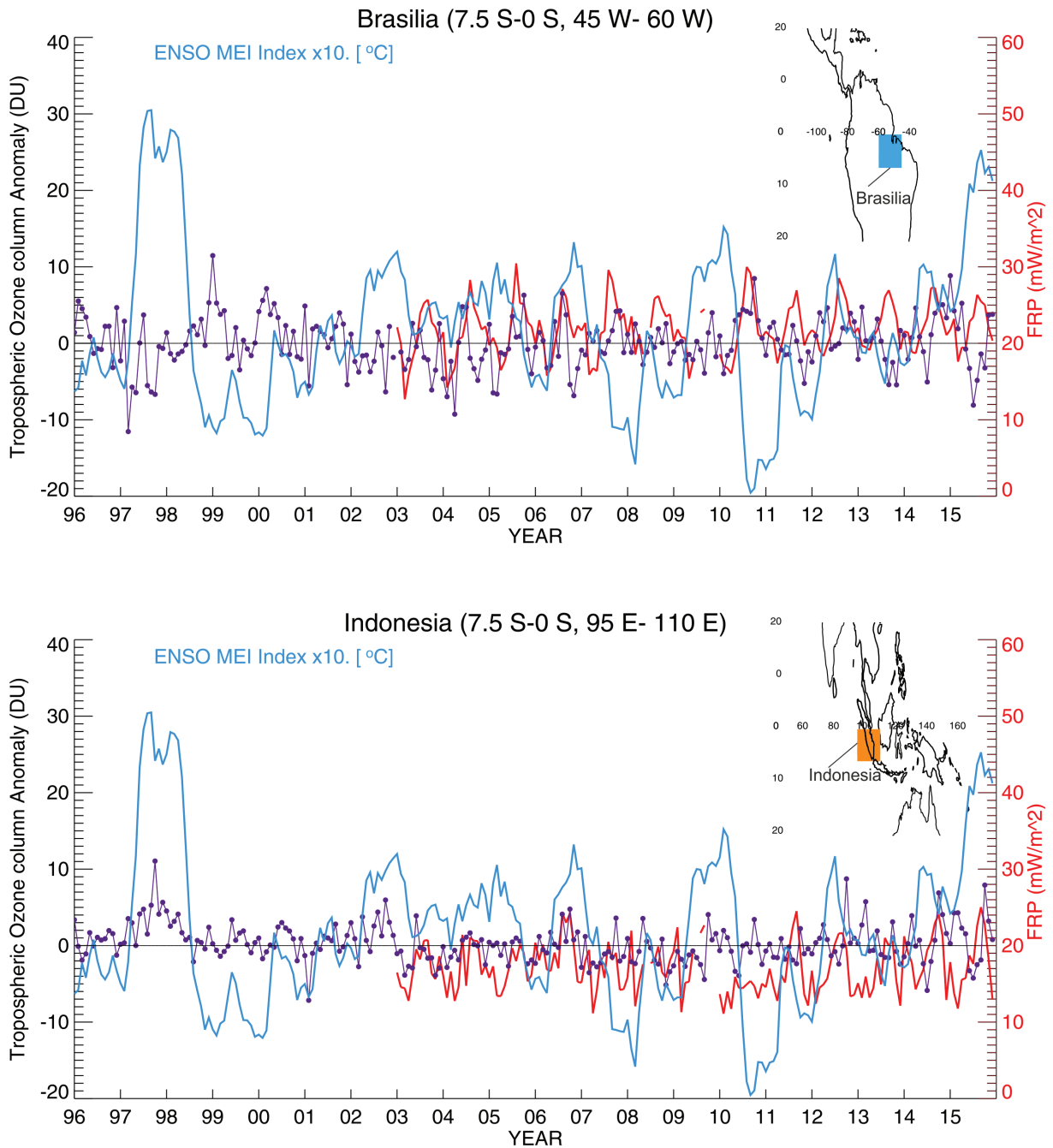


Figure 6.1: Monthly tropical tropospheric ozone anomalies for the regions of Brasilia (7.5°S–0°S, 45°W–60°W) and Indonesia (7.5°S–0°S, 95°E–110°E) in DU are plotted with blue lines. The ENSO index in °C is plotted with light blue line, and the Fire Radiative power (FRP) in mW/m<sup>2</sup> is plotted with red line.

during September to December, when the drought and biomass burning maximizes over Indonesia, south-eastern Sumatra, and Papua. Two of the strongest La Niña years were during September 1999 to March 2000, following the intense 1997–1998 El Niño event and during July 2010 to April 2011.

Table 6.1: ENSO-MEI index for September–December 1997, 1999, 2010, and 2015. With bold are indicated the months with maximum (El Niño) and minimum (La Niña) ENSO-MEI index values [Wolter and Timlin, 2011].

Month	1997	2015	1999	2010
<b>Sep</b>	<b>3.0</b>	<b>2.5</b>	-1.0	<b>-1.9</b>
<b>Oct</b>	2.4	2.2	-1.0	<b>-1.9</b>
<b>Nov</b>	2.6	2.3	-1.0	-1.5
<b>Dec</b>	2.4	2.1	<b>-1.2</b>	-1.5

The ENSO MEI index for September–December 1997, 1999, 2010, and 2015 is shown in Table 6.1. Positive values represent the warm ENSO phase (El Niño), while negative values represent the cold ENSO phase (La Niña). The September MEI (in bold) represents the peak of both El Niño events, whereas December and September represent the peak 1999 and 2010 La Niña events. The harmonised TTCO dataset has been monthly averaged for the period 1996–2015 and the tropospheric ozone anomalies have been calculated by subtracting the climatological monthly means from the monthly data for September–December 1997, 1999, 2010, and 2015. Figure 6.2 and 6.3 depict the CCD tropical tropospheric ozone anomalies for the selected autumn months in 1997, 1999, 2010, and 2015.

According to Fig. 6.2 (left), 1997 El Niño caused a strong increase in tropical tropospheric ozone by about +10 DU over the Indian Ocean and Indonesia, with maximum spatial extent in October and December due to limited deep convective clouds over the western Pacific there is no above cloud column ozone retrieved in most of the cases. The negative anomalies during 1997 El Niño are on the order of -10 DU, reaching -20 DU over the central-east tropical Pacific in September and over parts of central Africa in November. Specifically in November, tropospheric ozone is decreasing by -8 DU over the Indonesian islands of Sumatra and Borneo, which are one of the largest sources of biomass burning in the Indonesian peninsula [Giglio et al., 2013, Randerson et al., 2015]. Chandra et al. [1998] suggest a smaller ozone decrease over the east Pacific, on the order of -8 DU, for October and December 1997 compared to 1996. Nevertheless, the same east-west dipole feature with positive ozone anomalies over Indonesia and the Indian Ocean and negative ozone anomalies over the east Pacific was noticed.

A different anomaly feature is noticed in 2015 (see Fig. 6.2 on the right), with larger spatial extent of positive anomalies than in 1997. The tropospheric O<sub>3</sub> increase is on the order of ~10 DU reaching locally +15 DU in September and October 2015. As shown here, the increase in TTCO is not limited only to the dry region of Indonesia, but extends over thousands of kilometers, covering the southern part of India to Fiji in the south, and westward to central Atlantic and the south American continent. For all months, tropospheric ozone decreased mainly on the southern tropics and the Pacific Ocean by about -10 DU, and especially over the south-east Pacific Ocean the decrease reached -20 DU in September and October. For November and December, the positive anomalies are spatially restricted, having values less than +10 DU. However, the positive tropospheric ozone anomalies during September and October 2015 had larger spatial extent and absolute values compared with the same months of 1997 despite the fact that the ENSO-MEI index was smaller in 2015 (see Table 6.1) and the reported fires released four

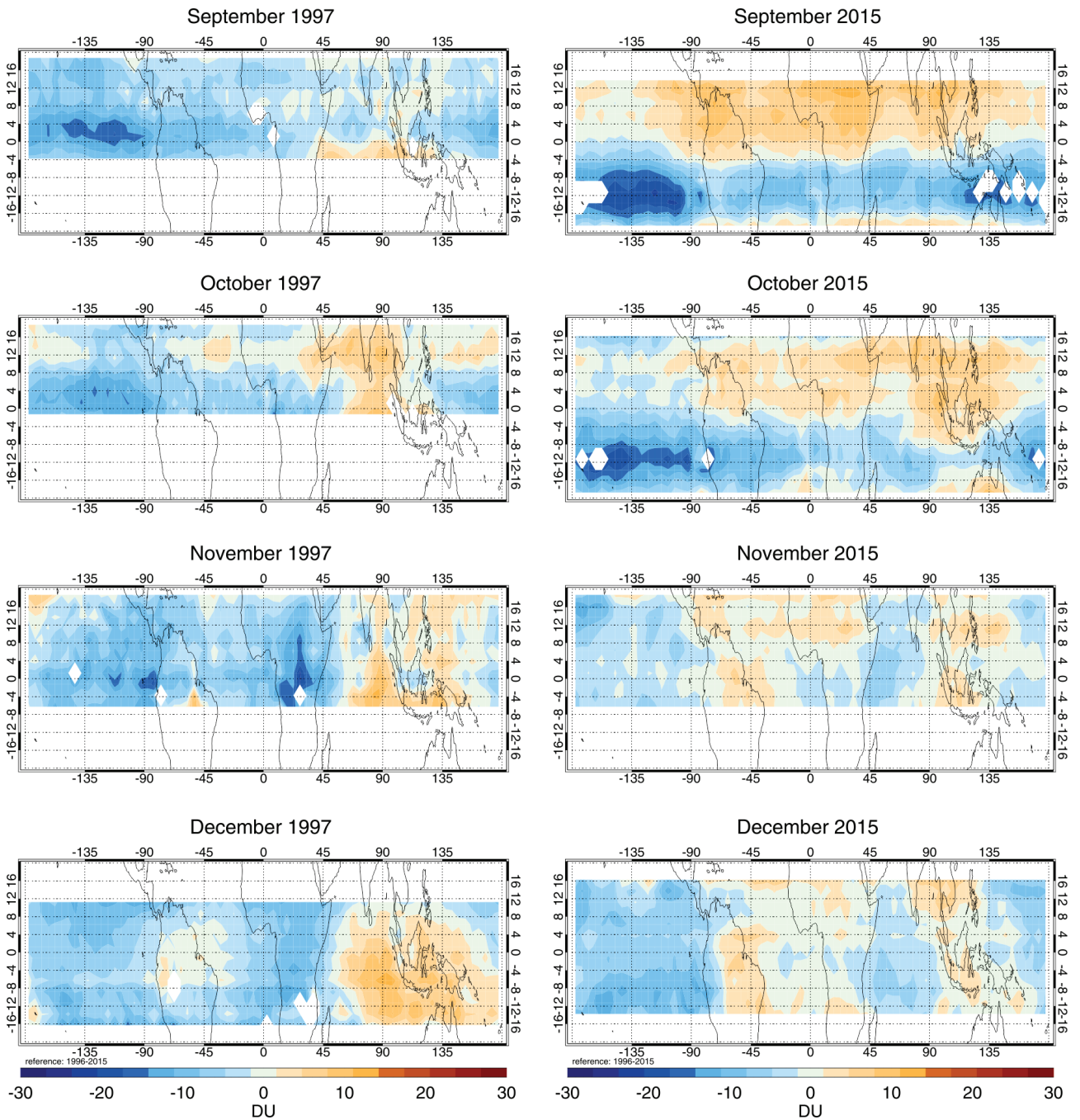


Figure 6.2: The tropical tropospheric ozone anomalies for September–December 1997 and 2015 calculated using as reference the monthly climatology produced from the harmonised CCD dataset during 1996–2015.

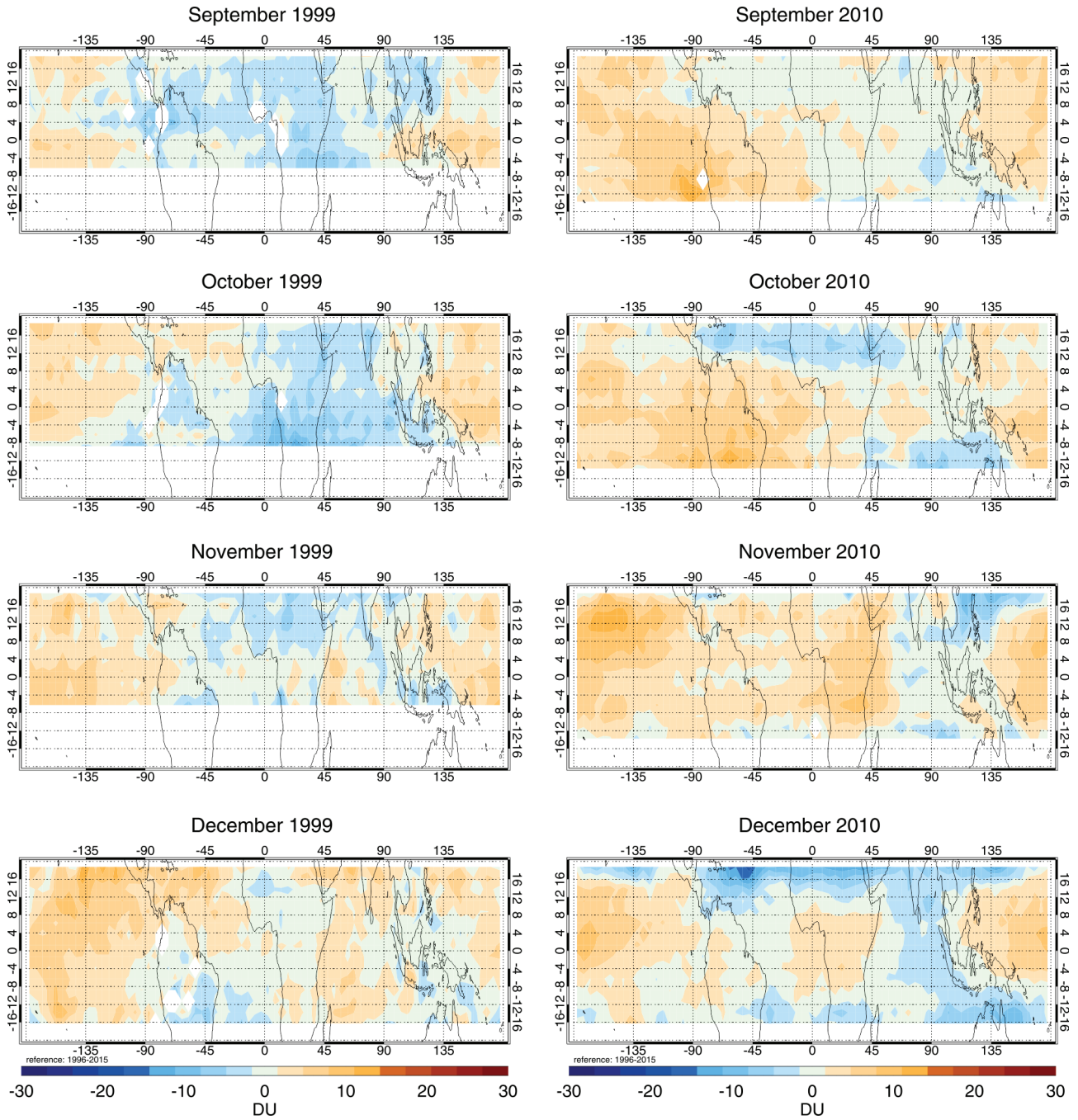


Figure 6.3: The tropical tropospheric ozone anomalies for September- December 1999 and 2010 calculated using as reference the monthly climatology produced from the harmonised CCD dataset during 1996-2015.

times less carbon than in 1997 in the Indonesian peninsula for the months September to November [Huijnen et al., 2016, Randerson et al., 2015]. The opposite situation appears in December when the spatial distribution of the positive ozone anomaly is much broader in 1997. In December the biomass burning season is mostly over and positive ozone anomalies can be attributed to atmospheric dynamics. The case of 2015 is further studied in Subsection 6.3 by comparisons with a global chemistry model to investigate possible causes of tropospheric ozone changes.

During 1999 La Niña tropospheric O<sub>3</sub> anomalies range between  $\pm 8$  DU. The anomalies between September to November present negative values over Africa, the Atlantic and Indian Ocean, and parts of northern South America, while positive O<sub>3</sub> values appear over the Pacific Ocean. In December, when La Niña is strongest, most of the tropics present increased tropospheric ozone by  $\sim +6$  DU with exception of South America, south Atlantic, parts of north Africa and Indonesia, where O<sub>3</sub> is slightly decreased by  $\sim 3$  DU. More specifically, during September and October we notice an increase in tropospheric ozone over Indonesia and the western Pacific despite the increased convection and precipitation in these area due to La Niña. It is assumed that this increase is attributable to the biomass burning. On the other hand over the eastern Pacific Ocean and South America, ozone increases slightly just after November 1999.

The 2010 La Niña was stronger than the corresponding 1999 event, with September and October 2010 being the most intense months. The positive TCO anomalies are on the order of 6–8 DU and cover most of the tropics with maximum values between September and November. O<sub>3</sub> decreased by  $\sim 10$  DU over the Indian Ocean and the northern tropics during October and December 2010. The notable difference between 2010 and 1999 La Niña is the strong tropospheric O<sub>3</sub> increase over South America in September and October 2010 and over central Africa during October–December 2010 compared with the moderate tropospheric O<sub>3</sub> changes in 1999.

Conclusively, the general pattern of the TCO anomalies during El Niño consist of a dipole with positive values ( $\sim 10$  DU) mainly over the western Pacific and Indian Oceans and secondarily over the central tropical Atlantic and South America. Negative TCO anomalies (10–17 DU) appear over the east Pacific Ocean due to the sea surface temperature (SST) and convection shifts. Atmospheric circulation during La Niña has the opposite effects in altering the TCO distribution. During La Niña events, CO and NO<sub>x</sub> emissions are reduced by a factor of 2–10 and 2–6 respectively compared to the El Niño years in the Indonesian region [Inness et al., 2015]. TCO is reduced over the Indian Ocean and central tropics by  $\sim 5$  DU whereas elsewhere it is enhanced by  $\sim 10$  DU for both La Niña years studied. The spatial distribution of positive tropospheric ozone anomalies during both La Niña events studied (1999 and 2010) is larger than the ones noticed for the El Niño years (1997 and 2015). This finding is in contrast with Ziemke and Chandra [2003] results who found that the changes in tropospheric column ozone during La Niña have similar spatial patterns and amplitudes as El Niño but reversed sign. The spatial distribution and magnitude of ozone anomalies varies significantly between the years considered here for both El Niño and La Niña. As shown in Figure A9, the differences in TCO between 2015 and 1997 El Niños range from about -10 to +25 DU. Despite the fact that 2015 El Niño was weaker compared with 1997, TCO anomalies had larger amplitude and spatial extent and accordingly, we could conclude that TCO anomalies are not directly proportional to the strength of an ENSO event. For the case of 2010 and 1999 La Niñas the differences are smaller, within  $\pm 10$  DU.

## 6.3 Tropical tropospheric ozone and its precursors during 2015 El Niño

Here, we compare the tropospheric ozone observations with other observables to evaluate the El Niño 2015 conditions in more detail. The tropospheric ozone anomalies between 2015 (strong El Niño) are compared with 2014 (neutral year with respect to El Niño and El Niña). The fire radiative power (FRP), CO and NO<sub>2</sub> emission measurements are compared in order to investigate the role of biomass burning and atmospheric dynamics during El Niño 2015. The CCD results are compared with tropospheric ozone columns (until 200 hPa) from a climate-chemistry model.

### 6.3.1 Tropospheric ozone precursors from satellite data

Biomass burning is the strongest source of ozone precursors during El Niño events [Chandra et al., 2002, 2009]. The location and strength of El Niño driven biomass burning areas are estimated using the Fire Radiative Power rates (FRP) (mW/m<sup>2</sup>) from MODIS (Moderate Resolution Imaging Spectroradiometer) [Justice et al., 2002, Kaufman et al., 1998] on board the TERRA satellite. MODIS measures brightness temperatures from different channels along with the distribution of other atmospheric constituents such as clouds and aerosols. When the temperature of a pixel exceeds a given threshold value, the pixel is classified as a fire pixel. Fire emissions are quantified by carbon monoxide (CO) total columns from MOPITT (Measurements of Pollution in the Troposphere), also on board, TERRA spacecraft [Drummond and Mand, 1996, Edwards et al., 2004]. Monthly averaged total columns of CO from MOPITT Version 7 data were used in this study with a spatial resolution of 1° × 1°. CO lifetime is in the order of years in the stratosphere therefore we assume that it is invariant for the years studied [Jacob, 2000]. MOPITT monthly gridded CO has been found to be consistent with those of TES [Luo et al., 2007a]. Most of the fires emit significant amount of NO<sub>x</sub> [Schreier et al., 2014]. NO<sub>2</sub> tropospheric columns are retrieved using upwelling radiances from GOME-2 on-board Metop-A [Callies et al., 2000] using the differential optical spectroscopy (DOAS) [Hilboll et al., 2013a,b, Richter et al., 2005]. NO<sub>2</sub> measurements are monthly averaged to 0.0625° square grids.

Figure 6.4 shows the Fire Radiative Power rates (FRP) (mW/m<sup>2</sup>) for Sept-Dec in 2014 and 2015 and their difference between 2015 and 2014. The FRP rates are increased in 2015 by about 5 mW/m<sup>2</sup> on average throughout the tropics. Some areas in Brasilia, southern Africa, Australia, and Indonesia show enhanced FRP by more than 10 mW/m<sup>2</sup> compared to 2014. FRP is lower over the African continent by 5 mW/m<sup>2</sup> and locally over Australia by more than 10 mW/m<sup>2</sup> compared to 2014. Figures 6.5–6.8 show the tropospheric NO<sub>2</sub> and total CO monthly mean abundances and differences between 2015 and 2014. NO<sub>2</sub> is higher in 2015 than in 2014 by about 0.5 – 1.5 × 10<sup>15</sup> mol/cm<sup>2</sup> (30-50%), with maximum differences observed over Brasilia and Indonesia (~2 × 10<sup>15</sup> mol/cm<sup>2</sup>). The strongest decrease in tropospheric NO<sub>2</sub> for 2015, reaching 1 × 10<sup>15</sup> mol/cm<sup>2</sup>, is noticed in September over the southern central tropics and the ITCZ and in December over the northern tropics and Australia. Total CO is higher in 2015 than 2014 by 2–4 × 10<sup>18</sup> mol/cm<sup>2</sup> (~60%), mainly over the Indian Ocean and south Atlantic. This increase in 2015 is not restricted to the areas of emission sources such as South America and Africa or locations surrounding tropical Mega-cities but also extends to areas such as Indian Ocean which is considered to be relatively clean. NO<sub>2</sub> lifetime is less than 15 days in the troposphere (~15

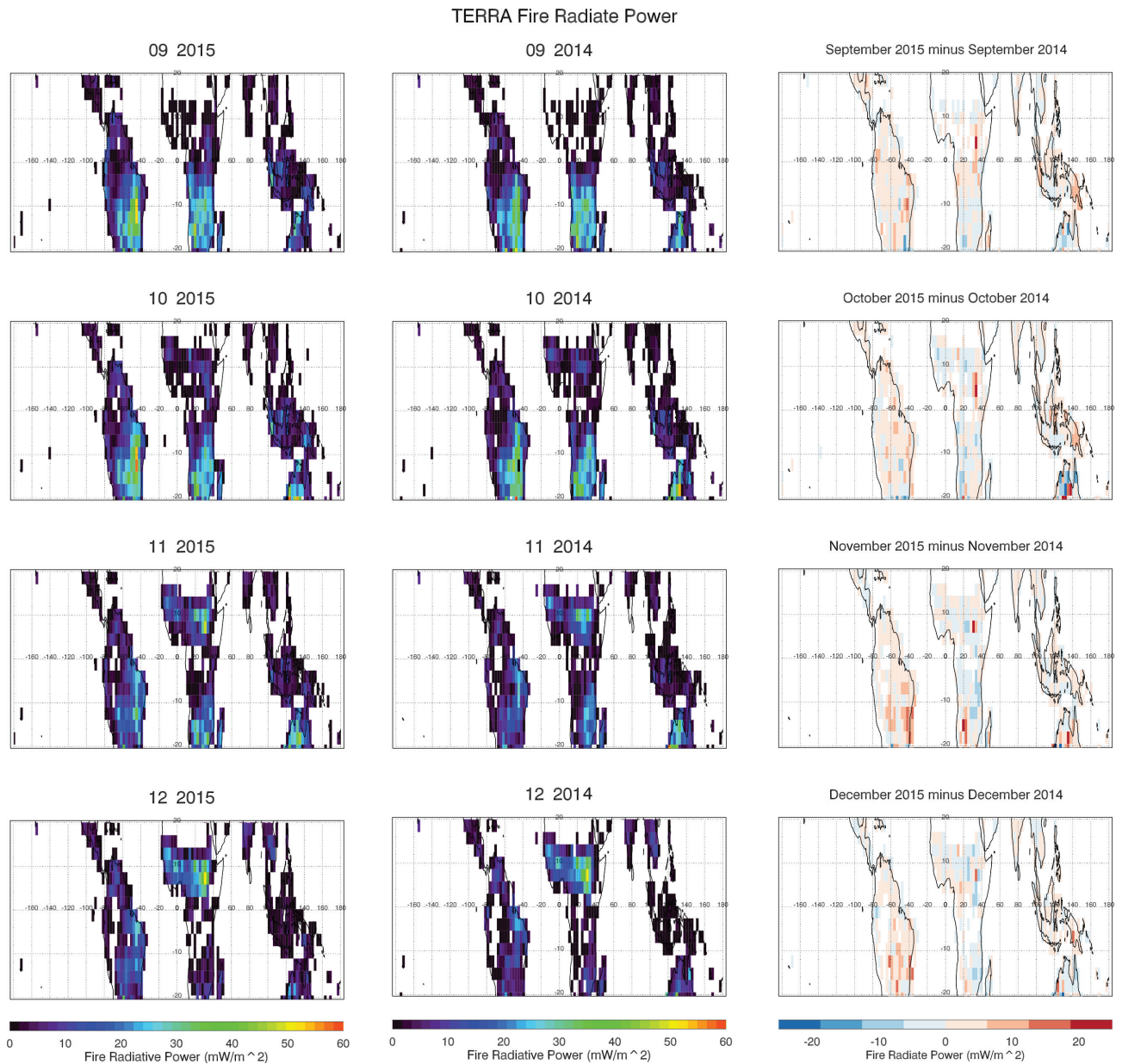


Figure 6.4: Fire radiative power ( $\text{mW/m}^2$ ) for September, October, November and December 2015 (left) and 2014 (middle) and the difference between 2015 and 2014 (right) (data from: <ftp://fuoco.geog.umd.edu/modis/C4/cmgs/monthly/hdf/>).

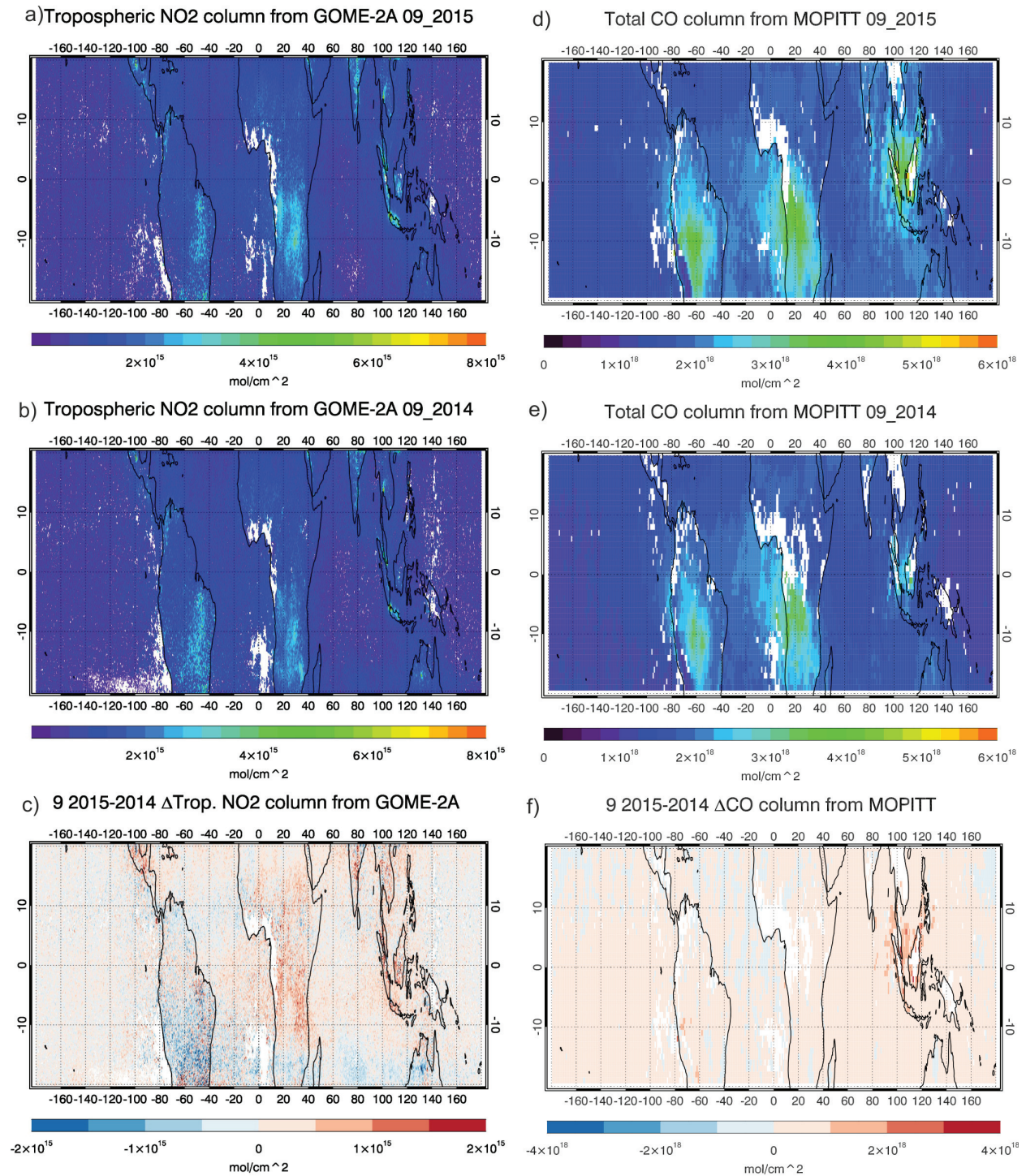


Figure 6.5: Tropical tropospheric nitrogen dioxide columns (data from: <http://www.iup.uni-bremen.de/doas/>) and carbon monoxide mixing ratios at 300 hPa (data form: <http://terra.nasa.gov/data/mopitt-data>) for September 2015 and 2014 and the differences between them. White pixels denote missing data due to clouds.

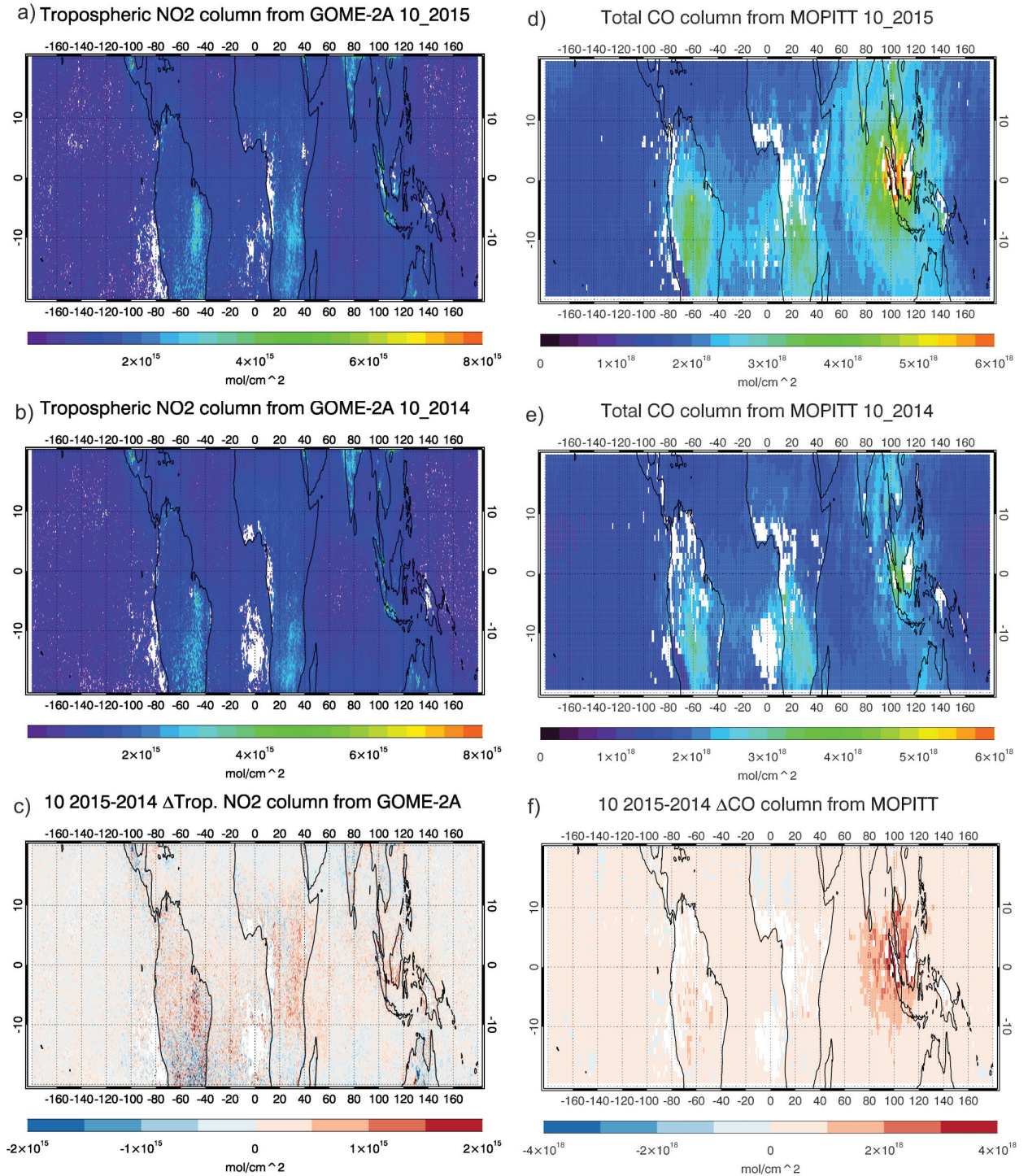


Figure 6.6: Same as Figure 6.5 for October 2015 and 2014.

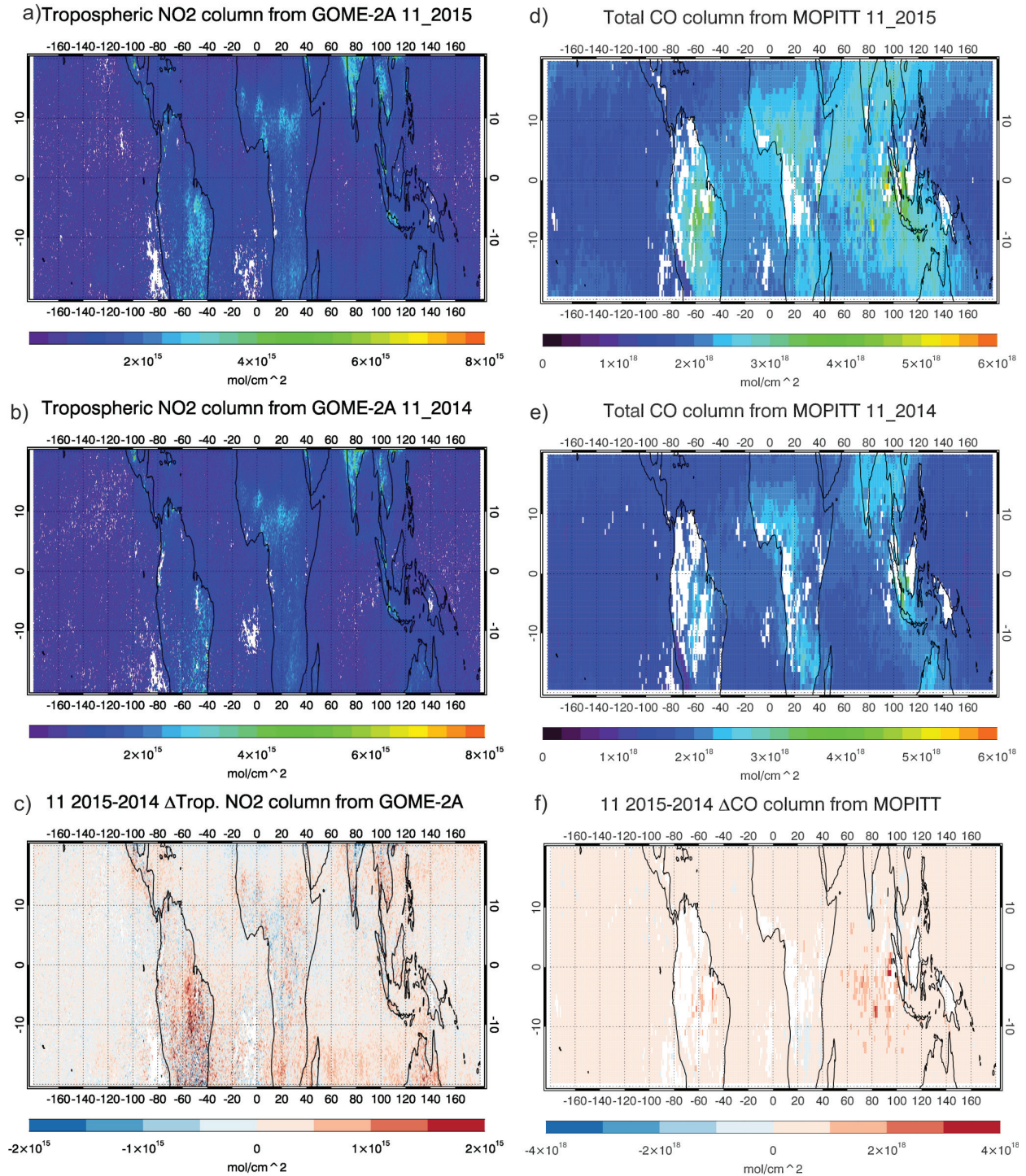


Figure 6.7: Same as Figure 6.5 for November 2015 and 2014.

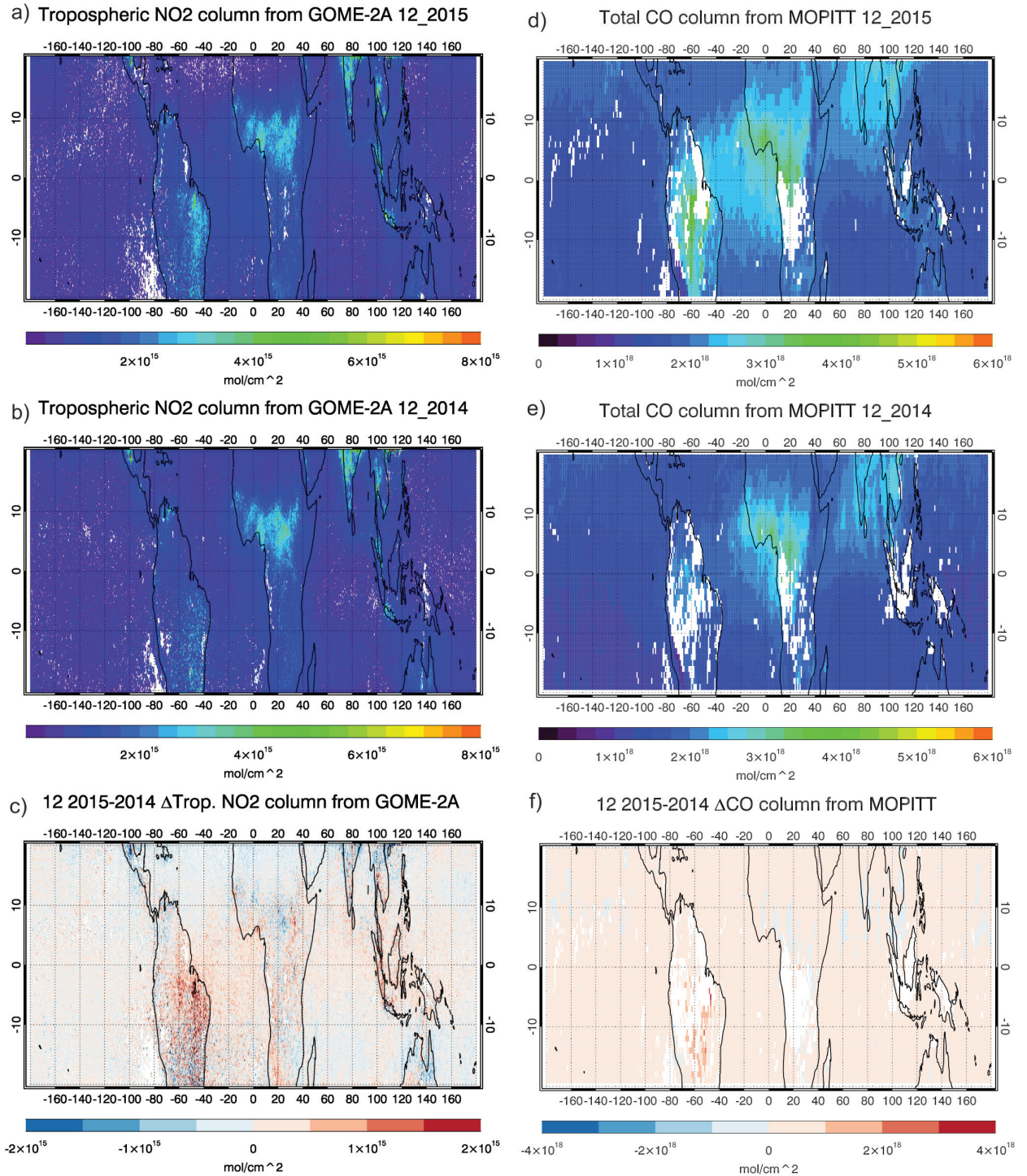


Figure 6.8: Same as Figure 6.5 for December 2015 and 2014.

days in UT and even less than a day at ground level), short enough to know where its source is [Levy et al., 1999]. Most of the NO<sub>2</sub> maxima agree very well with locations of increased FRP, suggesting that most of the tropospheric NO<sub>2</sub> concentration is related to biomass burning, especially for Sept–Oct over Indonesia and Nov–Dec over Brasilia and central Africa. The enhanced tropospheric NO<sub>2</sub> over India does not coincide with fires, having mainly industrial/anthropogenic emission sources. CO lifetime in the troposphere is between 1–2 months [Jacob, 2000] allowing for more transported and accumulated CO. Therefore, the CO maxima may not necessarily coincide with locations of enhanced FRP and may occur downwind of the fires. CO accumulates mostly over the Indian Ocean (Sept–Nov) and Brasilia (December).

### 6.3.2 Comparison with ECHAM5/MESSy Atmospheric Chemistry (EMAC) model simulations

In order to highlight the 2015 El Niño, tropospheric ozone in that year is compared to the previous year, using both observations and global chemistry model data. We use ECHAM5/MESSy Atmospheric Chemistry (EMAC) [Joeckel et al., 2016] model runs of tropospheric ozone. The results from the EMAC model together with observations of tropospheric NO<sub>2</sub> columns and total CO columns will be used to interpret the observed ozone changes.

EMAC is a numerical global coupled chemistry-climate model (CCM) for describing dynamical and chemical processes in the troposphere and middle atmosphere. It makes use of sub-models such as the dynamic model ECHAM5 (the 5th generation European Centre - Hamburg general circulation model, [Roeckner et al., 2006] and the Modular Earth Submodel System, MESSy [Joeckel et al., 2016], a chemistry module. Reanalysis of the European Centre for Medium-Range Weather Forecast (ECMWF) are used for meteorological input to the CCM. The EMAC model has a horizontal resolution of 100 to 500 km and uses time steps between 5 and 40 minutes. MESSy consists of more than 40 sub-models such as the Ocean model MPIOM, the Lagrangian transport scheme ATTILA, and the chemistry model MECCA in order to describe processes and to perform diagnoses. EMAC has the ability to be operated either as a general circulation model (GCM) without meteorological inputs or as a quasi chemistry transport model (QCTM) without feedbacks from the chemistry to the dynamics. Anthropogenic emissions are included as emission fluxes from the Atmospheric Chemistry and Climate Model Intercomparison Project (ACCMIP) <https://www.giss.nasa.gov/projects/accmip/> [Lamarque and Solomon, 2010] combined with Representative Concentration Pathways (RCP 6.0) greenhouse gas concentration (not emissions) trajectories adopted by the IPCC for its fifth Assessment Report (AR5) in 2014 [Fujino et al., 2006]. ACCMIP and RCP 6.0 monthly values have been linearly interpolated from annual emission fluxes, whereas seasonal varying values are only provided for biomass burning and ship emissions. The non-anthropogenic emissions such as NMHCs of biogenic origin, terrestrial dimethyl sulfide (DMS), volcanic SO<sub>2</sub>, NH<sub>3</sub>, halocarbons, CH<sub>3</sub>, I, and Organic Carbon (OC) from secondary organic aerosol have been mostly prescribed based on climatologies [Joeckel et al., 2016].

Tropospheric ozone distributions from the EMAC model have been evaluated with OMI/MLS tropospheric ozone data [Ziemke et al., 2006, 2011], showing that the model simulations overestimate ozone by ~ 30%. Comparison with ozonesondes [Tilmes et al., 2012] showed that EMAC overestimates

by 20-30% in the tropics, which corresponds to 5-10 DU [Joeckel et al., 2016, Righi et al., 2015]. Righi et al. [2015] showed that EMAC with ACCMIP emissions implementation overestimates  $\text{NO}_x$  compared to aircraft profiles [Emmons et al., 2000] in the lower troposphere, while it underestimates them in the upper troposphere, probably related to lightning emissions. On the other hand, CO is underestimated compared to NOAA GLOBALVIEW, mainly over regions with extreme anthropogenic influence. Pozzer et al. [2007] related the lower CO levels to emissions from fossil fuel combustion being too low in the model.

Figures 6.9–6.12 show  $\text{NO}_2$  and CO abundances and their differences between 2015 and 2014 as simulated by the EMAC model. The locations of maximum  $\text{NO}_2$  concentrations agree well with the ones retrieved from GOME-2 (Fig. Figures 6.9–6.12 left) for both years. The tropospheric  $\text{NO}_2$  columns from EMAC are found to be generally lower by about  $1 \times 10^{15}$  mol/cm<sup>2</sup> compared with satellite observations for all months with the exception of the Indonesian region in September and October 2015 (Fig. 6.9 and 6.10) where it is higher by  $\sim 2 \times 10^{15}$  mol/cm<sup>2</sup>. The increase in tropospheric  $\text{NO}_2$  by EMAC over the Indonesian region in October 2015 is on the order of  $6 \times 10^{15}$  mol/cm<sup>2</sup> compared to 2014, while GOME-2 observes an increase of less than  $1.5 \times 10^{15}$  mol/cm<sup>2</sup>. (note that the scale in Fig. 6.5–6.8e and Fig. 6.9–6.12e is different). In November and December 2015 (Fig. 6.11–6.12 left) EMAC does not capture the extent of enhanced  $\text{NO}_2$  over South America as observed by GOME-2 (Figures 6.7–6.8 left). The CO total columns from EMAC are generally lower than MOPITT observations by  $\sim 1\text{--}2 \times 10^{18}$  mol/cm<sup>2</sup>. The locations where CO maximises are generally well represented by the EMAC simulations, nevertheless their spatial extent is limited. EMAC does not show the profound CO maximum over Brasilia in Oct-Nov-Dec observed by MOPITT (Figures 6.10–6.12 right).

In order to compare tropical tropospheric ozone columns from CCD with the EMAC model, the CCD algorithm was modified to bin the retrievals to the model grid ( $2.8^\circ \times 2.8^\circ$ ) and EMAC ozone columns were integrated from the ground to 200 hPa. The TTCO abundances observed by GOME-2 in September 2015 are increased compared to 2014 (see Fig. 6.13.a, b and c) by about 8 DU over central Africa and South America, central Atlantic, and Indian Ocean. Positive tropospheric ozone anomalies in the EMAC model occupy slightly larger area and the negative anomalies have smaller magnitude ( $< 10$  DU). Overall the anomaly pattern is similar. The locations of positive anomalies agree well with increased fires (Fig 6.4) in the same area, enhanced tropospheric  $\text{NO}_2$  columns and higher CO mixing ratios from satellite and model data (Fig. 6.5 and 6.9, respectively). Comparing GOME-2A results in September 2015 with EMAC tropospheric ozone simulations (Fig. 6.13.d, e, g and h), the model overestimates tropospheric ozone columns by 10 to 20 DU over north Africa, the Arabian sea, India, Philippines, and Indonesia. The model underestimates strongly tropospheric ozone by about 20 DU in the Atlantic coast of Congo. The differences are even larger in 2015 exceeding 20 DU. EMAC underestimates tropospheric ozone columns by about  $\sim 10$  DU over central Africa, the Atlantic Ocean, and partly the Indian Ocean and central Pacific Ocean.

In October tropical tropospheric ozone in October 2015 is higher than in October 2014 compared with 2014 by 7 to 10 DU over the Indian and western Pacific Ocean and lower over the northern tropics by  $\sim 15$  DU according to Fig. 6.14.a, b and c. This tropospheric ozone decrease corresponds to changes in tropospheric water vapor following the dislocation of the convective cells from the western to the east Pacific [Bjerknes, 1966]. The mechanism of ozone loss by water vapor is given by Reactions ?? and ??.

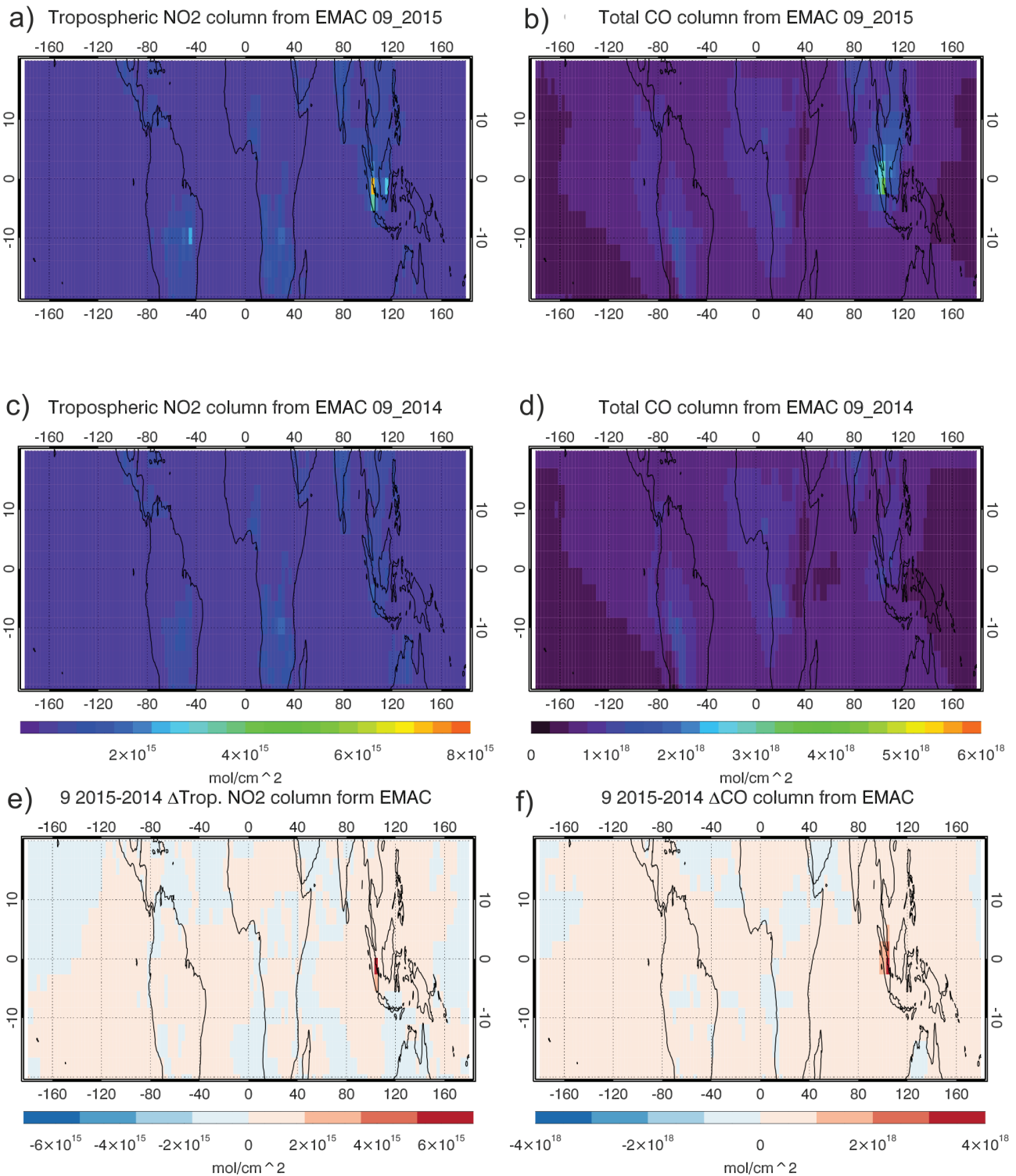


Figure 6.9: Tropical tropospheric nitrogen dioxide columns and carbon monoxide mixing ratios at 300 hPa for September 2015 (a,b) and 2014 (c,d) and the differences between them from EMAC (e,f) simulations.

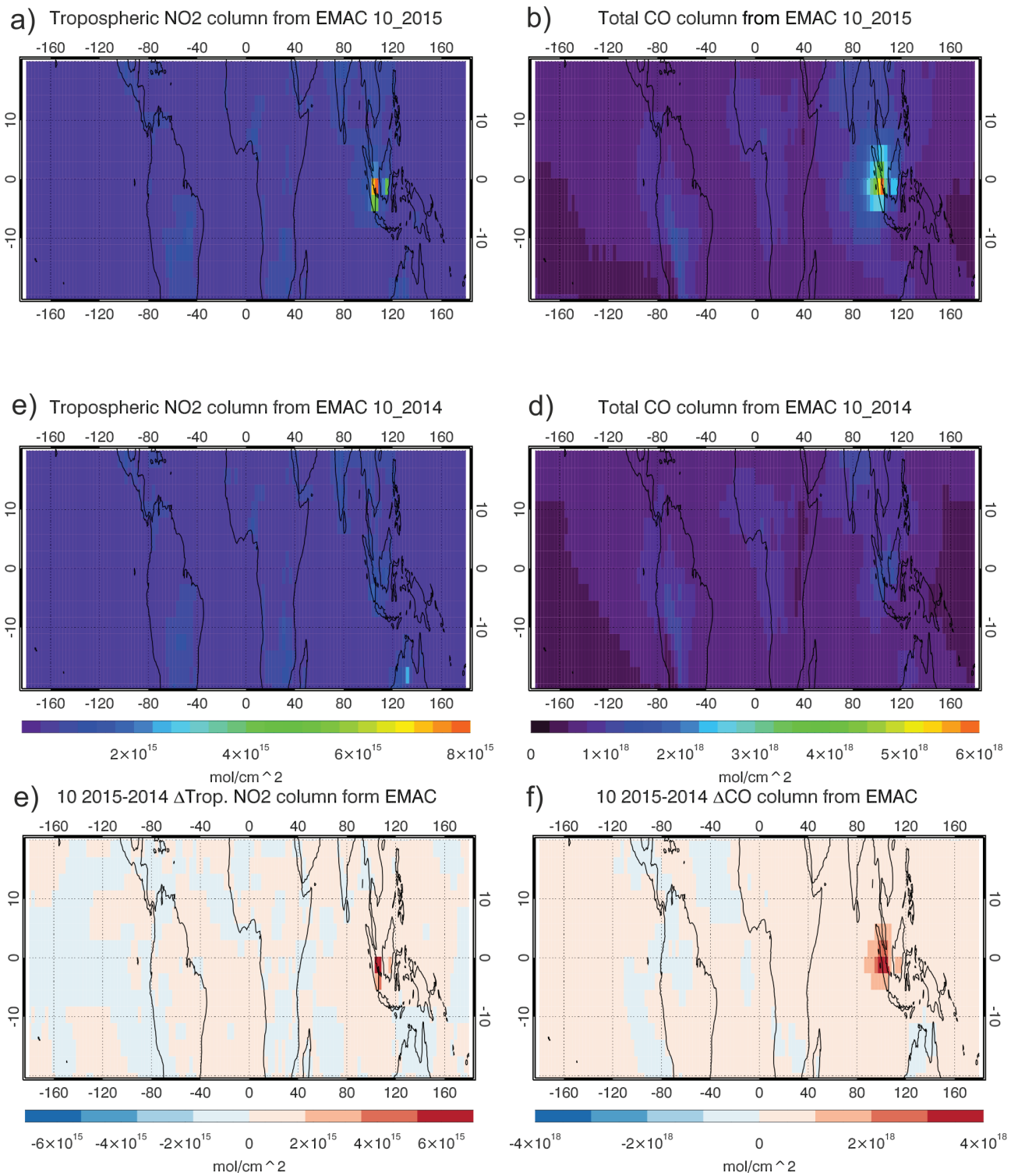


Figure 6.10: Same as Figure 6.9 for October 2015 and 2014.

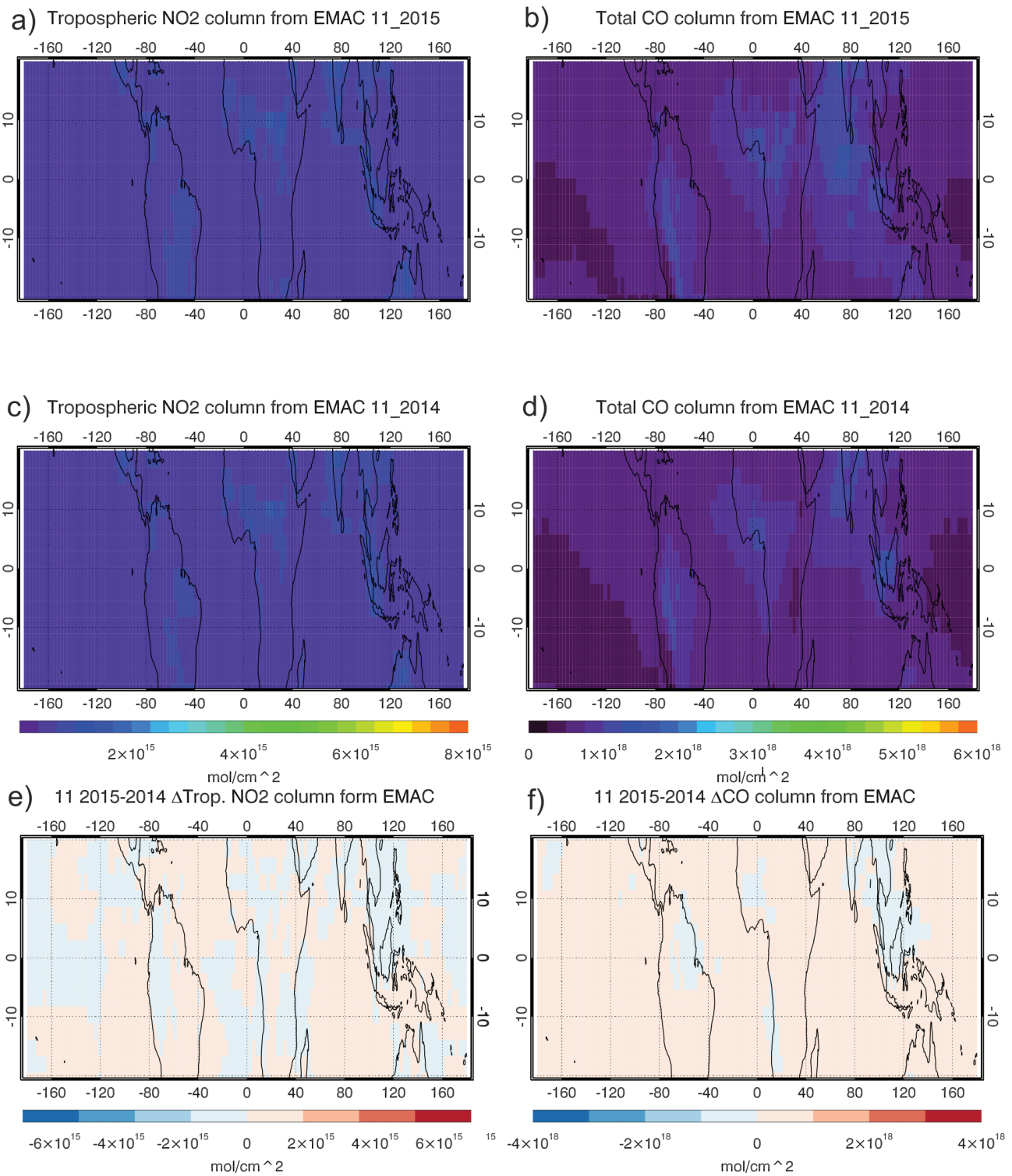


Figure 6.11: Same as Figure 6.9 for November 2015 and 2014.

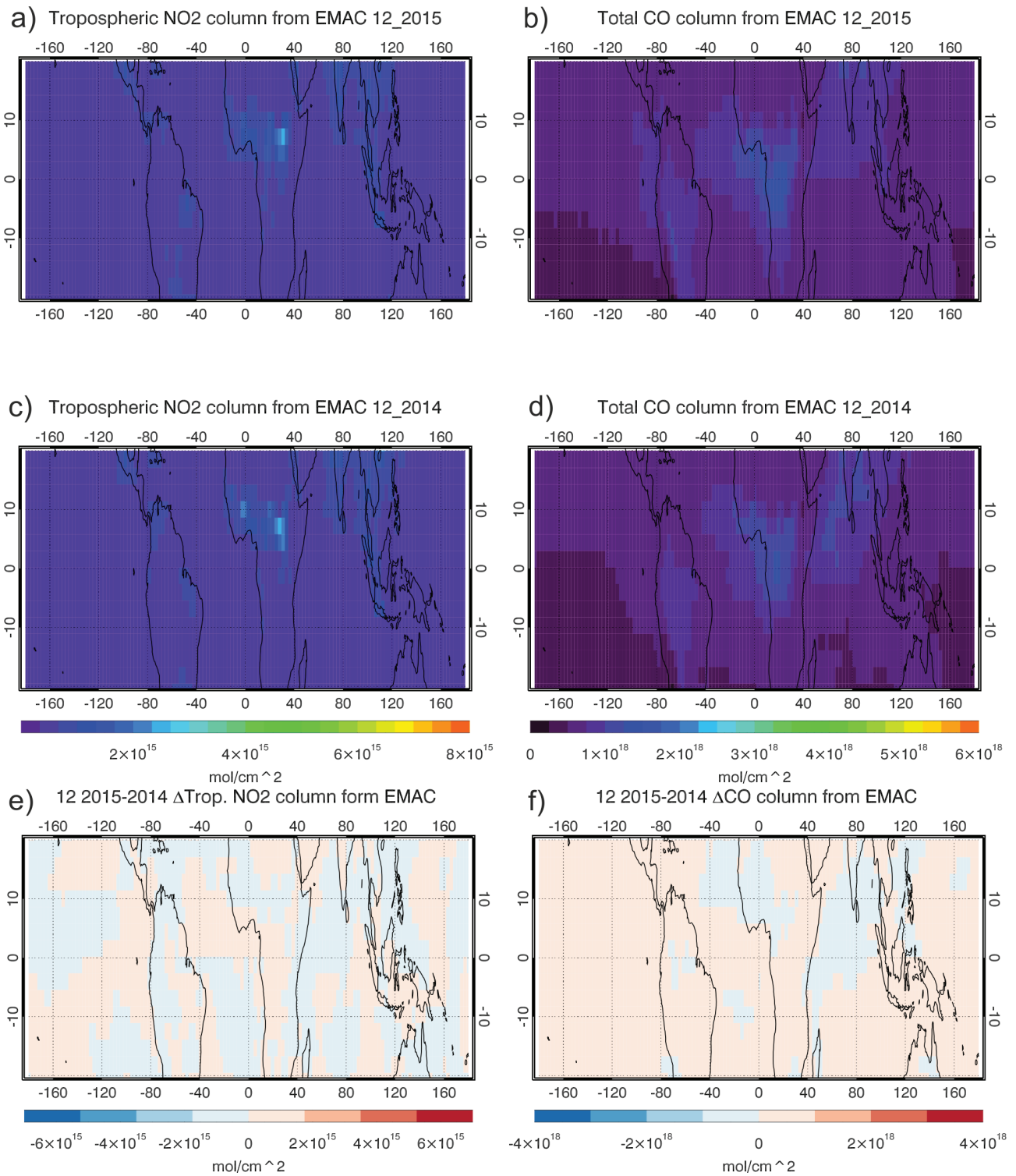


Figure 6.12: Same as Figure 6.9 for December 2015 and 2014.

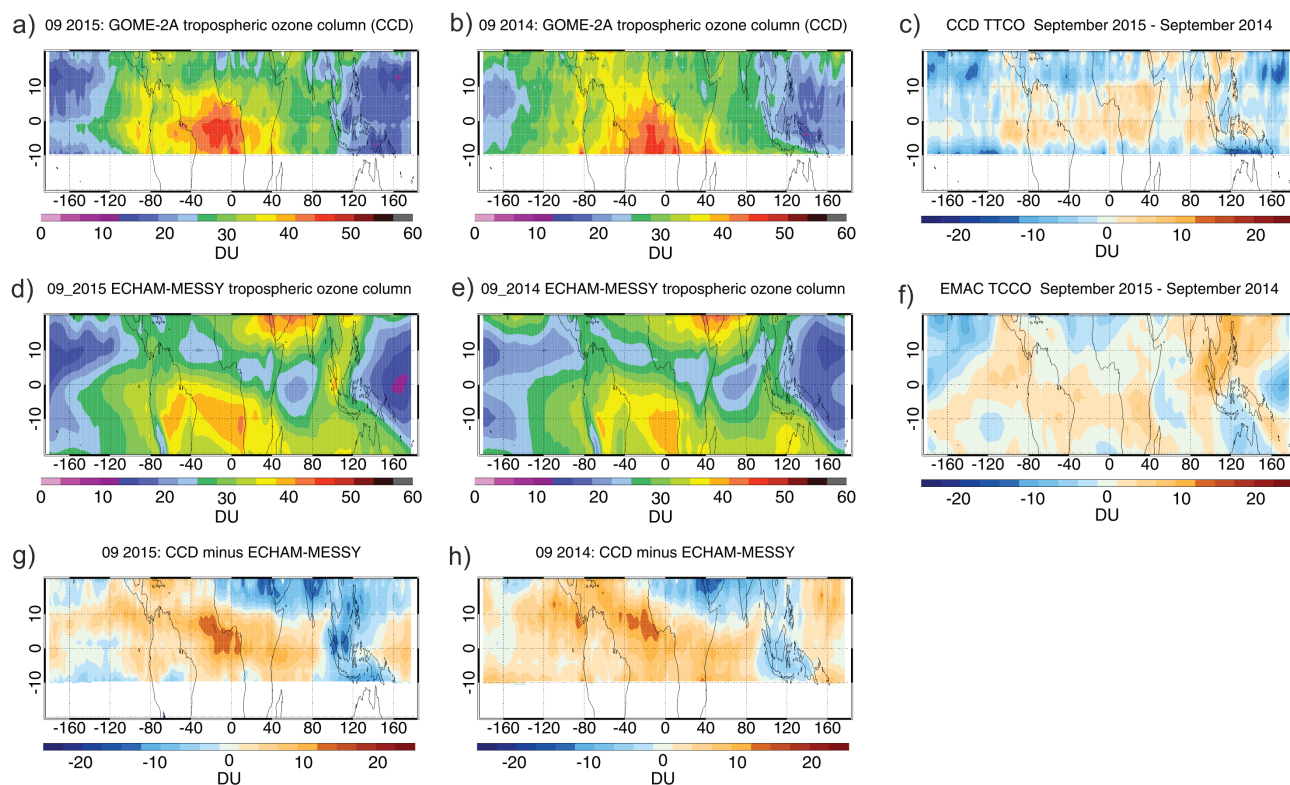


Figure 6.13: Tropical tropospheric ozone columns observed with GOME-2A and simulated by the ECHAM-MESSY atmospheric chemistry model (EMAC) for September 2015 (a,d) and 2014 (b,e), differences between 2015 and 2014 (c,f) and the differences between observations and model in 2014 and 2015, respectively (g, h).

EMAC simulates larger tropical tropospheric ozone columns by 10–20 DU than is observed by GOME-2 for both years with the exception of the Atlantic Ocean and central Africa where EMAC underestimates ozone by about the same amount (Fig. 6.14.g and h). Tropospheric  $\text{NO}_2$  columns over Indonesia in

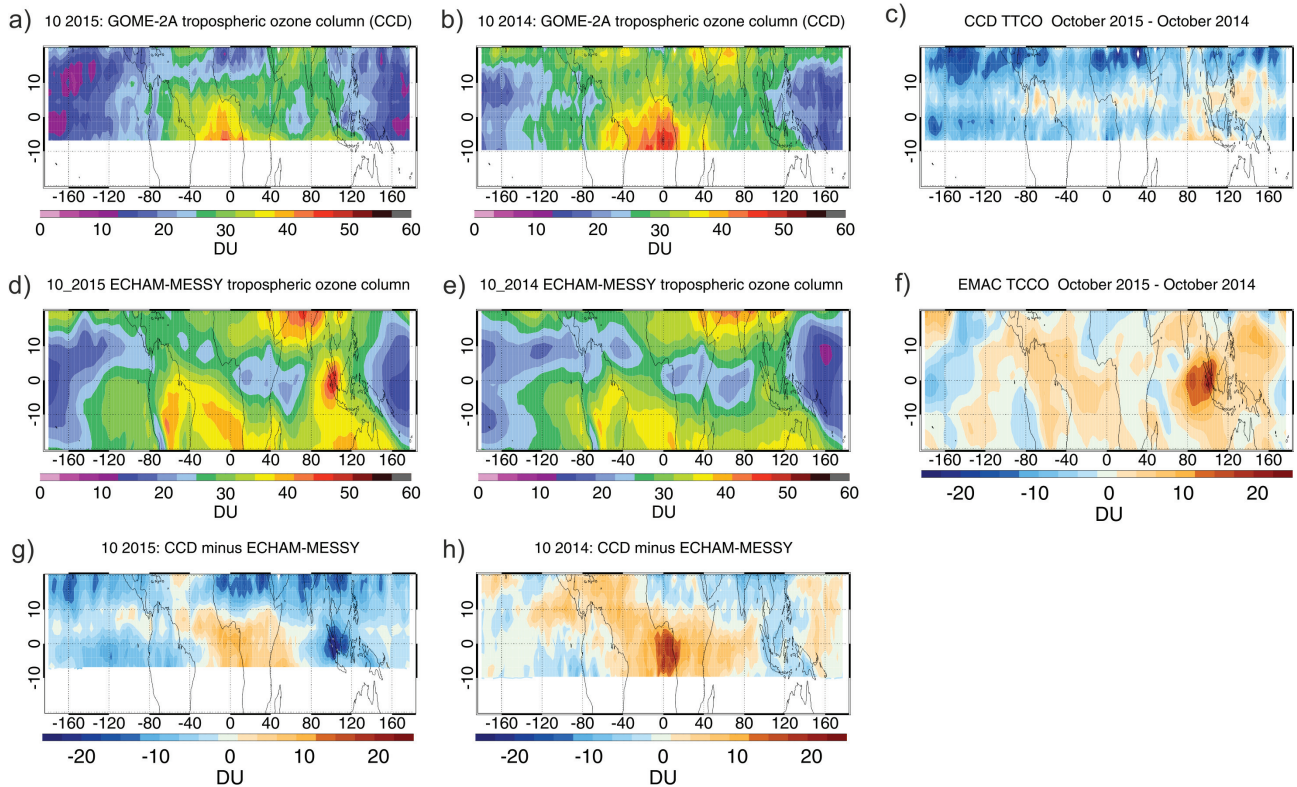


Figure 6.14: Same as Figure 6.13 for October 2015 and 2014.

October 2015 were found to be higher by  $6 \times 10^{15}$  mol/cm<sup>2</sup> compared to 2014 over the Indian Ocean which is  $2 \times 10^{15}$  mol/cm<sup>2</sup> higher compared with GOME-2 observations. The modeled CO is also larger in October 2015 than in 2014 by approximately  $4 \times 10^{15}$  mol/cm<sup>2</sup> but still smaller by almost 50% than MOPITT observations in the most of the Indian Ocean. However, the maximum tropospheric ozone anomalies from EMAC over the Indian Ocean seem to have the same spatial distribution as the CO anomalies.

In November 2015 GOME-2A TTCO (Fig. 6.15.a, b and c) is greater than in 2014 by  $\sim 8$  DU over Indonesia, north Atlantic, and South America and in some locations in central Pacific Ocean. Tropospheric ozone decreased ( $\sim 8$ -15 DU) over the north east Pacific and central Africa. The biomass burning season during November (Fig. 6.4) peaks in Brasilia, Australia, central and southern Africa that agrees well with increases in observed CO and  $\text{NO}_2$  from satellites. EMAC does not show these increases, conversely, it shows relatively small changes in tropospheric  $\text{NO}_2$  ( $\pm 1 \times 10^{15}$  mol/cm<sup>2</sup>) and total CO columns 2 ( $\pm 1 \times 10^{18}$  mol/cm<sup>2</sup>) (Fig. 6.15.f). EMAC shows a decrease in tropospheric ozone over Vietnam, possibly due to the decrease in simulated CO and  $\text{NO}_2$  over Indonesia in November 2015 compared to 2014 (Fig. 6.11). However, the agreement between CCD and EMAC TTCO is better than for the other months (Fig. 6.15.g and h).

Figures 6.16.a to c depict the TTCO burden and differences between 2015 and 2014 in December.

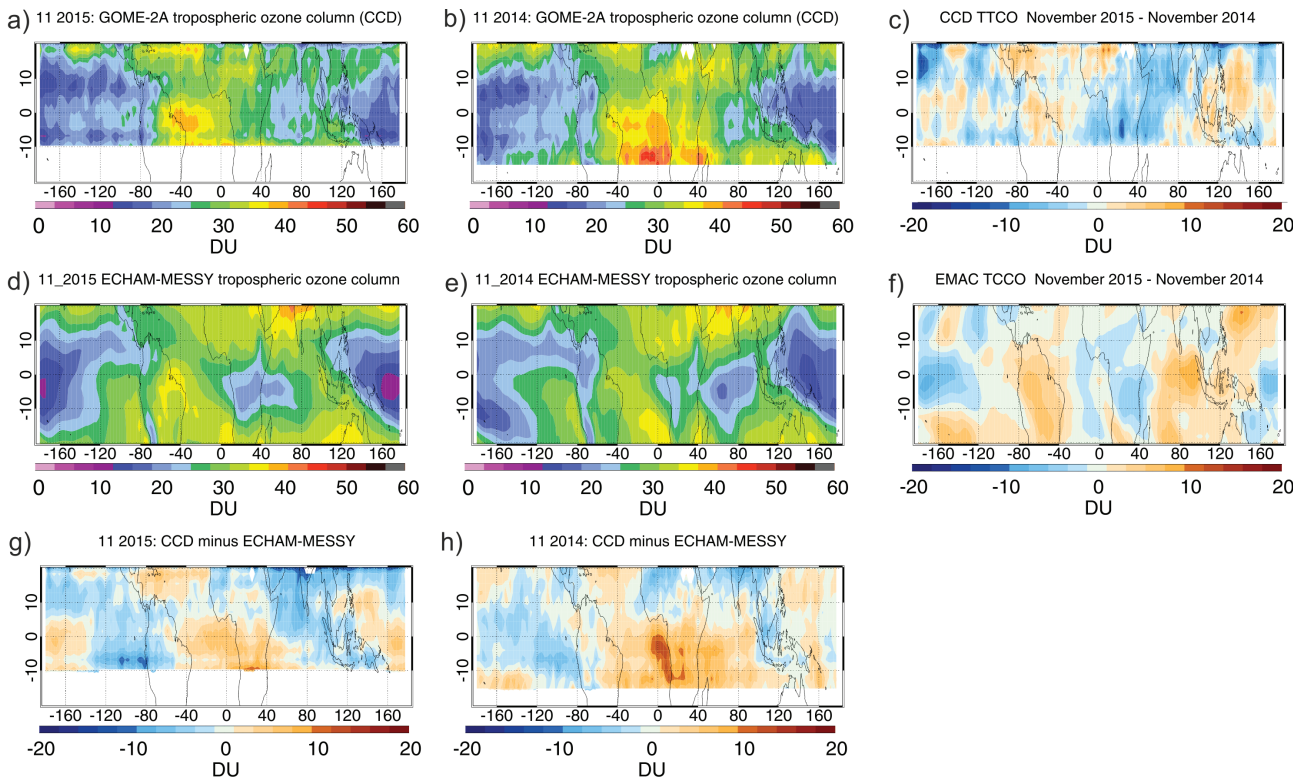


Figure 6.15: Same as Figure 6.13 for November 2015 and 2014.

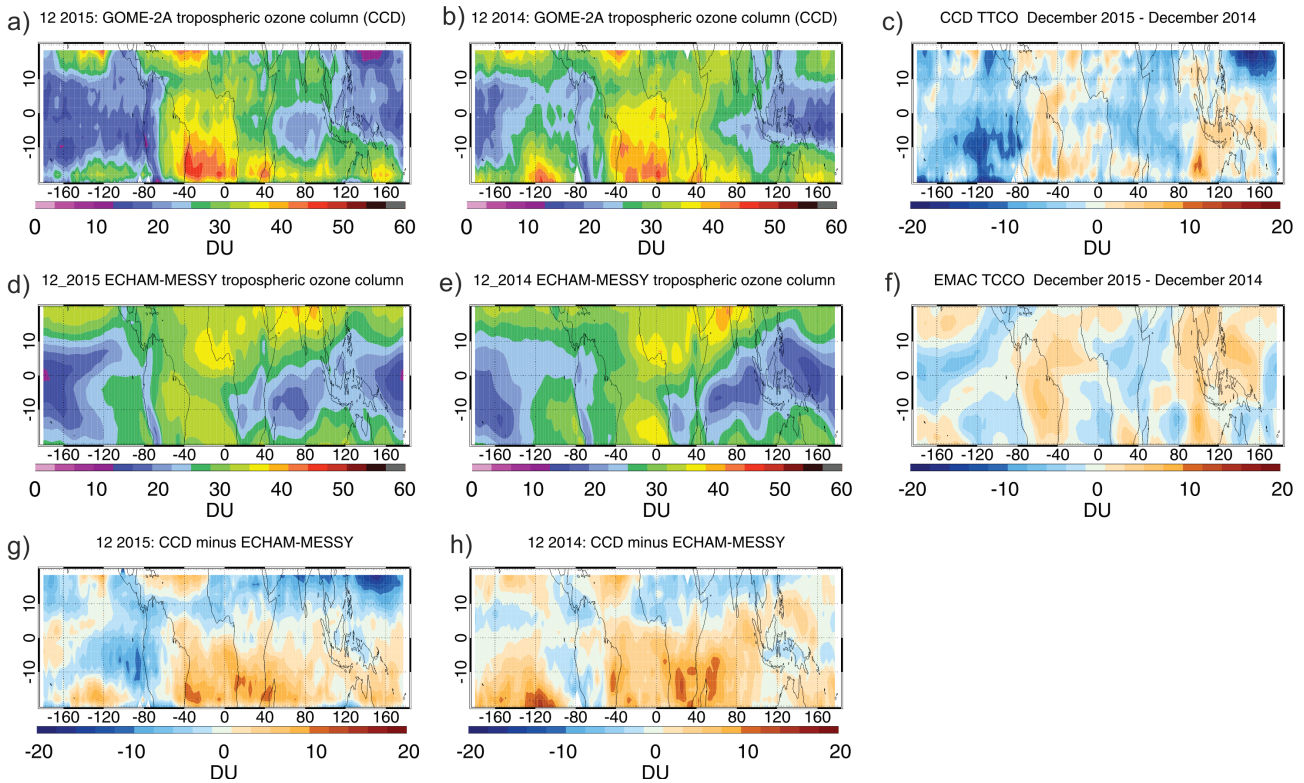


Figure 6.16: Same as Figure 6.13 for December 2015 and 2014.

The biomass burning season is already finished in Indonesia but still ongoing in north Africa and South America (Fig. 6.4). Nevertheless, tropospheric ozone increases considerably by more than 8 DU over the western Pacific Ocean (see Fig. 6.16.c and f) for both satellite and model results. This shows the persistence of tropospheric ozone modulated by dynamics while the ozone precursors (CO and NO<sub>2</sub>) do not show remarkable increases in that region (Fig. 6.8 and 6.12). The tropospheric ozone anomalies in EMAC are smaller over the north-east Pacific Ocean and central Africa and occupy a broader area than the observations (-5 DU instead of -20 DU). EMAC simulations result in a larger area of positive anomalies over Indonesia compared with CCD. EMAC model (Fig. 6.16.d, e) overestimates tropospheric ozone compared to GOME-2A observations by about less than 10 DU in the same regions as September, October, and November. The largest differences between CCD and EMAC are located again at the east African coast where they may exceed 15 DU for Dec 2014 (Fig. 6.16.g and h).

## 6.4 Impact of biomass burning and dynamics during 2015 El Niño event

In this section, the the main drivers for 2015 El Niño O<sub>3</sub> changes are investigated. These drivers are biomass burning and atmospheric dynamics (meteorology) in the tropical troposphere. Chandra et al. [2002, 2009] using GEOS-CHEM model runs in two modes were able to simulate the observed changes in tropical tropospheric ozone and estimate the contributions of biomass burning and large-scale transport/meteorology (winds humidity, clouds, temperatures) indicated here as "dynamical component". Based on their approach, the EMAC model was run in two modes:

- **Mode 1:** Standard EMAC simulations including biomass burning emissions from ACCMIP and RCP 6.0 databases.
- **Mode 2:** EMAC simulations exclude biomass burning emissions. This mode highlights the changes during El Niño due to atmospheric dynamics (long-range transport and stratosphere-to-troposphere exchange) (Fig. 6.17 left).
- The difference between the two modes provides the biomass burning contribution of the El Niño related tropospheric ozone changes (Fig. 6.17 right) assuming that the emissions from other sources are constant.

According to the EMAC model, dynamics are mainly responsible for the pattern of tropical tropospheric ozone anomalies in September (Fig. 6.17.a). Tropospheric ozone is increasing by ~ 6 – 8 DU over northern Indian Ocean, India, southern Africa, South America and the central Pacific Ocean in September 2015 whereas it is decreasing by the same amount over the north tropical Pacific, north Atlantic, and partly over the southern Indian Ocean. The contribution of biomass burning, ~ 6 – 8 DU is restricted to the Indian Ocean, central South America and parts of southern Africa (Fig. 6.17.b). In a small area over north Australia a decrease of ~ 2 DU in tropospheric ozone is noticed due to some biomass burning. In October 2015, the contribution of dynamics is similar, although the positive changes are more expanded in south-easterly direction (Fig. 6.17.c). The contribution of biomass burning is maximum this month with positive anomalies reaching 20 DU over Indonesia, partly due to the NO<sub>2</sub> overestimation from EMAC (Fig.6.17.d). In November dynamics reduce ozone concentrations mainly over Africa and the

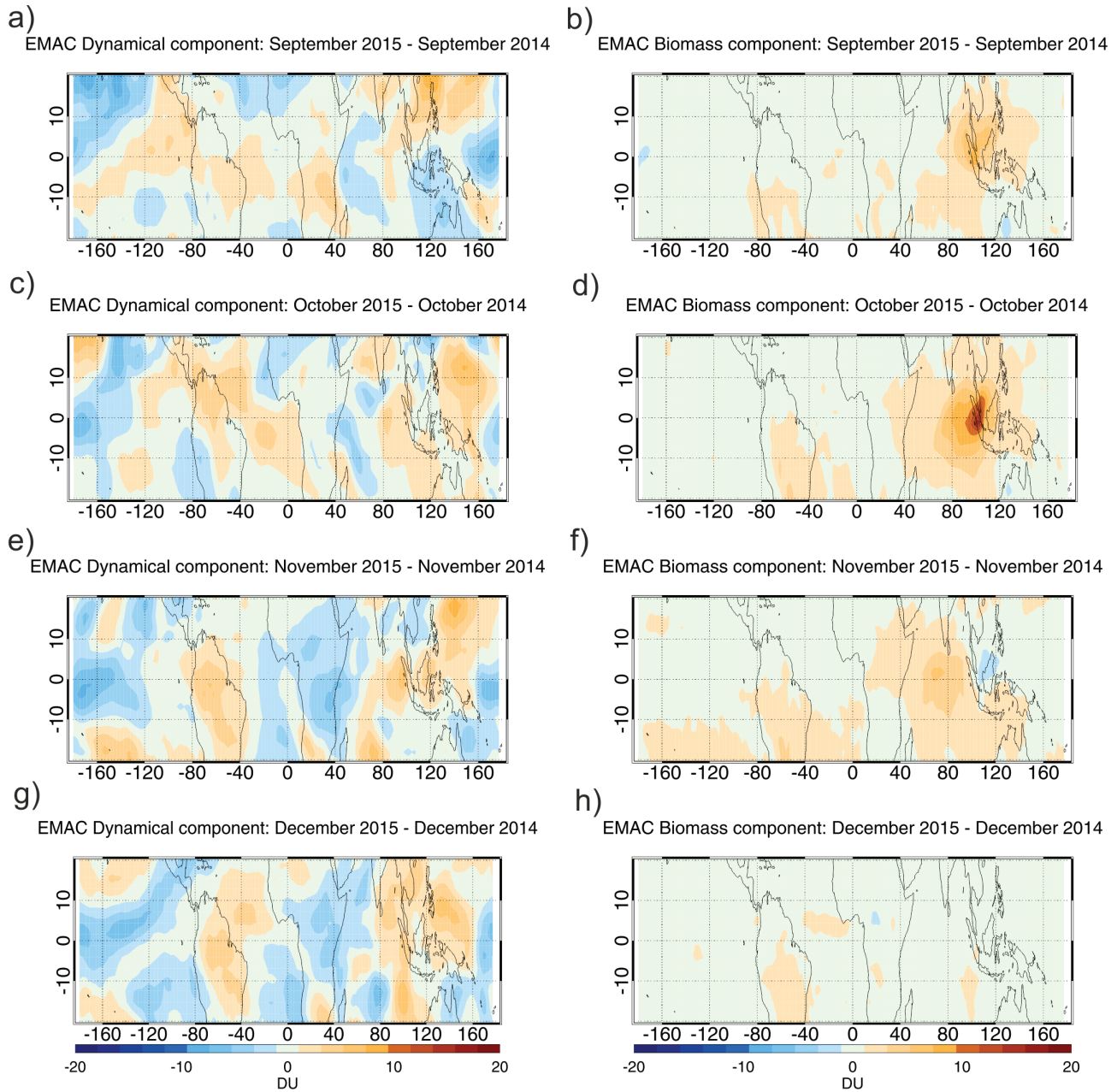


Figure 6.17: Inter-annual difference of EMAC tropical tropospheric ozone of the dynamical (left) and biomass burning (right) components (in DU) for the months Sept-Dec 2014-2015.

western Pacific by less than 10 DU. The increase of tropospheric ozone in November 2015 ( $\sim 8$  DU) over South America, the south Pacific Ocean, most of the Indian Ocean, mainly over Indonesia, the north-east Pacific Ocean and a small area over the north Pacific Ocean is mainly due to dynamics (Fig. 6.17.e). The positive contribution of biomass burning in November is smaller than in October, ranging between  $\sim 4-6$  DU, covering an extended area over the Indian Ocean (Fig. 6.17.f). Only in this month a positive ozone anomaly on the order of  $\sim 2-4$  DU appears over the southeast Pacific Ocean and a negative anomaly over Indonesia on the order of  $\sim 2-4$  DU (Fig. 6.17.f). The reason for this, as discussed above, is probably the decreased precursor emissions simulated by the model, especially CO. In the same area, dynamics contribute more than 6 DU so the net anomaly is positive (see Fig. 6.15.f). In December the dynamical contribution has a similar pattern and magnitude as in November with positive anomalies appearing over north Africa and north Atlantic Ocean (Fig. 6.17.g). The fire emissions over South America are the main biomass burning contribution in December, increasing ozone by  $\sim 2$  DU (Fig. 6.17.h). These findings are in agreement with results from Voulgarakis et al. [2010] indicating that 80% of the changes in "global" tropospheric ozone during El Niño is due to dynamics and only 20% is due to enhanced biomass burning.

In conclusion, GOME-2 captures the tropospheric ozone increase over Indonesia ( $\sim 8-10$  DU) and decrease over the east Pacific ( $\sim 10$  DU) due to El Niño in 2015 when comparing to 2014. The tropospheric ozone increase observed by GOME-2A in autumn 2015 is in agreement with enhanced ozone precursors according to GOME-2 ( $\text{NO}_2$ ), MOPITT (CO) and TERRA (fire emissions) satellite observations. EMAC model simulations of tropical tropospheric ozone seem to overestimate ozone observations by  $\sim 10$  DU (reaching locally  $\sim 20$  DU) over the northern tropics with the exception of the north Atlantic Ocean and underestimate most of the southern tropics by about the same amount. Despite the differences between GOME-2A and EMAC simulations, observed and modelled ozone anomalies from the difference between 2015 and 2014 agree well and range between  $+8$  to  $-10$  DU. However, the spatial distribution of these anomalies does not coincide for all months since simulated precursor abundances in the model do not always agree with observations. Ratios of CO and  $\text{NO}_2$  mixing ratios, from both satellite observations and model could reveal the degree of their relative change and could give an insight on the  $\text{NO}_x$  or VOCs limited regime of ozone production. It would be difficult to obtain  $\text{NO}_2$  volume mixing ratios from the available tropospheric column measurements as  $\text{NO}_2$  is not homogeneously mixed in the troposphere (at least for polluted areas). According to the EMAC model, dynamical processes are the dominant driver of tropospheric ozone changes, being responsible for most of the tropospheric ozone variability during the September-December period in 2014 and 2015. Over the Indian Ocean, the dominant factor controlling ozone production is biomass burning emissions. Their contribution is minimised in December, when biomass burning season ends in Indonesia and starts in South America.

## 6.5 Summary and discussion

Tropical tropospheric ozone anomalies during the El Niño events of 1997 and 2015 have been investigated. It has been shown that El Niño events increased tropospheric ozone over Indonesia ( $\sim 10-15$  DU) and decreased it over the east Pacific Ocean ( $\sim -10$  DU). La Niña was found to increase tropospheric

ozone in the entire tropics ( $\sim 6\text{--}8$  DU), except for the Indian Ocean and central tropics, were ozone decreased ( $-5\text{--}-10$  DU). The largest effects are observed during biomass burning season in boreal autumn. The magnitude of the anomalies agrees well with past studies [Chandra et al., 2002, 2009, Doherty et al., 2006, Logan et al., 2008, Ziemke et al., 2009b, 2015]. However, the comparisons between the 1997 and 2015 El Niños and 1999 and 2010 La Niñas showed that these events did not have the same impact on tropospheric ozone. The 2015 El Niño event resulted in 2–4 times more tropospheric ozone over parts of the northern tropics between September and November 2015 compared with 1997, while the ENSO-MEI index is 1.1–1.2 times larger in 1997 compared to 2015.

December 1997 was the month when tropospheric ozone increased the most over the Indian Ocean, while in 2015, the maximum positive anomalies were in September, covering the majority of the tropical belt. The 2015 El Niño event caused more tropospheric ozone (about 15–20 DU) over parts of the northern tropics between September and November 2015 compared with 1997. In December, the differences in tropospheric  $O_3$  between 2015 and 1997 are smaller ( $\sim 8\text{--}10$  DU), with more ozone in 2015 over Africa, central Atlantic and parts of the northern Pacific Ocean and less ozone ( $\sim 10$  DU) over the Indian and south tropical Pacific Oceans. For the La Niñas, the differences in tropospheric  $O_3$  between 1999 and 2010 are much smaller, on the order of  $\pm 5$  DU.

The 2015 El Niño was further investigated using tropospheric ozone simulations from the EMAC model [Joeckel et al., 2016]. The model mainly overestimates tropical tropospheric ozone (for both years studied, 2014 and 2015) by 10–15 DU over northern Africa, Indian Ocean, and north-east Pacific Ocean and underestimates by the same amount over the Atlantic, west Pacific Ocean, and central-southern Africa compared to observations. These findings agree well with model comparisons made by Righi et al. [2015], Ziemke et al. [2011] and Joeckel et al. [2016]. The comparison of precursors simulated by EMAC with satellite observations has shown that the model generally underestimate their abundances ( $\sim 30\%$  for  $NO_2$  tropospheric columns and  $\sim 50\%$  for 300 hPa CO volume mixing ratio) with the exception of October 2015 when EMAC simulates larger  $NO_2$  columns over Indonesia than GOME-2.

The contribution of dynamics and biomass burning in tropospheric ozone variability during the 2015 El Niño event was studied using the EMAC model. The model indicates that dynamics mainly modulate the tropical tropospheric ozone abundances with the exception of the Indonesian region where biomass burning dominates from September to November 2015 with maximum in October ( $\sim 15$  DU). Further studies using tagged model runs could provide more information about the tropospheric ozone production and loss during El Niño (e.g. Coates et al. [2015]) and assist in the development of emission policies that could improve the air quality and reduce climate change.



## Conclusions and Outlook

### 7.1 Conclusions

This thesis focused on developing an improved and homogenized tropical tropospheric ozone columns dataset along with an uncertainty budget, using the convective clouds differential (CCD) technique. Long-term changes, the variability, and in particular the influence of ENSO on tropical tropospheric ozone was investigated in details based upon the new dataset.

#### Improvements in the original CCD algorithm

CCD is a statistical method of retrieving tropical tropospheric ozone columns using monthly averaged total ozone data and cloud information, meaning that no additional radiative transfer calculations are applied. For this study, an advanced CCD-IUP algorithm has been developed taking into account the particularities of the satellite instruments used (GOME/ERS-2, SCIAMACHY/ENVISAT, and GOME-2/MetOp-A). Based on the original technique's assumption that ozone columns above deep convective clouds (ACCO) simulate stratospheric ozone, a classification of "cloudy" ozone measurements was performed using critical values for cloud fraction (cf) and cloud top height (cth) [Ziemke et al., 1998]. Each instrument has different spatial resolution and uses different cloud algorithms. For example, GOME and GOME-2 use FRESCO algorithm for the cloud top height retrieval, which assumes that clouds behave as opaque Lambertian surfaces, retrieving usually the effective (inside the cloud) and not the real cloud top heights [Koelemeijer et al., 2001]. SACURA algorithm on the other hand, which is used in SCIAMACHY, takes into account the radiative transfer inside, above and below the clouds, resulting in more realistic cloud top heights [Kokhanovsky et al., 2005, Lelli et al., 2014]. Therefore, in order to quantify the critical values to be used for the ACCO calculation, the frequency of "cloudy" measurements for each set of cth and cf values and each instrument was taken into account. Therefore the cf and cth critical values that have been selected to characterise cloudy pixels, differ accordingly. Due to the natural variability of clouds, a climatological correction term, taken from the Fortuin and Kelder [1998] climatology, was applied to each individual measurement of the ACCO to correct for different cloud top heights, and adjust the ACCO to a fixed level of 200 hPa ( $\sim 12$  km). Furthermore, the assumption that UV radiation does not penetrate the clouds is not completely true, since it contributes with a small

additional ozone absorption inside the clouds [Ziemke et al., 2008]. Based on the cloud slicing results from Ziemke et al. [2008], ozone concentrations inside the high reflective clouds at the reference region (Indian Ocean and western Pacific) are about 4–7 ppbv, which corresponds to an ozone column of  $\sim 1$  DU between the mean cloud top and the 200 hPa level. For this reason, for the cases where  $ctp > 200$  hPa, the value of 1 DU was subtracted from the climatological correction term in the case of GOME and GOME-2 ACCO, since the geometrical top of the cloud is hundreds of meters higher than the one retrieved by FRESCO and the climatological ozone column correction between the retrieved cloud top height and the 200 hPa level is higher than it should. At a final step, the outliers were screened out, in order to restrict the variability and homogenize the ACCO in every latitude band. It has been concluded that after applying the corrections to GOME-2 and SCIAMACHY ACCO, the agreement between them and with the integrated ozone profiles from ozonesondes above 200 hPa improves significantly. Finally, the monthly tropical tropospheric column of ozone (TTCO) is obtained by subtracting the monthly averaged ACCO per  $2.5^\circ$  latitude bands from the western Pacific region ( $70^\circ\text{E}$ – $170^\circ\text{W}$ ) from the monthly averaged total ozone column ( $2.5^\circ$  by  $5^\circ$  bins) of nearly cloud free areas ( $cf < 0.1$ ) in the same latitude band and for all longitudes.

#### **TTCO retrievals, validation and uncertainty estimation**

The TTCO results from the advanced CCD algorithm show the expected seasonal pattern and are similar for overlapping months of GOME–SCIAMACHY (2002 and 2003) and SCIAMACHY–GOME-2 (2007–2012) TTCO retrievals. However, a constant bias between the instruments has been noticed that is corrected for by harmonising the data before merging them into a consistent 20 year dataset (see further down). The uncertainty of the advanced CCD-IUP algorithm has been estimated and this is a first attempt to provide a complete error budget for CCD tropospheric ozone. The main sources of uncertainty arise from the WFDOAS total and above cloud ozone column retrieval, the cloud top height, and cloud parameter uncertainties. The first order autocorrelation of total and above cloud ozone columns has been implied in the uncertainties to account for the persistence of the time-series. Assuming that these uncertainties are Gaussian, the total uncertainty of the CCD-IUP retrieval algorithm has been calculated to be in the order of 3 DU ( $< 10\%$ ). Among the aforementioned factors,  $cf$  (for GOME-2) and ACCO retrieval (for GOME) have the largest contribution to the total uncertainty, while GOME has the greatest uncertainty between the three instruments. The CCD-IUP results have been extensively validated with in-situ ozone profiles (integrated up to 200 hPa altitude) at nine SHADOZ ozonesonde sites. The validation has shown mean biases of  $\sim 5$  DU, mean relative differences between  $-8$  and  $28\%$ , and RMS between 3.5 and 13 DU, all greater than the retrieval uncertainties. Sampling issues may be a possible reason for the large uncertainties noticed. The comparison with Limb-Nadir-Matching (LNM) observations from SCIAMACHY showed good agreement, with mean absolute bias  $< 5$  DU and mean relative difference of about  $\sim 12\%$  on average.

#### **Harmonising the TTCO retrievals into one consistent dataset**

Using SCIAMACHY TTCO as reference, the average difference (bias) with GOME and GOME-2 during the years of common operation (2002 and 2003 for SCIAMACHY–GOME and 2007–2012 for SCIAMACHY–

GOME-2) was found to range between -6 and 6 DU for GOME, and between -8 and 0 DU for the case of GOME-2 TTCO. Since the set up for the total ozone retrieval from the WFDOAS algorithm is the same for all instruments, it was concluded that these biases are related with the different cloud algorithms used for each instrument (SACURA for SCIAMACHY and FRESCO for GOME and GOME-2) and the simplified assumptions made in each cloud algorithm (simulation of reflectance spectrum, surface albedo, cloud albedo etc.). Different cloud algorithms calculate different cloud fractions and top heights [Lelli, 2013, Lelli et al., 2016], and as a result they yield different TCO and ACCO values, and consequently different TTCO values. Therefore, the individual TTCO datasets from GOME, SCIAMACHY, and GOME-2 have been harmonised into one consistent in order to remove the biases between the instruments. Correction offsets have been calculated using SCIAMACHY TTCOs as reference. Six different scenarios are tested in order to find the most appropriate approach to harmonise and merge the individual TTCO datasets. Comparisons with integrated ozone columns until 200 hPa from ozonesondes, showed that scenario 1 (no correction is applied to GOME data (which could be justified by the very short overlap period), while GOME-2 is corrected using for each grid-box the mean bias with respect SCIAMACHY for the common years of operation (2007–2012 for GOME-2)) has slightly smaller differences and better correlation, and for this reason it was the preferred scenario used for merging the CCD-IUP dataset.

### Trends of tropical tropospheric ozone

Although scenario 1 is the preferred scenario, there are no strong indications for rejecting the other approaches. Therefore, trends for all six scenarios, were calculated in order to study the influence of the dataset harmonisation on the tropospheric ozone trends between 1996 and 2015. The calculated trends range between  $\sim -4$  to 4 DU/decade. The maximum trend difference between the six scenarios has been found to be locally up to more than 4 DU/decade. It was concluded that the magnitude and significance of the trends dependent strongly on the harmonisation approach used. Nevertheless, all scenarios agree that tropospheric ozone increases over southern and central Africa, the southern tropical Atlantic, southern-east tropical Pacific Ocean, central Australia and south India, and decreases over the Caribbean sea and parts of north Pacific, and over some regions of the southern Pacific Ocean. By comparing the trend results from scenario 1 with tropospheric ozone trends using ozonesonde data from six SHADOZ stations, they are found to be within the  $2\sigma$  of the ozonesonde trend uncertainty. Ten grid boxes surrounding mega-cities have been selected for the comparison with the calculated trends using the tropospheric ozone dataset from the CCD method by Heue et al. [2016] and the published trend results from Ebojie et al. [2016] using the LNM technique. The comparison showed that despite the fact that the trends do not perfectly agree with each other, they still agree within the trends' uncertainties. Analysing the trends over mega-cities from the current study, it was noticed that tropospheric ozone decreased by  $-0.2 - -0.3$  DU/decade at the largest cities such as Jakarta and Mexico, and increased significantly in Manila, Bangkok, and Kinshasa by  $\sim 1$  DU/decade. The magnitude of the tropospheric ozone increase is not linearly related with the size and the industrialisation of the selected mega-cities, since tropospheric ozone production from its precursors,  $\text{NO}_x$  and VOCs, is not linear and also depends on local meteorology and transport.

### **TTCO variability**

The seasonal tropical tropospheric ozone variability of the last 20-year has been studied using the harmonised TTCO dataset. The distinctive wave-one pattern with higher values over the Atlantic and lower values over the Pacific ocean was observed, with higher tropospheric ozone values noticed, over the south Atlantic ocean in autumn. Additionally, the dataset has been latitudinally and longitudinally averaged in order to construct a zonal mean monthly mean tropical tropospheric ozone climatology record for the years 1996–2015. The pattern of the TTCO zonal climatology is in good agreement with Ziemke et al. [2011] using OMI/MLS data and Righi et al. [2015] using EMAC simulations. The response of various factors such as, ENSO, QBO, the solar and the seasonal cycle on tropospheric ozone was quantified. ENSO contributes to the tropical tropospheric ozone variability by about +7 DU over the western Pacific and Indian ocean and by <-10 DU over the eastern Pacific ocean. The magnitude and location of this response agrees well with other studies from Doherty et al. [2006], Oman et al. [2011] and Ziemke et al. [2010]. The solar cycle has been found to contribute by  $\pm 5$ –7 DU, mainly over the northern tropics. QBO contributed in total 5–6 DU to the tropical tropospheric ozone variability, mainly over the southern tropics. The seasonal cycle was found to have the strongest contribution in the TTCO variability, contributing by more than 15 DU over the northern tropics and the Atlantic ocean whereas elsewhere its total contribution is less than 10 DU, with the weakest contribution noticed over the west Pacific Ocean (< 5 DU).

### **El Niño and tropical tropospheric ozone**

The ENSO response on tropical tropospheric ozone has been quantified by calculating monthly tropospheric ozone anomalies during the two major El Niños, in 1997 and 2015 and La Niñas, in 1999 and 2010. It has been shown that the El Niño events increased tropospheric ozone over Indonesia by 10–15 DU, and decreased it over the east Pacific ocean by  $\sim 10$  DU. La Niña was found to increase tropospheric ozone in the entire tropics by  $\sim 6$ –8 DU with the exception of Indian Ocean and central tropics, where it decreases ozone by 5 to 10 DU. These findings are in agreement with studies made by Chandra et al. [2002, 2009], Doherty et al. [2006], Logan et al. [2008], Ziemke et al. [2009b, 2015]. When comparing tropospheric ozone anomalies between the 1997 and 2015 El Niños and 1999 and 2010 La Niñas, the 2015 El Niño and 2010 La Niña events resulted in much stronger ozone increase in the Tropics. The influence of the 2015 El Niño event on tropospheric ozone concentrations was further investigated using tropospheric O<sub>3</sub> simulations from the ECHAM-MESSY atmospheric chemistry model (EMAC). EMAC was found to overestimate tropical tropospheric ozone mainly over the northern Africa, the Indian ocean, and the north-east Pacific ocean by 10–15 DU and underestimated tropospheric ozone over the Atlantic, the west Pacific ocean, and the central-south Africa by 10–15 DU compared to CCD results. These findings are consistent with the EMAC validation made by Righi et al. [2015], Ziemke et al. [2011], and Joeckel et al. [2016]. The simulated ozone precursors (CO, and NO<sub>2</sub>) by EMAC are generally underestimated compared with satellite observations of GOME-2 and MOPITT ( $\sim 30\%$  for NO<sub>2</sub> tropospheric columns and  $\sim 50\%$  for CO volume mixing ratio at 300 hPa). EMAC simulations for two modes, one with and one without biomass burning emissions was studied for the 2015 El Niño event in order to separate the effect of biomass burning and dynamical processes (stratosphere-to-troposphere

exchange (STE), meteorology, long range transport, etc). The results suggest that dynamics have mainly modulated the TCO anomalies during 2015 El Niño event, with the exception of the Indonesian region where biomass burning resulted in a tropospheric ozone increase of about +10 DU.

## 7.2 Outlook

During this study, the retrieval of tropical tropospheric ozone from nadir data of GOME, SCIAMACHY and GOME-2 was successfully carried out using the CCD method. However, additional prospects for future research were identified. These concern (1) the optimisation of the CCD method, (2) efficient changes in the WFDOAS total ozone retrieval algorithm and (3) the interpretation of the TCO results.

- *CCD technique improvements:*

It has been shown that the stratospheric ozone columns are reasonably well approximated by the assumptions and corrections made for the ACCO retrieval, however there are still limitations in cases where only few cloudy data are available in some latitude bands as a result of the ITCZ seasonal migration. Therefore, the CCD algorithm could be extended to higher (lower) latitudes in boreal summer (winter) following the ITCZ movement. The ACCO adjustment to the 200 hPa level which is now based on a global latitudinally averaged ozone climatology [Fortuin and Kelder, 1998], could be switched to a climatology produced by the cloud slicing technique [Ziemke et al., 2001] only for the "clean" western Pacific reference region. This way, the latitudinally averaged ozone mixing ratios will be more representative for the reference region for the ACCO and will not include ozone values over polluted areas. The  $2.5^{\circ} \times 5^{\circ}$  degrees grid used in this study has been proven to be too large in order to study the long term evolution of tropospheric ozone from mega-cities. The instruments' spatial resolution (especially for GOME) was the limiting factor for the grid selection. It is expected that the high spatial resolution ( $7 \times 7$  km) of the TROPOMI instrument aboard S5p (expected launch middle of 2017), will allow smaller grids to be selected, which will result to more reliable tropospheric ozone results on smaller local scale, i.e. mega cities. The extension of the time-series should start with the use of the GOME-2/MetopC total ozone and cloud data and be further extended with the future Sentinel-5 mission [ESA, 2017]. The new missions are additionally expected to have more accurate cloud retrieval algorithms, which will be a promising improvement for the ACCO retrieval and the final TCO results.

- *Modifications on the WFDOAS total ozone retrieval:*

Further optimization of the WFDOAS data using the same algorithm for cloud properties for all satellite datasets would improve the consistency between the datasets. A sensitivity study for the WFDOAS ozone retrieval above different cloudy scenes (various cf, cth, and cot) could be quantified in a future study by testing synthetic data from a radiative transfer model (eg. SCIATRAN). This could improve further the insight to the impact on the TCO retrieval and the estimation of its uncertainty.

- *Interpretation of results:*

The knowledge of the tropospheric ozone production sensitivity upon its precursors ( $\text{NO}_x$  and VOCs) in specific locations is crucial in order to interpret changes in local concentrations. For example, there are urban regions where extremely large  $\text{NO}_x$  (mainly NO) concentrations may destroy (titrate) ozone locally, though later it is generated downwind of the cities, over rural areas due to VOCs oxidation [Pusede et al., 2012]. The relative change of formaldehyde (HCHO) (representing VOCs) to  $\text{NO}_2$  (representing  $\text{NO}_x$ ) concentrations, for both satellite observations and model simulations, could define the ozone production regime ( $\text{NO}_x$  or VOCs sensitive) using the reference  $R_{FN}$  ratio values calculated from Martin et al. [2004] and later improved by Duncan et al. [2010]. Alternatively, the glyoxal (CHO.CHO) to formaldehyde (HCHO) ratio ( $R_{GF}$ ) could be used in order to conclude whether the origin of ozone precursors emissions is biogenic or anthropogenic (e.g. Vrekoussis et al. [2010] and later Alvarado [2016]). In this way, the ozone production origin could be investigated over selected areas and better strategies of emissions regulations can be followed ( $\text{NO}_x$  or VOCs reduction) in order to effectively reduce the tropospheric ozone burden.

Alternatively to the approach combining different CCM runs, switching on and off the biomass burning emissions (see: Section 6.4) to quantify the contribution of biomass burning emissions and dynamics during the 2015 El Niño event, another approach could be applied using "tagged" chemical transport model (CTM) simulations. For example, Butler et al. [2011], Emmons et al. [2012] and Coates et al. [2015] used tagged/labeled chemical mechanisms for  $\text{NO}_x$  and VOCs emissions, and every hydrocarbon produced during the degradation of a VOC, in order to attribute ozone production to emission sources of  $\text{NO}_x$  and/or VOCs. With this method, the fate of the emitted species is followed and a track of their chemical reaction pathways is made [Coates et al., 2015, Grewe et al., 2012].



## Bibliography

Adler, F. R., Huffman G. J., Chang A., Ferraro R., Xie P.P., Janowiak J., Rudolf, Schneider B.U., Curtis S., Bolvin D, Gruber A., Susskind J., Arkin P, and Nelkin E.: The version-2 Global Precipitation Climatology Project (GPCP) monthly precipitation analysis (1979 - present), *J. Hydrometeor.*, 4, 1147-1167, 2003.

Alvarado Bonilla L.: Investigating the role of glyoxal using satellite and MAX-DOAS measurements, PhD thesis, University of Bremen, 2016

Anderson, J. G., W. H. Brune, and M. H. Proffitt: Ozone destruction by chlorine radicals within the Antarctic vortex: The spatial and temporal evolution of ClO-O<sub>3</sub> anticorrelation based on in situ ER-2 data, *J. Geophys. Res.*, 94(D9), 11465-11479, doi:10.1029/JD094iD09p11465, 1989.

Apel, E. C., et al.: Impact of the deep convection of isoprene and other reactive trace species on radicals and ozone in the upper troposphere, *Atmos. Chem. Phys.*, 12(2), 1135-1150, doi:10.5194/acp-12-1135-2012, 2012.

Avery, M., Twohy, C., McCabe, D., Joiner, J., Severance, K., Atlas, E., Blake, D., Bui, T. P., Crouse, J., Dibb, J., Diskin, G., Lawson, P., McGill, M., Rogers, D., Sachse, G., Scheuer, E., Thompson, A. M., Trepte, C., Wennberg, P. and Ziemke, J.: Convective distribution of tropospheric ozone and tracers in the Central American ITCZ region: Evidence from observations during TC4, *J. Geophys. Res. Atmos.*, 115(19), doi:10.1029/2009JD013450, 2010.

Baird Colin and Cann Michael: *Environmental Chemistry*, 3rd edition, W.H. Freeman and Company, New York, 2005

Baldwin, M. P., Gray, L. J., Dunkerton, T. J., Hamilton, K., Haynes, P. H., Randel, W. J., Holton, J. R., Alexander, M. J., Hirota, I., Horinouchi, T., Jones, D. B. A., Kinnersley, J. S., Marquardt, C., Sato, K., Takahashi, M.: The quasi-biennial oscillation, *Rev. Geophys.*, 39(2), 179-229, doi:10.1029/1999RG000073, 2001.

- Bhartia, P. K., McPeters, R. D., Flynn, L. E., Taylor, S., Kramarova, N. A., Frith, S., Fisher, B., and DeLand, M.: Solar Backscatter UV (SBUV) total ozone and profile algorithm, *Atmos. Meas. Tech.*, 6, 2533-2548, doi:10.5194/amt-6-2533-2013, 2013.
- Battino, Rubin and Rettich, Timothy R. and Tominaga, Toshihiro: The Solubility of Oxygen and Ozone in Liquids *Journal of Physical and Chemical Reference Data*, 12, 163-178, DOI: <http://dx.doi.org/10.1063/1.555680>, 1983.
- Beig, G. and Singh, V.: Trends in tropical tropospheric column ozone from satellite data and MOZART model, *Geophys. Res. Lett.*, 34(17), L17801, doi:10.1029/2007GL030460, 2007.
- Bjerknes, J.: A possible response of the atmospheric Hadley circulation to equatorial anomalies of ocean temperature. *Tellus*, 18(4), 820-829, 1966.
- Bojkov, R., L. Bishop, W. J. Hill, G. C. Reinsel, and G. C. Tiao: A statistical trend analysis of revised Dobson total ozone data over the northern hemisphere, *J. Geophys. Res.*, 95(D7), 9785-9807, doi:10.1029/JD095iD07p09785, 1990.
- Bojkov, R. D., V. E. Fioletov, and A. M. Shalamjansky: Total ozone changes over Eurasia since 1973 based on reevaluated filter ozonometer data, *J. Geophys. Res.*, 99(D11), 22985-22999, doi:10.1029/94JD02006, 1994.
- Bourassa, A. E., Degenstein, D. A., Randel, W. J., Zawodny, J. M., Kyrölä, E., McLinden, C. A., Sioris, C. E., and Roth, C. Z.: Trends in stratospheric ozone derived from merged SAGE II and Odin-OSIRIS satellite observations, *Atmos. Chem. Phys.*, 14, 6983-6994, doi:10.5194/acp-14-6983-2014, 2014.
- Bovensmann, H., Burrows, J. P., Buchwitz, M., Frerick, J., Noël, S., Rozanov, V. V., Chance, K. V. and Goede, A. P. H.: SCIAMACHY: Mission Objectives and Measurement Modes, *J. Atmos. Sci.*, 56(2), 127-150, doi:10.1175/1520-0469(1999)056<0127:SMOAMM>2.0.CO;2, 1999.
- Box, G. E. P., Jenkins, G. M., and Reinsel, G. C.: *Time Series Analysis, Forecasting and Control*, 3rd ed. Prentice Hall, Englewood Cliffs, NJ, 1994.
- Brewer, A. W.: Evidence for a world circulation provided by measurements of helium and water vapor distribution in the stratosphere, *Q. J. Roy. Meteorol. Soc.*, 75, 351-363, 1949.
- Boynard, A., Clerbaux, C., Coheur, P.-F., Hurtmans, D., Turquety, S., George, M., Hadji-Lazaro, J., Keim, C., and Meyer-Arnek, J.: Measurements of total and tropospheric ozone from IASI: comparison with correlative satellite, ground-based and ozonesonde observations, *Atmos. Chem. Phys.*, 9, 6255-6271, doi:10.5194/acp-9-6255-2009, 2009
- Bracher, A., Weber, M., Bramstedt, K., Coldewey-Egbers, M., Lamsal, L. N. and Burrows, J. P.: Global satellite validation of SCIAMACHY O<sub>3</sub> columns with GOME WFOAS, *Atmos. Chem. Phys. Discuss.*, 5(1), 795-813, doi:10.5194/acpd-5-795-2005, 2005.
- Beirle, S., Platt, U., Wenig, M., Wagner, T., Highly resolved global distribution of tropospheric NO<sub>2</sub> using GOME narrow swath mode data, *Atmos. Chem. Phys. Discuss.* 4, 1665-1689, 2004(a).

- Bruhwyler, L. P., and K. Hamilton: A numerical simulation of the stratospheric ozone quasi-biennial oscillation using a comprehensive general circulation model, *J. Geophys. Res.*, 104(D23), 30525-30557, doi:10.1029/1999JD900385, 1999.
- Buchwitz, M., V. V. Rozanov, and J. P. Burrows: A near-infrared optimized DOAS method for the fast global retrieval of atmospheric CH<sub>4</sub>, CO, CO<sub>2</sub>, H<sub>2</sub>O, and N<sub>2</sub>O total column amounts from SCIAMACHY Envisat-1 nadir radiances, *J. Geophys. Res.*, 105(D12), 15231-15245, doi:10.1029/2000JD900191, 2000.
- Burnett RT, Brook JR, Yung WT, Dales RE, Krewski D. Association between Ozone and Hospitalization for Respiratory Diseases in 16 Canadian Cities. *Environ Res.*, 72:24-31, 1997.
- Burrows, J. P., Hlzle, E., Goede, A., Visser, H., and Fricke, W.: SCIAMACHY - scanning imaging absorption spectrometer for atmospheric chartography, *Acta Astronautica*, 35, 445-451, 1995.
- Burrows, J. P., Weber, M., Buchwitz, M., Rozanov, V., Ladstätter-Weißenmayer, A., Richter, A., DeBeek, R., Hoogen, R., Bramstedt, K., Eichmann, K.-U., Eisinger, M. and Perner, D.: The Global Ozone Monitoring Experiment (GOME): Mission Concept and First Scientific Results, *J. Atmos. Sci.*, 56(2), 151-175, doi:10.1175/1520-0469(1999)056<0151:TGOMEG>2.0.CO;2, 1999.
- Burrows, J. P., Bovensmann, H., Bergametti, G., Flaud, J. ., Orphal, J., Noël, S., Monks, P. ., Corlett, G. ., Goede, A. ., von Clarmann, T., Steck, T., Fischer, H. and Friedl-Vallon, F: The geostationary tropospheric pollution explorer (GeoTROPE) mission: objectives, requirements and mission concept, *Adv. Sp. Res.*, 34(4), 682-687, doi:10.1016/j.asr.2003.08.067, 2004.
- Burrows, J.P., Platt, U., Borrell, P. (Eds.): The remote sensing of tropospheric composition from space, 978-3-642-14790-6, Springer-Verlag, Berlin, Heidelberg, pp. 259-313 <http://dx.doi.org/10.1007/978-3-642-14791-3>, 2011.
- Butchart, N.: The Brewer-Dobson circulation, *Rev. Geophys.*, 52, doi:10.1002/2013RG000448, 2014.
- Butler, T. , Lawrence, M., Taraborrelli, D. and Lelieveld, J.: Multi-day ozone production potential of volatile organic compounds calculated with a tagging approach. *Atmospheric Environment*, 45(24):4082 - 4090, 2011.
- Callies, J., Corpaccioli, E. and Eisinger, M., Hahne, A. and Lefebvre, A.: GOME-2 - Metop-s second-generation sensor for operational ozone monitoring, *ESA Bull. Sp. Agency*, 102, 28-36, 2000.
- Calvo, N., Garcia, R. R., Randel, W. J., Marsh, D. R.: Dynamical mechanism for the increase in tropical upwelling in the lowermost tropical stratosphere during warm ENSO events. *J. Atmos. Sci.* 67, 2331-2340, 2010.
- Castanheira, J. M., Peevey, T. R., Marques, C. A. F., and Olsen, M. A.: Relationships between Brewer-Dobson circulation, double tropopauses, ozone and stratospheric water vapour, *Atmos. Chem. Phys.*, 12, 10195-10208, doi:10.5194/acp-12-10195-2012, 2012.

- Chandra, S., J. R. Ziemke, W. Min, and W. G. Read, Effects of 1997-1998 El nino on tropospheric ozone and water vapor, *Geophys. Res. Lett.*, 25, 3867-3870, 1998.
- Chandra S, Ziemke JR, Stewart RW: An 11-year solar cycle in tropospheric ozone from TOMS measurements. *Geophys Res Letters* 1999;26(2):185-8. doi:10.1029/1998GL900272, 1999.
- Chandra, S., J. R. Ziemke, P. K. Bhartia, and R. V. Martin, Tropical tropospheric ozone: Implications for dynamics and biomass burning, *J. Geophys. Res.*, 107(D14), doi:10.1029/2001JD000447, 2002.
- Chandra, S., Ziemke, J.R., Tie, X. and Brasseur, G.: Elevated ozone in the troposphere over the Atlantic and Pacific oceans in the Northern Hemisphere. *Geophysical Research Letters* 31: doi: 10.1029/2004GL020821. issn: 0094-8276, 2004.
- Chandra, S., Ziemke, J. R., Duncan, B. N., Diehl, T. L., Livesey, N. J., and Froidevaux, L., Effects of the 2006 El Niño on tropospheric ozone and carbon monoxide: implications for dynamics and biomass burning, *Atmos. Chem. Phys.*, 9, 4239-4249, doi:10.5194/acp-9-4239-2009, 2009.
- Chameides, W. L. and Walker, J. C. G.: A photochemical theory for tropospheric ozone, *J. Geophys. Res.*, 78, 8751-8760, 1973.
- Chapman S.: A theory of upper-atmospheric ozone, *Mem. R. Meteorol. Soc.*, 3, pp. 103-125, 1930.
- Chehade, W., Gür, B., Spietz, P., Gorshelev, V., Serdyuchenko, A., Burrows, J. P, and Weber, M.: Temperature dependent ozone absorption cross section spectra measured with the GOME-2 FM3 spectrometer and first application in satellite retrievals, *Atmos. Meas. Tech.*, 6, 1623-1632, <https://doi.org/10.5194/amt-6-1623-2013>, 2013.
- Chehade, W., Weber, M., and Burrows, J. P: Total ozone trends and variability during 1979-2012 from merged data sets of various satellites, *Atmos. Chem. Phys.*, 14, 7059-7074, doi:10.5194/acp-14-7059-2014, 2014.
- Charles S. Cockell, Gerda Horneck, Christa Baumstark-Khan: *The Ultraviolet Radiation Environment of Earth and Mars: Past and Present*, Springer in *Astrobiology*, pp 219-232, 2002.
- Chen, B., and Z. Liu: Global water vapor variability and trend from the latest 36-year (1979 to 2014) data of ECMWF and NCEP reanalyses, radiosonde, GPS, and microwave satellite, *J. Geophys. Res. Atmos.*, 121, 11,442-11,462, doi:10.1002/2016JD024917, 2016.
- Coates, J. and Butler, T. M.: A comparison of chemical mechanisms using tagged ozone production potential (TOPP) analysis, *Atmos. Chem. Phys.*, 15, 8795-8808, doi:10.5194/acp-15-8795-2015, 2015.
- Coldewey-Egbers, M., Weber, M., Lamsal, L. N., de Beek, R., Buchwitz, M. and Burrows, J. P: Total ozone retrieval from GOME UV spectral data using the weighting function DOAS approach, *Atmos. Chem. Phys.*, 5(4), 1015-1025, doi:10.5194/acp-5-1015-2005, 2005.

- Cooper, O. R. et al. Increasing springtime ozone mixing ratios in the free troposphere over western North America. *Nature* 463, 344-348, 2010.
- Cooper, O. R., Parrish, D. D., Ziemke, J., Balashov, N. V., Cupeiro, M., Galbally, I. E., Gilge, S., Horowitz, L., Jensen, N. R., Lamarque, J.-F., Naik, V., Oltmans, S. J., Schwab, J., Shindell, D. T., Thompson, A. M., Thouret, V., Wang, Y. and Zbinden, R. M.: Global distribution and trends of tropospheric ozone: An observation-based review, *Elem. Sci. Anthr.*, 2, 000029, doi:10.12952/journal.elementa.000029, 2014.
- Coyle, M.: *The Gaseous Exchange of Ozone at Terrestrial Surfaces: Non-stomatal Deposition to Grassland*, School of Geosciences, Faculty of Science and Engineering, The University of Edinburgh, Edinburgh, 270 pp., 2005.
- Coyle, M., Nemitz, E., Storeton-West, R., Fowler, D., and Cape, J. N.: Measurements of ozone deposition to a potato canopy, *Agr. Forest Meteorol.*, 149, 655-666, doi:10.1016/j.agrformet.2008.10.020, 2009.
- Crutzen P. J.: The influence of nitrogen oxides on the atmospheric ozone content, *Quart. J. Roy. Meteorol. Soc.*, 96 , pp. 320-325, 1970.
- Crutzen, P. J.: Photochemical reactions initiated by and influencing ozone in unpolluted tropospheric air, *Tellus A*, 26(1-2), doi:10.3402/tellusa.v26i1-2.9736, 1974.
- Crutzen, P.J., Arnold, F.: Nitric acid cloud formation in the cold Antarctic stratosphere: A major cause for springtime ozone hole, *Nature*, 324, p. 651, 1986.
- Crutzen, P. J.: Ozone in the troposphere, in *Composition, Chemistry, and Climate of the Atmosphere*, pp. 349-393, Reinhold N., New York., 1995.
- Crutzen, P. J.: Geology of mankind: the anthropocene. *Nature* 415, 23, 2002.
- Cuesta, J., Eremenko, M., Liu, X., Dufour, G., Cai, Z., Hpfner, M., von Clarmann, T., Sellitto, P., Foret, G., Gaubert, B., Beekmann, M., Orphal, J., Chance, K., Spurr, R., and Flaud, J.-M.: Satellite observation of lowermost tropospheric ozone by multispectral synergism of IASI thermal infrared and GOME-2 ultraviolet measurements over Europe, *Atmos. Chem. Phys.*, 13, 9675-9693, doi:10.5194/acp-13-9675-2013, 2013.
- Dahlmann, K., Grewe, V., Ponater, M., Matthes, S.: Quantifying the contributions of individual NO<sub>x</sub> sources to the trend in ozone radiative forcing. *Atmos. Environ.* 45 (17), 2860e2868. doi:10.1016/j.atmosenv.2011.02.071, 2011
- Das, S. S., Venkat Ratnam, M., Uma, K. N., Patra, A. K., Subrahmanyam, K. V., Girach, I. A., Suneeth, K. V., Kumar, K. K. and Ramkumar, G: Stratospheric intrusion into the troposphere during the tropical cyclone Nilam (2012). *Q.J.R. Meteorol. Soc.*, 142: 2168-2179. doi:10.1002/qj.2810, 2016.
- Diab, R. D., Raghunandan, A., Thompson, A. M., and Thouret, V.: Classification of tropospheric ozone profiles over Johannesburg based on mozaic aircraft data, *Atmos. Chem. Phys.*, 3, 713-723, doi:10.5194/acp-3-713-2003, 2003.

- Dickerson, R. E.: The Phenomenon of Life. *Engineering and Science*, 34 (4). pp. 4-11. ISSN 0013-7812  
<http://resolver.caltech.edu/CaltechES:34.4.dickerson>, 1971
- Dickerson, R. R., K. P. Rhoads, T. P. Carsey, S. J. Oltmans, J. P. Burrows, and P. J. Crutzen: Ozone in the remote marine boundary layer: A possible role for halogens, *J. Geophys. Res.*, 104(D17), 21385-21395, doi:10.1029/1999JD900023, 1999.
- Dimitriades, B., and M. Dodge (Ed.), *Proceedings of the Empirical Kinetic Modeling Approach (EKMA) Validation Workshop*, EPA Rep. EPA-600/9-83-014, U.S. Environ. Prot. Agency, Research Triangle Park, N. C., 1983.
- Dobson, G. M.: Origin and distribution of the polyatomic molecules in the atmosphere, *Proc. Roy. Soc. Ldn.*, A236, 187-193, 1956.
- Doherty, R. M., Stevenson, D. S., Collins, W. J., and Sanderson, M. G.: Influence of convective transport on tropospheric ozone and its precursors in a chemistry-climate model, *Atmos. Chem. Phys.*, 5, 3205-3218, doi:10.5194/acp-5-3205-2005, 2005
- Doherty, R. M., D. S. Stevenson, C. E. Johnson, W. J. Collins, and M. G. Sanderson: Tropospheric ozone and El Niño Southern Oscillation: Influence of atmospheric dynamics, biomass burning emissions, and future climate change, *J. Geophys. Res.*, 111, D19304, doi:10.1029/2005JD006849, 2006.
- Drummond, J. R., and G. S. Mand: The Measurement of Pollution in the Troposphere (MOPITT) instrument: Overall performance and calibration requirements, *J. Atmos. Oceanic Technol.*, 13, 314-320, 1996.
- Duncan, B. N., Yoshida, Y., Olson, J. R., Sillman, S., Martin, R. V., Lamsal, L., Hu, Y., Pickering, K. E., Retscher, C., Allen, D. J., and Crawford, J. H.: Application of OMI observations to a spacebased indicator of NO<sub>x</sub> and VOC controls on surface ozone formation, *Atmos. Environ.*, 44, 2213-2223, 2010.
- Duncan, B. N., L. N. Lamsal, A. M. Thompson, Y. Yoshida, Z. Lu, D. G. Streets, M. M. Hurwitz, and K. E. Pickering: A space-based, high-resolution view of notable changes in urban NO<sub>x</sub> pollution around the world (2005-2014), *J. Geophys. Res. Atmos.*, 121, 976-996, doi:10.1002/2015JD024121, 2016.
- Ebojie, F., von Savigny, C., Ladstätter - Weißenmayer, A., Rozanov, A., Weber, M., Eichmann, K., Bötzel, S., Rapp, N., Bovensmann, H., and Burrows, J. P.: Tropospheric column amount of ozone retrieved from SCIAMACHY limb/nadir-matching observations, *Atmos. Meas. Tech.*, 7, 2073-2096, doi:10.5194/amt-7-2073-2014, 2014.
- Ebojie, F., Burrows, J. P., Gebhardt, C., Ladstätter-Weienmayer, A., von Savigny, C., Rozanov, A., Weber, M., and Bovensmann, H.: Global tropospheric ozone variations from 2003 to 2011 as seen by SCIAMACHY, *Atmos. Chem. Phys.*, 16, 417-436, doi:10.5194/acp-16-417-2016, 2016.
- Edwards, D. P., et al., Tropospheric ozone over the tropical Atlantic: A satellite perspective, *J. Geophys. Res.*, 108(D8), 4237, doi:10.1029/2002JD002927, 2003.

- Edwards, D. P., et al.: Observations of carbon monoxide and aerosols from the Terra satellite: Northern Hemisphere variability, *J. Geophys. Res.*, 109, D24202, doi:10.1029/2004JD004727, 2004.
- EEA, 2016, Air Quality in Europe – 2016 report, EEA Report No 28/2016, European Environment Agency.
- Ehhalt, D.H.: On the photochemical oxidation of natural trace gases and man made pollutants in the troposphere, *The Science of the Total Environment* 143 1-15, 1994.
- Emmons, L. K., Hauglustaine, D. A., Müller, J.-F., Carroll, M. A., Brasseur, G. P., Brunner, D., Staehelin, J., Thouret, V., and Marenco, A.: Data composites of airborne observations of tropospheric ozone and its precursors, *J. Geophys. Res.*, 105, 20497-20538, doi:10.1029/2000JD900232, 2000.
- Emmons, L. K., Hess, P. G., Lamarque, J.-F., and Pfister, G. G.: Tagged ozone mechanism for MOZART-4, CAM-Chem and other chemical transport models. *Geoscientific Model Development*, 5(6):1531-1542, 2012.
- Ermolli, I., K. Matthes, T. Dudok de Wit, N. A. Krivova, K. Tourpali, M. Weber, Y. C. Unruh, L. Gray, U. Langematz, P. Pilewskie, E. Rozanov, W. Schmutz, A. Shapiro, S. K. Solanki, G. Thuillier, and T. N. Woods, Recent variability of the solar spectral irradiance and its impact on climate modelling, *Atmos. Chem. Phys.*, 13, doi:10.5194/acp-13-3945-2013, 3945-3977, 2013
- ESA: About GOME-2, latest access: 04.01.17), 2006
- ESA Earthnet Online: SCIAMACHY Product Handbook, latest access: 05.01.17), 2013.
- ESA Earthnet Online: GOME yearly reports, latest access: 05.01.17), 2011.
- ESA: MetOp, latest access: 04.01.17), 2012
- ESA: Future Missions, latest access: 14.07.17), 2017
- EU: Directive 2008/50/EC of the European Parliament and of the Council of 21 May 2008 on ambient air quality and cleaner air for Europe (OJ L 152, 11.6.2008, pp. 1–44)(<http://eur-lex.europa.eu/exUriServ/LexUriServ.do?uri=OJ:L:2008:152:0001:0044:EN:PDF>) (Latest access: 28/02/2017), 2008.
- European Environment Agency: "Air Quality in Europe-2015", No.5, (available at: [http://www.eea.europa.eu/publications/air-quality-in-europe-2015/at\\_download/file](http://www.eea.europa.eu/publications/air-quality-in-europe-2015/at_download/file))(Latest access: 22/03/2017), 2015.
- EUMETSAT: Metop Mission, latest access: 04.01.17), 2017
- Farman, J.C., Gardiner, B.G., Shanklin, J.D.: Large losses of total ozone in Antarctica reveal seasonal ClO<sub>x</sub>/NO<sub>x</sub> interaction, *Nature*, 315, pp. 207-210, 1985.
- Farman, J.C.: Measurements of total ozone using Dobson spectrometers: Some comments on their history, *Planetary and Space Science*, Volume 37, Issue 12, Pages 1601-1604, ISSN 0032-0633, [http://dx.doi.org/10.1016/0032-0633\(89\)90148-7](http://dx.doi.org/10.1016/0032-0633(89)90148-7), 1989.

- Felzer, B., Kicklighter, D., Melillo, J., Wang, C., Zhuang, Q. and Prinn, R.: Effects of ozone on net primary production and carbon sequestration in the conterminous United States using a biogeochemistry model. *Tellus B*, 56: 230-248. doi:10.1111/j.1600-0889.2004.00097.x, 2004.
- Finlayson-Pitts, B.J., Pitts, J.N.: *Chemistry of the Upper and Lower Atmosphere*. Academic Press, San Diego, CA, 2000.
- Fioletov, V. E., L. J. B. McArthur, J. B. Kerr, and D. I. Wardle: Long-term variations of UV-B irradiance over Canada estimated from Brewer observations and derived from ozone and pyranometer measurements, *J. Geophys. Res.*, 106(D19), 23009-23027, doi:10.1029/2001JD000367, 2001.
- Fioletov, V. E.: Estimating the 27-day and 11-year solar cycle variations in tropical upper stratospheric ozone, *J. Geophys. Res.*, 114, D02302, doi:10.1029/2008JD010499, 2009
- Fishman, J., Watson, C. E., Larsen, J. C. and Logan, J. A.: Distribution of tropospheric ozone determined from satellite data, *J. Geophys. Res.*, 95(D4), 3599, doi:10.1029/JD095iD04p03599, 1990.
- Fishman, J., J. M. Hoell Jr., R. D. Bendura, R. J. McNeal, and V. W. J. H. Kirchhoff: NASA GTE TRACE A experiment (September-October 1992): Overview, *J. Geophys. Res.*, 101(D19), 23865-23879, doi:10.1029/96JD00123, 1996.
- Fontaine, B., Roucou, P., Gaetani, M. and Marteau, R.: Recent changes in precipitation, ITCZ convection and northern tropical circulation over North Africa (1979-2007). *Int. J. Climatol.*, 31: 633-648. doi:10.1002/joc.2108, 2011.
- Fortuin, P.J.F. and Kelder, H.: An ozone climatology based on ozonesonde and satellite measurements, *J. Geophys. Res.*, 103(D24), 31709-31734, doi:10.1029/1998JD200008, 1998.
- Fowler, D., Flechard, C., Cape, J. N., Storeton-West, R. L., and Coyle, M.: Measurements of ozone deposition to vegetation quantifying the flux, the stomatal and nonstomatal components, *Water Air Soil Pollut.*, 130, 63-74, doi:10.1023/a:1012243317471, 2001.
- Fowler, D, Amann, M, Anderson, R, Ashmore, M, Cox, P, Depledge, M, Derwent, D, Grennfelt, P, Hewitt, N, Hov, O, Jenkin, M, Kelly, F, Liss, P, Pilling, M, Pyle, J, Slingo, J and Stevenson, D Ground-level ozone in the 21st century: future trends, impacts and policy implications. Royal Society Policy Document 15/08, vol. 15/08, RS1276 edn, The Royal Society, London, 2008.
- Fowler, D., Pilegaard, K., Sutton, M. A., Ambus, P., Raivonen, M., Duyzer, J., Simpson, D., Fagerli, H., Fuzzi, S., Schjoerring, J. K., Granier, C., Neftel, A., Isaksen, I. S. A., Laj, P., Maione, M., Monks, P. S., Burkhardt, J., Daemmgen, U., Neirynek, J., Personne, E., Wichink-Kruit, R., Butterbach-Bahl, K., Flechard, C., Tuovinen, J. P., Coyle, M., Gerosa, G., Loubet, B., Altimir, N., Gruenhage, L., Ammann, C., Cieslik, S., Paoletti, E., Mikkelsen, T. N., Ro-Poulsen, H., Cellier, P., Cape, J. N., Horvath, L., Loreto, F., Niinemets, U., Palmer, P. I., Rinne, J., Misztal, P., Nemitz, E., Nilsson, D., Pryor, S., Gallagher, M. W., Vesala, T., Skiba, U., Brüeggemann, N., Zechmeister-Boltenstern, S., Williams, J., O'Dowd, C., Facchini, M. C., de Leeuw, G., Flossman, A., Chaumerliac, N., and Erisman, J.

- W.: Atmospheric composition change: Ecosystems-Atmosphere interactions, *Atmos. Environ.*, 43, 5193-5267, doi:10.1016/j.atmosenv.2009.07.068, 2009.
- Fahey, D.W. and Hegglin, M. I.: Twenty Questions and Answers About the Ozone Layer: 2010 Update, [online] Available from: <http://go.nature.com/btAZba>, World Meteorological Organization, 2011.
- Fueglistaler, S., Dessler, A. E., Dunkerton, T. J., Folkins, I., Fu, Q. and Mote, P. W.: Tropical tropopause layer, *Rev. Geophys.*, 47(1), RG1004, doi:10.1029/2008RG000267, 2009.
- Fujino, J., Nair, R., Kainuma, M., Masui, T., and Matsuoka, Y.: Multi-gas Mitigation Analysis on Stabilization Scenarios Using Aim Global Model, *The Energy Journal*, Multi Greenhouse Gas Mitigation and Climate Policy, 343-354, 2006
- Garcia-Herrera, R., N. Calvo, R. R. Garcia, and M. A. Giorgetta: Propagation of ENSO temperature signals into the middle atmosphere: A comparison of two general circulation models and ERA-40 reanalysis data, *J. Geophys. Res.*, 111, D06101, doi:10.1029/2005JD006061, 2006.
- Gottelman, A. and Forester, P. M. de F.: A Climatology of the Tropical Tropopause Layer, *J. Meteorol. Soc. Japan*, 80(4B), 911-924, doi:10.2151/jmsj.80.911, 2002.
- Gottelman, A., P. Hoor, L. L. Pan, W. J. Randel, M. I. Hegglin, and T. Birner: The extratropical upper troposphere and lower stratosphere, *Rev. Geophys.*, 49, RG3003, doi:10.1029/2011RG000355, 2011.
- Gebhardt, C., Rozanov, A., Hommel, R., Weber, M., Bovensmann, H., Burrows, J. P., Degenstein, D., Froidevaux, L., and Thompson, A. M.: Stratospheric ozone trends and variability as seen by SCIAMACHY from 2002 to 2012, *Atmos. Chem. Phys.*, 14, 831-846, doi:10.5194/acp-14-831-2014, 2014.
- Gergis, J.L., and Fowler A. M.: Classification of Synchronous Oceanic and Atmospheric El Nino-Southern Oscillation (ENSO) Events for Palaeoclimate Reconstruction." *International Journal of Climatology* 25, 1541-65, 2005
- Giglio, L., Randerson, J. T., and van der Werf, G. R.: Analysis of daily, monthly, and annual burned area using the fourth generation global fire emissions database (GFED4), *J. Geophys. Res.-Biogeo.*, 118, 3173-328, doi:10.1002/jgrg.20042, 2013
- Gottwald M., H. Bovensmann, G. Lichtenberg, S. Noel, A. von Bargaen, S. Slijkhuis, A. Pijters, R. Hoogeveen, C. von Savigny, M. Buchwitz, A. Kokhanovsky, A. Richter, A. Rozanov, T. Holzer-Popp, K. Bramstedt, J.-C. Lambert, J. Skupin, F. Wittrock, H. Schrijver, J.P. Burrows: SCIAMACHY, Monitoring the Changing Earth's Atmosphere; Published by DLR, 2006.
- Gottwald, M. and Bovensmann, H.: SCIAMACHY - Exploring the Changing Earth's Atmosphere. Springer Heidelberg Dordrecht London New York, ISBN 978-90-481-9895-5. 3, 17, 18, 2011
- Götz, F. W. P., A. R. Meetham, and G. M. B. Dobson: The vertical distribution of ozone in the atmosphere, *Proc. R. Soc. London, Ser. A*, 145, 416-443, 1934.

- Grainger, J.F., and J. Ring: Anomalous Fraunhofer Line Profiles, *Nature*, 193(4817), 762, 1962.
- Grebenshchikov S.Y., Zhu H., Schinke R., Qu Z.W.: New theoretical investigations of the photodissociation of ozone in the Hartley, Huggins, Chappuis, and Wulf bands, *Physical Chemistry Chemical Physics*, 9:2044-2067, 2007.
- Grenfell, J.L., D.T. Shindell, and V. Grewe, 2003: Sensitivity studies of oxidative changes in the troposphere in 2100 using the GISS GCM. *Atmos. Chem. Phys.*, 3, 1267-1283, doi:10.5194/acp-3-1267-2003.
- Grewe, V., M. Dameris, R. Hein, R. Sausen, and B. Steil: Future changes of the atmospheric composition and the impact of climate change. *Tellus*, 53B, 103-121, doi:10.1034/j.1600-0889.2001.d01-10.x, 2001.
- Grewe, Volker and Dahlmann, Katrin and Matthes, Sigrun and Steinbrecht, Wolfgang: Attributing ozone to NO<sub>x</sub> emissions: Implications for climate mitigation measures. *Atmospheric Environment*, 59, pp. 102-107. DOI: 10.1016/j.atmosenv.2012.05.002, 2012.
- Grontoft, T.: Measurements and modelling of the ozone deposition velocity to concrete tiles, including the effect of diffusion, *Atmos. Environ.*, 38, 49-58, 2004
- Gür, B.: Temperature Dependent Absorption Cross-Sections of O<sub>3</sub> and NO<sub>2</sub> in the 240 – 790 nm range determined by using the GOME-2 Satellite Spectrometers for use in Remote Sensing Applications, Ph.D. thesis, University of Bremen, 2006.
- Haagen-Smit, A. J.: Chemistry and Physiology of Los Angeles Smog, *Indust. Eng. Chem.*, 44, 1342-1346, doi:10.1021/ie50510a045, 1952
- Hardacre, C., Wild, O., and Emberson, L.: An evaluation of ozone dry deposition in global scale chemistry climate models, *Atmos. Chem. Phys.*, 15, 6419-6436, doi:10.5194/acp-15-6419-2015, 2015
- Heath, D. F., Mateer, C. L., Krueger, A. J: The Nimbus-4 backscatter ultraviolet (BUV) atmospheric ozone experiment two years operation, NASA-TM-X-66204, X-651-73-64, NASA Goddard Space Flight Center; Greenbelt, MD, United States, 1973.
- Heue, K.-P., Coldewey-Egbers, M., Delcloo, A., Lerot, C., Loyola, D., Valks, P., and van Roozendaal, M.: Trends of tropical tropospheric ozone from 20 years of European satellite measurements and perspectives for the Sentinel-5 Precursor, *Atmos. Meas. Tech.*, 9, 5037-5051, doi:10.5194/amt-9-5037-2016, 2016.
- Hilboll A, Richter A, Rozanov A, Hodnebrog O, Heckel A, Solberg S, Stordal F, Burrows JP: Improvements to the retrieval of tropospheric NO<sub>2</sub> from satellite stratospheric correction using SCIAMACHY limb/nadir matching and comparison to Oslo CTM2 simulations, *Atmos. Meas. Tech.*, 6, 565-584, doi:10.5194/amt-6-565-2013, 2013a.

- Hilboll, A., Richter, A., and Burrows, J. P.: Long-term changes of tropospheric NO<sub>2</sub> over megacities derived from multiple satellite instruments, *Atmos. Chem. Phys.*, 13, 4145-4169, doi:10.5194/acp-13-4145-2013, 2013b.
- Hilboll, A., Richter, A., and Burrows, J. P.: NO<sub>2</sub> pollution over India observed from space ? the impact of rapid economic growth, and a recent decline, *Atmos. Chem. Phys. Discuss.*, doi:10.5194/acp-2017-101, in review, 2017.
- Holloway, A.M. and Wayne R.: *Atmospheric Chemistry*. Royal Society of Chemistry Publishing, Cambridge, UK, ISBN: 978-1-84755-807-7, 2010
- Hong, G., Yang, P., Gao, B.-C., Baum, B. A., Hu, Y. X., King, M. D. and Platnick, S.: High Cloud Properties from Three Years of MODIS Terra and Aqua Collection-4 Data over the Tropics, *J. Appl. Meteorol. Climatol.*, 46(11), 1840-1856, doi:10.1175/2007JAMC1583.1, 2007.
- Hudson, R. D., and A. M. Thompson: Tropical tropospheric ozone from total ozone mapping spectrometer by a modified residual method, *J. Geophys. Res.*, 103(D17), 22129-22145, doi:10.1029/98JD00729, 1998.
- Huijnen, V., Wooster, M. J., Kaiser, J. W., Gaveau, D. L. A., Flemming, J., Parrington, M., Inness, A., Murdiyarsso, D., Main, B., van Weele, M.: Fire carbon emissions over maritime southeast Asia in 2015 largest since 1997, *Sci. Rep.* 6, 26886, doi: 10.1038/srep26886, 2016.
- Hwang, S.-H., Kim, J., Won, Y.-I., Cho, H. K., Kim, J. S., Lee, D.- H., Cho, G.-R., and Oh, S. N.: Statistical characteristics of secondary ozone density peak observed in Korea, *Adv. Space Res.*, 36, 952-957, <https://doi.org/10.1016/j.asr.2005.05.080>, 2005.
- Inness, A., Benedetti, A., Flemming, J., Huijnen, V., Kaiser, J. W., Parrington, M., and Remy, S.: The ENSO signal in atmospheric composition fields: emission-driven versus dynamically induced changes, *Atmos. Chem. Phys.*, 15, 9083-9097, doi:10.5194/acp-15-9083-2015, 2015.
- IPCC, 2001: climate change 2001: the scientific basis. Contribution of Working Group 1 to the Third Assessment Report of the Intergovernmental Panel on Climate Change, edited by J. T. Houghton, Y. Ding, D. J. Griggs, M. Noguer, P. J. van der Linden, X. Dai, K. Maskell and C. A. Johnson (eds). Cambridge University Press, Cambridge, UK, and New York, USA, 2001.
- IPCC: Climate Change 2007 - The Physical Science Basis: Working Group I Contribution to the Fourth Assessment Report of the IPCC (Climate Change 2007). [online] Available from: <http://www.amazon.ca/exec/obidos/redirect-tag=citeulike09-20&>, 2007.
- IPCC Working Group 1, I., Stocker, T. F., Qin, D., Plattner, G.-K., Tignor, M., Allen, S. K., Boschung, J., Nauels, A., Xia, Y., Bex, V. and Midgley, P. M.: IPCC, 2013: Climate Change 2013: The Physical Science Basis. Contribution of Working Group I to the Fifth Assessment Report of the Intergovernmental Panel on Climate Change, IPCC, AR5, 1535, 2013.

- Jackman, C. H., Randall, C. E., Harvey, V. L., Wang, S., Fleming, E. L., López-Puertas, M., Funke, B., and Bernath, P. F.: Middle atmospheric changes caused by the January and March 2012 solar proton events, *Atmos. Chem. Phys.*, 14, 1025-1038, doi:10.5194/acp-14-1025-2014, 2014.
- Jacob, D. J.: *Introduction to Atmospheric Chemistry*, Princeton University Press., 2000.
- Jana, P.K., Sarkar, D., Saha, D.K. et al.: Effect of cloud occurrences on tropospheric ozone over, Alipore (22.52N, 88.33E), India, *J Earth Syst Sci*121: 711. doi:10.1007/s12040-012-0196-4, 2012.
- JCGM 100: *Evaluation of measurement data - Guide to the expression of uncertainty in measurement*, Joint Committee for Guides in Metrology, 2008.
- Jia, J., Rozanov, A., Ladstätter - Weißenmayer, A., and P. Burrows, J.: Global validation of improved SCIAMACHY scientific ozone limb data using ozonesonde measurements, *Atmos. Meas. Tech. Discuss.*, 8, 4817-4858, doi:10.5194/amtd-8-4817-2015, 2015.
- Joeckel, P., Tost, H., Pozzer, A., Kunze, M., Kirner, O., Brenninkmeijer, C. A. M., Brinkop, S., Cai, D. S., Dyroff, C., Eckstein, J., Frank, F., Garny, H., Gottschaldt, K.-D., Graf, P., Grewe, V., Kerkweg, A., Kern, B., Matthes, S., Mertens, M., Meul, S., Neumaier, M., Nützel, M., Oberländer-Hayn, S., Ruhnke, R., Runde, T., Sander, R., Scharffe, D., and Zahn, A.: Earth System Chemistry integrated Modelling (ESCiMo) with the Modular Earth Submodel System (MESSy) version 2.51, *Geosci. Model Dev.*, 9, 1153-1200, doi:10.5194/gmd-9-1153-2016, 2016.
- Johnston Harold: Reduction of Stratospheric Ozone by Nitrogen Oxide Catalysts from Supersonic Transport Exhaust, *Science*, Vol. 173, Issue 3996, pp. 517-522, DOI: 10.1126/science.173.3996.517, 1971
- Joiner, J., and P. K. Bhartia: The determination of cloud pressures from rotational Raman scattering in satellite backscatter ultraviolet measurements, *J. Geophys. Res. - Atmospheres*,100(D11), 23019-23026. 1995.
- Jonquieres, I., A. Marengo, A. Maalej, and F Rohrer: Study of ozone formation and transatlantic transport from biomass burning emissions over West Africa during the airborne Tropospheric Ozone Campaigns TROPOZ I and TROPOZ II, *J. Geophys. Res.*, 103(D15), 19059-19073, doi:10.1029/98JD00819, 1998.
- Justice, C. O., Townshend, J. R. G., Vermote, E. F, Masuoka, E., Wolfe, R. E., Saleous, N. Morisette, J.: An overview of MODIS land data processing and product status, *Remote Sensing of Environment*, 83, 3-15, 2002.
- Kattawar, G.W., Young, A.T., Humphreys, T.J.: Inelastic-scattering in planetary-atmospheres.1. The ring effect, without Aerosols, *Astrophys. J.*, 243(3), 1049-1057, 1981.
- Katz, R. W.: Statistical evaluation of climate experiments with general circulation models: A parametric time series approach. *J. Atmos. Sci.*,39, 1446-1455, 1982.

- Kaufman, Y. J., Justice, C. O., Flynn, L. P., Kendall, J. D., Prins, E. M., Giglio, L., Ward, D. E., Menzel, W.P., and Setzer, A. W.: Potential global fire monitoring from EOS-MODIS, *J. Geophys. Res.-Atmos.*, 103, 32215-32238, 1998.
- Keim, C., Eremenko, M., Orphal, J., Dufour, G., Flaud, J.-M., Höpfner, M., Boynard, A., Clerbaux, C., Payan, S., Coheur, P.-F., Hurtmans, D., Claude, H., Dier, H., Johnson, B., Kelder, H., Kivi, R., Koide, T., López Bartolomé, M., Lambkin, K., Moore, D., Schmidlin, F. J., and Stübi, R.: Tropospheric ozone from IASI: comparison of different inversion algorithms and validation with ozone sondes in the northern middle latitudes, *Atmos. Chem. Phys.*, 9, 9329-9347, doi:10.5194/acp-9-9329-2009, 2009.
- Kim, J. H., Newchurch, M. J. and Han, K.: Distribution of Tropical Tropospheric Ozone Determined by the Scan-Angle Method Applied to TOMS Measurements, *J. Atmos. Sci.*, 58(18), 2699-2708, doi:10.1175/1520-0469(2001)058<2699:DOTTOD>2.0.CO;2, 2001.
- Koelemeijer, R. B. A., Stammes, P., Hovenier, J. W. and de Haan, J. F.: A fast method for retrieval of cloud parameters using oxygen A band measurements from the Global Ozone Monitoring Experiment, *J. Geophys. Res.*, 106(D4), 3475, doi:10.1029/2000JD900657, 2001.
- Komhyr, W.D.: A carbon-iodide ozone sensor for atmospheric sounding, *Proceedings of the Ozone Symposium*, Albuquerque, N.M., Edited by H.V. Dutsch, Secretariat of the World Meteorological Organization, Geneva, Switzerland, p. 26, 1964.
- Komhyr, W.D.: Nonreactive gas sampling pump, *Rev. Sci. Inst.*, 38, 981-983, 1967.
- Komhyr, W. D. and R. D. Grass, Dobson ozone spectrophotometer modification, *J. Appl. Meteorol.* 11, No. 5, 858-863, 1972.
- Komhyr, W. D., R. D. Grass, and R. K. Leonard: Dobson spectrophotometer 83: A standard for total ozone measurements, 1962-1987, *J. Geophys. Res.*, 94(D7), 9847-9861, doi:10.1029/JD094iD07p09847, 1989.
- Kulkarni, P. S., Ghude, S. D., and Bortoli, D.: Tropospheric ozone (TOR) trend over three major inland Indian cities: Delhi, Hyderabad and Bangalore, *Ann. Geophys.*, 28, 1879-1885, doi:10.5194/angeo-28-1879-2010, 2010.
- Kurpius, M. and Goldstein, A. H.: Gas-phase chemistry dominates O<sub>3</sub> loss to a forest, implying a source of aerosols and hydroxyl radicals to the atmosphere, *Geophys. Res. Lett.*, 30, 1371, doi:10.1029/2002GL016785, 2003.
- Kokhanovsky, A. A., Rozanov, V. V., Burrows, J. P., Eichmann, K.-U., Lotz, W. and Vountas, M.: The SCIAMACHY cloud products: Algorithms and examples from ENVISAT, *Adv. Sp. Res.*, 36(5), 789-799, doi:10.1016/j.asr.2005.03.026, 2005.
- Lamarque, J. F., Hess, P., Emmons, L., Buja, L., Washington, W., and Granier, C.: Tropospheric ozone evolution between 1890 and 1990, *J. Geophys. Res.-Atmos.*, 110, D08304, doi:10.1029/2004jd005537, 2005.

- Lamarque, J.-F. and Solomon, S.: Impact of changes in climate and halocarbons on recent lower stratosphere ozone and temperature trends, *J. Climate*, 23, 2599-2611, 2010.
- Lamsal, L. N., Martin, R. V., Parrish, D. D., and Krotkov, N. A.: Scaling relationship for NO<sub>2</sub> pollution and population size: a satellite perspective, *Environ. Sci. Technol.*, 47, 7855-7861, 2013.
- Larkinal N.K., Harrison D.E.: ENSO Warm (El Nino) and Cold (La Nina) event life cycles: ocean surface anomaly patterns, their symmetries, asymmetries, and implications. *J. Climate*, 15, 1118-1140, 2002.
- Leeds, A.R.: Lines of Discovery in the History of Ozone. *Annals of the New York Academy of Sciences*, 1 (3), 363-391. 12, 1880
- Leighton, P. A.: *Photochemistry of Air Pollution*, Academic Press, New York, 1961.
- Leith, C. E.: The standard error of time-average estimates of climatic means. *J. Appl. Meteor.*, 12, 1066-1069, 1973.
- Lelieveld, J., Evans, J. S., Fnais, M., Giannadaki, D. and Pozzer, A.: The contribution of outdoor air pollution sources to premature mortality on a global scale, *Nature*, 525, pp. 367-371, 2015.
- Lelli L.: Studies of global cloud field using measurements of GOME, SCIAMACHY and GOME-2, PhD Thesis, University of Bremen, 2013.
- Lelli, L., Kokhanovsky, A. A., Rozanov, V. V., Vountas, M., and Burrows, J. P: Linear trends in cloud top height from passive observations in the oxygen A-band, *Atmos. Chem. Phys.*, 14, 5679-5692, doi:10.5194/acp-14-5679-2014, 2014.
- Lelli, L., Weber M., Burrows J.: Evaluation of SCIAMACHY ESA/DLR cloud parameters version 5.02 by comparisons to ground-based and other satellite data. *Front. Environ. Sci.* 4:43. doi:10.3389/fenvs.2016.00043, 2016.
- Lelieveld, J., van Aardenne, J., Fischer, H., de Reus, M., Williams, J., and Winkler, P: Increasing ozone over the Atlantic Ocean, *Science*, 304, 1483-1487, 2004.
- Levelt, P., van den Oord, G., Dobber, M., Malkki, A., Visser, H., Vries, J. d., Stammes, P., Lundell, J., and Saari, H.: The ozone monitoring instrument, *IEEE Transactions on Geoscience and Remote Sensing*, 44, 1093 - 1101, 2006
- Leventidou, E., Eichmann, K.-U., Weber, M., and Burrows, J. P: Tropical tropospheric ozone columns from nadir retrievals of GOME-1/ERS-2, SCIAMACHY/Envisat, and GOME-2/MetOp-A (1996-2012), *Atmos. Meas. Tech.*, 9, 3407-3427, doi:10.5194/amt-9-3407-2016, 2016.
- Levy II, H., W. J. Moxim, A. A. Klonecki, and P. S. Kasibhatla: Simulated tropospheric NO<sub>x</sub> : Its evaluation, global distribution and individual source contributions, *J. Geophys. Res.*, 104(D21), 26279-26306, doi:10.1029/1999JD900442, 1999.

- Lightfoot, P. D., Cox, R., Crowley, J., Destriau, M., Hayman, G., Jenkin, M., Moortgat, G., and Zabel, F.: Organic peroxy radicals: kinetics, spectroscopy and tropospheric chemistry, *Atmos. Environ. Part A*, 26, 1805-1961, 1992.
- Lim SS, Vos T, Flaxman AD, Danaei G, Shibuya K, Adair-Rohani H, et al. A comparative risk assessment of burden of disease and injury attributable to 67 risk factors and risk factor clusters in 21 regions, 1990-2010: A systematic analysis for the global burden of disease study 2010, *Lancet*, 380(9859):2224-60, 2012.
- Lin, M., Horowitz, L. W., Oltmans, S. J., Fiore, A. M., and Fan, S.: Tropospheric ozone trends at Mauna Loa Observatory tied to decadal climate variability, *Nat. Geosci.*, 7, 136-143, doi:10.1038/ngeo2066, 2014.
- Liou K. N.: An introduction to atmospheric radiation, 2nd edn CA, USA: Academic, 2002
- Logan, J. A., I. Megretskaia, R. Nassar, L. T. Murray, L. Zhang, K. W. Bowman, H. M. Worden, and M. Luo: Effects of the 2006 El Nino on tropospheric composition as revealed by data from the Tropospheric Emission Spectrometer (TES), *Geophys. Res. Lett.*, 35, L03816, doi:10.1029/2007GL031698, 2008.
- Logan, J. A., Staehelin, J., Megretskaia, I. A., Cammas, J.-P., Thouret, V., Claude, H., De Backer, H., Steinbacher, M., Scheel, H.-E., Stübi, R., Fröhlich, M., Derwent, R.: Changes in ozone over Europe: Analysis of ozone measurements from sondes, regular aircraft (MOZAIC) and alpine surface sites, *J. Geophys. Res.*, 117, D09301, doi:10.1029/2011JD016952, 2012.
- Loschnigg, J. and Webster, P. J.: A Coupled Ocean-Atmosphere System of SST Modulation for the Indian Ocean, *J. Clim.*, 13(19), 3342-3360, doi:10.1175/1520-0442(2000)013<3342:ACOASO>2.0.CO;2, 2000.
- D. G. Loyola, M. Coldewey-Egbers, W. Zimmer, M. Koukouli, D. Balis, C. Lerot, M. Van Roozendaal, and M Dameris: Total Ozone Trends Derived From The 14-Years Merged Gome/Sciamachy/Gome-2 Data Record, *Proceedings: Proc. Atmospheric Science Conference, Barcelona, Spain, 7-11 September 2009 (ESA SP-676, November 2009)*, 2009.
- Lunine Jonathan I: Physical conditions on the early Earth, *Phil. Trans. R. Soc. B* 2006 361 1721-1731; DOI: 10.1098/rstb.2006.1900, 2006
- Luo, M., C. P. Rinsland, C. D. Rodgers, J. A. Logan, H. Worden, S. Kulawik, A. Eldering, A. Goldman, M. W. Shephard, M. Gunson, and M. Lampel: Comparison of carbon monoxide measurements by TES and MOPITT: Influence of a priori data and instrument characteristics on nadir atmospheric species retrievals, *J. Geophys. Res.*, 112, D09303, doi:10.1029/2006JD007663, 2007.
- Lyons, Timothy W. and Reinhard, Christopher T. and Planavsky, Noah J.: The rise of oxygen in Earth's early ocean and atmosphere. *Nature*, 506 (7488). pp. 307-315. ISSN 0028-0836, <http://dx.doi.org/10.1038/nature13068>, 2014.

- Madden, R. A., and P. R. Julian: Detection of a 40-50 day oscillation in the zonal wind in the tropical Pacific. *J. Atmos. Sci.*, 28, 702-708, 1971.
- Madronich, S., Shao, M., Wilson, S. R., Solomon, K. R., Longstreth, J. D., and Tang, X. Y.: Changes in air quality and tropospheric composition due to depletion of stratospheric ozone and interactions with changing climate: implications for human and environmental health, *Photochem. Photobiol. Sci.*, 14, 149- 169, doi:10.1039/C4PP90037E, 2015.
- Margulis, L.: Genetic and evolutionary consequences of symbiosis, *Experimental Parasitology*, 39 (2): 277-349. doi:10.1016/0014-4894(76)90127-2, 1976
- McPeters, R.D., Bhartia, P. K., Krueger, A. J., Herman, J. R., Schlesinger, B.M., Wellemeyer, C.G., Sefior, Glen Jaross, C. J., Taylor, S.L., Swissler, T., Torres, O., Labow, G., Byerly, W., Cebula, R. P.: Nimbus-7 Total Ozone Mapping Spectrometer (TOMS) Data Products User's Guide, URL: <http://jwocky.gsfc.nasa.gov/datainfo/n7usrguide.pdf>, 1996.
- McPhaden, M.J., S.E. Zebiak, and M.H. Glantz: ENSO as an integrating concept in Earth science. *Science*, 314, 1740-1745, 2006.
- Martin, R. V.: Interpretation of TOMS observations of tropical tropospheric ozone with a global model and in situ observations, *J. Geophys. Res.*, 107(D18), 4351, doi:10.1029/2001JD001480, 2002.
- Martin, R. V., A. M. Fiore, and A. Van Donkelaar: Space-based diagnosis of surface ozone sensitivity to anthropogenic emissions, *Geophys. Res. Lett.*, 31, L06120, doi:10.1029/2004GL019416, 2004.
- Medina-Ramn M, Zanobetti A, Schwartz J. The Effect of Ozone and PM10 on Hospital Admissions for Pneumonia and Chronic Obstructive Pulmonary Disease: a national multicity study. *Am J Epidemiol.*, 163(6):579-588, 2006.
- Mieruch, S., Noël, S., Bovensmann, H., and Burrows, J. P: Analysis of global water vapour trends from satellite measurements in the visible spectral range, *Atmos. Chem. Phys.*, 8, 491-504, doi:10.5194/acp-8-491-2008, 2008.
- Mieruch, S., M. Schröder, S. Noël, and J. Schulz: Comparison of decadal global water vapor changes derived from independent satellite time series, *J. Geophys. Res. Atmos.*, 119, 12,489-12,499, doi:10.1002/2014JD021588, 2014.
- Miles, G. M., Siddans, R., Kerridge, B. J., Latter, B. G., and Richards, N. A. D.: Tropospheric ozone and ozone profiles retrieved from GOME-2 and their validation, *Atmos. Meas. Tech.*, 8, 385-398, doi:10.5194/amt-8-385-2015, 2015.
- Mohankumar, K.: *Stratosphere Troposphere Interactions: An Introduction*, 416Cochin: Springer. ISBN 978-1-4020-8216-0, 2008
- Molina, L.T., Molina, M.J.: Production of Cl<sub>2</sub>O<sub>2</sub> from the self-reaction of the ClO radical, *J. Phys. Chem. A*, 91, pp. 433-436, 1987.

- Molina, M.J., Rowland, F.S.: Stratospheric sink for chlorofluoromethanes: Chlorine atom-catalysed destruction of ozone, *Nature*, 249 pp. 810-812, 1974.
- Monks, P. S.: Gas-phase radical chemistry in the troposphere, *Chem. Soc. Rev.*, 34, 376-395, 2005.
- Monks, P. S., Archibald, A. T., Colette, A., Cooper, O., Coyle, M., Derwent, R., Fowler, D., Granier, C., Law, K. S., Mills, G. E., Stevenson, D. S., Tarasova, O., Thouret, V., von Schneidemesser, E., Sommariva, R., Wild, O., and Williams, M. L.: Tropospheric ozone and its precursors from the urban to the global scale from air quality to short-lived climate forcer, *Atmos. Chem. Phys.*, 15, 8889-8973, doi:10.5194/acp-15-8889-2015, 2015.
- Morris, G. A., Thompson, A. M., Pickering, K. E., Chen, S., Bucsela, E. J., and Kucera, P. A.: Observations of ozone production in a dissipating tropical convective cell during TC4, *Atmos. Chem. Phys.*, 10, 11189-11208, doi:10.5194/acp-10-11189-2010, 2010.
- Munro, R., Siddans, R., Reburn, W. J., and Kerridge, B. J.: Direct measurement of tropospheric ozone distributions from space, *Nature*, 392, 168-171, doi:10.1038/32392, 1998.
- Murray, L. T., J. A. Logan, and D. J. Jacob: Inter-annual variability in tropical tropospheric ozone and OH: The role of lightning, *J. Geophys. Res. Atmos.*, 118, 11,468-11,480, doi:10.1002/jgrd.50857, 2013.
- Myhre, G., Shindell, D., Bréon, F.-M., Collins, W., Fuglestedt, J., Huang, J., Koch, D., Lamarque, J.-F., Lee, D., Mendoza, B., Nakajima, T., Robock, A., Stephens, G., Takemura, T., and Zhang, H.: Anthropogenic and Natural Radiative Forcing, in: *Climate Change, The Physical Science Base, Contribution of Working Group 1 to the Fifth Assessment report of the intergovernmental panel on climate change*, Cambridge, UK, 2013.
- Naujokat, B.: An update of the observed quasi-biennial oscillation of the stratospheric winds over the tropics. *J. Atmos. Sci.*, 43, 1873-1877, 1986.
- Neu, J. L., Flury, T., Manney, G. L., Santee, M. L., Livesey, N. J., and Worden, J.: Tropospheric ozone variations governed by changes in stratospheric circulation, *Nat. Geosci.*, 7, 340-344, doi:10.1038/ngeo2138, 2014
- Neiryneck, J., Gielen, B., Janssens, I. A., and Ceulemans, R.: Insights into ozone deposition patterns from decade-long ozone flux measurements over a mixed temperate forest, *J. Environ. Monit.*, 14, 1684-1695, doi:10.1039/c2em10937a, 2012.
- Newton, R., Vaughan, G., Ricketts, H. M. A., Pan, L. L., Weinheimer, A. J., and Chemel, C.: Ozone profile from the West Pacific Warm Pool: measurements and validation, *Atmos. Chem. Phys.*, 16, 619-634, doi:10.5194/acp-16-619-2016, 2016.
- NOAA National Centers for Environmental Information, State of the Climate: Global Analysis for January 2017, latest access: February 17, 2017 from <http://www.ncdc.noaa.gov/sotc/global/201701,2017>

- O'Connor, F. M., Law, K. S., Pyle, J. A., Barjat, H., Brough, N., Dewey, K., Green, T., Kent, J., and Phillips, G.: Tropospheric ozone budget: regional and global calculations, *Atmos. Chem. Phys. Discuss.*, 4, 991-1036, doi:10.5194/acpd-4-991-2004, 2004.
- Ojha, N., Pozzer, A., Akritidis, D., and Lelieveld, J.: Secondary ozone peaks in the troposphere over the Himalayas, *Atmos. Chem. Phys.*, 17, 6743-6757, <https://doi.org/10.5194/acp-17-6743-2017>, 2017.
- Oltmans, S. J., Johnson, B. J., Harris, J. M., Thompson, A. M., Liu, H. Y., Chan, C. Y., Voemel, H., Fujimoto, T., Brackett, V. G., Chang, W. L., Chen, J.-P., Kim, J. H., Chan, L. Y., and Chang, H.-W.: Tropospheric ozone over the North Pacific from ozonesonde observations, *J. Geophys. Res.*, 109, D15S01, doi:10.1029/2003JD003466, 2004.
- Oltmans, S., Lefohn, A., Shadwick, D., Harris, J., Scheel, H., Galbally, I., Tarasick, D., Johnson, B., Brunke, E.-G., and Claude, H.: Recent tropospheric ozone changes - a pattern dominated by slow or no growth, *Atmos. Environ.*, 67, 331-351, doi: 10.1016/j.atmosenv.2012.10.057, 2013.
- Oman, L. D., Ziemke, J. R., Douglass, A. R., Waugh, D. W., Lang, C., Rodriguez, J. M., and Nielsen, J. E.: The response of tropical tropospheric ozone to ENSO, *Geophys. Res. Lett.*, 38, L13706, doi:10.1029/2011GL047865, 2011.
- O3M SAF - EUMETSAT Satellite Application Facility on Ozone and Atmospheric Chemistry Monitoring: Information on Metop-B/GOME-2 products and measurement configurations of GOME-2 instruments on board Metop-A and B satellites, [ast access: 04.01.17](http://www.saf.o3m.org)), 2017.
- Page, S.E., Siegert, F., Rieley, J.O., Boehm, H.-D.V., Jaya, A., Limin, S.: The amount of carbon released from peat and forest fires in Indonesia during 1997, *Nature*, 2002/11/07/print, Article number:420, doi.org/10.1038/nature01131, 2002
- Parrish, D. D., Millet, D. B., and Goldstein, A. H. Increasing ozone in marine boundary layer inflow at the west coasts of North America and Europe. *Atmos. Chem. Phys.* 9, 1303-1323, 2009.
- Parrish, D. D., Singh, H. B., Molina, L., and Madronich, S.: Air quality progress in North American megacities: A review, *Atmos. Environ.*, 45, 7015-7025 CrossRef CAS, 2011.
- Pickering, K. E., Thompson, A. M., Dickerson, R. R., Luke, W. T., McNamara, D. P., Greenberg, J. P., and Zimmerman, R.: Model calculations of tropospheric ozone production potential following observed convective events, *J. Geophys. Res.*, 95, 14,049-14,062, doi:10.1029/JD095iD09p14049, 1990.
- Platt, U. and Perner, D.: Direct Measurements of Atmospheric CH<sub>2</sub>O, HNO<sub>2</sub>, O<sub>3</sub>, NO<sub>2</sub> and SO<sub>2</sub> by Differential Optical Absorption in the Near UV, *J. Geophys. Res.*, 85, 7453-7458, 1980.
- Plumb, R. A., and D. McEwan: The instability of a forced standing wave in a viscous stratified fluid: A laboratory analogue of the quasi-biennial oscillation. *J. Atmos. Sci.*, 35, 1827-1839, 1978.
- Pozzer, A., Jöckel, P., Tost, H., Sander, R., Ganzeveld, L., Kerkweg, A., and Lelieveld, J.: Simulating organic species with the global atmospheric chemistry general circulation model ECHAM5/MESy1: a

- comparison of model results with observations, *Atmos. Chem. Phys.*, 7, 2527-2550, doi:10.5194/acp-7-2527-2007, 2007.
- Preethi, B., Sabin, T. P., Adedoyin, J. A., Ashok, K. : Impacts of the ENSO Modoki and other Tropical Indo-Pacific Climate-Drivers on African Rainfall, *Scientific Reports* 5, Nature, Article number: 16653, doi:10.1038/srep16653, 2015
- Pusede, S. E. and Cohen, R. C.: On the observed response of ozone to NO<sub>x</sub> and VOC reactivity reductions in San Joaquin Valley California 1995-present, *Atmos. Chem. Phys.*, 12, 8323-8339, doi:10.5194/acp-12-8323-2012, 2012.
- Qu, Z.-W., H. Zhu, M. Tashiro, R. Schinke, and S. Farantos, *J. Chem. Phys.* 120, 6811, 2004.
- Rahpoe, N., von Savigny, C., Weber, M., Rozanov, A.V., Bovensmann, H., and Burrows, J. P.: Error budget analysis of SCIAMACHY limb ozone profile retrievals using the SCIATRAN model, *Atmos. Meas. Tech.*, 6, 2825-2837, doi:10.5194/amt-6-2825-2013, 2013.
- Randel, W. J., and A. M. Thompson: Interannual variability and trends in tropical ozone derived from SAGE II satellite data and SHADOZ ozonesondes, *J. Geophys. Res.*, 116, D07303, doi:10.1029/2010JD015195, 2011.
- Randel, W. J., and F. Wu: A stratospheric ozone profile data set for 1979-2005: Variability, trends, and comparisons with column ozone data, *J. Geophys. Res.*, 112, D06313, doi:10.1029/2006JD007339, 2007.
- Randel, W. J., R. R. Garcia, N. Calvo, and D. Marsh: ENSO influence on zonal mean temperature and ozone in the tropical lower stratosphere, *Geophys. Res. Lett.*, 36, L15822, doi:10.1029/2009GL039343, 2009.
- Randerson, J. T., van der Werf, G. R., Giglio, L., Collatz, G. J., Kasibhatla P. S.: Global Fire Emissions Database, Version 4, (GFEDv4). ORNL DAAC, Oak Ridge, Tennessee, USA, doi: 10.3334/ORNL-DAAC/1293, 2015.
- Rex, M. , Wohltmann, I. , Ridder, T. , Lehmann, R. , Rosenlof, K. , Wennberg, P., Weisenstein, D. K. , Notholt, J. , Krüger, K., Mohr, V. and Tegtmeier, S.: A Tropical West Pacific OH Minimum and Implications for Stratospheric Composition, *Atmospheric Chemistry and Physics*, 14 (9), pp. 4827-4841. doi: 10.5194/acp-14-4827-2014, 2014.
- Richter A, Burrows J P, Nüß H, Granier C, Niemeier U: Increase in tropospheric nitrogen dioxide over China observed from space, *Nature*, 437 (7055), 129-132, 2005.
- Richter A.: Differential optical absorption spectroscopy as a tool to measure pollution from space, *Spectroscopy Europe*, Vol. 18, No. 6, 2006.
- Rich DQ, Mittleman MA, Link MS, Schwartz J, Luttmann-Gibson H, Catalano PJ, Speizer FE, Gold DR, Dockery DW. Increased Risk of Paroxysmal Atrial Fibrillation Episodes Associated with Acute Increases in Ambient Air Pollution. *Environ Health Perspect.*, 114:120-123, 2006.

- Righi, M., Eyring, V., Gottschaldt, K.-D., Klinger, C., Frank, F., Jöckel, P., and Cionni, I.: Quantitative evaluation of ozone and selected climate parameters in a set of EMAC simulations, *Geosci. Model Dev.*, 8, 733-768, doi:10.5194/gmd-8-733-2015, 2015.
- Roeckner, E., Brokopf, R., Esch, M., Giorgetta, M., Hagemann, S., Kornbluh, L., Manzini, E., Schlese, U., and Schulzweida, U.: Sensitivity of simulated climate to horizontal and vertical resolution in the ECHAM5 atmosphere model, *J. Climate*, 19, 3771-3791, 2006.
- Rohli, R., and Vega, A.J.: *Applied Climatology, Climate Impacts, and Climatic data*, Jones And Bartlett Publishers, Inc, ISBN 978-0-7637-9101-8, 2nd edition, 2011
- Rolph, G.D.: Real-time Environmental Applications and Display sYstem (READY) Website (<http://www.ready.noaa.gov>). NOAA Air Resources Laboratory, College Park, MD, 2017.
- Royal Swedish Academy of Sciences, Press Release: "The 1995 Nobel Prize in Chemistry", latest access: 15 Feb 2017, 995
- Rozanov, V. V. and Rozanov, A. V.: Differential optical absorption spectroscopy (DOAS) and air mass factor concept for a multiply scattering vertically inhomogeneous medium: theoretical consideration, *Atmos. Meas. Tech.*, 3, 751-780, doi:10.5194/amt-3-751-2010, 2010.
- Rozanov, V. V., Rozanov, A. V., Kokhanovskiy, A. A., and Burrows, J. P.: Radiative transfer through terrestrial atmosphere and ocean: Software package SCIATRAN, *Quant. Spec. and Rad. Trans.*, 133, 13-71, doi:10.1016/j.jqsrt.2013.07.004, 2014
- S5P/TROPOMI Science Verification Report, S5P-IUP-L2-ScVR-RP, Richter A. and the Verification Teams: European Space Agency, [online] Available from: <https://earth.esa.int/documents/247904/2474724/Sentinel-5P-TROPOMI-Science-Verification-Report>, 2015.
- Saiz-Lopez, A., Lamarque, J.-F., Kinnison, D. E., Tilmes, S., Ordóñez, C., Orlando, J. J., Conley, A. J., Plane, J. M. C., Mahajan, A. S., Sousa Santos, G., Atlas, E. L., Blake, D. R., Sander, S. P., Schauffler, S., Thompson, A. M., and Brasseur, G.: Estimating the climate significance of halogen-driven ozone loss in the tropical marine troposphere, *Atmos. Chem. Phys.*, 12, 3939-3949, doi:10.5194/acp-12-3939-2012, 2012
- Sassen, K., Wang, Z. and Liu, D.: Cirrus clouds and deep convection in the tropics: Insights from CALIPSO and CloudSat, *J. Geophys. Res.*, 114(21), D00H06, doi:10.1029/2009JD011916, 2009.
- Sauvage, B., V. Thouret, A. M. Thompson, J. C. Witte, J.-P. Cammas, P. Nédélec, and G. Athier: Enhanced view of the "tropical Atlantic ozone paradox" and "zonal wave one" from the in situ MOZAIC and SHADOZ data, *J. Geophys. Res.*, 111, D01301, doi:10.1029/2005JD006241, 2006.
- Sauvage, B., Gheusi, F., Thouret, V., Cammas, J.-P., Duron, J., Escobar, J., Mari, C., Mascart, P., and Pont, V.: Medium-range mid-tropospheric transport of ozone and precursors over Africa: two numerical case studies in dry and wet seasons, *Atmos. Chem. Phys.*, 7, 5357-5370, doi:10.5194/acp-7-5357-2007, 2007.

- Schinke, R. and G. C. McBane: Photodissociation of ozone in the Hartley band: Potential energy surfaces, nonadiabatic couplings, and singlet/triplet branching ratio. *J. Chem. Phys.* 132, 044305, 2010.
- Schneider, P., Lahoz, W. A., and van der A, R.: Recent satellite-based trends of tropospheric nitrogen dioxide over large urban agglomerations worldwide, *Atmos. Chem. Phys.*, 15, 1205-1220, doi:10.5194/acp-15-1205-2015, 2015.
- Schreier, S. F., Richter, A., Kaiser, J. W., and Burrows, J. P.: The empirical relationship between satellite-derived tropospheric NO<sub>2</sub> and fire radiative power and possible implications for fire emission rates of NO<sub>x</sub>, *Atmos. Chem. Phys.*, 14, 2447-2466, doi:10.5194/acp-14-2447-2014, 2014.
- Schumann, U. and Huntrieser, H.: The global lightning-induced nitrogen oxides source, *Atmos. Chem. Phys.*, 7, 3823-3907, doi:10.5194/acp-7-3823-2007, 2007
- Seinfeld, J. H. and Pandis, S. N.: *Atmospheric Chemistry and Physics: From Air Pollution to Climate Change*. [online] Available from: <http://www.amazon.com/dp/0471178160>, 2006.
- Serdyuchenko, A., Gorshelev, V., Weber, M., Chehade, W., and Burrows, J. P.: High spectral resolution ozone absorption cross-sections –Part 2: Temperature dependence, *Atmos. Meas. Tech.*, 7, 625-636, <https://doi.org/10.5194/amt-7-625-2014>, 2014.
- Sherwood, S. C. and Dessler, A. E.: A model for transport across the tropical tropopause, *J. Atmos. Sci.*, 58(7), 765-779 [online] Available from: <Go to ISI>://000167550300006, 2001.
- Shindell, D. T., Faluvegi, G., Koch, D. M., Schmidt, G. a, Unger, N. and Bauer, S. E.: Improved attribution of climate forcing to emissions., *Science*, 326(5953), 716-8, doi:10.1126/science.1174760, 2009.
- Sierk, B., Richter, A., Rozanov, A., Savigny, C. von, Schmoltner, A. M., Buchwitz, M., Bovensmann, H. and Burrows, J. P.: Retrieval And Monitoring of Atmospheric Trace Gas Concentrations in Nadir and Limb Geometry Using the Space-Borne Sciamachy Instrument, *Environ. Monit. Assess.*, 120(1-3), 65-77, doi:10.1007/s10661-005-9049-9, 2006.
- Sillman, S., The relation between ozone, NO<sub>x</sub> and hydrocarbons in urban and polluted rural environments. *Millennial Review series, Atmos. Environ.*, 33, 12, 1821-1845, 1999.
- Silva RA, West JJ, Zhang Y, Anenberg SC, Lamarque J-F, Shindell DT, et al.: Global premature mortality due to anthropogenic outdoor air pollution and the contribution of past climate change. *Environ Res Lett* 8:034005; doi:10.1088/1748-9326/8/3/034005, 2013.
- Simpson I. R., Shepherd, T. G., Sigmund, M: Dynamics of the lower stratospheric circulation response to ENSO, *Journal of the Atmospheric Sciences*, 68, 2537-2556, 2011.
- Sentinel-5 Precursor : *ESA's Atmospheric Chemistry and Pollution-Monitoring Mission* [production editor: K. Fletcher; Scientific editors: K. McMullan], ISBN 978-92-9221-431-9, Noorwijk : ESA Communications, Engelska vi, 77 s., 2016.

- Solomon, S., Schmeltekopf, A. L., and Sanders, R. W.: On the interpretation of zenith sky measurements, *J. Geophys. Res.*, 92, D7, 8311-8319, 1987.
- Solomon S, Qin D, Manning M, Alley RB, Berntsen T, Bindoff NL, et al. Technical summary. In: *Climate Change 2007: The Physical Science Basis*. In: Solomon S, Qin D, Manning M, Chen Z, Marquis M, Averyt K, Tignor M, Miller HL, editors. *Contribution of Working Group I to the Fourth Assessment Report of the Intergovernmental Panel on Climate Change*. Cambridge, UK, /New York, NY: Cambridge University Press; pp. 19-91, 2007.
- Stevenson, D. S., C. E. Johnson, W. J. Collins, R. G. Derwent, and J. M. Edwards: Future tropospheric ozone radiative forcing and methane turnover-The impact of climate change, *Geophys. Res. Lett.*, 27, 2073-2076, 2000.
- Stevenson, D.S., F.J. Dentener, M.G. Schultz, K. Ellingsen, T.P.C. van Noije, O. Wild, G. Zeng, M. Amann, C.S. Atherton, N. Bell, D.J. Bergmann, I. Bey, T. Butler, J. Cofala, W.J. Collins, R.G. Derwent, R.M. Doherty, J. Drevet, H.J. Eskes, A.M. Fiore, M. Gauss, D.A. Hauglustaine, L.W. Horowitz, I.S.A. Isaksen, M.C. Krol, J.F. Lamarque, M.G. Lawrence, V. Montanaro, J.F. Müller, G. Pitari, M.J. Prather, J.A. Pyle, S. Rast, J.M. Rodriguez, M.G. Sanderson, N.H. Savage, D.T. Shindell, S.E. Strahan, K. Sudo, and S. Szopa: Multimodel ensemble simulations of present-day and near-future tropospheric ozone. *J. Geophys. Res.*, 111, D08301, doi:10.1029/2005JD006338, 2006.
- Stevenson, D. S., Young, P. J., Naik, V., Lamarque, J.-F., Shindell, D. T., Voulgarakis, a., Skeie, R. B., Dalsoren, S. B., Myhre, G., Berntsen, T. K., Folberth, G. A., Rumbold, S. T., Collins, W. J., MacKenzie, I. A., Doherty, R. M., Zeng, G., van Noije, T. P. C., Strunk, a., Bergmann, D., Cameron-Smith, P., Plummer, D. A., Strode, S. A., Horowitz, L., Lee, Y. H., Szopa, S., Sudo, K., Nagashima, T., Josse, B., Cionni, I., Righi, M., Eyring, V., Conley, a., Bowman, K. W., Wild, O. and Archibald, a.: Tropospheric ozone changes, radiative forcing and attribution to emissions in the Atmospheric Chemistry and Climate Model Intercomparison Project (ACCMIP), *Atmos. Chem. Phys.*, 13(6), 3063-3085, doi:10.5194/acp-13-3063-2013, 2013.
- Stocker, T.F., D. Qin, G.-K. Plattner, L.V. Alexander, S.K. Allen, N.L. Bindoff, F.-M. Bréon, J.A. Church, U. Cubasch, S. Emori, P. Forster, P. Friedlingstein, N. Gillett, J.M. Gregory, D.L. Hartmann, E. Jansen, B. Kirtman, R. Knutti, K. Krishna Kumar, P. Lemke, J. Marotzke, V. Masson-Delmotte, G.A. Meehl, I.I. Mokhov, S. Piao, V. Ramaswamy, D. Randall, M. Rhein, M. Rojas, C. Sabine, D. Shindell, L.D. Talley, D.G. Vaughan and S.-P. Xie: Technical Summary. In: *Climate Change 2013: The Physical Science Basis*. Contribution of Working Group I to the Fifth Assessment Report of the Intergovernmental Panel on Climate Change, Cambridge University Press, Cambridge, United Kingdom and New York, NY, USA, pp. 33–115, doi:10.1017/CBO9781107415324.005, 2013.
- Steffen W, Crutzen PJ, McNeill JR: The Anthropocene: Are humans now overwhelming the great forces of nature? *Ambio* 36,8 614-621, doi: 10.1579/0044-7447(2006)35[153:TAAES]2.0.CO<sub>2</sub>, 2007.
- Steffen, W., Broadgate, W., Deutsch, L., Gaffney, O., Ludwig, C.: The trajectory of the Anthropocene: The Great Acceleration, *The Anthropocene Review*, Vol 2, Issue 1, pp. 81 - 98, 2015.

- Swap, R. J., H. J. Annegarn, J. T. Suttles, M. D. King, S. Platnick, J. L. Privette, and R. J. Scholes: Africa burning: A thematic analysis of the Southern African Regional Science Initiative (SAFARI 2000), *J. Geophys. Res.*, 108, 8465, doi:10.1029/2003JD003747, D13, 2003.
- Tapping, K. F.: The 10.7 cm solar radio flux (F10.7), *Space Weather*, 11, 394-406, doi:10.1002/swe.20064, 2013.
- Terao, Y., Logan, J. A., Douglass, A. R., and Stolarski, R. S.: Contribution of stratospheric ozone to the interannual variability of tropospheric ozone in the northern extratropics, *J. Geophys. Res.-Atmos.*, 113, D18309, doi:10.1029/2008jd009854, 2008.
- Thompson, A. M., J. C. Witte, R. D. Hudson, H. Guo, J. R. Herman, and M. Fujiwara, Tropical tropospheric ozone and biomass burning, *Science*, 291, 2128 - 2132, 2001 Thompson, A. M., J. C. Witte, R. D. Hudson, H. Guo, J. R. Herman, and M. Fujiwara, Tropical tropospheric ozone and biomass burning, *Science*, 291, 2128- 2132, 2001
- Thompson, A.M., et al.: Southern Hemisphere Additional Ozonesondes (SHADOZ) 1998-2000 tropical ozone climatology 1. Comparison with Total Ozone Mapping Spectrometer (TOMS) and ground-based measurements, *J. Geophys. Res.*, 108, 8238, doi:10.1029/2001JD000967, 2003.
- Thompson, A. M., Balashov, N. V., Witte, J. C., Coetzee, J. G. R., Thouret, V., and Posny, F.: Tropospheric ozone increases over the southern Africa region: bellwether for rapid growth in Southern Hemisphere pollution, *Atmos. Chem. Phys.*, 14, 9855-9869, doi:10.5194/acp-14-9855-2014, 2014.
- Tilmes, S., Lamarque, J.-F., Emmons, L. K., Conley, A., Schultz, M. G., Saunio, M., Thouret, V., Thompson, A. M., Oltmans, S. J., Johnson, B., and Tarasick, D.: Technical Note: Ozonesonde climatology between 1995 and 2011: description, evaluation and applications, *Atmos. Chem. Phys.*, 12, 7475-7497, doi:10.5194/acp-12-7475-2012, 2012.
- Trenberth, K.E., Fasullo, J., and Smith, L.: Trends and variability in column-integrated atmospheric water vapor, *Climate Dynamics*, 24: 741. doi:10.1007/s00382-005-0017-4, 2005.
- Trenberth K. E.: Changes in precipitation with climate change. *Clim Res* 47:123-138. <https://doi.org/10.3354/cr00953>, 2011.
- United Nations, Department of Economic and Social Affairs, Population Division: World Population Prospects: The 2015 Revision, Key Findings and Advance Tables. ESA/P/WP.241., 2015. <https://esa.un.org/unpd/wpp/DataQuery/> (last access: 25 October 2016)
- UNEP Regional seas reports and studies No 83: Physical ocean environment in the South Pacific Commission Area, United Nations Environment Programme, 1986.
- UNEP, Environmental Effects of Ozone Depletion: 1998 Assessment, United Nations Environment Programme, 205pp, ISBN 92-807-1724-3, 1998.

- UNEP: Draft Guidelines on Best Available Techniques and Provisional Guidance on Best Environmental Practices, 2004c. Available at: [http://chm.pops.int/Portals/0/docs/from\\_old\\_website/documents/meetings/bat\\_bep/3rd\\_session/EGB\\_3\\_2/EGB3\\_2\\_TheGuide.pdf](http://chm.pops.int/Portals/0/docs/from_old_website/documents/meetings/bat_bep/3rd_session/EGB_3_2/EGB3_2_TheGuide.pdf) (last access: 09 February 2017)
- UNEP, Integrated Assessment of Black Carbon and Tropospheric Ozone, UNEP and WMO, Available at: [http://www.unep.org/dewa/Portals/67/pdf/BlackCarbon\\_report.pdf](http://www.unep.org/dewa/Portals/67/pdf/BlackCarbon_report.pdf), latest access: 20.02.2017, 2011.
- U.S. Department of Agriculture, Natural Resources Conservation Service: Air Quality Impacts-Ozone Precursors, <https://www.nrcs.usda.gov/wps/portal/nrcs/main/national/air/quality/>, (latest access: 21/02/2017), 2012
- U.S. Government Printing Office: U.S. Standard Atmosphere, 1976, U.S. Government Printing Office, Washington, D.C., 1976.
- U.S. Environmental Protection Agency: Terms of Environment: Glossary, Abbreviations, and Acronyms, [http://iaspub.epa.gov/sor\\_internet/registry/termreg/searchandretrieve/glossariesandkeywordlists/search.do?details=](http://iaspub.epa.gov/sor_internet/registry/termreg/searchandretrieve/glossariesandkeywordlists/search.do?details=), latest access: 17/2/2017, 2009.
- U.S. National Research Council, Committee on Tropospheric Ozone Formation and Measurement, Rethinking The Ozone Problem In Urban And Regional Air Pollution, National Academy Press, Washington DC, 1992.
- Uysal, N., and Schapira, R. M.: Effects of ozone on lung function and lung diseases. *Curr. Opin. Pulm. Med.* 9, 144-150. doi: 10.1097/00063198-200303000-00009, 2003.
- Valks, P.J. M., R. B. A. Koelemeijer, M. van Weele, P. van Velthoven, J. P.F. Fortuin, and H. Kelder, Variability in tropical tropospheric ozone: Analysis with Global Ozone Monitoring Experiment observations and a global model, *J. Geophys. Res.*, 108(D11), 4328, doi:10.1029/2002JD002894, 2003.
- Valks, P, Loyola, D., Hao, N., Rix, M., and Slijkhuis, S.: Algorithm Theoretical Basis Document for GOME-2 Total Column Products of Ozone, Minor Trace Gases and Cloud Properties(GDP 4.5 for O3M-SAF OTO and NTO), DLR/GOME-2/ATBD/01, Iss./Rev.: 2/E, available at: [http://atmos.eoc.dlr.de/gome2/docs/DLR\\_GOME-2\\_ATBD.pdf](http://atmos.eoc.dlr.de/gome2/docs/DLR_GOME-2_ATBD.pdf), 2011.
- Valks, P, Hao, N., Gimeno Garcia, S., Loyola, D., Dameris, M., Jöckel, P and Delcloo, A.: Tropical tropospheric ozone column retrieval for GOME-2, *Atmos. Meas. Tech. Discuss.*, 7(1), 727-768, doi:10.5194/amtd-7-727-2014, 2014.
- Van Dingenen R, Dentener FJ, Raes F, Krol MC, Emberson L, Cofala J. The global impact of ozone on agricultural crop yields under current and future air quality legislation, *Atmos Environ.*, 43(3):604-18, 2009.
- Vance E.: Mexico passes climate-change law, *Nature News*, Nature Publishing Group, doi:10.1038/nature.2012.10496, 2012

- Vecchi Gabriel A., Wittenberg Andrew T.: El Niño and our future climate: where do we stand? *WIREs Clim Change* 2010, 1: 260-270. doi: 10.1002/wcc.33, 2010
- Veihelmann B., Meijer Y., Langen J., Koopman I., Wright N., Bazalgette Courreges-Lacoste G., Bagnasco G.: The Sentinel-4 Mission and its Atmospheric Composition Products, available at: <http://seom.esa.int/atmos2015/files/presentation69.pdf> (latestaccess:26.01.2017), ATMOS Conference 2015, Heraklion, Crete, Greece, 2015.
- Verstraeten W. W. , Neu L. J., Williams E.J., Bowman W. K., Worden R.J. and, Boersma F.K.:Rapid increases in tropospheric ozone production and export from China, *Nature Geoscience* 8, 690-695, doi:10.1038/ngeo2493, 2016.
- Voulgarakis, A., Savage, N. H., Wild, O., Braesicke, P, Young, P. J., Carver, G. D., and Pyle, J. A.: Interannual variability of tropospheric composition: the influence of changes in emissions, meteorology and clouds, *Atmos. Chem. Phys.*, 10, 2491-2506, doi:10.5194/acp-10-2491-2010, 2010.
- Vrekoussis, M., Wittrock, F., Richter, A., and Burrows, J. P: GOME-2 observations of oxygenated VOCs: what can we learn from the ratio glyoxal to formaldehyde on a global scale?, *Atmos. Chem. Phys.*, 10, 10145-10160, doi:10.5194/acp-10-10145-2010, 2010.
- Vrekoussis, M., A. Richter, A. Hilboll, J. P Burrows, E. Gerasopoulos, J. Lelieveld, L. Barrie, C. Zerefos, and N. Mihalopoulos: Economic crisis detected from space: Air quality observations over Athens/Greece, *Geophys. Res. Lett.*, 40, 458-463, doi:10.1002/grl.50118, 2013.
- Wai, K. M., Wu, S., Kumar, A., and Liao, H.: Seasonal variability and long-term evolution of tropospheric composition in the tropics and Southern Hemisphere, *Atmos. Chem. Phys.*, 14, 4859-4874, doi:10.5194/acp-14-4859-2014, 2014.
- Wallace J.M. and P.V. Hobbs: *Atmospheric science: an introductory survey* (2nd edition). International Geophysics Series 92, Associated press, 484pp, 2006.
- Wayne R.P: *Chemistry of Atmospheres*, second edition Oxford University Press, 1991.
- Weatherhead E. C., Reinsel, Gregory C. and Tiao, George C. and Meng, Xiao-Li and Choi, Dongseok and Cheang, Wai-Kwong and Keller, Teddie and DeLuisi, John and Wuebbles, Donald J. and Kerr, James B. and Miller, Alvin J. and Oltmans, Samuel J. and Frederick, John E.: Factors affecting the detection of trends: Statistical considerations and applications to environmental data, *J. Geophys. Res.*, 103(D14), 17149-17161, doi:10.1029/98JD00995, 1998.
- Weber, M., Lamsal, L. N., Coldewey-Egbers, M., Bramstedt, K. and Burrows, J. P: Pole-to-pole validation of GOME WFDOS total ozone with groundbased data, *Atmos. Chem. Phys. Discuss.*, 4(5), 6909-6941, doi:10.5194/acpd-4-6909-2004, 2004.
- Weber, M., W. Chehade, V. E. Fioletov, S. M. Frith, C. S. Long, W. Steinbrecht, J. D. Wild, [Global Climate] Stratospheric ozone [in "State of the Climate in 2012"], *Bull. Amer. Meteor. Soc.*, 94, S36-S37, 2013

- Weber, M., Gorshelev, V., and Serdyuchenko, A.: Uncertainty budgets of major ozone absorption cross sections used in UV remote sensing applications, *Atmos. Meas. Tech.*, 9, 4459-4470, <https://doi.org/10.5194/amt-9-4459-2016>, 2016.
- Wellemeyer, C. G., Taylor, S. L., Seftor, C. J., McPeters, R. D., and Bhartia, P. K.: A correction for the Total Ozone Mapping Spectrometer profile shape errors at high latitude, *J. Geophys. Res.*, 102, 9029-9038, 1997.
- Wesely, M. L. and Hicks, B. B.: A review of the current status of knowledge in dry deposition, *Atmos. Environ.*, 34, 2261-2282, 2000.
- WHO.: Health risks of particulate matter from long-range transboundary air pollution. [online] Available from:[http://www.euro.who.int/data/assets/pdf\\_file/0006/78657/E88189.pdf](http://www.euro.who.int/data/assets/pdf_file/0006/78657/E88189.pdf), (latest access:01/03/2017) 2006.
- WHO: Reducing Global Health Risks Through mitigation of short-lived climate pollutants, Scoping report for policymakers [online] Available from:[http://apps.who.int/iris/bitstream/10665/189524/1/9789241565080\\_eng.pdf](http://apps.who.int/iris/bitstream/10665/189524/1/9789241565080_eng.pdf) (latest access:01/03/2017), 2015.
- Wild, O., Fiore, A. M., Shindell, D. T., Doherty, R. M., Collins, W. J., Dentener, F. J., Schultz, M. G., Gong, S., MacKenzie, I. A., Zeng, G., Hess, P., Duncan, B. N., Bergmann, D. J., Szopa, S., Jonson, J. E., Keating, T. J., and Zuber, A.: Modelling future changes in surface ozone: a parameterized approach, *Atmos. Chem. Phys.*, 12, 2037-2054, doi:10.5194/acp-12-2037-2012, 2012.
- Wilks Daniel S.: Resampling hypothesis tests for autocorrelated fields. *J. Clim.* 10: 65-82, 1997.
- Wilks, Daniel S. *Statistical Methods in the Atmospheric Sciences*. 3rd ed. Oxford ; Waltham, MA: Academic Press, 2011.
- Winterrath, T. and Kurosu, T. and Richter, A. and Burrows, J.P: Enhanced O<sub>3</sub> and NO<sub>2</sub> in thunderstorm clouds: Convection or production? *Geophysical Research Letter*, 26 (9). pp. 1291-1295, 1999.
- WMO: Meteorology—A three-dimensional science, *WMO Bull.*, 6, 134-138, 1957.
- WMO : *Atmospheric Ozone 1985 Assessment of our Understanding of the Processes Controlling its Present Distribution and Change* (3 volumes), 1985.
- WMO: Report of the Third Meeting of the Ozone Research Managers of Parties to the Vienna Convention for the Protection of the Ozone Layer, Geneva, 19-21 March 1996
- WMO: Report of the Fourth Meeting of the Ozone Research Managers of the Parties to the Vienna Convention for the Protection of the Ozone Layer, Geneva, 28-30 April 1999
- WMO: World Meteorological Organization, *Scientific Assessment of Ozone Depletion: 2006*, WMO Global Ozone Research and Monitoring Project- Report No. 50, 2007.

- WMO: World Meteorological Organization: Global Ozone Research and Monitoring Project. Scientific Assessment of Ozone Depletion: 2010, Report No. 52, World Meteorological Organization, Geneva, Switzerland, 2-4 May 2011.
- WMO: World Meteorological Organization/International Global Atmospheric Chemistry: WMO/IGAC Impacts of Megacities on air pollution and climate, GAW Report No. 205, Ch. 7, pp. 250-275, 2012.
- WMO: World Meteorological Organization, Assessment for Decision-Makers: Scientific Assessment of Ozone Depletion: 2014, 88 pp., Global Ozone Research and Monitoring Project, Report No. 56, Geneva, Switzerland, 2014.
- Wolter, K., and M.S. Timlin: Monitoring ENSO in COADS with a seasonally adjusted principal component index. Proc. of the 17th Climate Diagnostics Workshop, Norman, OK, NOAA/NMC/CAC, NSSL, Oklahoma Clim. Survey, CIMMS and the School of Meteor., Univ. of Oklahoma, 52-57, 1993.
- Wolter, K., and Timlin, M. S.: Measuring the Strength of ENSO Events: How Does 1997/98 Rank?, *Weather* 53.9, 315-24, 1998
- Wolter, K. and Timlin, M. S.: El Nino/Southern Oscillation behaviour since 1871 as diagnosed in an extended multivariate ENSO index (MEI.ext), *Int. J. Climatol.*, 31: 1074-1087. doi:10.1002/joc.2336, 2011
- Xie, F., Li, J., Tian, W., Zhang, J., and Shu, J.: The Impacts of Two Types of El Niño on Global Ozone Variations in the Last Three Decades, *Adv. Atmos. Sci.* (2014) 31: 1113. doi:10.1007/s00376-013-3166-0
- Xu, X., and W. Lin: Trends of tropospheric ozone over China based on satellite data (1979-2005). *Adv. Clim. Change Res.*, 2(1), doi: 10.3724/SPJ.1248.2011.00043, 2011.
- Yonemura, S., H. Tsuruta, S. Kawashima, S. Sudo, L. C. Peng, L. S. Fook, Z. Johar, and M. Hayashi, Tropospheric ozone climatology over Peninsular Malaysia from 1992 to 1999, *J. Geophys. Res.*, 107(D15), doi:10.1029/2001JD000993, 2002.
- Young, P. J., A.T. Archibald, K.W. Bowman, J.-F. Lamarque, V. Naik, D.S. Stevenson, S. Tilmes, A. Voulgarakis, O. Wild, D. Bergmann, P. Cameron-Smith, I. Cionni, W.J. Collins, S.B. Dalsøren, R.M. Doherty, V. Eyring, G. Faluvegi, L.W. Horowitz, B. Josse, Y.H. Lee, I.A. MacKenzie, T. Nagashima, D.A. Plummer, M. Righi, S.T. Rumbold, R.B. Skeie, D.T. Shindell, S.A. Strode, K. Sudo, S. Szopa, and G. Zeng: Pre-industrial to end 21st century projections of tropospheric ozone from the Atmospheric Chemistry and Climate Model Intercomparison Project (ACCMIP). *Atmos. Chem. Phys.*, 13, 2063-2090, 2013.
- Zanis, P., Trickl, T., Stohl, A., Wernli, H., Cooper, O., Zerefos, C., Gaeggeler, H., Schnabel, C., Tobler, L., Kubik, P. W., Priller, A., Scheel, H. E., Kanter, H. J., Cristofanelli, P., Forster, C., James, P., Gerasopoulos, E., Delcloo, A., Papayannis, A., and Claude, H.: Forecast, observation and modelling of a deep stratospheric intrusion event over Europe, *Atmos. Chem. Phys.*, 3, 763-777, doi:10.5194/acp-3-763-2003, 2003

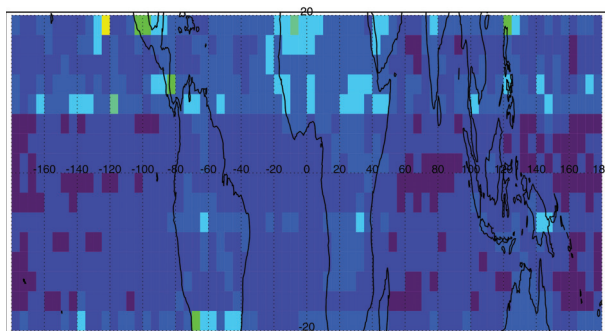
- Zhang, L., Brook, J. R., and Vet, R.: A revised parameterization for gaseous dry deposition in air-quality models, *Atmos. Chem. Phys.*, 3, 2067-2082, doi:10.5194/acp-3-2067-2003, 2003.
- Ziemke, J. R. and Stanford, J. L.: Kelvin waves in total column ozone, *Geophys. Res. Lett.*, 21(2), 105-108, doi:10.1029/93GL03287, 1994.
- Ziemke, J. R., Chandra, S. and Bhartia, P. K.: Two new methods for deriving tropospheric column ozone from TOMS measurements: Assimilated UARS MLS/HALOE and convective-cloud differential techniques, *J. Geophys. Res.*, 103(D17), 22115, doi:10.1029/98JD01567, 1998.
- Ziemke, J. R., and S. Chandra: Seasonal and interannual variabilities in tropical tropospheric ozone, *J. Geophys. Res.*, 104, 21,425, 21,442, 1999.
- Ziemke, J. R., S. Chandra, and P. K. Bhartia: "Cloud slicing": A new technique to derive upper tropospheric ozone from satellite measurements, *J. Geophys. Res.*, 106(D9), 9853-9867, doi:10.1029/2000JD900768, 2001.
- Ziemke, J. R., and S. Chandra: La Nina and El Nino-induced variabilities of ozone in the tropical lower atmosphere during 1970-2001, *Geophys. Res. Lett.*, 30, 1142, doi:10.1029/2002GL016387, 3, 2003.
- Ziemke, J. R., S. Chandra, and P. K. Bhartia: A 25-year data record of atmospheric ozone in the Pacific from TotalOzone Mapping Spectrometer (TOMS) cloud slicing: Implications for ozone trends in the stratosphere and troposphere, *J. Geophys. Res.*, 110, D15105, doi:10.1029/2004JD00568, 2005.
- Ziemke, J. R., S. Chandra, B. N. Duncan, L. Froidevaux, P. K. Bhartia, P. F. Levelt, and J. W. Waters: Tropospheric ozone determined from Aura OMI and MLS: Evaluation of measurements and comparison with the Global Modeling Initiative's Chemical Transport Model, *J. Geophys. Res.*, 111, D19303, doi:10.1029/2006JD007089, 2006.
- Ziemke, J. R., Joiner, J., Chandra, S., Bhartia, P. K., Vasilkov, A., Haffner, D. P., Yang, K., Schoeberl, M. R., Froidevaux, L. and Levelt, P. F.: Ozone mixing ratios inside tropical deep convective clouds from OMI satellite measurements, *Atmos. Chem. Phys. Discuss.*, 8(4), 16381-16407, doi:10.5194/acpd-8-16381-2008, 2008.
- Ziemke, J. R., Chandra, S., Duncan, B. N., Schoeberl, M. R., Torres, O., Damon, M. R., and Bhartia, P. K.: Recent biomass burnings in the tropics and related changes in tropospheric ozone, *Geophys. Res. Lett.*, 36, L15819, doi:10.1029/2009GL039303, 2009b.
- Ziemke, J. R., Chandra, S., Oman, L. D., and Bhartia, P. K.: A new ENSO index derived from satellite measurements of column ozone, *Atmos. Chem. Phys.*, 10, 3711-3721, doi:10.5194/acp-10-3711-2010, 2010.
- Ziemke, J. R., Chandra, S., Labow, G. J., Bhartia, P. K., Froidevaux, L., and Witte, J. C.: A global climatology of tropospheric and stratospheric ozone derived from Aura OMI and MLS measurements, *Atmos. Chem. Phys.*, 11, 9237-9251, doi:10.5194/acp-11-9237-2011, 2011.

Ziemke, J. R. and Chandra, S.: Development of a climate record of tropospheric and stratospheric column ozone from satellite remote sensing: evidence of an early recovery of global stratospheric ozone, *Atmos. Chem. Phys.*, 12, 5737-5753, doi:10.5194/acp-12-5737-2012, 2012.

Ziemke, J. R., Douglass, A. R., Oman, L. D., Strahan, S. E., and Duncan, B. N.: Tropospheric ozone variability in the tropics from ENSO to MJO and shorter timescales, *Atmos. Chem. Phys.*, 15, 8037-8049, doi:10.5194/acp-15-8037-2015, 2015.



SCIA VS GOME mean correction factor



SCIA VS GOME-2 mean correction factor

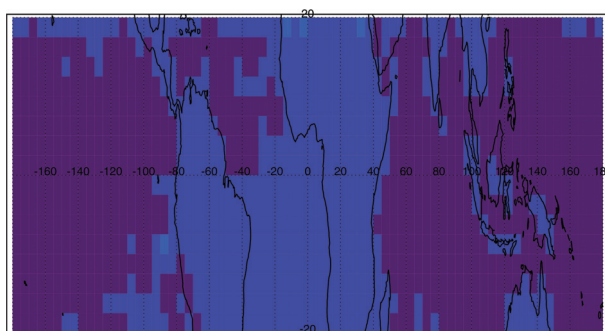


Figure 1: Correction factors using SCIAMACHY TCO as reference (top) Correction factors for GOME: average ratio of SCIAMACHY to GOME TCO for the years Jan 2002 – Jun 2003 (bottom) correction factors for GOME-2: average ratio of SCIAMACHY to GOME-2 TCO (in DU) for 2007–2012.

Number of TCO data for SCIAMACHY and GOME-2 (2007-2012)

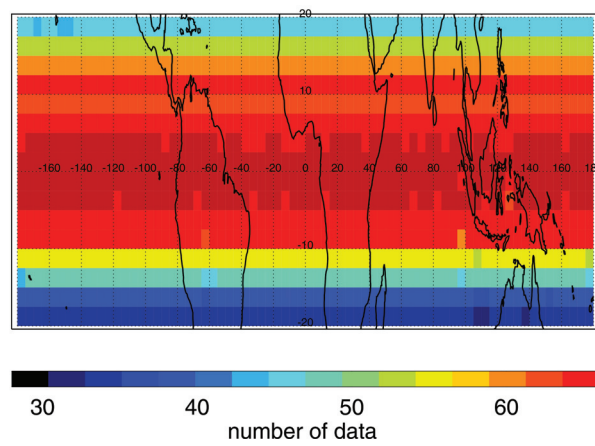


Figure 2: Number of TCO data for SCIAMACHY and GOME-2 for 2007 – 2012.

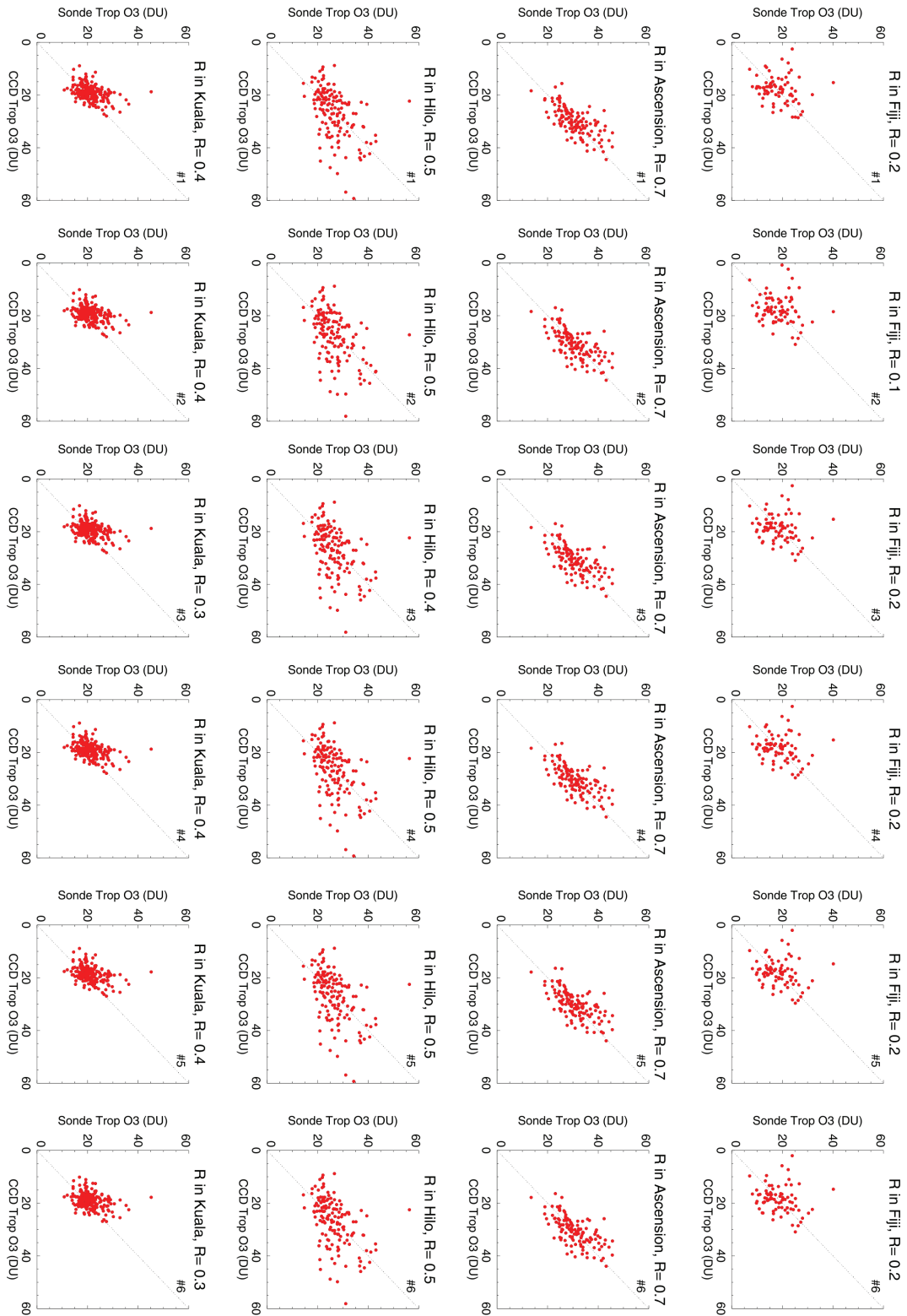


Figure 3: Correlation R between the TCO from the six harmonised scenarios and ozone columns until 200 hPa from ozonesonde data in Fiji, Ascension, Hilo, and Kuala Lumpur.

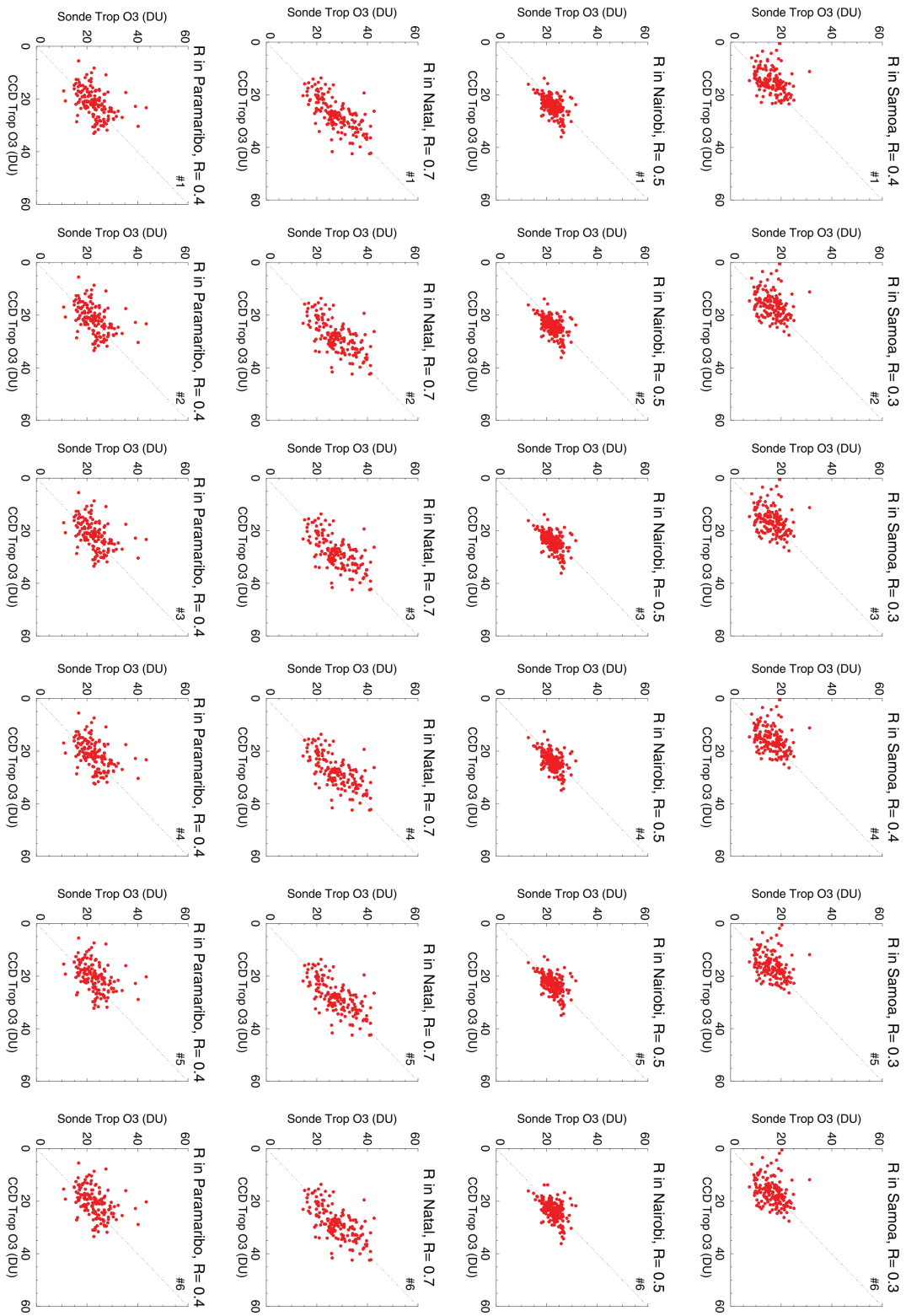


Figure 4: The same as Fig. 3 for American Samoa, Nairobi, Natal, and Paramaribo.

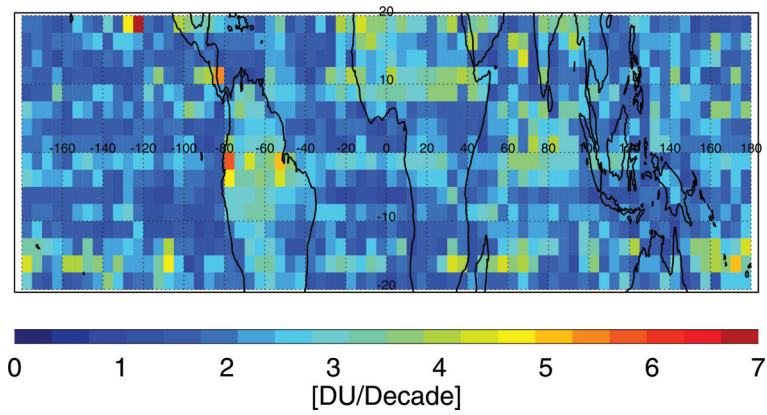


Figure 5: Maximum trend difference among all six harmonisation scenarios.

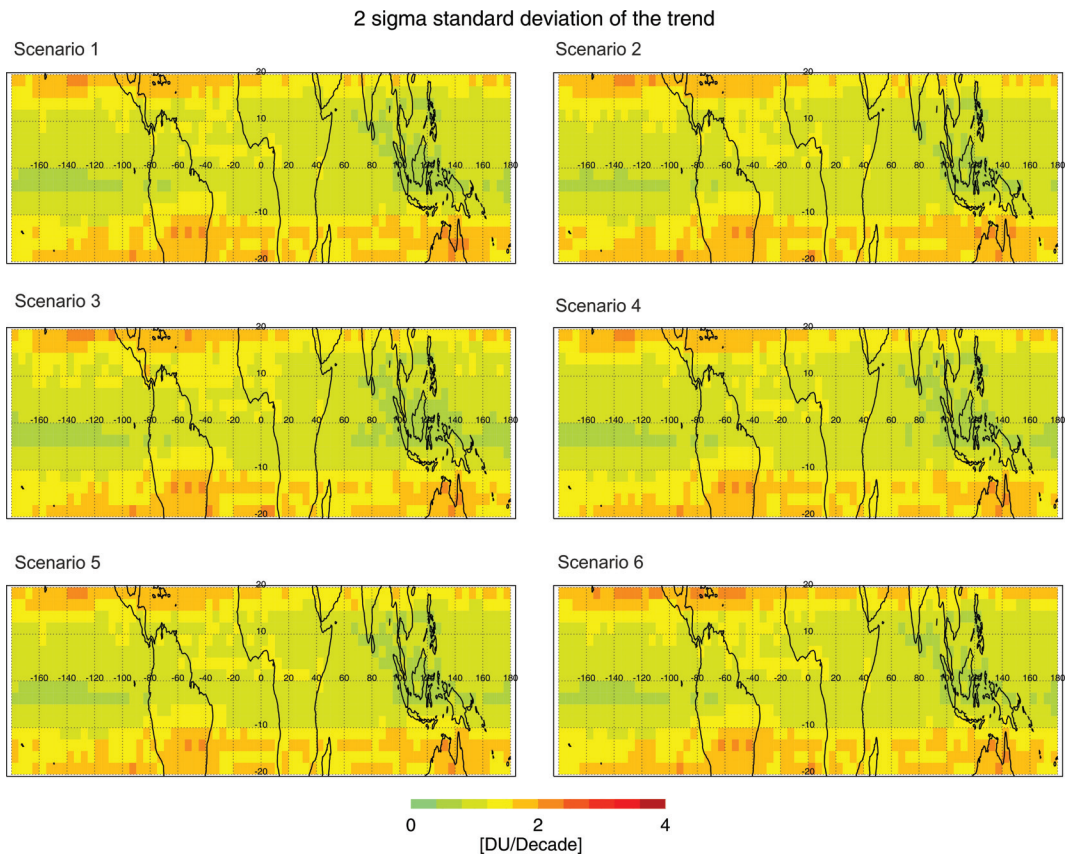


Figure 6: The  $2\sigma$  uncertainty of the trend using six harmonisation scenarios.

Correlation (R) between the trend model and the timeseries

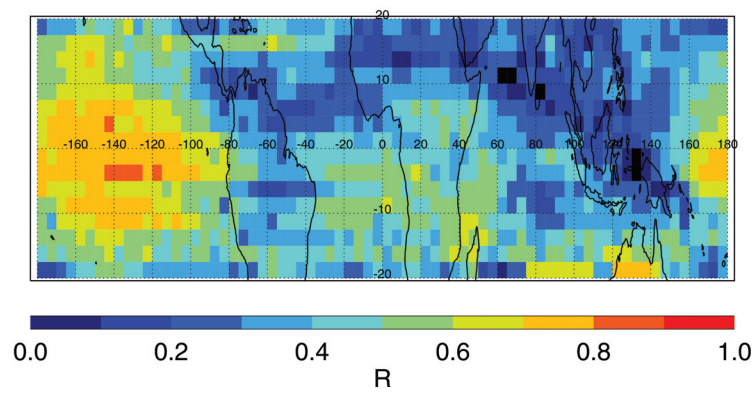


Figure 7: Correlation coefficient,  $R$ , between the multi-linear trend model fit and the original time-series excluding the seasonal cycle.

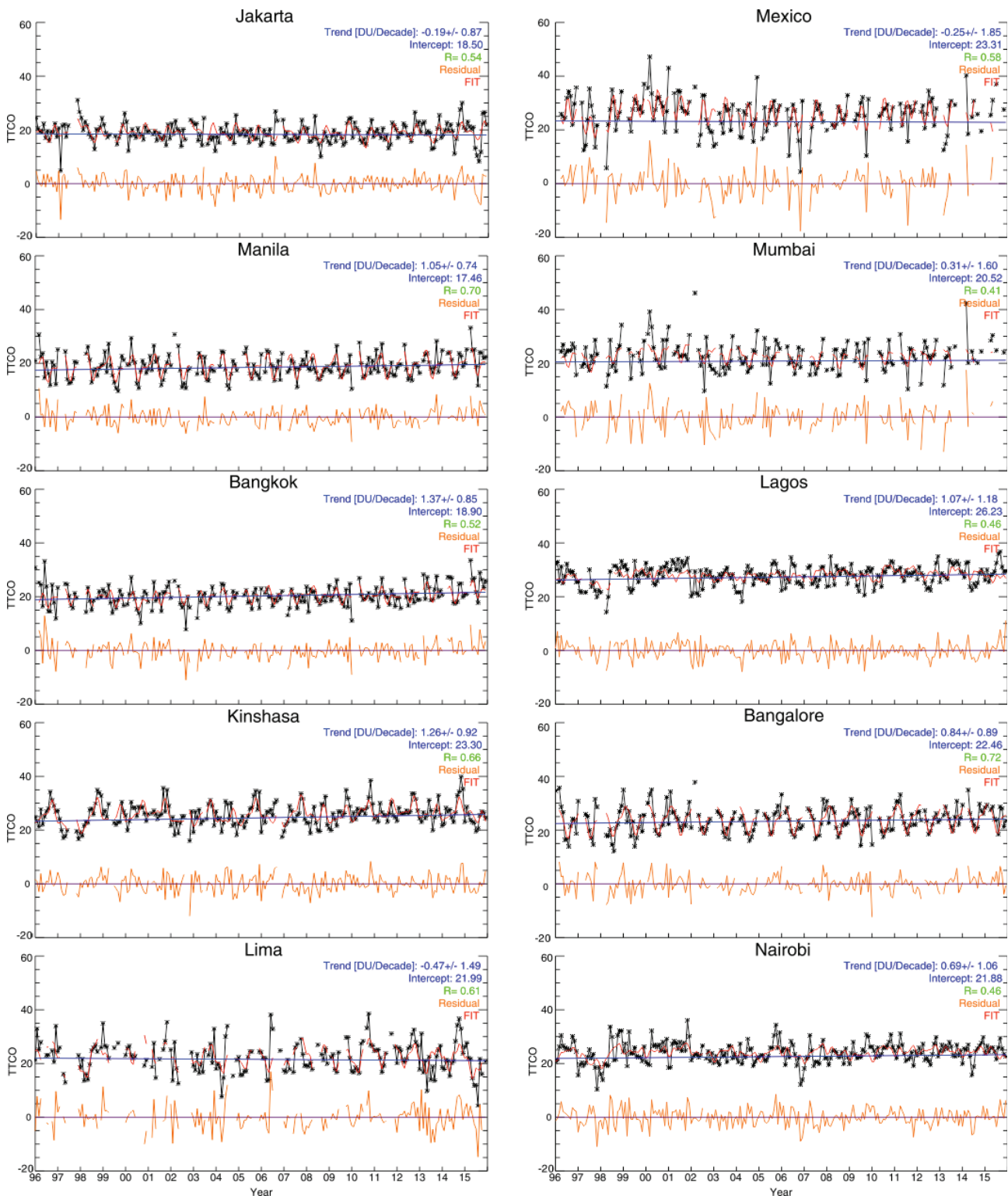


Figure 8: Tropical tropospheric ozone time-series in DU (blue stars) and trend (black line) in Jakarta, Mexico, Manila, Mumbai, Bangkok, Lagos, Kinshasa, Bangalore, Lima, and Nairobi (in descending population size; size taken from United Nations [2015])). The regression fit is plotted with red lines while the residuals are plotted with yellow lines. The  $2\sigma$  uncertainties are reported beside the trends.

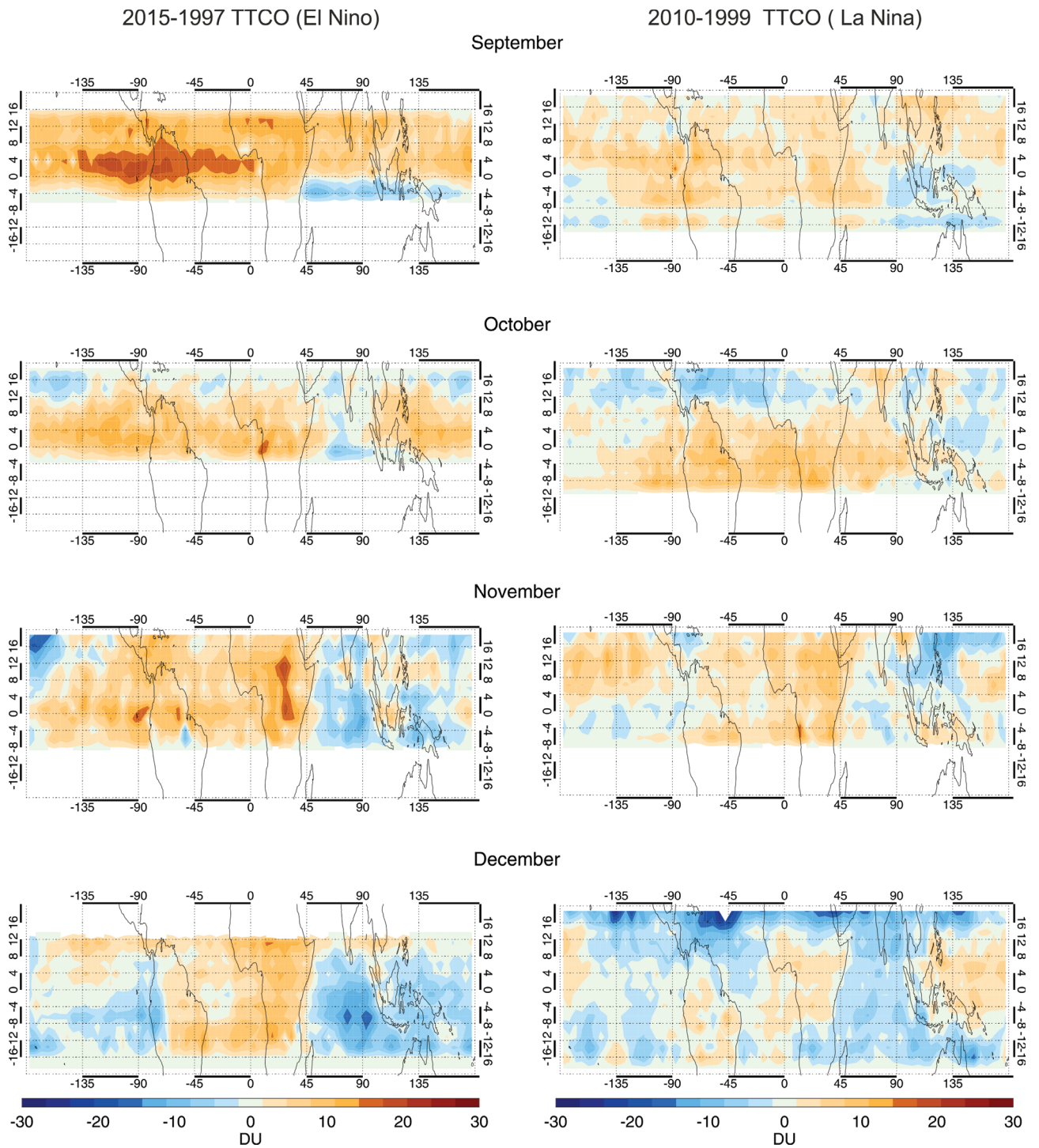


Figure 9: Difference of tropical tropospheric ozone for September- December 2015–1997 (El Niño) and 2010–1999 (La Niña).

## List of Figures

1	Socio-economic and Earth System trends from 1750 to 2010 [Steffen et al., 2015]. . . .	xviii
2	Global tropospheric ozone burden and its changes between 1850 and 2100 simulated by different models. Two scenarios of future emissions have been used as defined by the Intergovernmental Panel on Climate Change, IPCC. RCP 2.6, assumes that ozone precursors peak between 2010-2020 and decline thereafter (green) and RCP 8.5 assumes high precursor emissions (mainly methane) and a strong warming throughout the 21st century (red). Thin lines are for individual model results and thick lines are multi-model averages. (Source: Madronich et al. [2015], figure based on data from Young et al. [2013]). . . . .	xix
1.1	Temperature and ozone profile in the atmosphere. Temperature data taken from the U.S. Standard Atmosphere 1976, see U.S. Government Printing Office [1976]. The volume mixing ratio with red solid line and the partial pressure of ozone ( <i>mixing ratio</i> × <i>atmospheric pressure</i> ) with solid green line are taken from SHADOZ ozonesonde network, for October 2008 in Natal [Thompson et al., 2003]. The dashed lines represent the ideal ozone profile after the ozonesonde burst altitude. . . . .	4
1.2	Lewis structure of Ozone molecule. . . . .	5
1.3	Zonal mean climatology (1996-2015) of total ozone columns in DU from GOME/SCIAMACHY/GOME-2 merged WFDOAS total ozone measurements (Global mean 290 DU). Red dashed lines indicate the tropics (20 °N–20 °S). Data found in: <a href="http://www.iup.uni-bremen.de/UVSAT_material/data/to3/GSG_merged_zonalmean.dat">http://www.iup.uni-bremen.de/UVSAT_material/data/to3/GSG_merged_zonalmean.dat</a> (Courtesy: M. Weber). . . .	6
1.4	Zonal mean tropospheric ozone climatology (in Dobson Units) from OMI/MLS for the period October 2004 until December 2010. Red dashed lines indicate the tropics (20 °N–20 °S). Data found in: <a href="https://acd-ext.gsfc.nasa.gov/Data_services/cloud_slice/">https://acd-ext.gsfc.nasa.gov/Data_services/cloud_slice/</a> [Ziemke et al., 2011]. . . . .	10

- 1.5 a) Two typical dimensional peak ozone isopleths from the EKMA (Empirical Kinetic Modeling Approach) model [Dimitriadis and Dodge, 1983], versus the initial VOCs and  $\text{NO}_x$  mixing ratios. b) Two-dimensional plot of the VOC-  $\text{NO}_x$  limited regions. The VOC-limited region (Point D) is located in a highly polluted urban area while the  $\text{NO}_x$  limited region (point A) is typical for a rural area, downwind of a suburban or urban areas (Figure adapted from: Finlayson-Pitts and Pitts [2000]). . . . . 15
- 1.6 North hemisphere longitudinal section showing the Hadley, Ferrel, Polar cells, the sub-tropical and polar jet streams, and the tropopause elevations (Figure taken from NOAA/NWS: <http://www.srh.noaa.gov/jetstream/global/jet.html>). . . . . 17
- 1.7 Standard Walker Circulation for December-February during neutral (Top), El Niño (middle), and La Niña (bottom) conditions. (Figure taken from NOAA: <https://www.climate.gov/news-features/blogs/enso/walker-circulation-ensos-atmospheric-buddy>, drawing by Fiona Martin.) . . . . . 18
- 1.8 Pathway of resistances (R) to dry deposition of ozone. . . . . 20
- 1.9 Radiative forcing, (RF), (hatched) and effective radiative forcing, (ERF), (solid) of several forcing agents and their confidence level for the period 1750–2011. (Figure taken from: Stocker et al. [2013], as part of the Physical Science Basis, contributing in the Working Group I (WGI) to the Fifth Assessment Report (AR5) of IPCC [2013]). . . . . 21
- 1.10 Current premature mortality due to ozone pollution (2000–1850). The results from a 14 models are presented in deaths/year per 1000  $\text{km}^2$  (Figure taken from: Silva et al. [2013].) . . . . . 23
- 1.11 Sketch of the electromagnetic spectrum at different wavelength (m) ranges from  $\gamma$ -rays to radio waves. (Figure taken from: <http://www.livescience.com/38169-electromagnetism.html>) . . . . . 24
- 1.12 Franck-Condon principle diagram for a diatomic molecule. The curves represent the electronic energy levels ( $E_0$  is the ground, and  $E_1$  is the excited electronic state) as function of the distance between the nuclei of the atoms within the molecule. The lines marked with  $\nu$  describe the vibrational states, and the green lines above the  $\nu'' = 0$  vibrational levels represent the rotational states. . . . . 26
- 1.13 The annual global mean energy balance of the Earth. (Figure taken from: IPCC [2007].) 28
- 1.14 Spectral distribution of solar radiation (yellow shaded area) at the top of the atmosphere (TOA), solar irradiance at the surface of the Earth (red shaded area), and solar irradiance at 10 m below the ocean surface (blue shaded area). The black body curve at 5250 °C is plotted with black line. Absorption bands for  $\text{O}_3$ ,  $\text{O}_2$ ,  $\text{H}_2\text{O}$ , and  $\text{CO}_2$  are indicated in the plot. (Figure taken from: <http://book.bionumbers.org/how-much-energy-is-carried-by-photons-used-in-photosynthesis/>.) . . . . . 29
- 1.15 The radiative transfer in the atmosphere. . . . . 30
- 1.16 Vertical optical thicknesses of  $\text{O}_2$ ,  $\text{O}_3$ ,  $\text{SO}_2$ ,  $\text{NO}_2$ ,  $\text{H}_2\text{O}$ ,  $\text{O}_4$ , ClO, OClO, HClO, BrO, and HCHO in UV-Visible spectral ranges. (Figure taken from: Rozanov et al. [2014]) . . . . . 32

1.17	(a) Absorption cross section (in $\text{cm}^2$ ; logarithmic scale) of ozone as function of the excitation energy. (b) One-dimensional cuts through the potential energy surfaces (PESs) relevant for the photodissociation of ozone. $R_1$ is one of the O–O bond lengths; the other one is fixed at $R_2 = 2.43 a_0$ and the bond angle is $\alpha = 117^\circ$ . $E = 0$ corresponds to $\text{O}_3(\bar{X})$ in the ground vibrational state (zero point energy). A, B, and R indicate the three states relevant for the Hartley and Huggins bands. The horizontal arrows illustrate the electronic assignments of the absorption bands. Color coding in (a) and (b) stresses the relation between the absorption bands and the underlying electronic states. Figure taken from: Grebenshchikov et al. [2007]. . . . .	33
1.18	a) Absorption cross sections of ozone from 240 to 280 nm measured with the GOME-2 FM3 spectrometer at 5 temperatures ranging between 203 K to 293 K. b) Temperature dependent ozone absorption cross section spectra covering the Hartley, Huggins and the Chappuis bands (230–790 nm). Figures taken from: . . . . .	34
1.19	The main steps of the DOAS retrieval (Figure taken from: Gottwald et al. [2006]). . . . .	36
2.1	The convective cloud differential method. . . . .	46
2.2	a) Above-cloud column ozone (ACCO for the latitude bands $5^\circ\text{N} - 7.5^\circ\text{N}$ and $15^\circ\text{S} - 12.5^\circ\text{S}$ ( $cf > 0.8$ and $cth > 9$ km) from SCIAMACHY (using OCRA/SACURA for cloud detection). b) Above-cloud column ozone (ACCO for the latitude bands $5^\circ\text{N} - 7.5^\circ\text{N}$ and $15^\circ\text{S} - 12.5^\circ\text{S}$ ( $cf > 0.8$ and $cth > 9$ km) from GOME-2 (using FRESCO for cloud detection) in August 2008. The $1\sigma$ standard deviation is less than 5 DU. . . . .	47
2.3	a) The number of counts per gridbox with $cf$ greater than 0.8 and $cth$ greater than 9 km (SCIAMACHY) and $cth$ greater than 7 km (GOME-2) for January and August 2008. b) Frequency of cloud top heights ( $cth$ ) for August 2008 from SCIAMACHY (SACURA) and GOME-2 (FRESCO) in the Western Pacific area ( $20^\circ\text{S} - 20^\circ\text{N}$ , $70^\circ\text{E} - 170^\circ\text{W}$ ). Pink shaded data are used for the ACCO calculation . . . . .	48
2.4	a) SCIAMACHY (left) and GOME-2 (right) ACCO per $2.5^\circ$ latitude bands in the Indian and western Pacific Ocean ( $70^\circ\text{E} - 170^\circ\text{W}$ ) for different cloud fractions (0.8, 0.9) and cloud top heights (7-9 km) in August 2008. b) Above cloud column of ozone (ACCO) for $2.5^\circ$ latitude bands in the Indian and western Pacific Ocean from GOME-2 ( $cf < 0.8$ and $cth < 7\text{km}$ ) and SCIAMACHY ( $cf < 0.8$ and $cth < 9\text{km}$ ) in August 2008. Blue and yellow dashed lines are the zonal ACCO values before applying any corrections for GOME-2 and SCIAMACHY, respectively. Red and green lines are the zonal ACCO values after corrections applied for adjusting to the 200 hPa level and screening out outlier data. Error bars denote $1\sigma$ standard deviation. Black boxes show the stratospheric ozone columns from ozonesondes, of the stations Ascension, Natal, Nairobi, Kuala Lumpur, Paramaribo, and Hilo. . . . .	49
3.1	Tropical tropospheric ozone column (TTCO) derived with the convective cloud differential (CCD) technique for January, April, July, and October 2002 and January and April 2003 using GOME data. . . . .	54

- 3.2 Tropical tropospheric ozone column (TTCO) derived with the convective cloud differential (CCD) technique for January and April 2003 and January, April, July, and October 2008 using SCIAMACHY data. . . . . 55
- 3.3 Tropical tropospheric ozone column (TTCO) derived with the convective cloud differential (CCD) technique for January, April, July, and October 2008 using GOME-2 data. . . . . 56
- 3.4 First-order (lag-1) autocorrelation of cloud-free ( $cf < 0.1$ ) monthly mean total ozone data for a) GOME (2002), b) SCIAMACHY (2008) and c) GOME-2 (2008) WFDOAS data. . . 57
- 3.5 a) The uncertainty in the WFDOAS TCO retrieval in August 2002 using GOME, and in August 2008 using SCIAMACHY and GOME-2 data b) the uncertainty of monthly averaged zonal ACCO for 2002 using GOME data and 2008 using SCIAMACHY and GOME-2 c) the uncertainty in the monthly averaged zonal ACCO due to CF for the same years as before d) the uncertainty in the monthly averaged zonal ACCO due to CTH for the same years as before e) the total uncertainty in the TTCO using the CCD method on GOME WFDOAS total ozone data in 2002 and SCIAMACHY and GOME-2 WFDOAS total ozone data in 2008. . . . . 60
- 3.6 Time series of monthly mean CCD tropospheric ozone columns and collocated monthly mean SHADOZ ozonesonde TTCO in Hilo, Paramaribo, and Kuala Lumpur (from top to bottom). The red lines give the integrated ozone column from sonde ozone up to the fixed level of 200 hPa (roughly 12 km). The blue tinted lines are: (a) GOME-1 CCD ozone columns (1996-2003), (b) SCIAMACHY CCD ozone columns (2003-2012), and (c) GOME-2 CCD ozone columns (2007-2015). Error bars indicate the  $1 \sigma$  uncertainty of the monthly mean. No error bars are shown for months with only one ozonesonde launch available. The average TTCO for each instrument and sondes with the standard deviation of the mean is shown on top of each plot. The difference between CCD and ozonesondes is plotted in the bottom. . . . . 64
- 3.7 Time series of monthly mean CCD tropospheric ozone columns and collocated monthly mean SHADOZ ozonesonde TTCO in Nairobi, Natal, and Java (from top to bottom). The red lines give the integrated ozone column from sonde ozone up to the fixed level of 200 hPa (roughly 12 km). The blue tinted lines are: (a) GOME-1 CCD ozone columns (1996-2003), (b) SCIAMACHY CCD ozone columns (2003-2012), and (c) GOME-2 CCD ozone columns (2007-2015). Error bars indicate the  $1 \sigma$  uncertainty of the monthly mean. No error bars are shown for months with only one ozonesonde launch available. The average TTCO for each instrument and sondes with the standard deviation of the mean is shown on top of each plot. The difference between CCD and ozonesondes is plotted in the bottom. . . . . 65

- 3.8 Time series of monthly mean CCD tropospheric ozone columns and collocated monthly mean SHADOZ ozonesonde TCO in Ascension, Samoa, and Fiji (from top to bottom). The red lines give the integrated ozone column from sonde ozone up to the fixed level of 200 hPa (roughly 12 km). The blue tinted lines are: (a) GOME-1 CCD ozone columns (1996-2003), (b) SCIAMACHY CCD ozone columns (2003-2012), and (c) GOME-2 CCD ozone columns (2007-2015). Error bars indicate the  $1\sigma$  uncertainty of the monthly mean. No error bars are shown for months with only one ozonesonde launch available. The average TCO for each instrument and sondes with the standard deviation of the mean is shown on top of each plot. The difference between CCD and ozonesondes is plotted in the bottom. . . . . 66
- 3.9 a) Tropical tropospheric ozone column from CCD-IUP SCIAMACHY for August 2008. b) SCIAMACHY tropical tropospheric ozone column from Limb/Nadir matching technique up to 200 hPa for August 2008. c) Difference between CCD-IUP and LNM SCIAMACHY data in August 2008. . . . . 69
- 3.10 a) Mean bias between CCD and LNM for the years 2003 until 2011. b) Correlation (R) between CCD and LNM SCIAMACHY tropospheric ozone for the years 2003 until 2011. 70
- 4.1 Correction offsets using SCIAMACHY TCO as reference. (left) Correction offset for GOME: average difference of GOME from SCIAMACHY TCO for the years 2002-2003. (right). Correction offset for GOME-2: average difference of GOME-2 from SCIAMACHY TCO (in DU) for the years 2007-2012. The error bars denote the  $1\sigma$  standard deviations of the latitudinally averaged biases. . . . . 75
- 4.2 Trend in the correction offset for GOME-2. Black "x" denotes statistically non significant trend. . . . . 75
- 4.3 Time-series of the explanatory variables used in the regression (Up) ENSO-MEI indexes, (middle) QBO at 30 and 50 hPa from FU-Berlin and (bottom) Solar Cycle (10.7 cm) index from Natural Resources Canada. . . . . 81
- 4.4 a) Example of noise autocorrelation,  $\phi$ , for lags of zero to 4 months. The autocorrelation is equal to 1 for unlagged data ( $p=0$ ) and decays gradually with number of lagged months ( $p=1-4$ ) b) Maps of noise autocorrelation for 1 to 4-month lag. . . . . 83
- 4.5 Tropical tropospheric ozone trends using a linear multivariate first order auto-regression model for 6 harmonisation scenarios, see Sec. 4.1. The trends are given in DU per decade. Grid-boxes marked with "x" are statistically non-significant at the 95% confidence level. 86
- 4.6 Probability density function (PDF) (black) and cumulative density function (CDF) (green) of a) the trend (the frequency equals the number of grid-boxes) and b) the noise (shows the distribution of the noise time-series in all grid boxes for all months). Red lines show the Gaussian distribution calculated using the standard deviation from the distributions. 86

- 4.7 Tropospheric ozone trends for the global tropical tropospheric ozone between the years 1996 to 2015. Top: The multivariate linear trend (black), the fit (red) and the residual (orange) are over-plotted. The  $2\sigma$  uncertainty of the trend is reported. The next panels show the harmonic functions (green), ENSO (light blue), QBO (red), solar (orange). Overlaid in black for all proxies are the time series with all fit terms removed except the particular fit parameter. . . . . 87
- 4.8 (a) Tropical tropospheric ozone trends using a linear multivariate first order auto-regression model for the selected harmonised scenario 1 in DU/decade. Grid- boxes marked with "x" are statistically non-significant at the 95% confidence level ( $b > 2\sigma_\beta$ ) b)  $2\sigma$  standard deviation of the trend c) The correlation coefficient, R, between the multi-linear trend model fit and the original time-series. d) The RMS error between the trend model and the time-series e) The statistically significant trend that exceeds the maximum absolute difference of the trends calculated for all six scenarios. f) The significant tropical tropospheric ozone trend in %/year. . . . . 88
- 4.9 Tropical tropospheric ozone trend in A) central America, B) India, C) east Pacific Ocean, D) South America, E) central Atlantic Ocean, F) Indian Ocean, G) south Atlantic Ocean, and H) southern Africa. With orange color is plotted the residual noise. . . . . 90
- 4.10 Tropical tropospheric ozone trends for winter (DJF), spring (MAM), summer (JJA), and autumn (SON) for the years 1996 to 2015. . . . . 93
- 4.11 Tropospheric ozone trend in A) Ascension, B) Java, C) Kuala Lumpur, D) Nairobi, E) Natal, and F) Paramaribo, calculated using the CCD TCO dataset and integrated ozonesone measurements from the SHADOZ network. . . . . 95
- 5.1 Seasonally averaged harmonised tropical tropospheric ozone columns (TTCO) derived from the CCD technique between 1996 and 2015. . . . . 102
- 5.2 Zonal mean climatology (1996-2015) of tropical tropospheric ozone columns in DU using the harmonised CCD dataset. Latitude intervals are  $2.5^\circ$ . Values in DU. . . . . 103
- 5.3 Time versus longitude plot of CCD tropical tropospheric ozone; Left: absolute value. Middle: anomalies from January 1996 to December 2015. Right: the ENSO-MEI index [Wolter and Timlin, 1993, 1998]. . . . . 104
- 5.4 Contribution of various factors responsible for tropospheric ozone variability. Their response is derived by subtracting the minimum from the maximum proxy response in the time-series for each grid box. For a)-d) the contribution of each parameter is calculated as:  $FitCoef \cdot (max(index) - min(index))$ . For e) and f) the total contribution is calculated as:  $max(\sum(FitCoef)_i \cdot (index)_i) - min(\sum(FitCoef)_i \cdot (index)_i)$ , where  $i$  is  $i_{th}$  QBO proxy or  $i_{th}$  seasonal term used in the regression. Grid- boxes marked with "x" are statistically non-significant at the 95% confidence level. For e) and f) red "x" is marked only when all the parameters are statistically non-significant. . . . . 106

6.1	Monthly tropical tropospheric ozone anomalies for the regions of Brasilia (7.5°S–0°S, 45°W–60°W) and Indonesia (7.5°S–0°S, 95°E–110°E) in DU are plotted with blue lines. The ENSO index in °C is plotted with light blue line, and the Fire Radiative power (FRP) in mW/m <sup>2</sup> is plotted with red line. . . . .	112
6.2	The tropical tropospheric ozone anomalies for September–December 1997 and 2015 calculated using as reference the monthly climatology produced from the harmonised CCD dataset during 1996-2015. . . . .	114
6.3	The tropical tropospheric ozone anomalies for September- December 1999 and 2010 calculated using as reference the monthly climatology produced from the harmonised CCD dataset during 1996-2015. . . . .	115
6.4	Fire radiative power (mW/m <sup>2</sup> ) for September, October, November and December 2015 (left) and 2014 (middle) and the difference between 2015 and 2014 (right) (data from: <a href="ftp://fuoco.geog.umd.edu/modis/C4/cmgl/monthly/hdf/">ftp://fuoco.geog.umd.edu/modis/C4/cmgl/monthly/hdf/</a> ). . . . .	118
6.5	Tropical tropospheric nitrogen dioxide columns (data from: <a href="http://www.iup.uni-bremen.de/doas/">http://www.iup.uni-bremen.de/doas/</a> ) and carbon monoxide mixing ratios at 300 hPa (data form: <a href="http://terra.nasa.gov/data/mopitt-data">http://terra.nasa.gov/data/mopitt-data</a> ) for September 2015 and 2014 and the differences between them. White pixels denote missing data due to clouds. . . . .	119
6.6	Same as Figure 6.5 for October 2015 and 2014. . . . .	120
6.7	Same as Figure 6.5 for November 2015 and 2014. . . . .	121
6.8	Same as Figure 6.5 for December 2015 and 2014. . . . .	122
6.9	Tropical tropospheric nitrogen dioxide columns and carbon monoxide mixing ratios at 300 hPa for September 2015 (a,b) and 2014 (c,d) and the differences between them from EMAC (e,f) simulations. . . . .	125
6.10	Same as Figure 6.9 for October 2015 and 2014. . . . .	126
6.11	Same as Figure 6.9 for November 2015 and 2014. . . . .	127
6.12	Same as Figure 6.9 for December 2015 and 2014. . . . .	128
6.13	Tropical tropospheric ozone columns observed with GOME-2A and simulated by the ECHAM-MESSY atmospheric chemistry model (EMAC) for September 2015 (a,d) and 2014 (b,e), differences between 2015 and 2014 (c,f) and the differences between observations and model in 2014 and 2015, respectively (g, h). . . . .	129
6.14	Same as Figure 6.13 for October 2015 and 2014. . . . .	130
6.15	Same as Figure 6.13 for November 2015 and 2014. . . . .	131
6.16	Same as Figure 6.13 for December 2015 and 2014. . . . .	131
6.17	Inter-annual difference of EMAC tropical tropospheric ozone of the dynamical (left ) and biomass burning (right) components (in DU) for the months Sept-Dec 2014-2015. . . . .	133
1	Correction factors using SCIAMACHY TTCO as reference (top) Correction factors for GOME: average ratio of SCIAMACHY to GOME TTCO for the years Jan 2002 – Jun 2003 (bottom) correction factors for GOME-2: average ratio of SCIAMACHY to GOME-2 TTCO (in DU) for 2007–2012. . . . .	173
2	Number of TTCO data for SCIAMACHY and GOME-2 for 2007 – 2012. . . . .	174

3	Correlation R between the TTCO from the six harmonised scenarios and ozone columns until 200 hPa from ozonesonde data in Fiji, Ascension, Hilo, and Kuala Lumpur. . . . .	175
4	The same as Fig. 3 for American Samoa, Nairobi, Natal, and Paramaribo. . . . .	176
5	Maximum trend difference among all six harmonisation scenarios. . . . .	177
6	The $2\sigma$ uncertainty of the trend using six harmonisation scenarios. . . . .	177
7	Correlation coefficient, R, between the multi-linear trend model fit and the original time-series excluding the seasonal cycle. . . . .	178
8	Tropical tropospheric ozone time-series in DU (blue stars) and trend (black line) in Jakarta, Mexico, Manila, Mumbai, Bangkok, Lagos, Kinshasa, Bangalore, Lima, and Nairobi (in descending population size; size taken from United Nations [2015])). The regression fit is plotted with red lines while the residuals are plotted with yellow lines. The $2\sigma$ uncertainties are reported beside the trends. . . . .	179
9	Difference of tropical tropospheric ozone for September- December 2015–1997 (El Niño) and 2010–1999 (La Niña). . . . .	180

## List of Tables

1.1	Mixing ratio of gases in the Earth's atmosphere, with respect to dry air (taken from Jacob [2000], p.4 and <a href="http://library.wmo.int/opac/doc_num.php?explnum_id=3084">http://library.wmo.int/opac/doc_num.php?explnum_id=3084</a> . $10^{-6}$ mol/mol = 1 ppmv (parts per million volume) and $10^{-9}$ mol/mol=1 ppbv (parts per billion volume). Values followed by an asterisc (*) denote mean values in 2015. . . .	3
1.2	Characteristics of satellite instruments. . . . .	43
3.1	Statistical comparison between GOME, SCIAMACHY, and GOME-2 TCOs with ozonesondes for nine SHADOZ sites. Information presented here are the ozonesonde site, the mean TCO for GOME/SCIAMACHY and for ozonesondes, the relative difference, the bias and the RMS difference between CCD-IUP TCO and sondes and finally the correlation coefficient. . . . .	63
4.1	Mean differences (in DU) between the harmonised TCO datasets using six different harmonisation scenarios with integrated ozone columns until 200 hPa from nine ozonesonde stations. Bold are marked the harmonisation scenarios that have the smallest biases with ozonesondes for a given station. . . . .	77
4.2	Regional tropospheric ozone trends in 8 tropical regions. Bold are the regions where the trend is greater than three times the standard deviation of the trend ( $3\sigma$ ). . . . .	91
4.3	Tropospheric ozone trends in 6 sites, calculated from the CCD TCO dataset and ozonesonde profiles. With bold are marked the trends if they are greater than two times the standard deviation of the trend ( $2\sigma$ ). . . . .	94
4.4	Tropospheric ozone trends in 10 tropical Mega-cities using $CCD_{IUP}$ , (in DU/decade and %/year), $CCD_{DLR}$ , and LNM (in %/year) data and tropospheric $NO_2$ trends with their $2\sigma$ uncertainties. With bold are shown the statistically significant trends at the 95% confidence ( $p < 0.05$ ) level. . . . .	96
5.1	Zonal climatology of tropical tropospheric ozone column. . . . .	105

- 6.1 ENSO-MEI index for September–December 1997, 1999, 2010, and 2015. With bold are indicated the months with maximum (El Niño) and minimum (La Niña) ENSO-MEI index values [Wolter and Timlin, 2011]. . . . . 113